

COLLECTIVE PHENOMENA
IN THE NON-EQUILIBRIUM
QUARK-GLUON PLASMA

Dissertation
zur Erlangung des Doktorgrades
der Naturwissenschaften

vorgelegt beim Fachbereich Physik
der Johann Wolfgang Goethe-Universität
in Frankfurt am Main

von
Björn Peter Schenke
aus Iserlohn

Frankfurt am Main 2008
(D30)

vom Fachbereich Physik (13) der Johann Wolfgang Goethe-Universität
als Dissertation angenommen.

Dekan: Prof. Dr. D. H. Rischke

Gutachter: Prof. Dr. C. Greiner, JProf. Dr. A. Dumitru

Datum der Disputation: 03.07.2008

Zusammenfassung

Übersicht

In dieser Arbeit werden die Eigenschaften und die dynamische Entwicklung des Quark-Gluon-Plasmas, wie es in Schwerionen-Kollisionen erzeugt wird, behandelt. Insbesondere wird untersucht welche Rolle instabile kollektive Moden bei der Isotropisierung und Thermalisierung des Systems spielen können. Dazu wird zunächst der Einfluss von Kollisionen zwischen Teilchen im Medium auf die Wachstumsraten dieser Instabilitäten sowohl in einer Modellrechnung als auch in einer dynamischen WONG-YANG-MILLS Realzeit-Gitter-Rechnung bestimmt. Diese Simulation beinhaltet neben direkten elastischen Teilchen-Kollisionen auch die Wechselwirkung der Teilchen mit selbstkonsistent generierten Farbfeldern. Sie wird weiterhin benutzt, um dynamisch den Energieverlust und die Aufweitung von Jets (Teilchen(-schauer) mit hohem Transversalimpuls) zu betrachten. Insbesondere ist es auf diese Weise möglich, den Transportkoeffizienten \hat{q} zu bestimmen, wobei das Ergebnis weitgehend von der Gittergröße unabhängig ist. Des Weiteren wird die Jet-Propagation in Nichtgleichgewichts-Systemen untersucht. So wird ein anisotropes System in dem eine Chromo-WEIBEL-Instabilität auftritt simuliert, und der Einfluss der dadurch entstehenden großen Domänen von starken Farbfeldern auf die propagierenden Jet-Teilchen bestimmt. Weiterhin werden fermionische Moden in anisotropen Systemen untersucht. Dabei wird gezeigt, dass zumindest in der Hard-Loop-Näherung keine instabilen fermionischen Moden auftreten. Schließlich wird die Möglichkeit studiert, ob hochenergetische Photonen zur Bestimmung der Impulsraum-Anisotropie des in Schwerionen-Kollisionen erzeugten Systems verwendet werden können. Das Ausmaß der auftretenden Anisotropie ist entscheidend für die Rolle, welche Instabilitäten für Isotropisierung oder gar Thermalisierung spielen können, denn je größer die Anisotropie, desto größer sind die Wachstumsraten der instabilen Moden. Daher ist ihre Kenntnis extrem wichtig.

Einleitung

Vor bereits über dreißig Jahren wurde vorgeschlagen sich einen tieferen Einblick in die Natur der starken Wechselwirkung zu verschaffen, indem man “hohe Energie oder hohe Nukleonendichten über ein relativ großes Volumen” [1] verteilt. Erst später wurde realisiert, dass die asymptotische Freiheit [2, 3] der Theorie der starken Wechselwirkung (QCD) impliziert, dass bei hohen Energiedichten ein Zustand mit freien Quarks und Gluonen erreicht werden kann, welcher später Quark-Gluon-Plasma (QGP) [4, 5, 6, 7, 8] genannt wurde. Die einzige Möglichkeit, auf der Erde ausgedehnte Systeme mit entsprechend hohen Energiedichten zu erzeugen, sind Schwerionen-Kollisionen. Erste systematische Studien fanden am BEVALAC in Berkeley [9] statt, gefolgt von Experimenten am Alternating Gradient Synchrotron (AGS) [10] im Brookhaven National Laboratory (BNL), am CERN Super

Proton Synchrotron (SPS) [11] sowie am Relativistic Heavy Ion Collider (RHIC) [12] am BNL. In naher Zukunft werden noch höhere Energien am CERN Large Hadron Collider (LHC) [13] untersucht werden, sowie hohe Netto-Baryondichten am RHIC und am internationalen Beschleunigerzentrum FAIR (Facility for Antiproton and Ion Research at GSI, Darmstadt).

Besonders die Experimente am RHIC haben wichtige Ergebnisse über die Erzeugung und die Eigenschaften des QGPs geliefert. Neben vielen Indizien für ein Entstehen des QGPs in Schwerionen-Kollisionen bei RHIC-Energien, deutet der starke elliptische Fluss auf eine frühe Thermalisierung und eine sehr niedrige Viskosität des Mediums hin. Weiterhin lässt die starke Unterdrückung von Jets auf einen hohen Energieverlust der Partonen (Quarks und Gluonen) im Medium schließen.

In dieser Arbeit wird insbesondere die Möglichkeit der schnellen Isotropisierung und Thermalisierung durch Plasma-Instabilitäten näher untersucht. Sie bieten eine Erklärung für schnelle Equilibrierung, auch ohne die Annahme eines stark-gekoppelten QGPs, welche der asymptotischen Freiheit bei hohen Energiedichten widersprechen würde. Des Weiteren wird die Wechselwirkung von hochenergetischen Partonen mit dem Medium untersucht. Dabei wird besonderer Wert auf die Bestimmung des Einflusses der instabilen Moden in Nichtgleichgewichtssystemen gelegt.

Theoretischer Hintergrund

Zunächst werden die kinetischen Gleichungen für ein System von Quarks und Gluonen aus den KADANOFF-BAYM-Gleichungen abgeleitet. Dazu wird eine Mean-field Näherung sowie eine Gradienten-Entwicklung herangezogen. Man erhält so eine effektive Theorie für die kollektiven Moden des Systems bei der Skala gT , wobei T die Temperatur ist und g die zunächst als infinitesimal klein angenommene Kopplungskonstante. Im Limes unendlich hoher Energien ist diese Annahme korrekt. Im kollisionslosen Fall findet man auf diese Weise folgende VLASOV-Gleichungen für Gluonen bzw. Quarks

$$\begin{aligned} [V \cdot D_X, \delta n^g(\mathbf{k}, X)] + g V_\mu F^{\mu\nu} \partial_\nu n^g(K) &= 0, \\ [V \cdot D_X, \delta n^{q/\bar{q}}(\mathbf{k}, X)] \pm g V_\mu F^{\mu\nu}(X) \partial_\nu n(K) &= 0, \end{aligned} \quad (0.1)$$

wobei $D_X = \partial_X + igA_X$ die kovariante Ableitung bezüglich der Koordinate X bezeichnet, V^μ die Vierergeschwindigkeit der Teilchen, n_i die Hintergrunds-Verteilungsfunktion der Gluonen ($i = g$) bzw. Quarks ($i = q/\bar{q}$), sowie δn_i die entsprechenden Abweichungen vom statischen (zum Beispiel Gleichgewichts-) Hintergrund. $F^{\mu\nu} \equiv [D^\mu, D^\nu]/(ig)$ ist der Feldstärketensor des Eichfeldes. Die VLASOV-Gleichungen beschreiben die zeitliche Entwicklung eines Teilchensystems unter dem Einfluss selbstkonsistent erzeugter Farbfelder.

Löst man die kinetischen Gleichungen für die "harten" Teilchen, d.h. solche mit hohem Impuls, so lässt sich der induzierte Strom allein durch die Freiheitsgrade niedrigen Impulses darstellen. Dies führt letztlich zu einer effektiven Theorie für die kollektiven Moden mit Impulsen der Größenordnung gT . Aus dem induzierten Strom erhält man die Selbstenergie

$$\Pi_{ab}^{\mu\nu}(K) = g^2 \delta_{ab} \int_{\mathbf{p}} V^\mu \partial_\beta^{(p)} f(\mathbf{p}) \left(g^{\nu\beta} - \frac{V^\nu K^\beta}{K \cdot V + i\epsilon} \right), \quad (0.2)$$

das selbe Ergebnis, wie man es mittels der diagrammatischen Methode in der so genannten “hard-thermal-loop”-Näherung erhält, in der alle externen Impulse als klein gegenüber den Loop-Impulsen angenommen werden. Mit Hilfe der Selbstenergie (0.2) lassen sich die Dispersionsrelationen der kollektiven Moden bestimmen. Dies wird neben einem isotropen System auch für ein System mit einer Impulsraum-Anisotropie durchgeführt. Man findet, dass in diesem Falle auch instabile Moden auftreten, welche der WEIBEL-Instabilität in elektro-magnetischen Plasmen entsprechen. Die anisotrope Verteilung wird in den expliziten Rechnungen durch Strecken bzw. Stauchen einer isotropen Verteilung erhalten:

$$f(\mathbf{p}) = \mathcal{N}(\xi) f_{\text{iso}} (\mathbf{p}^2 + \xi(\mathbf{p} \cdot \hat{\mathbf{n}})^2) \quad (0.3)$$

Die Richtung der Anisotropie ist durch $\hat{\mathbf{n}}$ gegeben, $\xi > -1$ ist ein veränderlicher Anisotropieparameter und $\mathcal{N}(\xi)$ ein Normierungsfaktor. Neben der Ableitung der Wachstumsraten dieser Instabilitäten unter der Annahme der oben angegebenen Art von Anisotropie, werden die physikalischen Mechanismen besprochen, die zu einer solchen Instabilität führen.

Um numerische Simulationen mittels Testteilchen durchzuführen, werden die WONG-Gleichungen abgeleitet, welche, gekoppelt an die YANG-MILLS-Gleichungen für die Felder

$$D_\mu F^{\mu\nu} = J^\nu = g \sum_i q_i v_i^\nu \delta(\mathbf{x} - \mathbf{x}_i(t)), \quad (0.4)$$

die Entwicklung eines mikroskopischen Systems individueller Teilchen beschreiben. Sie lauten

$$\dot{\mathbf{x}}_i(t) = \mathbf{v}_i(t), \quad (0.5)$$

$$\dot{\mathbf{p}}_i(t) = g q_i^a(t) (\mathbf{E}^a(t) + \mathbf{v}_i(t) \times \mathbf{B}^a(t)), \quad (0.6)$$

$$\dot{q}_i(t) = -i g v_i^\mu(t) [A_\mu(t), q_i(t)]. \quad (0.7)$$

Besonders interessant ist die letzte Gleichung, die es in der Elektrodynamik nicht gibt. Sie beschreibt die Rotation der Farbladung q (Farbvektor) durch die Farbfelder. Es wird gezeigt, dass die WONG-Gleichungen äquivalent zu den VLASOV-Gleichungen sind, sofern man die kontinuierliche Teilchenverteilung n durch eine große Menge Testteilchen ersetzt.

Nach der detaillierten Beschreibung der numerischen Simulation wird erläutert, wie binäre Kollisionen in die Simulation, welche zunächst nur Teilchen-Feld-Wechselwirkungen beschreibt, aufgenommen werden können. Mittels der stochastischen Methode wird anhand der Wirkungsquerschnitte für Kollisionen zwischen zwei Teilchen bestimmt, ob eine Kollision stattfindet und welcher Impuls ausgetauscht wird.

Da die Wechselwirkung über die Felder sozusagen schon niedrige Impulsaustausche zwischen Teilchen enthält (ein Teilchen erzeugt durch seine Farbladung ein Feld, in dem ein anderes Teilchen abgelenkt wird), werden nur solche Kollisionen implementiert, deren Impulsaustausch größer ist als der Impuls der maximalen Feldmode auf dem Gitter $k^* \sim \pi/a$, wobei a der Gitterabstand ist.

Physikalisch ist es sinnvoll, k^* so zu wählen, dass es im Bereich der Temperatur (für ein System im Gleichgewicht), welche die Impulsskala der Teilchen festlegt, liegt, denn oberhalb der Temperatur ist eine Beschreibung mittels klassischer Felder nicht mehr anwendbar.

Die Simulation erlaubt das Studium von Nichtgleichgewichtssituationen, da die Infrarotdivergenz der Kollisionsterme nicht künstlich mit Hilfe von Größen aus der Gleichgewichtsbeschreibung, wie der DEBYE-Masse, reguliert werden müssen.

Ergebnisse

Modell-Beschreibung des Effekts von Kollisionen auf Plasma-Instabilitäten

Kollisionen zwischen den ‘‘harten’’ Teilchen werden mittels eines zusätzlichen Kollisions-terms in den Gleichungen (0.1) eingeführt:

$$V \cdot \partial_X \delta f_a^i(p, X) + g\theta_i V_\mu F_a^{\mu\nu}(X) \partial_\nu^{(p)} f^i(\mathbf{p}) = C_a^i(p, X), \quad (0.8)$$

mit

$$C_a^i(p, X) = -\nu \left[f_a^i(p, X) - \frac{N_a^i(X)}{N_{\text{eq}}^i} f_{\text{eq}}^i(|\mathbf{p}|) \right]. \quad (0.9)$$

Dieser der Relaxationszeit-Näherung ähnliche Term beschreibt, wie die Kollisionen das System innerhalb einer Zeit proportional zur inversen Kollisionsrate ν^{-1} ins Gleichgewicht bringen. Gleichung (0.8) gilt im effektiv Abelschen Limes, welcher gilt, solange die Felder A nicht zu groß werden. Daher $D_X \rightarrow \partial_X$, $F^{\mu\nu} \rightarrow \partial^\mu A^\nu - \partial^\nu A^\mu$, und die Gleichungen für die einzelnen Farbkomponenten entkoppeln. Die f bezeichnen hier die Komponenten der Teilchenverteilungen, f_{eq} ist die Verteilung im Gleichgewicht.

Nun können die kinetischen Gleichungen gelöst werden und analog zum kollisionslosen Fall der induzierte Strom und daraus die Selbstenergie der kollektiven Moden bestimmt werden. Nachdem der Einfluss des Kollisionsterms auf die stabilen Moden besprochen wurde, wird die Unterdrückung der Wachstumsrate der instabilen Moden bestimmt. Fig. 0.1 zeigt die Abhängigkeit der maximalen Wachstumsrate von der Kollisionsrate in Einheiten der DEBYE-Masse für unterschiedliche Anisotropieparameter ξ . Es stellt sich heraus, dass

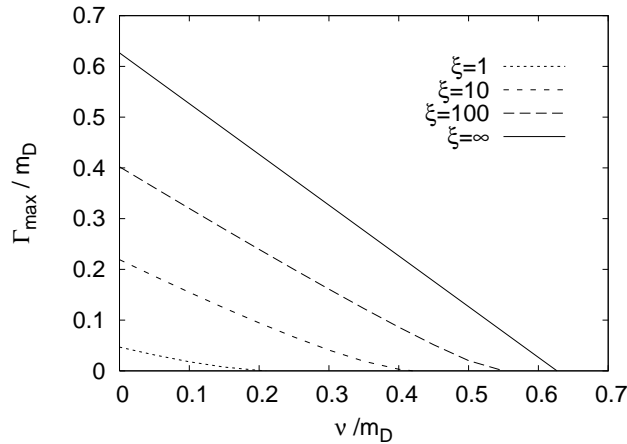


Figure 0.1: Die maximale Wachstumsrate der Instabilität als Funktion der Kollisionsrate ν .

abhängig vom Grad der Anisotropie maximale Kollisionsraten existieren, oberhalb derer keine Instabilitäten mehr auftreten.

Die Abschätzung der Kollisionsrate ν wird dadurch erschwert, dass alle bisherigen Rechnungen strikt perturbativ sind und bei für Schwerionen-Kollisionen relevanten Kopplungskonstanten $\alpha_s \approx 0.2 - 0.3$ nicht uneingeschränkt verwertbar sind. Eine grobe Abschätzung

jedoch führt auf $\nu \approx 0.1 - 0.2 m_D$, was für starke Anisotropien deutlich unterhalb der kritischen Kollisionsrate liegt, oberhalb derer keine Instabilitäten mehr auftreten.

Wong-Yang-Mills Simulation

Die eingangs bereits beschriebene numerische Simulation eines nicht-Abelschen Plasmas einschließlich Feld-Teilchen und Teilchen-Teilchen-Wechselwirkung erlaubt das Studium von Plasmen im und weit entfernt vom Gleichgewicht. Im Falle eines isotropen Plasmas wird die Impulsdiffusion von Teilchen mit hohem Impuls (Jets) untersucht. Es stellt sich heraus, dass wenn die Energiedichte und das Spektrum der Felder der Teilchenverteilung korrekt angepasst wird, weitgehend Gitter-unabhängige Ergebnisse für den Transportkoeffizienten \hat{q} , definiert als

$$\hat{q} = \frac{1}{\sigma\lambda} \int d^2p_{\perp} p_{\perp}^2 \frac{d\sigma}{dp_{\perp}^2}, \quad (0.10)$$

erzielt werden. Letztlich ist dies die Steigung des akkumulierten $\langle p_{\perp}^2 \rangle(t)$, gezeigt in Fig. 0.2. Je größer das Gitter, desto größer der Anteil der Felder an der Wechselwirkung zwischen den Jet-Teilchen und dem Medium. Je kleiner das Gitter, desto größer der Anteil der direkten Kollisionen. Dennoch ist deutlich zu sehen, dass bei verschiedenen Gittergrößen, also unterschiedlichen k^* , das gleiche Ergebnis für $\langle p_{\perp}^2 \rangle(t)$ erhalten wird.

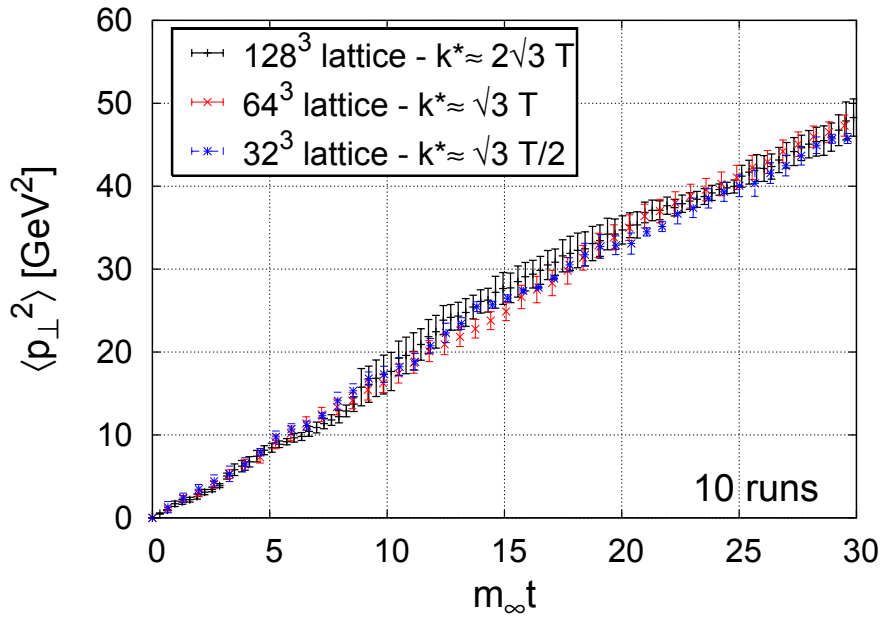


Figure 0.2: Jet Impulsraum-Diffusion bedingt durch unterschiedliche Anteile Feld-Teilchen Wechselwirkung und direkter binärer Kollisionen. $T = 4$ GeV, $g = 2$, $n_g = 10/\text{fm}^3$, $m_{\infty} = 1.4/\text{fm}$.

Wie bereits erwähnt können auch Nichtgleichgewichtssituationen simuliert werden. Für den Fall eines Teilchenhintergrundes mit anisotroper Impulsverteilung treten auch in der

Simulation Plasma-Instabilitäten auf. Erlaubt man Kollisionen zwischen den Teilchen wird eine Verringerung der mittleren Wachstumsrate um zwischen 10 und 15% festgestellt. In diesem Fall ist das Ergebnis abhängig von der Wahl von k^* . Dieses sollte jedoch wie oben erwähnt aus physikalischen Gründen in den Bereich des mittleren Impulses der Teilchen gelegt werden. Kollisionen reduzieren das Anwachsen von Instabilitäten also nicht dramatisch, wie bereits aufgrund von Ergebnissen der Modell-Rechnung geschlossen werden konnte.

Betrachtet man nun, wie im isotropen Fall zuvor, Jets und misst ihren transversalen Impuls, stellt sich heraus dass dieser entlang der Richtung der Anisotropie $\hat{\mathbf{n}}$ stärker anwächst als senkrecht dazu. Im Falle einer Schwerionen-Kollision entspricht dies einer stärkeren Aufweitung des Jets in Richtung der Strahlachse (z) als senkrecht zu dieser. Dies wurde auch experimentell in Zwei-Teilchen-Korrelationen gefunden. Fig. 0.3 zeigt, wie während der Zeit in der die Instabilität anwächst, $\langle p_z^2 \rangle$ deutlich stärker ansteigt als $\langle p_\perp^2 \rangle$. Der Grund

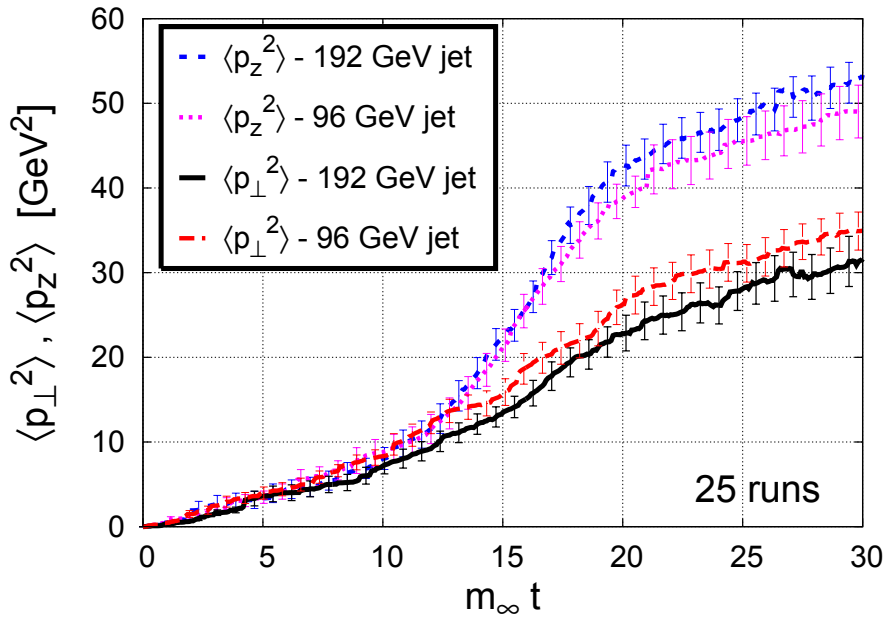


Figure 0.3: Impulsaufweitung von Jets in die Richtungen senkrecht zu seinem anfänglichen Impuls. p_z zeigt entlang der Strahlrichtung, p_\perp steht senkrecht zum Strahl.

für diesen Effekt ist das Entstehen ausgedehnter Domänen von starken Farbfeldern mit $E_z > B_z$ und $B_\perp > E_\perp$ durch die Instabilität, wodurch eine stärkere Ablenkung in die z -Richtung bewirkt wird. Dass dies geschieht ist nicht trivial, denn im nicht-Abelschen Fall wachsen im Gegensatz zum Abelschen Fall alle Komponenten des Farbfeldes an. Der Quotient der Steigungen von $\langle p_z^2 \rangle$ und $\langle p_\perp^2 \rangle$ im Bereich der Instabilität beträgt ca. 2.3, was für die Messgröße $\langle \Delta\eta \rangle / \langle \Delta\phi \rangle \approx 1.5$ ergibt, wobei η die Pseudorapidität und ϕ der azimuthale Winkel ist. Chromo-WEIBEL-Instabilitäten im anisotropen Plasma bieten also zumindest qualitativ eine mögliche Erklärung für die experimentell bestimmte asymmetrische Aufweitung von Jets in Schwerionen-Kollisionen.

Fermionische kollektive Moden

Um zu bestimmen, ob auch instabile fermionische kollektive Moden zur Isotropisierung des Plasmas beitragen können werden diese im Rahmen der “hard-loop” (HL) Näherung untersucht. Es wird sowohl numerisch als auch für bestimmte Fälle analytisch mit Hilfe komplexer Kontur-Integration gezeigt, dass zumindest im Rahmen der HL-Näherung keine fermionischen Instabilitäten im QGP auftreten.

Photonenproduktion als Maß für die Anisotropie des Quark-Gluon-Plasmas

Wie eingangs erwähnt ist die Stärke der Impulsraum-Anisotropie des Systems entscheidend für die Rolle, welche Instabilitäten für Isotropisierung und Thermalisierung spielen können. Zudem gibt es keinen theoretischen Beweis dafür, dass das System tatsächlich so schnell isotropisiert, wie aus der Anwendbarkeit idealer Hydrodynamik auf die Beschreibung experimenteller Daten geschlossen wurde.

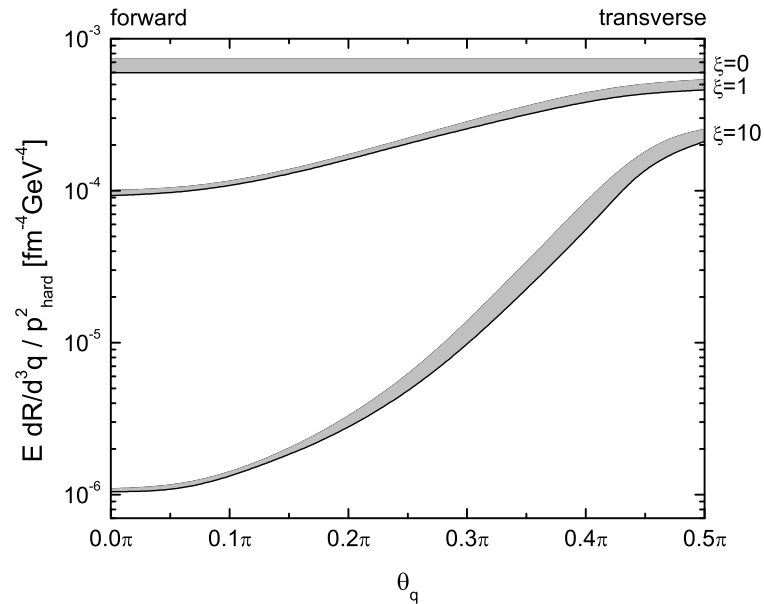


Figure 0.4: Photonenrate für $\xi = \{0, 1, 10\}$ als Funktion des Winkels zwischen Photon und Strahlachse, θ_q , für $E/p_{\text{hard}} = 5$ und $\alpha_s = 0.3$.

Daher ist man gezwungen nach Observablen zu suchen, welche sensitiv auf frühe Anisotropien in den Quark und Gluon Verteilungsfunktionen sind. Ideale Kandidaten sind elektromagnetische Observable, wie hochenergetische Dileptonen oder Photonen. Ihre hohe Energie lässt darauf schließen, dass sie frühzeitig in der Kollision entstanden sind. Weiterhin wechselwirken sie nur elektromagnetisch mit dem Medium, haben daher eine lange mittlere freie Weglänge und können das Medium nahezu immer ohne weitere Wechselwirkung verlassen. Daher bieten sie ungestörte Informationen über die frühen Stadien des in Schwerionen-Kollisionen erzeugten Mediums.

In dieser Arbeit wird die Produktion von Photonen in einem Quark-Gluon-Plasma mit einer Impulsraum-Anisotropie, wie sie im frühen Stadium einer Schwerionen-Kollision auf-

grund der longitudinalen Expansion erwartet wird, berechnet. Dabei werden sowohl der Mechanismus der COMPTON-Streuung, $q(\bar{q})g \rightarrow q(\bar{q})\gamma$, als auch der Quark-Antiquark-Anihilation, $q\bar{q} \rightarrow g\gamma$, einbezogen.

Es wird gezeigt, dass die BRAATEN-YUAN-Methode zur Regulierung der Infrarot-Divergenz der Photonenerate auch im anisotropen Fall angewandt werden kann. Für kleine Kopplungskonstanten $g \ll 1$ ist im Bereich des geometrischen Mittels zwischen der harten Impulsskala T und der Skala der niedrigen Impulse gT die totale Rate nahezu unabhängig von der Lage der Separation zwischen den beiden Bereichen. Für größere g findet sich dort anstelle eines Plateaus nur ein Minimum. In diesem Bereich kann die totale Rate berechnet werden. Fig. 0.4 zeigt die Winkelabhängigkeit der Rate in Plasmen mit unterschiedlichen Anisotropieparametern ξ . Man erkennt eine starke Winkelabhängigkeit

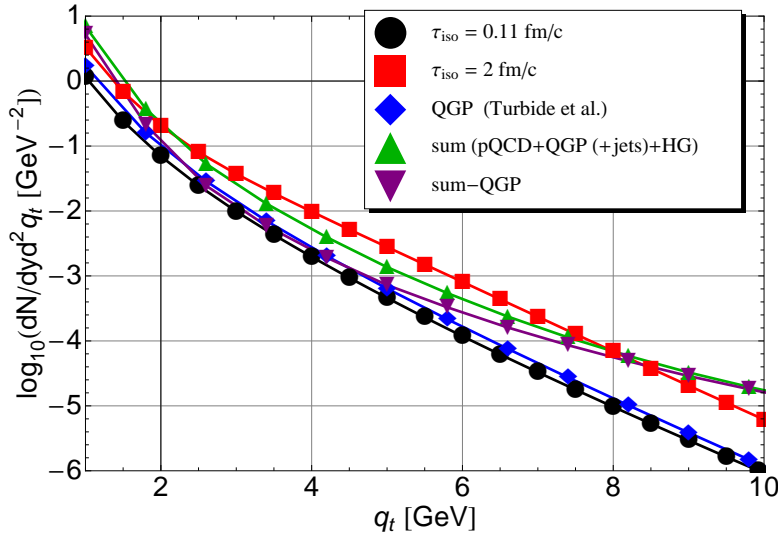


Figure 0.5: Photonenerate bei festen Anfangsbedingungen. $\sqrt{s} = 5.5$ TeV, $T_0 = 845$ MeV, $y_\gamma = 0$. Die Rechnungen für $\tau_{\text{iso}} = \tau_0 = 0.11$ fm/c (reine hydrodynamische Expansion) und $\tau_{\text{iso}} = 2$ fm/c werden mit den Ergebnissen von Turbide et al. [14] verglichen, wobei bei diesen das Ergebnis für den thermischen QGP-Beitrag (auch mit $\tau_{\text{iso}} = \tau_0 = 0.11$ fm/c) zusätzlich Bremsstrahlung und inelastische Paar-Anihilation in führender Ordnung enthält.

der Rate in anisotropen Plasmen. Observabel ist aber nur der totale Ertrag an Photonen, den wir erhalten, wenn wir die Rate über die gesamte Raum-Zeit-Geschichte der Schwerionen-Kollision integrieren. Fig. 0.5 zeigt das Ergebnis für den Yield bei instantaner Isotropisierung und einer Isotropisierungszeit von 2 fm, in der das System vom frei strömenden Zustand in hydrodynamische Expansion übergeht. Zum Vergleich sind weitere Beiträge, auch aus der Hadronengas-Phase aufgeführt.

Insgesamt zeigt sich, dass obwohl die starke Abhängigkeit der Rate von der Stärke der Anisotropie sich nicht in der Gesamtzahl der Photonen widerspiegelt, ein Effekt in der messbaren Photonenerate bestehen bleibt. Die experimentelle Extraktion der berechneten Unterschiede im Bereich eines Faktors 2-6 ist aufgrund des starken Hintergrundes, besonders auch von Photonen aus Pion-Zerfällen, ein schwieriges Unterfangen. Weitere Untersuchun-

gen des Einflusses einer Impulsraum-Anisotropie auf die anderen Beiträge zur Photonproduktion könnten weiteren Aufschluss geben und werden in Zukunft durchgeführt werden.

Abstract

In this work we study the non-equilibrium dynamics of a quark-gluon plasma, as created in heavy-ion collisions. We investigate how big of a role plasma instabilities can play in the isotropization and equilibration of a quark-gluon plasma. In particular, we determine, among other things, how much collisions between the particles can reduce the growth rate of unstable modes. This is done both in a model calculation using the hard-loop approximation, as well as in a real-time lattice simulation combining both classical YANG-MILLS-fields as well as inter-particle collisions. The new extended version of the simulation is also used to investigate jet transport in isotropic media, leading to a cutoff-independent result for the transport coefficient \hat{q} . The precise determination of such transport coefficients is essential, since they can provide important information about the medium created in heavy-ion collisions. In anisotropic media, the effect of instabilities on jet transport is studied, leading to a possible explanation for the experimental observation that high-energy jets traversing the plasma perpendicular to the beam axis experience much stronger broadening in rapidity than in azimuth. The investigation of collective modes in the hard-loop limit is extended to fermionic modes, which are shown to be all stable. Finally, we study the possibility of using high energy photon production as a tool to experimentally determine the anisotropy of the created system. Knowledge of the degree of local momentum-space anisotropy reached in a heavy-ion collision is essential for the study of instabilities and their role for isotropization and thermalization, because their growth rate depends strongly on the anisotropy.

Contents

1	Introduction	1
1.1	Nuclear matter under extreme conditions	1
1.2	Important results from RHIC	4
1.3	Thermalization of the QGP and plasma instabilities	5
1.4	Hard observables	7
1.5	Electromagnetic probes	9
1.6	Outline of this work	9
2	Kinetic theory for hot QCD plasmas	11
2.1	Non-Abelian plasmas	11
2.2	Derivation of the kinetic equations in background field gauge	12
2.2.1	Mean field approximation	16
2.2.2	Gradient expansion	17
2.3	The non-Abelian Vlasov equations	21
2.3.1	Vlasov equation for gluons	21
2.3.2	Vlasov equation for quarks	22
3	Effective theory for the soft modes	25
3.1	Solving the kinetic equations	25
3.2	Dispersion relations in the isotropic limit	27
4	The anisotropic quark-gluon plasma	31
4.1	Tensor decomposition	33
4.2	Stable modes	34
4.3	Unstable modes	35
4.4	Discussion of instabilities	35
4.4.1	Seeds and mechanism of filamentation	37
4.4.2	Isotropization and Abelianization	38
4.4.3	Summary of recent numerical simulations	38
5	A model approach to the inclusion of collisions	45
5.1	Structure functions and dispersion relations	45
5.2	Stable modes	50
5.3	Unstable modes	52
5.4	Discussions	54
6	Wong-Yang-Mills simulation including collisions	59
6.1	The Wong equations	59
6.2	The relation between the Wong and the Vlasov equations	61

6.3	Numerical methods for solving the Wong-Yang-Mills system	62
6.3.1	Lattice simulation	63
6.3.2	Coordinate and current update	63
6.3.3	The field updates	70
6.3.4	Momentum update	71
6.4	Inclusion of binary collisions	72
6.4.1	Cross section and transition rate	73
6.4.2	Momentum transfer	76
6.5	Momentum space diffusion	77
6.5.1	The separation scale	77
6.5.2	Initial energy density	78
6.5.3	Jet momentum diffusion	79
7	Real-time simulation of plasma instabilities	85
7.1	The collisionless limit	85
7.2	Instabilities under the influence of collisions	89
7.3	Isotropization	91
7.4	Collective effects on jet propagation	93
8	Fermionic collective modes of an anisotropic quark-gluon plasma	101
8.1	Quark self-energy in an anisotropic system	101
8.2	Analytical investigation	105
8.2.1	Special case: $\mathbf{k} \parallel \hat{\mathbf{n}}$	105
8.2.2	Large- ξ limit	108
8.3	Summary	109
9	Photon production from an anisotropic quark-gluon plasma	111
9.1	Medium photon production rate	111
9.1.1	Cross sections	113
9.2	Infrared divergence and Braaten-Yuan method	117
9.2.1	Hard contribution	117
9.2.2	Soft contribution	119
9.2.3	Total contribution	124
9.2.4	The isotropic limit	125
9.3	Results for the anisotropic case	127
9.4	Total photon yield	128
9.5	Conclusions	132
10	Conclusions and Outlook	135
	Appendices	139
A	Gauge covariance of the Coulomb type gauge fixing term	141
B	Experimental evidence of the Weibel instability in plasma physics	143
C	Abelianization	145

D	Hamiltonian formulation of lattice gauge theory	149
D.1	Fermion fields on a lattice	149
D.2	Gauge field on a lattice and analogy to the rigid rotator	151
D.3	Gauge-invariant space of states	152
D.4	The gauge-field Hamiltonian	154
E	The relativistic relative velocity	157
F	Validity of the equilibrium fluctuation dissipation relation in the hard-loop limit	161
	Bibliography	163
	Index	183

1 Introduction

Auf diesem beweglichen Erdball ist doch nur in der wahren Liebe, der Wohltätigkeit und den Wissenschaften die einzige Freude und Ruhe.

an Charlotte von Stein, 6. Dezember 1781
Johann Wolfgang von Goethe (1749-1832)

1.1 Nuclear matter under extreme conditions

Over thirty years ago (1974) [1], it was suggested to explore new phenomena “by distributing high energy or high nucleon density over a relatively large volume”, to temporarily restore broken symmetries of the physical vacuum and possibly create novel states of nuclear matter [15]. At this point, the idea of quark matter as the ultimate state of nuclear matter at high energy density had not taken hold. However, concurrently COLLINS and PERRY and others [16, 17, 18, 19] realized that the asymptotic freedom of the theory of strong interactions, quantum chromodynamics (QCD), shown in 1973 by GROSS, WILCZEK and POLITZER [2, 3]¹, implies the existence of an ultra-dense form of matter with deconfined quarks and gluons, later called the quark-gluon plasma (QGP) [4, 5, 6, 7, 8]. Fig. 1.1 shows the experimental verification of the running of α_s and of asymptotic freedom in excellent agreement with the predictions from QCD.

The possibility of accelerating and colliding uranium ions in the CERN² Intersecting Storage Rings (ISR) to create states of high energy density was contemplated already in the late 1960’s. In the following years, due to the arising expectations described above, heavy-ion physics was moved to the forefront as a research tool. Heavy-ion experiments have sometimes been referred to as little Big-Bangs in the laboratory because the produced conditions are also expected to have existed for a brief time shortly after the Big Bang, with temperatures exceeding 200 MeV (about 2×10^{12} K, which is about 100,000 times the temperature of the core of the sun [23]) for the first 10 μ s in the history of our universe. Systematic studies with heavy-ions started with experiments at the BEVALAC [9]³ at Berkeley, followed by the Alternating Gradient Synchrotron (AGS) [10] at Brookhaven National Laboratory (BNL) and the CERN Super Proton Synchrotron (SPS) [11], culminating at present at the Relativistic Heavy Ion Collider (RHIC) [12] at BNL. In the near future, even higher energies will be explored at the CERN Large Hadron Collider (LHC) [13], and large net

¹Gross, Politzer and Wilczek won the 2004 Nobel Prize in physics “for the discovery of asymptotic freedom in the theory of the strong interaction”[20]

²*European Organization for Nuclear Research*, acronym derived from the name of the council formed to set up the laboratory: *Conseil Européen pour la Recherche Nucléaire* (CERN)

³The references indicated after the facilities’ names are brief descriptions of the respective facility.

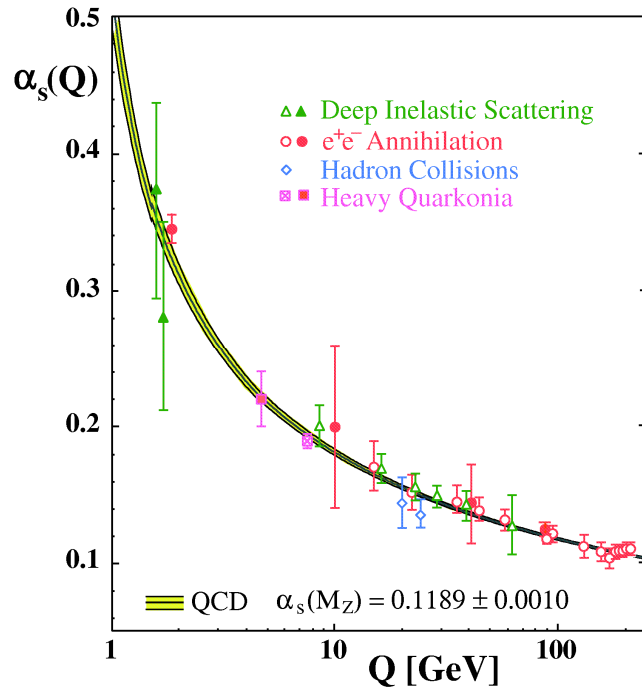


Figure 1.1: Summary of measurements of $\alpha_s(Q)$ as a function of the respective energy scale Q . Open symbols indicate (resummed) next-to-leading-order (NLO), and filled symbols next-to-NLO (NNLO) QCD calculations used in the respective analysis. The curves are the QCD predictions for the combined world average value of $\alpha_s(M_{Z^0}) = 0.1189 \pm 0.0010$ [21] (the value of the strong coupling constant at the Z^0 -boson mass $M_{Z^0} = 91.1876 \pm 0.0021$ GeV [22]), in 4-loop approximation and using 3-loop threshold matching at the heavy quark pole masses $M_c = 1.5$ GeV and $M_b = 4.7$ GeV. Figure taken from [21]. Please see [21] for the references to the respective experiments.

baryon densities will be studied at RHIC and, later, at GSI-FAIR⁴ [24]. At RHIC, a vast data base [25] on $p+p$, $D+Au$, and $Au+Au$ at a center of mass energy $\sqrt{s} = 20-200$ AGeV (GeV per nucleon) has been harvested. Energies at the LHC will reach up to $\sqrt{s} = 5.5$ TeV for $Pb+Pb$ collisions.

To estimate when the transition to the QGP takes place, one can calculate the pressure depending on the degrees of freedom in a hadron gas and in the QGP using the bag model. When the pressures become equal, a phase transition occurs. The degrees of freedom for a gas of massless pions are 3, for a QGP with 2 active light flavors (u and d) they are 16 for the gluons and 24 for the quarks and antiquarks together. Equating the resulting pressures leads to a transition temperature $T_c \approx 160$ MeV at zero quark chemical potential. This corresponds to an energy density of $\varepsilon \approx 1$ GeV fm⁻³, roughly 7.5 times that of normal nuclear matter ($\varepsilon_0 \approx 0.135$ GeV fm⁻³). To obtain more reliable information about the equation of state of QCD matter or to find out in which temperature domain the above

⁴Gesellschaft für Schwerionenforschung, Darmstadt, Germany. Facility for Antiproton and Ion Research at GSI.

rough estimate applies, one must turn to exact calculations of the energy density. At present, this requires massive computer simulations of QCD discretized on a lattice. Over the past few years, increasingly precise lattice calculations of thermal QCD, extrapolated to the continuum and thermodynamic limits and to small quark masses, have become available [26, 27, 28, 29, 30, 31, 32, 33, 34]. Such computations show that there is a rapid rise of

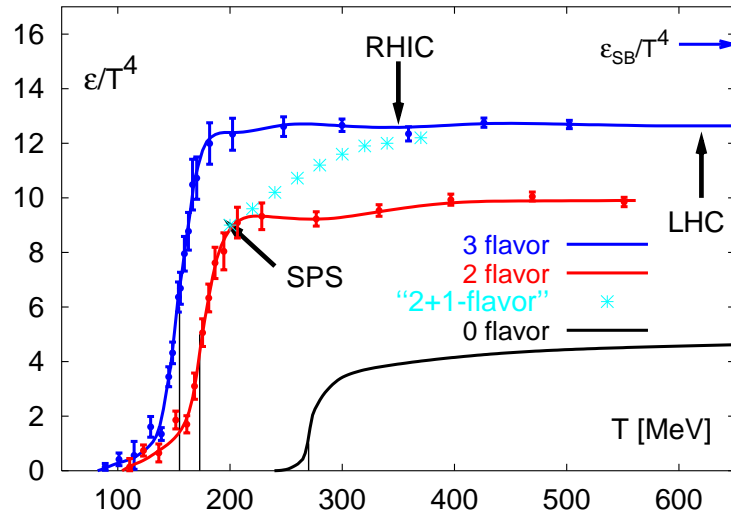


Figure 1.2: The energy density as a function of temperature scaled by T^4 from lattice QCD [26, 27, 28], taken from [35]. Various number of species of quarks are considered, including the realistic case of 2+1 flavors. An estimate of the typical temperature reached at SPS and RHIC, and estimated for LHC is included in the figure.

the energy density $\varepsilon(T)$ of matter when the temperature reaches $T \approx T_c \sim 160$ MeV, about the same temperature found for the phase transition using the rough estimate. The energy density changes about an order of magnitude in a narrow range of temperatures $\Delta T \sim 10$ -20 MeV as can be seen from Fig. 1.2. Since the energy density, pressure and entropy are all roughly proportional to the number of degrees of freedom, one can understand this rapid rise in the energy density over a narrow range of temperature as a change in the degrees of freedom between the confined and deconfined states. The system above T_c is called a plasma because the degrees of freedom carry the non-Abelian analog of charge, the so-called color-charge. Note that the transition between the confined hadronic state and the deconfined QGP may or may not be a phase transition in the strict statistical mechanical sense. Strictly speaking, a phase transition requires a mathematical discontinuity in the energy density or one of its derivatives in the infinite volume limit. The QGP transition may in fact be a “cross over”, or rapid change, as is suggested by numerical computations and a number of theoretical arguments. Nevertheless, the change as measured in numerical computation is very abrupt as seen in Fig. 1.2. Note that the lattice calculations are performed for matter with an equal number of baryons and anti-baryons, i.e., for vanishing baryo-chemical potential μ_b . The ab-initio evaluation of the phase boundary in the (T, μ_b) -plane poses major numerical difficulties, related to the FERMI-DIRAC-statistics of the quarks

(fermion-sign problem). Only recently new methods have been developed to investigate the region of finite μ_b [26, 36, 37]. To derive the full structure of the phase diagram one has to rely on a combination of information from several models. The bag-model (see [38]) predicts that the critical temperature decreases with increasing μ_b . It describes a first-order phase transition for all chemical potentials by construction. There are also indications from various QCD-inspired model studies, mainly the NAMBU-JONA-LASINIO (NJL) model, that the (chiral) phase transition is indeed a first-order one. Since the lattice results discussed above indicate a cross over at small μ_b , this would imply the existence of a critical endpoint in the phase diagram (see [39] for details). Fig. 1.3 shows a contemporary sketch of the

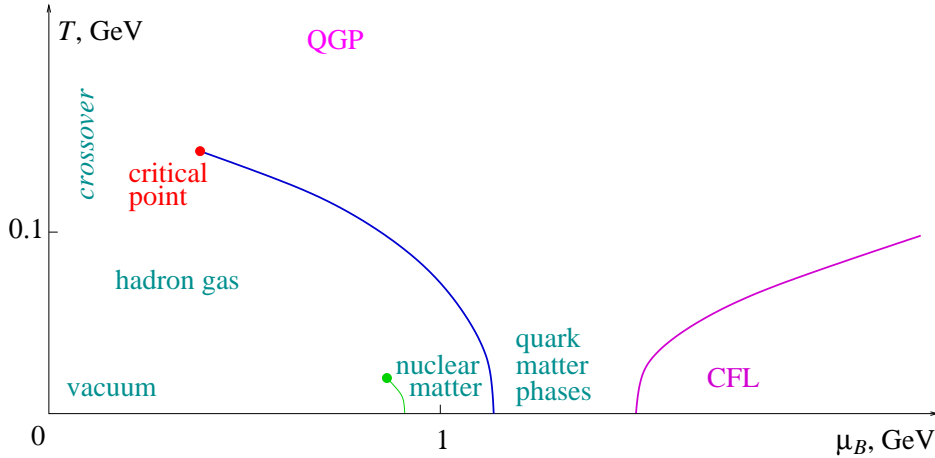


Figure 1.3: Semi-quantitative QCD-phase-diagram. Figure taken from [40].

phase diagram of strongly-interacting matter, including color-super-conducting phases at high μ_b (particularly the color-flavor-locked (CFL) phase, shown to be present for QCD with 3 quark flavors; see [41] for more details). For a recent overview of the properties of the phase-diagram of strongly interacting matter, see [42].

1.2 Important results from RHIC

Due to the many insights into the nature of the quark-gluon plasma the first phase of RHIC has become a great success. In its first six runs (2000-2006), RHIC has collected data on four different collision systems ($Au+Au$, $d+Au$, $Cu+Cu$, and $p+p$) at a variety of energies, ranging from nucleon-nucleon center-of-mass energies of 19.6 to 200 GeV. The largest data samples were collected at the highest energy of 200 GeV, where the accelerator has achieved sustained operation at four times the design luminosity. The ability to study proton-proton, deuteron-nucleus, and nucleus-nucleus collisions at identical center-of-mass energies with the same detectors allows for systematic control of the measurements to large extent. The experiments also measure the impact parameter (distance of closest approach) and the orientation of the reaction plane in each event. This detailed categorization of the collision geometry provides a wealth of differential observables, which have proven to be essential for a precise, quantitative study of the plasma. The results obtained by the four RHIC

experiments (BRAHMS, PHENIX, PHOBOS, and STAR), summarized in [43, 44, 45, 46] are in remarkable quantitative agreement with each other. The initial set of heavy-ion results from RHIC has provided evidence for the creation of a new state of thermalized matter at an unprecedented energy density of $(30 - 100)\varepsilon_0$, which exhibits almost ideal hydrodynamic behavior. Important results from the RHIC experiments include [47, 48]

- chemical (flavor) and thermal equilibration of all observed hadrons including multi-strange baryons; only the reaction $gg \rightarrow \bar{s}s$ is known to achieve this on the time-scale of the nuclear reaction
- strong elliptic flow, indicating early thermalization (at times on the order of 1 fm/c) and a very low viscosity of the produced medium
- collective flow patterns described well by the recombination model, related to independently flowing valence quarks, not hadrons
- strong jet quenching, implying a very large parton energy loss in the medium and a high color opacity of the produced matter
- strong suppression of open heavy flavor mesons at high transverse momentum, implying a large energy loss of heavy (c and b) quarks in the medium
- direct photon emission at high transverse momentum that remains unaffected by the medium
- charmonium suppression effects, likely due to the screening of color charges, that are similar to those observed at the lower energies of the CERN SPS.

In the following we will concentrate mainly on the second and fourth point, because this work deals particularly with the theoretical explanation of the apparent fast isotropization and/or thermalization, and the observed energy loss and broadening of jets.

1.3 Thermalization of the QGP and plasma instabilities

The matter created in relativistic heavy-ion collisions at RHIC manifests a strongly collective hydrodynamic behavior [49] which is particularly evident in studies of the so-called elliptic flow [50]. When the heavy nuclei do not collide head-on, the initial energy density is not azimuthally isotropic. As flow follows the energy density gradient, it will be stronger along the short overlap direction (so-called in-plane) than along the long overlap direction (out-of-plane), leading to an azimuthal momentum anisotropy of the particle emission. This anisotropy is quantified by decomposing the particle azimuthal momentum distribution in FOURIER coefficients such as [51]

$$\frac{dN}{dp_{\perp} d\varphi} = \frac{dN}{dp_{\perp}} (1 + 2v_1 \cos(\varphi) + 2v_2 \cos(2\varphi) + 2v_4 \cos(4\varphi) + \dots), \quad (1.1)$$

where v_2 is the elliptic flow coefficient. For ideal hydrodynamic models to apply, it is assumed that the stress-energy tensor is isotropic in momentum space, since having a local

momentum-space anisotropy requires the inclusion of shear viscosity. Furthermore the assumption of local thermal equilibrium is required, because an equilibrium equation of state (EOS) is used. Therefore, the success of ideal hydrodynamic models in describing the measured elliptic flow implies that the equilibration time of the system is as short as 1 fm/c [52]. Note, however, that it has also been argued [53] that the hydrodynamic collective behavior does not require local thermodynamic equilibrium but merely an isotropic momentum distribution of liquid components, meaning that the pressure in $T_{ij} = p\delta_{ij}$ does not have to be the equilibrium pressure. Thus, the above mentioned estimate of 1 fm/c would apply to the isotropization rather than to the equilibration time.

Such a fast isotropization or even equilibration can be explained assuming that the quark-gluon plasma is strongly-coupled [54]. However, it can not be excluded that due to the high-energy density at the early stage of the collision, when the elliptic flow is generated [55], the plasma is weakly-coupled because of asymptotic freedom. Thus, the question arises whether the weakly-coupled plasma can be equilibrated or at least isotropized within 1 fm/c.

Models that assume parton-parton collisions to be responsible for the thermalization of weakly-coupled plasmas lead to a longer equilibration time. Calculations performed within the “bottom-up” thermalization scenario [56], where binary and $2 \rightarrow 3$ collision processes are taken into account, give an equilibration time of at least 2.6 fm/c [57]. Numerical parton-cascade simulations also including $2 \leftrightarrow 3$ collisions lead to a value of ~ 1 fm/c for the equilibration time [58]. To thermalize the system one needs either a few hard collisions of momentum transfer of order of the characteristic parton momentum, usually denoted by p_{hard} or T as the temperature of an equilibrium system, or many collisions of smaller momentum transfer. For small coupling g , the orders of g are used to classify the different time scales in the system. When only regarding binary collisions, the inverse equilibration time is of order $g^4 \ln(g)T$ (with g being the QCD coupling constant) [59].

However, it has been proven recently that the previous calculations of the isotropization and equilibration times had overlooked an important aspect of non-equilibrium gauge field dynamics, namely the possibility of plasma instabilities [60, 61, 53]. These unstable collective modes cause the early stage QGP to have non-perturbative occupation numbers for soft fields. These non-perturbatively large field amplitudes ($f \sim 1/\alpha_s$, with $\alpha_s = g^2/4\pi$) mean that even at small values of the strong coupling constant the system can be strongly-interacting due to strong possible coherent particle-field interactions. The possibility of generating strongly-coupled systems from a system which does not necessarily have a strong coupling constant is familiar from studies of conventional QED plasmas where the electromagnetic coupling is very small and still the system can be strongly-coupled via collective modes.

One of the chief obstacles to thermalization in ultra-relativistic heavy-ion collisions is the intrinsic expansion of the produced matter. If the matter expands too quickly then there will not be time enough for its constituents to interact before flying apart and therefore the system will not reach thermal equilibrium. In a heavy-ion collision the longitudinal expansion (along the beam-line) is the most relevant, because at early times it is much faster than the radial expansion. At weak coupling this longitudinal expansion causes the system to quickly become much “colder” in the longitudinal than in the transverse (radial) direction, $\langle p_L \rangle \ll \langle p_\perp \rangle$.

The question is now how long it would take for interactions to restore isotropy in the $p_\perp - p_L$ plane. In the bottom-up scenario [56] isotropy is reached through hard collisions

between the high-momentum modes (particles) which interact via an isotropically screened gauge interaction (DEBYE-screening). In deriving the results, it was assumed that the underlying soft gauge modes responsible for the screening were the same in an anisotropic plasma as in an isotropic one. In fact, this turns out to be incorrect and in anisotropic plasmas the most important collective mode corresponds to an instability to transverse magnetic field fluctuations [61, 53].

Equilibration is sped up by these instabilities, as growth of the unstable modes is associated with the system's isotropization. This is due to the fact that the unstable modes generate large longitudinal pressure, which compensates for the decreased longitudinal pressure due to expansion. The characteristic inverse time of instability development is roughly of order gT for a sufficiently anisotropic momentum distribution [61, 53, 62, 63, 64, 65]. Thus, the instabilities are much faster than the collisions in the weak coupling regime (recall that the inverse equilibration was determined to be of order $g^4 \ln(g)T$ for binary collisions).

Note again that the isotropization should be clearly distinguished from the equilibration. The instabilities driven isotropization is a mean-field reversible phenomenon which is not accompanied by entropy production [61, 66]. Therefore, the collisions, which are responsible for the dissipation, are needed to reach the equilibrium state of maximal entropy. The instabilities contribute to the equilibration indirectly, shaping the parton momentum distributions.

To understand the full dynamics, in this work we study the interplay between collisions and instabilities for the realistic situation in heavy-ion collisions, when the coupling is not arbitrarily small, both in an analytic model calculation as well as in a detailed microscopic simulation including binary hard momentum exchange collisions as well as particle field interactions.

1.4 Hard observables

Via the hard scattering of incoming quarks and gluons and their subsequent fragmentation into directionally aligned hadrons, so-called jets are created. The rates for jet production and other hard-scattering processes grow rapidly with increasing collision energy, which was a primary motivation for constructing RHIC with high center-of-mass energy. The investment paid off with the discovery of jet quenching and its development as a quantitative tomographic probe of the QGP. Jet quenching means the suppression of high transverse momentum hadrons, such as π^0 and η mesons in central $Au + Au$ collisions compared with expectations from measurements in $p + p$ collisions. Whereas pions and η mesons show the same amount of suppression at high p_\perp , where quark fragmentation is the dominant production mechanism, direct photons were found to be unsuppressed⁵. This indicates that the suppression is a final-state effect related to the absorption (energy loss) of energetic partons in the medium. A quantitative measure of jet quenching, shown in Fig. 1.4 as a function of p_\perp , is the nuclear modification factor R_{AA} , the measured yield of hadrons relative to the expected yield from proton-proton reactions scaled by the ratio of the incident

⁵Note that when using the measured $p+p$ direct-photon data as reference, direct photons are also suppressed at high p_\perp (preliminary data presented at QM2006, see e.g. [67]). If $R_{AA}^\pi = R_{AA}^\gamma$, the whole concept of energy loss changes, since then the modification is more likely to be an initial state effect due to the modification of the parton distribution functions.

parton flux of two gold nuclei to that of two protons. In contrast to the direct-photon data, a suppression by a factor of 5 is observed for the hadrons.

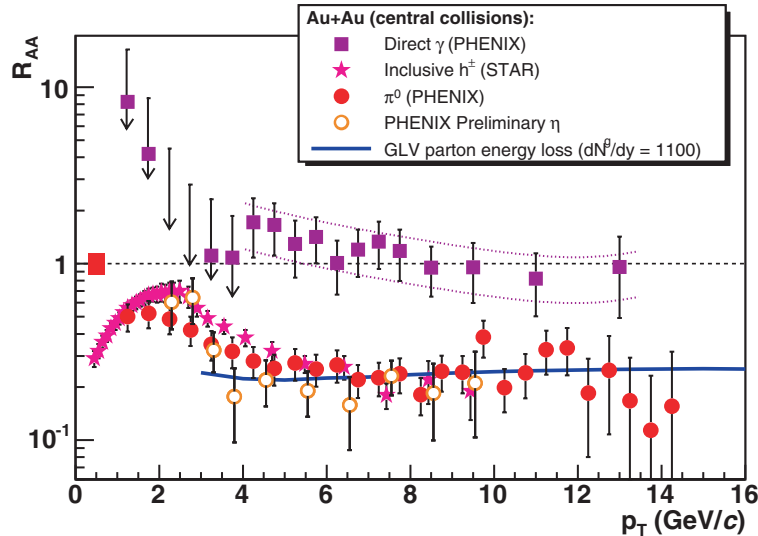


Figure 1.4: $R_{AA}(p_{\perp})$ measured in central $Au+Au$ at $\sqrt{s} = 200$ GeV for: direct photons [68], inclusive charged hadrons [69], π^0 , and η [70] compared to theoretical predictions for parton energy loss in a dense medium with $dN_g/dy = 1100$ [71]. The shaded band at $R_{AA} = 1$ represents the overall fractional uncertainty of the data. The baseline $p+p$ reference of the direct γ $Au+Au$ data is a NLO calculation whose uncertainties are indicated by the dotted lines around the points [68]. Figure taken from [72].

Additional evidence for the color opacity of the medium is seen in studies of the angular correlation of the radiation associated with a high- p_{\perp} trigger particle [73, 74]. In $p+p$ and $d+Au$ collisions, a hard recoiling hadron frequently occurs at 180 degrees in azimuth to the trigger, showing the back-to-back nature of jets in leading order QCD. In contrast to this, central $Au+Au$ collisions show a strong suppression of such recoils, accompanied by an enhancement and broadening of low- p_{\perp} particle production. Detailed analyses indicate that the response of the medium to the passage of an energetic parton may be of a characteristic hydrodynamical nature: the energy lost by a high-energy parton may re-appear as a collective Mach cone [75, 76, 77].

Furthermore, recent measurements of di-hadron correlations provide evidence for an asymmetric broadening of jet profiles in the plane of pseudo-rapidity (η) and azimuthal angle (ϕ). The interaction with the medium causes a much stronger broadening in η than in ϕ [78, 79], the so-called “ridge”. The detailed origin of this effect is yet unknown, and in this work we study the influence of plasma instabilities on jet broadening that can lead to an explanation.

1.5 Electromagnetic probes

Photons, as well as dileptons, interact only electromagnetically with the surrounding matter during the evolution of the plasma and subsequent hadronic phases. Due to the smallness of the electromagnetic coupling they have a very long mean-free-path and can leave the reaction region without further interaction. This makes them a valuable tool for gaining undistorted information on the early stages of a heavy-ion reaction. For this reason isotropic thermal photon production [5, 80, 81, 82, 83, 84, 85, 86, 87, 88, 89, 90, 91, 92, 93] as well as dilepton production [94, 95, 96, 97, 98, 99, 100, 101, 102, 103, 104] has been studied extensively.

Low-mass dileptons, for example, may provide information on chiral symmetry restoration via the measurement of the ρ meson and its medium modifications. It is expected to become degenerate with the a_1 meson, i.e., the two masses should approach each other when chiral symmetry is restored [105, 106]. This is complicated by the fact that the a_1 decays solely into hadrons, however, the ρ -meson (as well as others, like the ω - and ϕ - or J/Ψ -meson) has a finite branching ratio for decays into dileptons and thus may be investigated using $e^+ - e^-$ or $\mu^+ - \mu^-$ measurements (see e.g. [107, 108]).

Coming back to the isotropization and thermalization of the QGP, it would be useful to have an experimental observable, which is sensitive to a momentum-space anisotropy in the quark and gluon distribution functions. One such observable is the high-energy photon production. In this work we will calculate the photon production from an anisotropic QGP and discuss under which circumstances it may provide a means to estimate the evolving anisotropy of the system. Knowledge of the degree of local momentum-space anisotropy reached in a heavy-ion collision is essential for the study of instabilities and their role for isotropization and thermalization, as will be discussed in detail in Chapter 4.4.

1.6 Outline of this work

This work is organized as follows: In Chapter 2, we introduce the kinetic theory for QCD plasmas and present a derivation of the non-Abelian VLASOV equations for quarks and gluons. In Chapter 3, we show how by solving the kinetic equations an effective theory for the soft plasma modes, the so-called hard-thermal-loop effective theory, can be obtained. We extend the discussion to anisotropic plasmas in Chapter 4, and discuss in detail the appearing unstable modes and the physical processes leading to them. In addition, we present recent development, mostly of the numerical simulations of instabilities in non-Abelian plasmas.

In Chapter 5, we investigate the question whether collisions, which can become important for a coupling that is not arbitrarily small, reduce the growth of the unstable modes. Therefore we present a model for the inclusion of collisions to the non-Abelian VLASOV equations, and study their effect on instability growth. Without collisions the system will never thermalize because the pure VLASOV-equation is time reversible. Hence, to achieve fast thermalization the instability and the collisions are needed, and it is necessary to understand the dynamics including both processes.

This study is then extended to a microscopic computation, a so-called WONG-YANG-MILLS simulation, in which we included the possibility of hard binary scatterings among

particles in addition to the particle-field interactions. The used techniques and implementation of the collision term are discussed, together with the investigation of jet transport in isotropic media in great detail in Chapter 6, whereas the simulation of instabilities including collisions is covered in Chapter 7. Here we also present results on the influence of instabilities on jet transport and a potential explanation for the observed asymmetric broadening of jets along the longitudinal and transverse direction in heavy-ion collisions.

We complete the discussion of collective modes in Chapter 8, where we present studies of the fermionic modes and show that in the hard-loop approximation no unstable modes appear. Finally to experimentally determine how strong the parton momentum-space anisotropy becomes in a heavy-ion collision, and by that how much potential there is for instabilities, we study the photon production from an anisotropic QGP and determine to what extent the resulting yield can provide information on the system's anisotropy in Chapter 9.

2 Kinetic theory for hot QCD plasmas

Wenn man sich nur bewegt, andere in Bewegung bringt,
so fugt sich gar manches schon und gut.

an Friedrich Heinrich Jacobi, 18. Oktober 1784
Johann Wolfgang von Goethe (1749-1832)

Kinetic theory, as derived from quantum field theory, is a powerful tool to construct effective theories for the soft modes of a QCD plasma, which then can be treated non-perturbatively [109, 110, 111, 112, 113]. Therefore, kinetic theory is an ideal tool to investigate plasma instabilities.

For now, we assume the temperature T to be high enough such that $g(T) \ll 1$ and a weak coupling expansion can be performed. The plasma constituents, i.e., the quarks and gluons, have typical momenta $k \sim T$ and take part in collective excitations, which typically develop on a space-time scale $\lambda \sim 1/(gT)$ (The mean particle distance is $\bar{r} \sim 1/T$). Those excitations are similar to the familiar charge oscillations of the electromagnetic plasma [114], and can indeed be described by simple kinetic equations of the VLASOV type. By formally solving these equations for the hard particles, one can express the induced current in terms of the soft gauge fields and thus obtain an effective YANG-MILLS equation, which involves the soft fields alone. At the softer scale g^2T the non-Abelian plasmas enter a non-perturbative regime where the coupling constant is small but the field strengths are large such that perturbation theory breaks down due to non-linear effects [115].

Following [113], in this chapter we will derive the collisionless kinetic equations from the KADANOFF-BAYM equations in the mean-field approximation using a gradient expansion. This leads to an effective theory for the collective modes at the scale gT . We will also derive the response function of a QCD plasma and the induced current.

2.1 Non-Abelian plasmas

For sufficiently weak gauge fields A_a^μ the linear response approximation is valid even for a non-Abelian theory as QCD and the induced current is of the form

$$J_{\text{ind}}^{\mu a}(x) = \int d^4y \Pi_{ab}^{\mu\nu}(x, y) A_\nu^b(y), \quad (2.1)$$

where the polarization tensor $\Pi_{ab}^{\mu\nu}$ is diagonal in color $\Pi_{ab}^{\mu\nu}(x, y) = \delta_{ab} \Pi^{\mu\nu}(x, y)$ and receives contributions from all colored particles. Considering the scale gT , at which collective motion first appears, to leading order in g the color channels are decoupled and individually conserved: $\partial_\mu J_{\text{ind}}^{\mu a} = 0$. Note, however, that in QCD the fields have to be much weaker than in QED for the linear approximation to hold, because $J_{\text{ind}}^{\mu a}$ needs to be covariantly

conserved, i.e.,

$$[D_\mu, J_{\text{ind}}^\mu] = 0, \quad (2.2)$$

with the covariant derivative $D_\mu = \partial_\mu + igA_\mu$, and a commutator of the color generators. $J_{\text{ind}}^\mu = J_{\text{ind}}^{\mu a} T^a$, with the generator T^a in the appropriate representation for gluons (adjoint) or quarks (fundamental). The linearized conservation law $\partial_\mu J_{\text{ind}}^\mu = 0$ is only a good approximation to the exact law $[D_\mu, J_{\text{ind}}^\mu] = 0$ when the fields are so weak that the term gA_μ in the soft covariant derivative can be neglected over the derivative $\partial_x \sim gT$. This requires $A \ll T$, a limit in that all non-linear terms in the YANG-MILLS equation

$$[D_\nu, F^{\nu\mu}]^a(x) = J_{\text{ind}}^{\mu a}(x) \quad (2.3)$$

can be neglected and the equation reduces to a set of uncoupled MAXWELL equations. This means that the linear approximation is only good if the theory is effectively Abelian. Otherwise, in non-Abelian theory, linear response is not sufficient: constraints due to gauge symmetry force us to take into account specific non-linear effects and a more complicated formalism needs to be worked out. Still, simple kinetic equations can be obtained in this case also, but in contrast to QED, the resulting induced current is a non-linear functional of the gauge fields. It may be expanded in powers of A^μ , thus generating the one-particle irreducible amplitudes of the soft gauge fields:

$$J_\mu^a = \Pi_{\mu\nu}^{ab} A_b^\nu + \frac{1}{2} \Gamma_{\mu\nu\rho}^{abc} A_b^\nu A_c^\rho + \dots \quad (2.4)$$

The additional terms represent vertex corrections. These amplitudes are the ‘‘hard thermal loops’’ (HTL) [116, 117] which define the effective theory for the soft gauge fields at the scale gT . In the following we present a derivation of the kinetic equations and the induced current beyond the linear approximation, leading to the same result as the diagrammatic approach which isolates the leading order contributions to one-loop diagrams with soft external lines.

2.2 Derivation of the kinetic equations in background field gauge

To preserve explicit gauge covariance with respect to the background fields in the derivation of the kinetic equations we follow [113] and introduce the background field gauge [118, 119, 120, 121]. We express the generating functional $Z[J]$ as the following functional integral in imaginary time:

$$Z[J] = \int \mathcal{D}A \det \left(\frac{\delta G^a}{\delta \theta^b} \right) \exp \left\{ - \int d^4x \left(\frac{1}{4} (F_{\mu\nu}^a)^2 + \frac{1}{2\lambda} (G^a[A])^2 + J_\mu^a A_\mu^a \right) \right\}, \quad (2.5)$$

where $G^a[A]$ is the gauge fixing term (e.g. $G^a = \partial^\mu A_\mu^a$ for covariant gauges or $G^a = \partial^i A_i^a$ for COULOMB gauges). $F_{\mu\nu}^a = \partial_\mu A_\nu^a - \partial_\nu A_\mu^a - gf^{abc} A_\mu^b A_\nu^c$ is the gauge field strength tensor, λ is the free gauge fixing parameter, and $\theta^a(x)$ the parameter of the infinitesimal gauge transformations

$$A_\mu^a \rightarrow A_\mu^a - \frac{1}{g} \partial_\mu \theta^a + f^{abc} A_\mu^b \theta^c = A_\mu^a - \frac{1}{g} [D_\mu, \theta]^a. \quad (2.6)$$

The gauge fixed Lagrangian in Eq. (2.5) is not gauge invariant and hence the corresponding equations of motion do not have simple transformation properties under the gauge transformations of the external sources or the average fields. In order to derive equations of

motion which do fulfill these properties, we use the method of the background field gauge [118, 119, 120], in which the gauge field is split into a classical background field A_μ^a and a fluctuating quantum field a_μ^a . The corresponding generating functional is then defined to be

$$Z[J, A] = \int \mathcal{D}a \det \left(\frac{\delta G^a}{\delta \theta^b} \right) \exp \left\{ - \int d^4x \left(\frac{1}{4} (F_{\mu\nu}^a[A+a])^2 + \frac{1}{2\lambda} (G^a[a])^2 + J_\mu^b a_b^\mu \right) \right\}, \quad (2.7)$$

where the new gauge fixing term G^a is chosen to be covariant under the gauge transformations of the background fields. We show explicitly in Appendix A that the COULOMB type gauge fixing term

$$G^a \equiv [D_i[A], a^i]^a = \partial^i a_i^a - g f^{abc} A_i^b a^{ic} \quad (2.8)$$

transforms covariantly under the following gauge transformations of the fields

$$\begin{aligned} A_\mu &\rightarrow h A_\mu h^\dagger - \frac{i}{g} h \partial_\mu h^\dagger, \\ a_\mu &\rightarrow h a_\mu h^\dagger, \end{aligned} \quad (2.9)$$

with

$$h(x) = \exp(i\theta^a(x)T^a) = 1 + i\theta^a(x)T^a + \mathcal{O}(\theta^2). \quad (2.10)$$

These are accompanied by the transformations

$$J_\mu \rightarrow h J_\mu h^\dagger, \quad \zeta \rightarrow h \zeta h^\dagger \quad \text{and} \quad \bar{\zeta} \rightarrow h \bar{\zeta} h^\dagger \quad (2.11)$$

of the current J_μ and the anticommuting ghost fields in the adjoint representation, ζ^a and $\bar{\zeta}^a$, which appear when we rewrite the FADDEEV-POPOV determinant as a functional integral:

$$\det \left(\frac{\delta G^a}{\delta \theta^b} \right) = \int \mathcal{D}\bar{\zeta} \mathcal{D}\zeta \exp \left\{ - \int d^4x \bar{\zeta}^a \left(D_i[A] D^i[A+a] \right)_{ab} \zeta^b \right\}. \quad (2.12)$$

We thus obtain:

$$Z[J, A] = \int \mathcal{D}a \mathcal{D}\bar{\zeta} \mathcal{D}\zeta \exp \left\{ -S_{FP}[a, \zeta, \bar{\zeta}; A] - \int d^4x J_\mu^b a_b^\mu \right\}, \quad (2.13)$$

with the FADDEEV-POPOV action:

$$S_{FP}[a, \zeta, \bar{\zeta}; A] = \int d^4x \left\{ \frac{1}{4} (F_{\mu\nu}^a[A+a])^2 + \frac{1}{2\lambda} (D_i[A] a^i)^2 + \bar{\zeta}^a (D_i[A] D^i[A+a])_{ab} \zeta^b \right\}.$$

The complete action in the generating functional (2.13) is invariant with respect to the gauge transformations (2.9) and (2.11), and so is the generating functional itself, which can be seen when transforming the integration variables as well. This symmetry of $Z[J, A]$ guarantees the covariance of the GREEN functions under the gauge transformations (2.9) and (2.11) of the external field and current [113], which was the desired property and reason for the introduction of the background field gauge. After adding fermionic fields and sources, the full generating functional reads

$$Z[j, \eta, \bar{\eta}, A, \Psi, \bar{\Psi}] = \int \mathcal{D}a \mathcal{D}\bar{\zeta} \mathcal{D}\zeta \mathcal{D}\bar{\psi} \mathcal{D}\psi \exp \left\{ -S_{FP} - \int d^4x (j_\mu^b a_b^\mu + \bar{\eta}\psi + \bar{\psi}\eta) \right\}, \quad (2.14)$$

with

$$S_{FP} \equiv \int d^4x \left\{ \frac{1}{4} (F_{\mu\nu}^a[A+a])^2 + (\bar{\Psi} + \bar{\psi}) (-i\not{D}[A+a]) (\Psi + \psi) + \frac{1}{2\lambda} (D_i[A]a^i)^2 + \bar{\zeta}^a (D_i[A]D^i[A+a])_{ab} \zeta^b \right\}. \quad (2.15)$$

At finite temperature, the gluonic fields to be integrated over are periodic in imaginary time with period $\beta = 1/T$: $a_\mu(\tau = 0) = a_\mu(\tau = \beta)$. The fermionic fields ψ , $\bar{\psi}$ satisfy antiperiodic boundary conditions (e.g., $\psi(\tau = 0) = -\psi(\tau = \beta)$), and the ghost fields ζ and $\bar{\zeta}$ are again periodic in spite of their GRASSMANNIAN nature: this is because the FADDEEV-POPOV determinant is defined on the space of periodic gauge fields. The full generating functional (2.14) is invariant under the gauge transformations (2.9) and (2.11) together with the transformations of the fermionic fields and sources:

$$\begin{aligned} \Psi &\rightarrow h\Psi, & \bar{\Psi} &\rightarrow \bar{\Psi}h^{-1}, \\ \eta &\rightarrow h\eta, & \bar{\eta} &\rightarrow \bar{\eta}h^{-1}. \end{aligned} \quad (2.16)$$

The associated GREEN functions are covariant under the same transformations. Finally, the classical fields A , Ψ , and $\bar{\Psi}$ can be identified with the respective average fields by requiring that

$$\langle a_\mu \rangle = \langle \psi \rangle = \langle \bar{\psi} \rangle = 0, \quad (2.17)$$

which are conditions that have a gauge invariant meaning because the average values of the quantum fields transform covariantly [113].

With the full generating functional (2.14) at hand, we can derive the mean field kinetic equations. First, we choose to work in COULOMB gauge, which can be defined by imposing the transversality constraint

$$D_i[A]a^i = 0, \quad (2.18)$$

within (2.15). In this gauge the gluon GREEN functions are transverse, meaning that

$$D_x^i[A]G_{i\nu}(x, y) = 0. \quad (2.19)$$

Only the physical transverse gluons are present in this gauge at tree level, which is convenient because in other gauges contributions from present longitudinal gluons and ghosts cancel in the final result [117, 110, 111]. Hence ghosts shall be ignored from now on.

Ignoring the ghost fields as motivated above, the equations of motion following from (2.14) read

$$\left\langle D_{ab}^\nu[A+a]F_{\nu\mu}^b[A+a] \right\rangle - g \left\langle (\bar{\Psi} + \bar{\psi}) \gamma_\mu t^a (\Psi + \psi) \right\rangle = J_\mu^a(x), \quad (2.20)$$

$$i \left\langle \not{D}[A+a](\Psi + \psi) \right\rangle = \eta(x), \quad (2.21)$$

together with the hermitian conjugate equation for $\bar{\Psi}$. Note that the first term on the left hand side of Eq. (2.20) is to be understood as

$$\begin{aligned} \left\langle D_{ab}^\nu[A+a]F_{\nu\mu}^b[A+a] \right\rangle &= \left\langle (\partial_\nu \delta_{ab} + ig(A_\nu^c + a_\nu^c)(T^c)_{ab}) \right. \\ &\quad \left. \times \left(\partial^\nu (A+a)_b^\mu - \partial^\mu (A+a)_b^\nu - g(A+a)_e^\nu (A+a)_d^\mu f^{edb} \right) \right\rangle, \end{aligned} \quad (2.22)$$

where $(T^c)_{ab} = -if^{abc}$. After imposing the conditions (2.17) we obtain the physically relevant equations

$$[D^\nu, F_{\nu\mu}(x)]^a - g\bar{\Psi}(x)\gamma_\mu t^a \Psi(x) = J_\mu^a(x) + J_\mu^{\text{ind}a}(x), \quad (2.23)$$

$$i\not{D}\Psi(x) = \eta(x) + \eta^{\text{ind}}(x), \quad (2.24)$$

where D_μ and $F_{\mu\nu}$ are the covariant derivative and field strength tensor associated with the background field only. The induced currents on the right hand side follow from the non-vanishing correlators of two or three fluctuating quantum fields in Eqs. (2.20) and (2.21). In detail, we can write

$$J_a^{\text{ind}\mu}(x) = J_{\text{f}a}^\mu(x) + J_{\text{g}a}^\mu(x), \quad (2.25)$$

with the quark and gluon contributions

$$J_{\text{f}}^{\mu a}(x) = g \langle \bar{\psi}(x) \gamma^\mu t^a \psi(x) \rangle, \quad (2.26)$$

$$J_{\text{g}}^{\mu a}(x) = g f^{abc} \Gamma^{\mu\rho\lambda\nu} \langle a_\nu^b (D_\lambda a_\rho)^c \rangle + g^2 f^{abc} f^{cde} \langle a_\nu^b a_d^\mu a_e^\nu \rangle, \quad (2.27)$$

where $\Gamma_{\mu\rho\lambda\nu} \equiv 2g_{\mu\rho}g_{\lambda\nu} - g_{\mu\lambda}g_{\rho\nu} - g_{\mu\nu}g_{\rho\lambda}$. The induced fermionic source reads

$$\eta^{\text{ind}}(x) = g\gamma^\nu t^a \langle a_\nu^a(x) \psi(x) \rangle. \quad (2.28)$$

In equilibrium, symmetry causes both the mean fields and the induced sources to vanish, because the expectation values are then thermal averages over color singlet states. We now introduce notations for the appearing two-point functions (The appearing three-point function in (2.27) is negligible at leading order because it contains at least two more powers of g than the other terms). The usual quark and gluon propagators read

$$\begin{aligned} S_{ij}(x, y) &\equiv \langle T\psi_i(x)\bar{\psi}_j(y) \rangle = -\frac{\delta\langle\psi_i(x)\rangle}{\delta\eta_j(y)}, \\ G_{\mu\nu}^{ab}(x, y) &\equiv \langle T a_\mu^a(x) a_\nu^b(y) \rangle = -\frac{\delta\langle a_\mu^a(x) \rangle}{\delta j_\nu^b(y)}, \end{aligned} \quad (2.29)$$

with the time-ordering operator T . We shall also define the following ‘‘abnormal’’ propagators:

$$\begin{aligned} K_{i\nu}^b(x, y) &\equiv \langle T\psi_i(x) a_\nu^b(y) \rangle = -\frac{\delta\langle\psi_i(x)\rangle}{\delta j_\nu^b(y)} = -\frac{\delta\langle a_\nu^b(y) \rangle}{\delta\bar{\eta}_i(x)}, \\ H_{\nu i}^b(x, y) &\equiv \langle T a_\nu^b(x) \bar{\psi}_i(y) \rangle = -\frac{\delta\langle\bar{\psi}_i(y)\rangle}{\delta j_\nu^b(x)} = \frac{\delta\langle a_\nu(x) \rangle}{\delta\eta(y)}, \end{aligned} \quad (2.30)$$

which mix fermionic and bosonic degrees of freedom and vanish in equilibrium.

We can express the time-ordered propagators by

$$\begin{aligned} S_{ij}(x, y) &= \theta(\tau_x - \tau_y) S_{ij}^>(x, y) - \theta(\tau_y - \tau_x) S_{ij}^<(x, y), \\ G_{\mu\nu}^{ab}(x, y) &= \theta(\tau_x - \tau_y) G_{\mu\nu}^{>ab}(x, y) - \theta(\tau_y - \tau_x) G_{\mu\nu}^{<ab}(x, y), \end{aligned} \quad (2.31)$$

and find analogous expressions for K and H .

The induced sources in (2.26) - (2.28) involve products of fields with equal time arguments and may be expressed by

$$\begin{aligned} J_f^{\mu a}(x) &= g \operatorname{Tr} (\gamma^\mu t^a S^<(x, x)), \\ J_g^{\mu a}(x) &= i g \Gamma^{\mu\rho\lambda\nu} \operatorname{Tr} T^a D_\lambda^x G_{\rho\nu}^<(x, y)|_{y \rightarrow x^+}, \\ \eta^{\text{ind}}(x) &= g \gamma^\nu t^a K_{a\nu}^<(x, x). \end{aligned} \quad (2.32)$$

To arrive at the second equation it was used that

$$\begin{aligned} i \operatorname{Tr} (T^a D^x G^<(x, y)) &= i N D^x G^<^a(x, y) = i (T^a)_{bc} D^x (G^<^a(x, y) T^a)^{cb} \\ &= f^{abc} D^x G^<^{cb}(x, y) = f^{abc} \langle a(y)^b (D a(x))^c \rangle, \end{aligned}$$

because $T^a T^a = N$.

2.2.1 Mean field approximation

Approximations are needed to develop kinetic equations for the QCD plasma. The first approximation is a mean field approximation, equivalent to the one-loop approximation in the diagrammatic approach. First, let us write down the general equation of motion for the quark propagator, found by differentiating Eq. (2.21) with respect to $\eta(y)$:

$$-i \not{D}_x S(x, y) - g \gamma^\nu t^a \Psi(x) H_\nu^a(x, y) + \int d^4 z \Sigma(x, z) S(z, y) = \delta(x - y) \quad (2.33)$$

with the quark self-energy $\Sigma(x, y)$, defined as

$$\int d^4 z \Sigma(x, z) S(z, y) \equiv \frac{\delta \eta^{\text{ind}}(x)}{\delta \eta(y)} = g \langle T \not{a}(x) \psi(x) \bar{\psi}(y) \rangle_c. \quad (2.34)$$

The equations of motion for the other propagators are found analogously. To justify the mean field approximation, where the hard particles only interact via the soft mean fields, i.e., where we neglect the last term in Eq. (2.33), let us analyze the magnitude of the different terms in the equations of motion. For simplicity let us consider the gluon propagator $G(x, y)$ in a soft color background field $A_a^\mu(x)$. Its WIGNER transform will obey a kinetic equation, which involves a drift term $(K \cdot \partial_X) G^<$, a mean field term and a collision term $C(K, X) = -(G^> \Sigma^< - \Sigma^> G^<)$.¹ Both the drift and the collision term vanish in equilibrium [113]. Considering small fluctuations of the GREEN function and self energy

$$\begin{aligned} G^<(K, X) &= G_{\text{eq}}(K) + \delta G^<(K, X) \\ \Sigma^<(K, X) &= \Sigma_{\text{eq}}^<(K) + \delta \Sigma^<(K, X), \end{aligned}$$

the drift term becomes $(K \cdot \partial_X) \delta G^<$, while the collision term reads

$$C(K, X) = -(\Sigma_{\text{eq}}^< \delta G^> - \Sigma_{\text{eq}}^> \delta G^<) + (\delta \Sigma^> G_{\text{eq}}^< - \delta \Sigma^< G_{\text{eq}}^>) + \dots, \quad (2.35)$$

where the dots stand for higher order deviations from equilibrium. The order $\Sigma_{\text{eq}}(k) \sim g^2 T^2$ is fixed by the physics in equilibrium, such that the order of the drift term, which is given

¹Note, that we will use capital letters for four-momenta to avoid confusion with the absolute values of three-momenta, for which we will use lower case letters.

by the scale ∂_X of inhomogeneities, determines the relative importance of the two terms. For $\partial_X \sim gT$ the collision term is suppressed by one order of g relative to the drift term, whereas for $\partial_X \sim g^2T$ or less, the collisions are as important as the drift term. Alterations of this argument due to accidental cancellations are discussed in [113]. Regarding strict perturbation theory to leading order for the collective dynamics at the scale gT the collision terms can be neglected and the mean field approximation is valid. That is, the hard particles only interact with the soft mean fields and do not collide among each other. In this limit, the relevant equations for the two-point functions read in COULOMB gauge:

$$\not{D}_x S^<(x, y) = ig\gamma^\nu t^a \Psi(x) H_\nu^{<a}(x, y), \quad (2.36)$$

$$\not{D}_x K_\nu^{<b}(x, y) = -igt^a \gamma^\mu \Psi(x) G_{\mu\nu}^{<ab}(x, y), \quad (2.37)$$

$$\left(g_{\mu\nu} D^2 - D_\mu D_\nu + 2igF_{\mu\nu}\right)_y^{ab} K_b^{<\nu}(x, y) = -gS^<(x, y) \gamma_\mu t^a \Psi(y), \quad (2.38)$$

$$\left(g_\mu^\rho D^2 - D_\mu D^\rho + 2igF_\mu^\rho\right)_x^{ac} G_{\rho\nu}^{<cb}(x, y) = g\bar{\Psi}(x) \gamma_\mu t^a K_\nu^{<b}(x, y) + gH_\nu^{<b}(y, x) \gamma_\mu t^a \Psi(x). \quad (2.39)$$

The COULOMB gauge fixing conditions read

$$\begin{aligned} D_x^i G_{i\nu}^{<}(x, y) &= 0, & G_{\mu j}^{<}(x, y) D_y^{j\dagger} &= 0, \\ D_x^i H_i^{<a}(x, y) &= 0, & D_y^i K_i^{<a}(x, y) &= 0, \end{aligned} \quad (2.40)$$

and the initial conditions are to be chosen such that without external sources the system is in equilibrium: The mean fields vanish and the two-point functions reduce to their equilibrium form, which, to the order of interest, are the free functions.

Under the gauge transformations (2.9) and (2.16) the equations (2.36) - (2.39) transform covariantly. Solving these equations without further approximations would yield the induced sources to one-loop order. However, by itself the mean field approximation is not consistent: Additional powers of g are hidden in the soft non-equilibrium inhomogeneities. These can be isolated by the gradient expansion.

2.2.2 Gradient expansion

To set the stage for the gradient expansion we first rewrite the two-point functions in terms of WIGNER functions. Let $G_{ab}(x, y)$ be a generic two-point function. Its WIGNER transform is

$$\mathcal{G}_{ab}(K, X) = \int d^4s G_{ab}\left(X + \frac{s}{2}, X - \frac{s}{2}\right), \quad (2.41)$$

with

$$s^\mu = x^\mu - y^\mu, \quad X^\mu = \frac{x^\mu + y^\mu}{2}. \quad (2.42)$$

The problem with this definition is that unlike $G_{ab}(x, y)$, which is gauge covariant at x and y separately, $\mathcal{G}_{ab}(K, X)$, which mixes x and y in its definition, is not covariant. It is, however, possible to construct a gauge covariant WIGNER function. First we define

$$\tilde{G}_{ab}(s, X) = U_{a\bar{a}}\left(X, X + \frac{s}{2}\right) G_{\bar{a}\bar{b}}\left(X + \frac{s}{2}, X - \frac{s}{2}\right) U_{\bar{b}b}\left(X - \frac{s}{2}, X\right), \quad (2.43)$$

using the non-Abelian transporter or WILSON line

$$U(x, y) = P \exp \left(-ig \int_{\mathcal{C}} dz^\mu A_\mu(z) \right), \quad (2.44)$$

where \mathcal{C} is an arbitrary path going from y to x , $A_\mu = A_\mu^a T^a$, and the symbol P denotes the path ordering of the color matrices in the exponential. Under the gauge transformations of A_μ the WILSON line transforms as

$$U(x, y) \rightarrow h(x)U(x, y)h^\dagger(y), \quad (2.45)$$

such that the function (2.43) transforms covariantly at X for any given s :

$$\tilde{G}(s, X) \rightarrow h(X)\tilde{G}(s, X)h^\dagger(X) \quad (2.46)$$

Its WIGNER transform

$$G_{ab}(K, X) = \int d^4s e^{iK \cdot s} \tilde{G}_{ab}(s, X) \quad (2.47)$$

transforms covariantly as well: For any given k we have

$$G(K, X) \rightarrow h(X)G(K, X)h^\dagger(X), \quad (2.48)$$

and this WIGNER function will satisfy a gauge covariant equation of motion, which makes the physical interpretation more transparent than one that is not gauge covariant. This way all two-point functions can be expressed by the corresponding gauge covariant WIGNER functions, where we will not use different notations, because their arguments clearly identify them.

The induced sources (2.32) can now be expressed in terms of the newly defined WIGNER functions:

$$J_f^{\mu a}(X) = g \int \frac{d^4k}{(2\pi)^4} \text{Tr} \left(\gamma^\mu t^a S(K, X) \right), \quad (2.49)$$

$$J_g^{\mu a}(X) = g \Gamma^{\mu\rho\lambda\nu} \int \frac{d^4k}{(2\pi)^4} \text{Tr} T^a \left\{ k_\lambda G_{\rho\nu}(K, X) + \frac{i}{2} [D_\lambda^X, G_{\rho\nu}(K, X)] \right\}, \quad (2.50)$$

$$\eta^{\text{ind}}(X) = g \int \frac{d^4k}{(2\pi)^4} \gamma^\mu t^a K_\mu^a(K, X). \quad (2.51)$$

The path \mathcal{C} is still arbitrary and in fact, the results will not depend on the exact form of the path, because we need $U(x, y)$ only in situations where x is close to y as we will argue below. Choosing \mathcal{C} to be a straight line connecting y and x , the transition from the non-covariant to the gauge covariant WIGNER function corresponds to the replacement of the canonical momentum $K^\mu = i\partial_s$ by the kinetic momentum $P^\mu = K^\mu - gA^\mu(X)$ as discussed in [122],[123] (also see [124] for details). For soft and rather weak background fields, $\tilde{G}(s, X)$ stays close to its equilibrium value, meaning that it is peaked at $s = 0$ and vanishes for $s \gtrsim 1/T$. Over this short range the mean field does not vary significantly and we may write

$$g \int_{\mathcal{C}} dz^\mu A_\mu(z) \approx g(s \cdot A(X)), \quad (2.52)$$

omitting terms which involve at least one soft derivative $\partial_X A \sim gTA$. For $s \sim 1/T$, $g(s \cdot A) \sim g$, because $gA \sim gT$, and we can expand the exponent in (2.44) giving

$$U_{ab}(x, y) \approx \delta_{ab} - ig(s \cdot A_{ab}(X)). \quad (2.53)$$

For the off-equilibrium derivation $\delta G = G - G_{\text{eq}}$, this yields

$$\delta \tilde{G}(s, X) \simeq \delta G(x, y) + ig(s \cdot A(X))G_{\text{eq}}(s), \quad (2.54)$$

and for its WIGNER transform

$$\delta G(K, X) \simeq \delta \mathcal{G}(K, X) + g(A(X)\partial_k)G_{\text{eq}}(K). \quad (2.55)$$

Using

$$D_x^\mu G(x, y)|_{x=y} = \partial_s^\mu \tilde{G}(s, X)|_{s=0}, \quad (2.56)$$

we can perform a similar simplification on the gluonic current (2.50) to get:

$$J_g^{\mu a}(X) = g \int \frac{d^4 k}{(2\pi)^4} \text{Tr} T^a \left\{ -K^\mu \delta G_\nu{}^\nu(K, X) + \delta G^{\mu\nu}(K, X) K_\nu \right\}. \quad (2.57)$$

Since the gauge-fixing conditions (2.40) imply that the gauge covariant gluon WIGNER function is spatially transverse, we can write

$$\delta G(K, X) = (\delta_{ij} - K_i K_j) \delta G(K, X). \quad (2.58)$$

The spatial components are the only ones to contribute to the induced current to leading order in g . This is specific to the COULOMB gauge and shall be shown later. With that and Eq. (2.58) we can write

$$J_g^{\mu a}(X) = 2g \int \frac{d^4 k}{(2\pi)^4} K^\mu \text{Tr} \left\{ T^a \delta G(K, X) \right\}. \quad (2.59)$$

We are now ready to perform a gauge covariant gradient expansion and by that extract the terms of leading order in g in Eqs. (2.36)-(2.39).

Consider the gluon two-point function $G_{\mu\nu}^{<ab}(x, y)$ in the presence of a soft background field A_a^μ , but without fermionic fields ($\Psi = \bar{\Psi} = 0$). We start with the following KADANOFF-BAYM equations (cf. Eq. (2.39)) :

$$\begin{aligned} (g_\mu{}^\rho D^2 - D_\mu D^\rho + 2igF_\mu{}^\rho)_x G_{\rho\nu}^{<}(x, y) &= 0, \\ G_\mu^{<\rho}(x, y) \left(g_{\rho\nu} (D^\dagger)^2 - D_\rho^\dagger D_\nu^\dagger + 2igF_{\rho\nu} \right)_y &= 0, \end{aligned} \quad (2.60)$$

and take their difference, which then includes terms like

$$\Xi(x, y) \equiv D_x^2 G(x, y) - G(x, y) (D_y^\dagger)^2, \quad (2.61)$$

where $D_x^2 = \partial_x^2 + 2igA \cdot \partial_x + ig(\partial \cdot A) - g^2 A^2$, and MINKOWSKI indices are omitted to simplify notation. We will concentrate on the quantity Ξ to illustrate the performed approximations.

After introduction of the relative and center variables (2.42), we typically have $s \sim 1/T$, $\partial_s \sim T$, $\partial_X \sim gT$, meaning that the system is slowly varying in space and time with respect to the center variable. We expand in powers of the soft derivative ∂_X and keep only terms involving up to one soft derivative. For example

$$A_\mu \left(X + \frac{s}{2} \right) \approx A_\mu(X) + \frac{1}{2}(s \cdot \partial_X)A_\mu(X). \quad (2.62)$$

We find after explicit insertion of D_x^2 and $(D_y^\dagger)^2$:

$$\begin{aligned} \Xi(s, X) = & 2\partial_s \cdot \partial_X G + 2ig \left[A_\mu(X), \partial_s^\mu G \right] + ig \left\{ A_\mu(X), \partial_X^\mu G \right\} + ig \left\{ (s \cdot \partial_X)A_\mu, \partial_s^\mu G \right\} \\ & + ig \left\{ (\partial_X \cdot A), G \right\} - g^2 \left[A^2(X), G \right] - \frac{g^2}{2} \left\{ (s \cdot \partial_X)A^2, G \right\} + \dots, \end{aligned} \quad (2.63)$$

where $[\cdot, \cdot]$ denote commutators and $\{\cdot, \cdot\}$ anticommutators of color matrices.

As done in [113] we use $A \sim T$ and $\delta G = G - G_{\text{eq}} \sim gG_{\text{eq}}$, with $G_{\text{eq}} \approx G_0$ in the present approximation. Note that at the momentum scale gT A is actually of order $\sqrt{g}T$.² However, for now we assume it to be larger in order to include all non-linear effects in the theory. We will later use the fact that $A \sim \sqrt{g}T$ to linearize the theory.

Keeping only terms of leading order in g , (2.63) simplifies to

$$\Xi(s, X) \approx 2(\partial_s \cdot \partial_X)\delta G + 2ig \left[A_\mu, \partial_s^\mu \delta G \right] + 2ig(s \cdot \partial_X)A_\mu (\partial_s^\mu G_0) + 2ig(\partial_X \cdot A)G_0, \quad (2.64)$$

where all terms on the right hand side are of order $g^2 T^2 G_0$. FOURIER transformation leads to

$$\Xi(K, X) \approx 2 \left[K \cdot D_X, \delta \mathcal{G}(K, X) \right] + 2gK^\mu \left(\partial_X^\nu A_\mu(X) \right) \partial_\nu G_0(K). \quad (2.65)$$

The ordinary WIGNER transform $\delta \mathcal{G}(K, X)$ can be expressed by the gauge covariant one using (2.55), which finally leads to:

$$\Xi_{\mu\nu}(K, X) \approx 2 \left[K \cdot D_X, \delta G_{\mu\nu}(K, X) \right] - 2gK^\alpha F_{\alpha\beta}(X) \partial^\beta G_{\mu\nu}^{(0)}(K), \quad (2.66)$$

where we reintroduced the MINKOWSKI indices.

We recognize here the familiar structure of the VLASOV equation, generalized to a non-Abelian plasma: Eq. (2.66) involves a (gauge-covariant) drift term $(K \cdot D_X)\delta G$, together with a “force term” proportional to the background field strength tensor. In fact, this “force term” involves the equilibrium distribution function $G_0 \equiv G_0^<$, so, in this respect, it is closer to the linearized version of the VLASOV equation. However, Eq. (2.66) is still non-linear, because of the presence of the covariant drift operator $(K \cdot D_X)$, and because the non-Abelian field strength tensor is itself non-linear.

² To see this, consider the free propagator of the magnetic gluon in imaginary time:

$$\langle A(\tau, x)A(0) \rangle = T \sum_n \int \frac{d^3k}{(2\pi)^3} e^{-i\omega_n \tau + i\mathbf{k} \cdot \mathbf{x}} \frac{1}{k^2 + \omega_n^2}$$

By letting $\tau \rightarrow 0$ and $x \rightarrow 0$ and keeping only the contribution of the static modes ($\omega_n = 0$) one obtains for momenta of order gT :

$$\langle A^2 \rangle \simeq T \int \frac{d^3k}{k^2} \sim gT^2,$$

so that $|A| = \sqrt{\langle A^2 \rangle} \sim \sqrt{g}T$.

2.3 The non-Abelian Vlasov equations

We will now derive the kinetic equations which determine the color current induced by a soft gauge field A_a^μ , disregarding the fermionic mean fields. This is done using the expressions for the currents (2.49) and (2.59). In order to evaluate these expressions, we need the equations satisfied by the appearing quark and gluon WIGNER functions δS and $\delta G_{\mu\nu}$ in the presence of the background field A_a^μ .

2.3.1 Vlasov equation for gluons

We start with the determination of the kinetic equation for the gluon WIGNER function. The transverse components δG_{ij} are expected to be dominant, and we concentrate on the spatial components of Eq. (2.60):

$$\begin{aligned} D_x^2 G_{ij} - D_i^x D_0^x G_{0j} + 2igF_i^\rho(x)G_{\rho j} &= 0, \\ G_{ij} \left(D_y^\dagger \right)^2 - G_{i0} D_{0y}^\dagger D_{jy}^\dagger + 2igG_{i\rho} F_j^\rho(y) &= 0, \end{aligned} \quad (2.67)$$

where we used the gauge fixing conditions (2.40) for simplifications. As in the last section we take their difference and meet

$$D_x^2 G_{ij} - G_{ij} \left(D_y^\dagger \right)^2 \longrightarrow 2 \left[K \cdot D_X, \delta G_{ij} \right] - 2gK^\alpha F_{\alpha\beta}(X) \partial^\beta G_{ij}^{(0)}(k). \quad (2.68)$$

It was stated in Eq. (2.58) that δG_{ij} is transverse. However, the second term on the right hand side of Eq. (2.68) involves non-transverse components:

$$\begin{aligned} K^\alpha F_{\alpha\beta} \partial^\beta G_{ij}^{(0)}(K) &\equiv K^\alpha F_{\alpha\beta} \partial^\beta [(\delta_{ij} - \hat{K}_i \hat{K}_j) G_0(K)] \\ &= (\delta_{ij} - \hat{K}_i \hat{K}_j) K^\alpha F_{\alpha\beta} \partial^\beta G_0 - K^\alpha F_{\alpha l} \frac{K_i \delta_{jl} + K_j \delta_{il} - 2\hat{K}_i \hat{K}_j K_l}{\mathbf{k}^2} G_0. \end{aligned} \quad (2.69)$$

because the derivative acts on both the projector and G^0 . It can be shown [113] that the non-transverse components cancel with other terms present in the full difference equation, such that Eq. (2.58) holds and $\delta G(K, X)$ satisfies

$$\left[K \cdot D_X, \delta G(K, X) \right] = g K^\alpha F_{\alpha\beta}(X) \partial^\beta G_0(K). \quad (2.70)$$

Indeed it follows that the transverse part is dominant because $D_X \sim gT$ and $gF_{\alpha\beta} \sim (D_X)^2 \sim g^2 T^2$ and $k \sim T$ we have

$$\delta G \sim (D_X/T) G_0 \sim g G_0, \quad (2.71)$$

whereas $G_{0j} \sim (gF_{0i}/T^2) G_0 \sim g^2 G_0$ is suppressed by one order of g .

Remember that $G_0 \equiv G_0^<(K) = 2\pi (K_0/|K_0|) \delta(K^2) n^g(K)$, which only has support on the tree-level mass shell ($K^2 = 0$). It follows from Eq. (2.70) that the same holds for $\delta G(K, X)$. Using the symmetry property

$$G_{\mu\nu}^{>ab}(x, y) = G_{\nu\mu}^{<ba}(y, x), \quad (2.72)$$

we can write

$$\delta G_{ab}(K, X) = 2\pi\delta(K^2) \{ \theta(K_0)\delta n_{ab}^g(\mathbf{k}, X) + \theta(-K_0)\delta n_{ba}^g(-\mathbf{k}, X) \}, \quad (2.73)$$

where $\delta n_{ab}^g(\mathbf{k}, X)$ is a density matrix, which satisfies the following VLASOV equation:

$$[V \cdot D_X, \delta n^g(\mathbf{k}, X)] + gV_\mu F^{\mu\nu} \partial_\nu n^g(K) = 0, \quad (2.74)$$

with $V^\mu = (1, \mathbf{k}/k)$. The δn^g have the same color structure as the fields, which is $\delta f_a^g T^a$ assuming that they are small fluctuations. Otherwise more complicated structures are possible. The components $\delta f_a^g(\mathbf{k}, X)$ transform like a color vector in the adjoint representation. They are found by the projections

$$\delta f_a^g(p, X) = \frac{1}{N_c} \text{Tr} [T_a n^g(p, X)], \quad (2.75)$$

while the scalar coefficient in the color neutral background field $n^g(\mathbf{p}) = f^g(\mathbf{p})\mathcal{I}$ is given by

$$f^g(\mathbf{p}) = \frac{1}{N_c^2 - 1} \text{Tr} [n^g(p, X)]. \quad (2.76)$$

In terms of the density matrix δn^g the induced gluonic current (2.59) reads

$$J_g^{\mu a}(X) = 2g \int \frac{d^3k}{(2\pi)^3} V^\mu \text{Tr} (T^a \delta n^g(\mathbf{k}, X)) = 2gN_c \int \frac{d^3k}{(2\pi)^3} V^\mu \delta f_a^g(\mathbf{k}, X). \quad (2.77)$$

Equation (2.74) is covariant under the gauge transformation of the background field and independent of the gauge-fixing for the quantum fields, as proven in [110, 111].

2.3.2 Vlasov equation for quarks

For the evaluation of Eq. (2.49) we need the kinetic equation for the quark WIGNER function $S \equiv S^<$. We start with Eq. (2.36) for $\Psi = 0$,

$$\not{D}_x S(x, y) = 0, \quad S(x, y) \not{D}_y^\dagger = 0. \quad (2.78)$$

Using

$$\begin{aligned} \not{D} \not{D} &= \gamma^\mu \gamma^\nu D_\mu D_\nu = 2g^{\mu\nu} D_\mu D_\nu - \gamma^\nu \gamma^\mu D_\mu D_\nu \\ &= 2D^2 - 2i\sigma^{\mu\nu} D_\mu D_\nu - \gamma^\mu \gamma^\nu D_\mu D_\nu \\ \Leftrightarrow \not{D} \not{D} &= D^2 - i\sigma^{\mu\nu} D_\mu D_\nu = D^2 - \frac{i}{2} (\sigma^{\mu\nu} D_\mu D_\nu - \sigma^{\mu\nu} D_\nu D_\mu) \\ \Leftrightarrow \not{D} \not{D} &= D^2 + \frac{g}{2} \sigma^{\mu\nu} F_{\mu\nu}(x), \end{aligned} \quad (2.79)$$

with $\sigma^{\mu\nu} = -\sigma^{\nu\mu} = i/2 [\gamma^\mu, \gamma^\nu]$, and $F_{\mu\nu} = [D_\mu, D_\nu]/(ig)$, we find the following difference equation:

$$D_x^2 S(x, y) - S(x, y) (D_y^\dagger)^2 + \frac{g}{2} \left(\sigma^{\mu\nu} F_{\mu\nu}(x) S(x, y) - S(x, y) \sigma^{\mu\nu} F_{\mu\nu}(y) \right) = 0. \quad (2.80)$$

As before we perform a covariant gradient expansion, which leads to

$$[K \cdot D_X, \delta S(K, X)] = gK \cdot F(X) \partial_k S_0 - i \frac{g}{4} F^{\mu\nu}(X) [\sigma_{\mu\nu}, S_0], \quad (2.81)$$

where $F(X) = F_\mu^\mu(X)$. Using $S_0 \equiv S_0^<(K) = \not{K} \rho_0(K) n(K)$,

$$\partial_k (\not{K} \rho_0(K) n(K)) = \not{K} /k \rho_0(K) n(K) + \not{K} \partial_k (\rho_0(K) n(K)),$$

and $[\sigma^{\mu\nu}, \not{K}] = 2i(K^\nu \gamma^\mu - K^\mu \gamma^\nu)$, we find

$$[K \cdot D_X, \delta S(K, X)] = g \not{K} K \cdot F(X) \partial_k (\rho_0(K) n(K)). \quad (2.82)$$

δS is a color matrix of the form $\delta S = \delta S_a t^a$, with the components δS_a transforming as a color vector in the fundamental representation. It also has the same spin and mass-shell structure as the free two-point function $S_0^<$:

$$\delta S(K, X) = \not{K} 2\pi \delta(K^2) \{ \theta(k_0) \delta n^q(\mathbf{k}, X) + \theta(-k_0) \delta n^{\bar{q}}(-\mathbf{k}, X) \}. \quad (2.83)$$

The density matrices $\delta n^{q/\bar{q}}(\mathbf{k}, X) \equiv \delta f_a^{q/\bar{q}}(\mathbf{k}, X) t^a$ satisfy the following kinetic equation:

$$\left[V \cdot D_X, \delta n^{q/\bar{q}}(\mathbf{k}, X) \right] \pm g V_\mu F^{\mu\nu}(X) \partial_\nu n(K) = 0, \quad (2.84)$$

which is the non-Abelian version of the VLASOV equation for quarks. The components $\delta f_a^{q/\bar{q}}$ are found by the projections

$$\delta f_a^{q/\bar{q}}(p, X) = 2 \text{Tr} \left[t_a n^{q/\bar{q}}(p, X) \right], \quad (2.85)$$

while the scalar coefficient in the color neutral background field $n^{q/\bar{q}}(\mathbf{p}) = f^{q/\bar{q}}(\mathbf{p}) I$ is given by

$$f^{q/\bar{q}}(\mathbf{p}) = \frac{1}{N_c} \text{Tr} \left[n^{q/\bar{q}}(p, X) \right]. \quad (2.86)$$

The induced current finally reads (cf. eq. (2.49)):

$$J_f^{\mu a}(X) = g N_f \int \frac{d^3 k}{(2\pi)^3} V^\mu \left(\delta f_a^q(\mathbf{k}, X) - \delta f_a^{\bar{q}}(\mathbf{k}, X) \right). \quad (2.87)$$

Altogether we find for the induced current:

$$\begin{aligned} J^{\mu a}(X) &= J_g^{\mu a}(X) + J_f^{\mu a}(X) \\ &= g \int \frac{d^3 k}{(2\pi)^3} V^\mu \left\{ 2N_c \delta f_a^q(\mathbf{k}, X) + N_f \left[\delta f_a^q(\mathbf{k}, X) - \delta f_a^{\bar{q}}(\mathbf{k}, X) \right] \right\} \end{aligned} \quad (2.88)$$

3 Effective theory for the soft modes

In order to obtain an effective theory for the soft collective modes with momenta of the order gT we have to solve the kinetic equations (2.74) and (2.84) for the hard particles and by that express the current (2.88) in terms of the soft fields alone. This leads to an effective YANG-MILLS equation for the soft modes, in which the hard modes do not appear explicitly.

3.1 Solving the kinetic equations

We combine Eqs. (2.74) and (2.84) by writing

$$[V \cdot D_X, \delta n^i(\mathbf{p}, X)] + g\theta_i V_\mu F^{\mu\nu}(X) \partial_\nu^{(p)} n^i(\mathbf{p}) = 0, \quad (3.1)$$

with $i \in \{g, q, \bar{q}\}$, $\theta_g = \theta_q = 1$ and $\theta_{\bar{q}} = -1$. We remind the reader of the color structure, which for the color neutral background fields is $n^{q/\bar{q}}(\mathbf{p}) = f^{q/\bar{q}}(\mathbf{p})I$ and $n^g(\mathbf{p}) = f^g(\mathbf{p})\mathcal{I}$. I and \mathcal{I} are unit matrices in the fundamental and adjoint representation, respectively. The induced color fluctuations are constructed like $\delta n^{q/\bar{q}}(\mathbf{p}, X) = \delta f_b^{q/\bar{q}}(\mathbf{p}, X)t^b$ and $\delta n^g(\mathbf{p}, X) = \delta f_b^g(\mathbf{p}, X)T^b$, with the generators t_b and T_b in the fundamental and adjoint representation, respectively.

The induced current (2.88) reads

$$J_{\text{ind } a}^{i\mu} = g \int_{\mathbf{p}} V^\mu \{2N_c \delta f_a^g(\mathbf{p}, X) + N_f [\delta f_a^q(\mathbf{p}, X) - \delta f_a^{\bar{q}}(\mathbf{p}, X)]\}, \quad (3.2)$$

where we introduced

$$\int_{\mathbf{p}} := \int \frac{d^3 p}{(2\pi)^3} \quad (3.3)$$

for convenience.

As mentioned before (see footnote on page 20) $A \sim \sqrt{g}T$ and when we neglect terms of subleading order in g the theory becomes effectively Abelian as $D_X \rightarrow \partial_X$ and $F^{\mu\nu} \rightarrow \partial^\mu A^\nu - \partial^\nu A^\mu$. The color channels decouple and Eq. (3.1) can be written for each color channel separately:

$$V \cdot \partial_X \delta f_a^i(\mathbf{p}, X) + g\theta_i V_\mu F_a^{\mu\nu}(X) \partial_\nu^{(p)} f^i(\mathbf{p}) = 0, \quad (3.4)$$

where $F_a^{\mu\nu} = \partial^\mu A_a^\nu - \partial^\nu A_a^\mu$. This equation can be solved using a FOURIER transformation. First we write

$$\begin{aligned} & (\partial_t + \mathbf{v} \cdot \nabla) \delta f_a^i(\mathbf{p}, X) + g\theta_i V_\mu F_a^{\mu\nu}(X) \partial_\nu^{(p)} f^i(\mathbf{p}) = 0 \\ \xrightarrow{\text{FOURIER}} & (-i\omega + i\mathbf{k} \cdot \mathbf{v}) \delta f_a^i(\mathbf{p}, K) + g\theta_i V_\mu F_a^{\mu\nu}(K) \partial_\nu^{(p)} f^i(\mathbf{p}) = 0. \end{aligned} \quad (3.5)$$

Solving for $\delta f_a^i(\mathbf{p}, K)$ we get

$$\begin{aligned}
\delta f_a^i(\mathbf{p}, K) &= -g\theta_i \frac{V_\mu F_a^{\mu\nu}(K) \partial_\nu^{(p)} f^i(\mathbf{p})}{-i\omega + i\mathbf{k} \cdot \mathbf{v} + \epsilon} = -i g\theta_i \frac{i V_\mu (K^\mu A_a^\nu - K^\nu A_a^\mu) \partial_\nu^{(p)} f^i(\mathbf{p})}{\omega - \mathbf{k} \cdot \mathbf{v} + i\epsilon} \\
&= g\theta_i \frac{[(\omega - \mathbf{k} \cdot \mathbf{v}) A_a^\nu - V_\mu K^\nu A_a^\mu] \partial_\nu^{(p)} f^i(\mathbf{p})}{\omega - \mathbf{k} \cdot \mathbf{v} + i\epsilon} \\
&= g\theta_i \partial_\nu^{(p)} f^i(\mathbf{p}) \left(A_a^\nu + \frac{V_\mu K^\nu A_a^\mu}{\omega - \mathbf{k} \cdot \mathbf{v} + i\epsilon} \right) \\
&= g\theta_i \partial_{(p)}^\beta f^i(\mathbf{p}) \left(g_{\nu\beta} + \frac{V_\nu K_\beta}{\omega - \mathbf{k} \cdot \mathbf{v} + i\epsilon} \right) A_a^\nu. \tag{3.6}
\end{aligned}$$

The induced current finally reads

$$J_{\text{ind}a}^\mu(K) = g^2 \int_{\mathbf{p}} V^\mu \partial_{(p)}^\beta f(\mathbf{p}) \left(g_{\gamma\beta} - \frac{V_\gamma K_\beta}{K \cdot V + i\epsilon} \right) A_a^\gamma(K) + \mathcal{O}(g^3 A^2), \tag{3.7}$$

where we combined the gluon and quark distributions in

$$f(\mathbf{p}) = 2N_c f^g(\mathbf{p}) + N_f [f^q(\mathbf{p}) + f^{\bar{q}}(\mathbf{p})]. \tag{3.8}$$

By functional differentiation

$$\Pi_{ab}^{\mu\nu}(K) = \frac{\delta J_{\text{ind}a}^\mu(K)}{\delta A_b^\nu(K)}, \tag{3.9}$$

we obtain the self energy

$$\Pi_{ab}^{\mu\nu}(K) = g^2 \delta_{ab} \int_{\mathbf{p}} V^\mu \partial_\beta^{(p)} f(\mathbf{p}) \left(g^{\nu\beta} - \frac{V^\nu K^\beta}{K \cdot V + i\epsilon} \right), \tag{3.10}$$

the same result that one gets in the diagrammatic approach using the HTL approximation and the assumption that f is symmetric under $\mathbf{p} \rightarrow -\mathbf{p}$ [125]. One finds that this tensor is symmetric $\Pi^{\mu\nu} = \Pi^{\nu\mu}$ and transverse $K_\mu \Pi^{\mu\nu} = 0$, if $f(\mathbf{p})$ vanishes on a two-sphere at infinity: $\lim_{\mathbf{p} \rightarrow \infty} f(\mathbf{p}) = 0$. We demonstrate the transversality for one example:

$$\begin{aligned}
K^\mu \Pi_{\mu 0} &= g^2 \int_{\mathbf{p}} K^\mu V_\mu \partial_j f(\mathbf{p}) \frac{k^j}{K \cdot V + i\epsilon} \\
&= g^2 \int_{\mathbf{p}} v_j k^j \frac{d}{dp} f(\mathbf{p}) \\
&= g^2 k \int_{\mathbf{p}} \cos \theta \frac{d}{dp} f(\mathbf{p}) \\
&= 0. \tag{3.11}
\end{aligned}$$

Due to the transversality not all components of $\Pi^{\mu\nu}$ are independent, and we can restrict our investigation to the spatial components. As we have already seen, in the linear approximation the current that is induced by the fluctuations can be expressed in terms of the self energy:

$$J_{\text{ind}}^\mu(K) = \Pi^{\mu\nu}(K) A_\nu(K). \tag{3.12}$$

Inserting this into MAXWELL's equation

$$iK_\mu F^{\mu\nu}(K) = J_{\text{ind}}^\nu + J_{\text{ext}}^\nu, \quad (3.13)$$

we get

$$[K^2 g^{\mu\nu} - K^\mu K^\nu + \Pi^{\mu\nu}(K)] A_\mu(K) = J_{\text{ext}}^\nu(K), \quad (3.14)$$

with the external current J_{ext}^ν . Using the gauge covariance of the self energy in the HTL-approximation we can write this in terms of a physical electric field by specifying a certain gauge. Using the temporal axial gauge, where $A_0 = 0$, yields

$$[(k^2 - \omega^2)\delta^{ij} - k^i k^j + \Pi^{ij}(K)] E^j(K) = [\Delta^{-1}(K)]^{ij} E^j(K) = i\omega J_{\text{ext}}^i(K), \quad (3.15)$$

and the response of the system to the external source is given by

$$E^i(K) = i\omega \Delta^{ij}(K) J_{\text{ext}}^j(K). \quad (3.16)$$

The dispersion relations are obtained by finding the poles of the propagator $\Delta^{ij}(K)$, defined in (3.15).

3.2 Dispersion relations in the isotropic limit

To determine the dispersion relations for an isotropic system, we assume f to depend on the length of \mathbf{p} only, and take a closer look at the spatial components of the self energy:

$$\Pi_{ab}^{ij}(K) = -g^2 \delta_{ab} \int_{\mathbf{p}} v^i \partial_l^{(p)} f(p) \left(\delta^{jl} + \frac{v^j k^l}{K \cdot V + i\epsilon} \right). \quad (3.17)$$

First, the derivative becomes

$$\partial_l f(p) = \frac{p_l}{p} \frac{df(p)}{dp} = v_l \frac{df(p)}{dp}. \quad (3.18)$$

Then, we can perform the radial and ϕ integrations to obtain

$$\Pi^{ij}(K) = \frac{m_D^2}{2} \int_0^\pi \sin \theta d\theta v^i v^l \left(\delta^{jl} + \frac{v^j k^l}{K \cdot V + i\epsilon} \right), \quad (3.19)$$

after neglecting the trivial color structure and introducing the DEBYE mass

$$m_D^2 = -\frac{g^2}{2\pi^2} \int_0^\infty dp p^2 \frac{df(p)}{dp} \xrightarrow{\text{equilibrium}} g^2 T^2 \left(\frac{2N_c + N_f}{6} \right), \quad (3.20)$$

for zero quark chemical potential. In the isotropic case there is only one distinct spatial direction in the system, the direction of \mathbf{k} . Therefore we can decompose the self energy into components parallel and transverse to \mathbf{k} :

$$\Pi^{ij} = P_T \Pi_T + P_L \Pi_L, \quad (3.21)$$

with the projectors

$$P_T = \left(\delta^{ij} - \frac{k^i k^j}{k^2} \right) \quad \text{and} \quad P_L = \frac{k^i k^j}{k^2}. \quad (3.22)$$

They obey the usual projector properties

$$(P_T)^2 = P_T, (P_L)^2 = P_L, \quad (3.23)$$

$$P_T P_L = P_L P_T = 0. \quad (3.24)$$

The scalar self energies are defined by the following projections, for which the integrals can be solved analytically:

$$\Pi_T = \frac{1}{2} P_T \Pi^{ij} = \frac{m_D^2}{2} \left[\frac{\omega^2}{k^2} + \omega \frac{(k^2 - \omega^2)}{2k^3} \ln \left(\frac{\omega + k}{\omega - k} \right) \right], \quad (3.25)$$

$$\Pi_L = P_L \Pi^{ij} = m_D^2 \frac{\omega^2}{k^2} \left[-1 + \frac{\omega}{2k} \ln \left(\frac{\omega + k}{\omega - k} \right) \right]. \quad (3.26)$$

The factor $1/2$ in the definition of Π_T is convenient because there are two transverse modes in three dimensions. Generally it is a factor of $1/(d-1)$, where d is the number of dimensions. Without it, the $1/2$ would show up in front of Π_T in Eq. (3.27) below.

Making use of the projectors (3.22), we can determine the dispersion relations of the transverse and longitudinal modes separately. By applying P_T to the equation that determines the zeros of the inverse propagator $\Delta^{-1}(K)$ (see Eq. (3.15)), we get the transverse dispersion relation:

$$k^2 - \omega_T^2 + \Pi_T = 0, \quad (3.27)$$

whereas application of P_L leads to the longitudinal one:

$$\Pi_L - \omega_L^2 = 0. \quad (3.28)$$

The solutions to Eqs. (3.27) and (3.28) are shown in Fig. 3.1. Taking the limit $k \rightarrow 0$ we get $\omega \rightarrow 1/3 m_D^2 = m_g^2$, representing the lowest frequency with which modes can propagate. We present the dispersion laws in units of $m_g = m_D/\sqrt{3}$ in linear scales in Fig. 3.1(a) and in quadratic scales in Fig. 3.1(b) in order to include both propagating modes and screening phenomena in one plot.

Propagating modes exist above a common plasma frequency $\omega > \omega_{\text{pl}} = \sqrt{m_D^2/3}$, are always above the light cone ($\omega > k$) and are called normal modes. For large momenta the transverse mode tends to a mass hyperboloid with asymptotic mass $m_\infty^2 = m_D^2/2$, whereas the longitudinal one approaches the light-cone with exponentially vanishing residue. For $\omega < m_g$, $|\mathbf{k}|$ is the inverse screening length, which in the static limit ($\omega \rightarrow 0$) vanishes for the transverse mode (absence of magnetostatic screening) but reaches the DEBYE mass, $m_D^2 = 3 m_g^2$, for the longitudinal mode (electrostatic screening). For $0 < \omega < \omega_{\text{pl}}$, k becomes imaginary [126] and there are no stable normal modes, however, there is a collective behavior which corresponds to dynamical screening both in the electric and magnetic sector as long as $\omega > 0$.

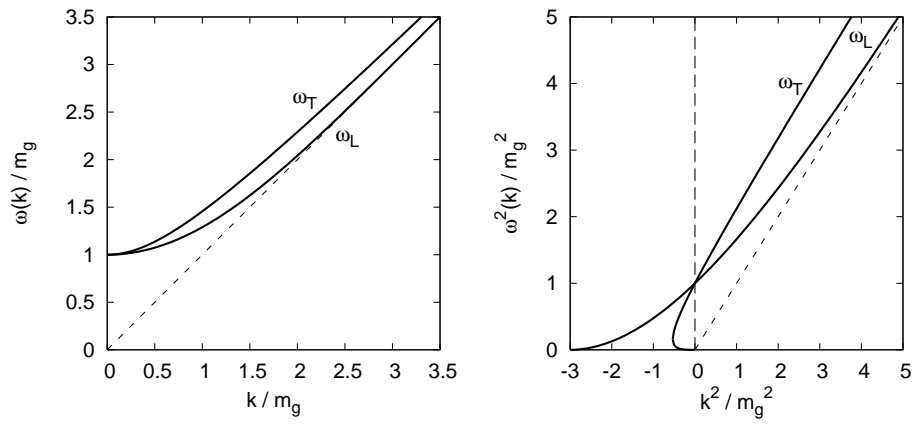


Figure 3.1: Dispersion laws for transverse and longitudinal gluons (left) on a linear scale in units of $m_g = m_D/\sqrt{3}$, and (right) in quadratic scales. Modes with $k^2 > 0$ are propagating whereas solutions for negative k^2 show screening phenomena.

4 The anisotropic quark-gluon plasma

Ungleich erscheint im Leben viel,
doch bald und unerwartet ist es ausgeglichen.

*Die natürliche Tochter. Vierter Aufzug.
Zweiter Auftritt. Gerichtsrat.*
Johann Wolfgang von Goethe (1749-1832)

The only system above the QCD-deconfinement transition one can (probably) study on earth, namely that of a fireball following an ultra-relativistic heavy-ion collision, is anisotropic in nature. Therefore, it is interesting to investigate which effects the presence of an anisotropy has on the dynamics of the system and which differences one can expect when comparing to the usually studied isotropic case.

We will consider systems which are anisotropic only in *momentum space*, therefore taking a snapshot of the system at some short time after the collision and before the system had time to convert the anisotropy from momentum space to configuration space. The appearance of local momentum anisotropies can be best understood when regarding a local cell in which initially the transverse momentum (transverse to the beam line) is set by the hard momentum scale Q_s , while the transverse momentum drops like $1/\tau$ (where τ is the proper time) as particles with momenta larger than that of the cell leave it. For pure free streaming only particles with a certain longitudinal momentum remain in the cell.

The momentum scale Q_s comes about the following way. The bulk of multiparticle production at central rapidities in A-A collisions emerges from partons with very small momentum fractions x (at LHC $x \leq 10^{-3}$). They interact coherently over distances much larger than the radius of the nucleus, which potentially makes understanding the properties of the nuclear wave function at small x a difficult task. However, some features of these wave functions simplify the problem. First, perturbative QCD predicts that parton distributions grow very rapidly at small x . At sufficiently small x , the parton distributions saturate, i.e., when the density of partons is such that they overlap in the transverse plane, their repulsive interactions are sufficiently strong to limit further growth to be at most logarithmic [127, 128, 129]. The large parton density per transverse area then provides a scale, Q_s . The physics of small- x parton distributions can be formulated in an effective field theory, where the saturation scale Q_s appears as the only scale [130, 131, 132]. The coupling must therefore run as a function of this scale, and since $Q_s^2 \ll \Lambda_{\text{QCD}}^2$ at RHIC or the LHC, $\alpha_s \ll 1$. Small coupling also ensures that the occupation number is large, $\sim 1/\alpha_s$. Thus, although the physics of small- x partons is non-perturbative, it can be studied with weak coupling [133, 134, 135, 136, 137, 138, 139, 140]. This is analogous to many systems in condensed-matter physics. In particular, the physics of small- x wave functions is similar to that of a spin glass [141, 135, 136, 137, 138, 139]. Further, since in this state the mean transverse momentum of the partons is of order Q_s , and their occupation numbers are large, of order

$1/\alpha_s$, as in a condensate, the partons in the nuclear wave function form a so called color glass condensate (CGC) [140, 141].

Considering momentum anisotropies alone is certainly not the whole story. However, the generalization from fully isotropic distributions already provides great insight into the properties of the QGP within the fireball. Moreover, a treatment of configuration space anisotropies would involve a full non-equilibrium quantum field theoretical description of the system, which despite recent progress is not yet available.

In this chapter we will analyze the collective modes of high-temperature QCD in the case when there is an anisotropy in the momentum-space distribution function. We concentrate on a class of anisotropic distribution functions, which can be obtained by stretching or squeezing an isotropic one along a certain direction, thereby preserving a cylindrical symmetry in momentum space. This particular class of distribution functions has been first discussed by ROMATSCHKE and STRICKLAND in [63] and [142]. We write

$$f(\mathbf{p}) = \mathcal{N}(\xi) f_{\text{iso}}(\mathbf{p}^2 + \xi(\mathbf{p} \cdot \hat{\mathbf{n}})^2), \quad (4.1)$$

for an arbitrary isotropic distribution function $f_{\text{iso}}(|\mathbf{p}|)$. The direction of the anisotropy is given by $\hat{\mathbf{n}}$ and $\xi > -1$ is an adjustable anisotropy parameter. $\xi > 0$ corresponds to a contraction of the distribution in the $\hat{\mathbf{n}}$ direction, whereas $-1 < \xi < 0$ represents a stretching of the distribution in the $\hat{\mathbf{n}}$ direction. The factor $\mathcal{N}(\xi)$ is used for normalization. For example, when choosing $\mathcal{N}(\xi) = \sqrt{1 + \xi}$, we ensure that the overall particle number is the same for both the anisotropic and the isotropic distribution function.¹ For a certain anisotropy Fig. 4.1 shows how this procedure deforms the FERMI-DIRAC distribution. One

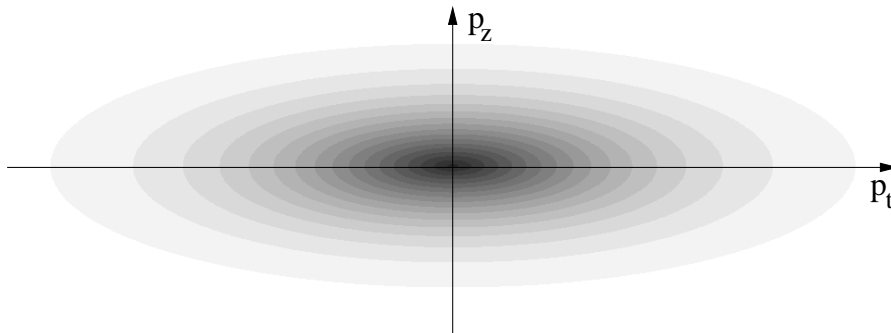


Figure 4.1: Contour plot of a squeezed FERMI-DIRAC distribution with anisotropy parameter $\xi = 10$. The anisotropy vector $\hat{\mathbf{n}}$ is taken to be along the p_z direction.

of the most interesting aspects of the anisotropic QGP is the appearance of unstable gluonic modes, which we discuss in detail in Sec. 4.4.

¹Note that for the FERMI distribution this way of normalizing f is not appropriate, because it violates the PAULI exclusion principle. The following considerations will not depend on the particular choice of $\mathcal{N}(\xi)$ qualitatively. When we turn to the discussion of photon production from an anisotropic QGP we will set $\mathcal{N}(\xi) = 1$, because there the compliance with the PAULI exclusion principle becomes important - otherwise the PAULI blocking term may become negative.

4.1 Tensor decomposition

The anisotropy vector introduces a second special direction and we can no longer decompose the propagator and the self energy into transverse and longitudinal parts. However, we can decompose the spatial part of the self energy into four structure functions using the tensor basis introduced in [63, 143]:

$$\Pi^{ij} = \alpha A^{ij} + \beta B^{ij} + \gamma C^{ij} + \delta D^{ij}, \quad (4.2)$$

where

$$\begin{aligned} A^{ij} &= \delta^{ij} - k^i k^j / k^2 \\ B^{ij} &= k^i k^j / k^2 \\ C^{ij} &= \tilde{n}^i \tilde{n}^j / \tilde{n}^2 \\ D^{ij} &= k^i \tilde{n}^j + k^j \tilde{n}^i, \end{aligned} \quad (4.3)$$

with $\tilde{n}^i = A^{ij} n^j$ the part of \mathbf{n} that is perpendicular to \mathbf{k} , i.e., $\tilde{\mathbf{n}} \cdot \mathbf{k} = 0$. We determine the structure functions by taking the contractions:

$$\begin{aligned} k^i \Pi^{ij} k^j &= k^2 \beta \\ \tilde{n}^i \Pi^{ij} k^j &= \tilde{n}^2 k^2 \delta \\ \tilde{n}^i \Pi^{ij} \tilde{n}^j &= \tilde{n}^2 (\alpha + \gamma) \\ \text{Tr } \Pi^{ij} &= 2\alpha + \beta + \gamma. \end{aligned} \quad (4.4)$$

The four structure functions $\alpha, \beta, \gamma, \delta$ depend on the DEBYE mass m_D , the frequency and spatial momentum ω and k , the strength of the anisotropy ξ and the angle between the spatial momentum and the anisotropy direction $\hat{\mathbf{k}} \cdot \hat{\mathbf{n}} = \cos \theta_n$. In the isotropic limit ($\xi \rightarrow 0$) the structure functions $\alpha(K, \xi)$ and $\beta(K, \xi)$ reduce to the isotropic HTL self-energies and γ and δ vanish,

$$\begin{aligned} \alpha(K, 0) &= \Pi_T(K), \\ \beta(K, 0) &= \Pi_L(K), \\ \gamma(K, 0) &= 0, \\ \delta(K, 0) &= 0, \end{aligned} \quad (4.5)$$

where $\Pi_T(K)$ and $\Pi_L(k)$ are given by Eqs. (3.25) and (3.26). Note that for finite ξ the analytic structure of $\alpha, \beta, \gamma, \delta$ is the same as for Π_L, Π_T in the isotropic case, namely there is a cut in the complex ω plane which can be chosen to run along the real ω axis within $-k < \omega < k$. For real-valued ω the structure functions are complex for all $\omega < k$ (corresponding to the LANDAU damping regime) and real for $\omega > k$ while for imaginary-valued ω all four structure functions are real-valued.

In this basis, the inverse of the propagator in Eq. (3.15) can be written as

$$\Delta^{-1}(K) = (k^2 - \omega^2 + \alpha)\mathbf{A} + (\beta - \omega^2)\mathbf{B} + \gamma\mathbf{C} + \delta\mathbf{D}, \quad (4.6)$$

while the propagator itself is given by [63]:

$$\Delta(K) = \Delta_A(\mathbf{A} - \mathbf{C}) + \Delta_G [(k^2 - \omega^2 + \alpha + \gamma)\mathbf{B} + (\beta - \omega^2)\mathbf{C} - \delta\mathbf{D}], \quad (4.7)$$

with

$$\Delta_A^{-1}(K) = k^2 - \omega^2 + \alpha, \quad (4.8)$$

$$\Delta_G^{-1}(K) = (k^2 - \omega^2 + \alpha + \gamma)(\beta - \omega^2) - k^2 \tilde{n}^2 \delta^2. \quad (4.9)$$

Furthermore, with the particular choice for the distribution functions (4.1), the spatial components of the self energy (3.10)

$$\Pi_{ab}^{ij}(K) = -g^2 \delta_{ab} \int_{\mathbf{p}} v^i \partial_l^{(p)} f(\mathbf{p}) \left(\delta^{jl} + \frac{v^j k^l}{K \cdot V + i\epsilon} \right) \quad (4.10)$$

can be simplified by performing the change of variables to \tilde{p} :

$$\tilde{p}^2 = p^2 [1 + \xi(\mathbf{v} \cdot \hat{\mathbf{n}})^2], \quad (4.11)$$

which allows for integrating out the \tilde{p} -dependence. We find

$$\Pi^{ij}(K) = m_D^2 \int \frac{d\Omega}{4\pi} v^i \frac{v^l + \xi(\mathbf{v} \cdot \hat{\mathbf{n}})n^l}{(1 + \xi(\mathbf{v} \cdot \hat{\mathbf{n}})^2)^2} \left(\delta^{jl} + \frac{v^j k^l}{K \cdot V + i\epsilon} \right), \quad (4.12)$$

where (cf. Eq. (3.20))

$$m_D^2 = -\frac{g^2}{2\pi^2} \int_0^\infty dp p^2 \frac{df_{\text{iso}}(p)}{dp}. \quad (4.13)$$

4.2 Stable modes

Considering first the stable collective modes which correspond to poles of the propagator at real-valued $\omega > k$ one factorizes Δ_G^{-1} as [63]:

$$\Delta_G^{-1} = (\omega^2 - \Omega_+^2)(\omega^2 - \Omega_-^2), \quad (4.14)$$

where

$$2\Omega_\pm^2 = \bar{\Omega}^2 \pm \sqrt{\bar{\Omega}^4 - 4((\alpha + \gamma + k^2)\beta - k^2 \tilde{n}^2 \delta^2)}, \quad (4.15)$$

and

$$\bar{\Omega}^2 = \alpha + \beta + \gamma + k^2. \quad (4.16)$$

Since the quantity under the square root in (4.15) can be written as $(\alpha - \beta + \gamma + k^2)^2 + 4k^2 \tilde{n}^2 \delta^2$ (which is always positive for real $\omega > k$), there are at most two stable modes coming from Δ_G , while the remaining stable collective mode comes from the zero of Δ_A^{-1} .

The dispersion relations for all of the collective modes are then given by the solutions to

$$\omega_\pm^2 = \Omega_\pm^2(\omega_\pm), \quad (4.17)$$

$$\omega_\alpha^2 = k^2 + \alpha(\omega_\alpha). \quad (4.18)$$

In the isotropic limit ($\xi \rightarrow 0$) one finds the correspondence $\omega_\alpha = \omega_+ = \omega_T$ and $\omega_- = \omega_L$. Accordingly, for finite ξ , there are three stable quasi-particle modes with dispersion relations that depend on the angle of propagation with respect to the anisotropy vector, θ_n . The resulting dispersion relations for all three modes for the case $\xi = 10$ and different angles θ_n are shown in Ref. [63].

4.3 Unstable modes

One of the most interesting features of the anisotropic quark-gluon plasma is the presence of unstable modes that, instead of being damped, grow exponentially with time. Mathematically they arise due to poles of the propagator along the positive imaginary ω axis. We will discuss the physical explanation for these so called WEIBEL instabilities in Section 4.4. There are also additional damped modes along the negative imaginary ω -axis, which are not present in the isotropic case. Checking for poles at complex (not purely imaginary) ω can be done numerically but no poles on the physical sheet have been found [63]. In [142] it was shown analytically for certain special cases that there are no other modes than the ones listed above. However, there exist solutions on unphysical sheets, which come very close to the border of the physical sheet for sufficiently large values of the anisotropy parameter ξ (see Ref. [142]).

For the unstable modes of the system we can write $\omega \rightarrow i\Gamma$, with Γ being the real-valued solution to the equations

$$\begin{aligned}\Delta_G^{-1} &= (\Gamma^2 + \Omega_+^2)(\Gamma^2 + \Omega_-^2) = 0, \\ \Delta_A^{-1} &= (\Gamma^2 + k^2 + \alpha) = 0.\end{aligned}\tag{4.19}$$

It turns out that in contrast to the stable modes there is at most one solution for $\Delta_G^{-1}(\omega = i\Gamma) = 0$ since numerically one finds that $\Omega_+^2 > 0$ for all $\Gamma > 0$, while $\Delta_A^{-1}(\omega = i\Gamma) = 0$ has only solutions for $\xi > 0$. Therefore, the system possesses one or two unstable modes depending on the sign of the anisotropy parameter [63].

We present a plot of the growth rate Γ_α for the case that $\mathbf{k} \parallel \hat{\mathbf{n}}$ ($\theta_n = 0$) and different anisotropy parameters ξ in Fig. 4.2. For solutions for arbitrary angles see [63]. It turns out that the growth rate is the largest for $\theta_n = 0$, which we will explain on physical grounds in Section 4.4. One can also see that the growth rate and the maximal value of k for the unstable mode become larger with increasing anisotropy.

4.4 Discussion of instabilities

The electron-ion plasma is known to experience a large variety of instabilities [144]. They can be either caused by coordinate space inhomogeneities, in particular by the boundaries of finite systems (hydrodynamic instabilities) or by non-equilibrium momentum distributions of plasma particles (kinetic instabilities). Hardly anything is known about hydrodynamic instabilities of the quark-gluon plasma and we will concentrate on the kinetic instabilities, which are initiated either by charge or current fluctuations. In the first case, the electric field is parallel to the wave vector \mathbf{k} ($\mathbf{E} \parallel \mathbf{k}$), while in the second case the field is perpendicular to \mathbf{k} ($\mathbf{E} \perp \mathbf{k}$). This is why the corresponding instabilities are called longitudinal and transverse, respectively. Since the electric field plays a crucial role in the generation of longitudinal modes, they are also called electric, while the transverse modes are called magnetic.

Soon after the concept of quark-gluon plasma had been established, the existence of the color kinetic instabilities, fully analogous to those known in the electrodynamic plasma, was suggested [145, 146, 147, 148, 149, 150, 151].

However, in these works a two-stream system, or more generally, a momentum distribution with more than one maximum, was considered. Such a distribution is common in

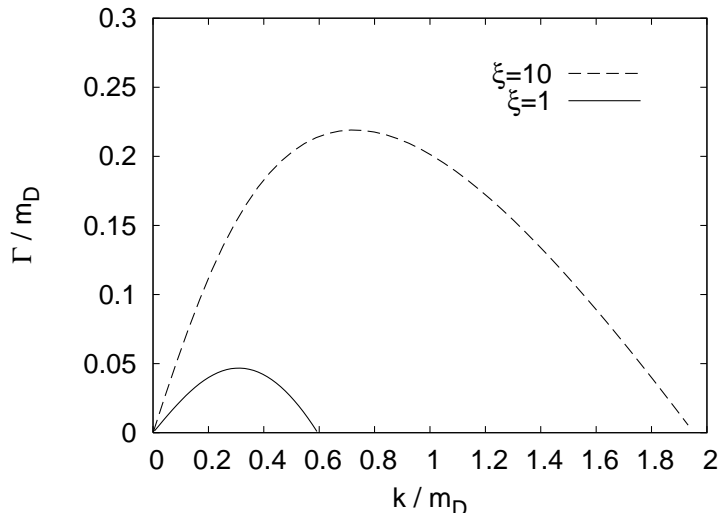


Figure 4.2: Growth rate of the unstable α -mode for the case $\mathbf{k} \parallel \hat{\mathbf{n}}$ (where this is the only unstable mode) and different anisotropy parameters ξ . The maximal growth rate as well as the maximal k increase with increasing ξ .

the electron-ion plasma, however it is rather inappropriate for describing the quark-gluon plasma produced in relativistic heavy-ion collisions where the global as well as local momentum distribution is expected to be monotonously decreasing in every direction from the maximum. Electric instabilities are absent in such a system but, as we have already seen in Section 4.3 and was first demonstrated in [60, 61], a magnetic unstable mode known as the filamentation or WEIBEL instability [152] can possibly appear since a sufficient condition for its existence is the anisotropy of the momentum distribution. That these instabilities really exist in nature is strongly supported by rather recent experimental observations in plasma physics. Please refer to Appendix B for further details.

The filamentation instability was shown [60, 61] to be possibly relevant for the quark-gluon plasma produced in relativistic heavy-ion collisions. The characteristic time of instability growth is shorter or at least comparable to other time scales of the parton system evolution. And the instabilities – usually not one but several modes are generated – drive the system towards isotropy, thus speeding up its equilibration. Since the apparent very fast equilibration of the QGP is not understood so far, this aspect has been under strong investigation in the recent past [125, 153, 62, 63, 64, 142, 154, 65, 66, 155, 156].

The equilibration due to instabilities only happens indirectly, because the instabilities driven isotropization is a mean-field reversible process, which does not produce entropy [61, 66]. Therefore, the collisions, which are responsible for the dissipation, are needed to reach the equilibrium state of maximal entropy. Recently it has been argued [53] that the hydrodynamic collective behavior does not require local thermodynamic equilibrium but a merely isotropic momentum distribution of liquid components. This would mean that the success of hydrodynamic models in describing the data indicates that not the equilibration time but rather the isotropization time is of order 1 fm/c.

In 2003, MRÓWCZYŃSKI and RANDRUP [62] have performed a phenomenological estimate of the growth rate of the instabilities for scenarios relevant to the quark-gluon plasma produced at RHIC or LHC, using however a different implementation of the anisotropy than Eq. (4.1). They found that the degree of amplification of the instabilities is not expected to dominate the dynamics of the quark-gluon plasma, but instead their effect would be comparable to the contribution from elastic BOLTZMANN collisions. However, they also pointed out that if a large number of unstable modes would be excited then their combined effect on the overall dynamics could well be significant. In the same year, ARNOLD, LENAGHAN and MOORE [64] investigated the case corresponding to the $\xi \rightarrow \infty$ limit in the prescription described above, arguing that it drastically modifies the scenario of “bottom-up thermalization” advocated by BAIER, MUELLER, SCHIFF and SON [56], which would then have to be replaced by a different scheme.

4.4.1 Seeds and mechanism of filamentation

An anisotropic system has a natural tendency to split into current filaments parallel to the direction of the momentum surplus. These currents are seeds of the filamentation instability. We now explain in terms of elementary physics why the fluctuating currents, which flow in the direction of the momentum surplus, can grow in time. To simplify the discussion, which follows [157], we consider an electromagnetic anisotropic system. The form of the fluctuating current is chosen to be²

$$\mathbf{j}(x) = j \hat{\mathbf{e}}_z \cos(k_x x), \quad (4.20)$$

where $\hat{\mathbf{e}}_z$ is the unit vector in the z direction. From Eq. (4.20) we can infer the existence of current filaments of the thickness $\pi/|k_x|$ with the current flowing in the opposite directions in the neighboring filaments. The magnetic field generated by the current (4.20) is given by

$$\mathbf{B}(x) = \frac{j}{k_x} \hat{\mathbf{e}}_y \sin(k_x x), \quad (4.21)$$

and the LORENTZ force acting on the partons, which move along the z direction, equals

$$\mathbf{F}(x) = q \mathbf{v} \times \mathbf{B}(x) = -q v_z \frac{j}{k_x} \hat{\mathbf{e}}_x \sin(k_x x), \quad (4.22)$$

where q is the electric charge. In Fig. 4.3 it is shown how the force distributes the partons in such a way that those, which positively contribute to the current in a given filament, are focused in the filament center while those, which negatively contribute, are moved to the neighboring one. Thus, both the initial current and the magnetic field generated by this current are growing. The instability is driven by the energy transferred from the particles to fields. More specifically, the kinetic energy related to a motion along the direction of the momentum surplus is used to generate the magnetic field. A somewhat different explanation of the mechanism of the WEIBEL instability is given in [64].

²For now we assume a distribution with the momentum surplus in the z direction.

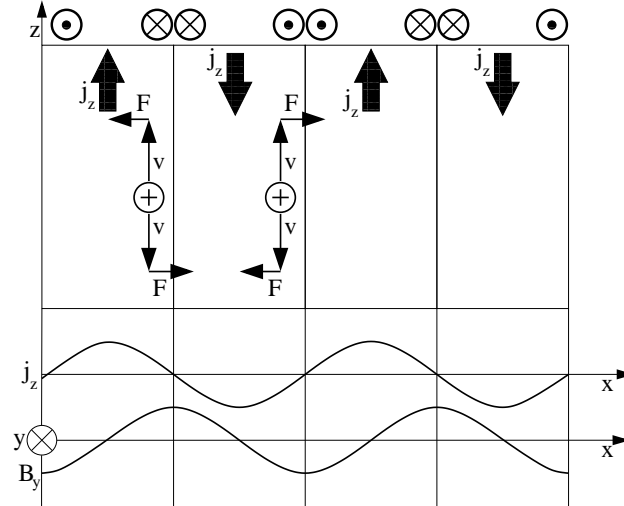


Figure 4.3: The mechanism that leads to the filamentation instability, see text for a description.

4.4.2 Isotropization and Abelianization

When the instabilities grow the system becomes more isotropic because the LORENTZ force changes the particles' momenta. Additionally the growing fields carry momentum directed into directions with momentum deficit. Let us stick with the assumption that there is a momentum surplus in the z direction. The fluctuating current flows in the z direction with the wave vector pointing in the x direction. Since the magnetic field has a y component, the LORENTZ force, which acts on partons flying along the z axis, pushes the partons in the x direction where there is a momentum deficit. Numerical simulations [65, 66, 155, 156] show that growth of the instabilities is indeed accompanied by the system's fast isotropization.

The system isotropizes not only due to the effect of the LORENTZ force but also due to the momentum carried by the growing field. When the magnetic and electric fields are oriented along the y and z axes, respectively, the POYNTING vector points in the direction x that is along the wave vector. Thus, the momentum carried by the fields is oriented in the direction of the momentum deficit of particles.

Unstable modes cannot grow to infinity and even in the electron-ion plasma there are several possible mechanisms which stop the instability growth [158]. The actual mechanism depends on the plasma state as well as on the external conditions. In the case of the quark-gluon plasma one suspects that non-Abelian non-linearities can play an important role here. An elegant argument [159] suggests that the non-linearities do not stabilize the unstable modes because the system spontaneously chooses an Abelian configuration in the course of instability development. In Appendix C we explain this argument in detail.

4.4.3 Summary of recent numerical simulations

As mentioned above, the temporal evolution of an anisotropic quark-gluon plasma has been studied numerically [65, 66, 155, 156, 160, 161, 162, 163]. The three groups of authors

use two very different dynamical schemes. In the simulations [65, 155, 156, 160, 163] the dynamics are described by Eq. (3.1) together with the YANG-MILLS equation, both in the local representation, where the quark, anti-quark and gluon distributions are parameterized by the field $W^\mu(\mathbf{v}, X)$ through the relations

$$\begin{aligned}\delta n^q(\mathbf{p}, X) &= g \frac{\partial f^q(\mathbf{p})}{\partial p^\mu} W(\mathbf{v}, X), \\ \delta n^{\bar{q}}(\mathbf{p}, X) &= -g \frac{\partial f^{\bar{q}}(\mathbf{p})}{\partial p^\mu} W(\mathbf{v}, X), \\ \delta n^g(\mathbf{p}, X) &= g \frac{\partial f_a^g(\mathbf{p})}{\partial p^\mu} T^a \text{Tr}(t^a W(\mathbf{v}, X)).\end{aligned}\quad (4.23)$$

Note that all used quantities have been defined below Eq. (3.1). Instead of the three transport equations (3.1) one has only one equation

$$v_\mu D^\mu W^\nu(\mathbf{v}, X) = -v_\rho F^{\rho\nu}(X), \quad (4.24)$$

and the YANG-MILLS equation reads

$$D_\mu F^{\mu\nu}(X) = J^\nu(X) = -g^2 \int \frac{d^3p}{(2\pi)^3} \frac{p^\nu}{|\mathbf{p}|} \frac{\partial f(\mathbf{p})}{\partial p^\rho} W^\rho(\mathbf{v}, X), \quad (4.25)$$

with $f(\mathbf{p})$ as in Eq. (3.8). These simulations are reliable as long as the potential's amplitude is not too large, i.e., $A_a^\mu \ll p_{\text{hard}}/g$, where p_{hard} is the characteristic momentum of the hard partons. Note that Eqs. (4.24) and (4.25) only describe small fluctuations around the stationary homogeneous state, and therefore only a small fraction of the hard particles is actually influenced by the growing chromo-dynamic field. Hence, one may consider the hard particles an effective stationary (anisotropic) background.

The simulations [66, 161, 162] use the classical, not linearized version of Eqs. (3.1). This means that the QGP is treated as a completely classical system, in which partons, that carry classical color charges, interact with the self-consistently generated classical chromodynamic field. In Chapter 6, we will discuss this kind of simulation in great detail.

The simulations [65, 66] have been performed in 1+1 dimensions, whereas the calculations [155, 156] are full 1+3 dimensional simulations. In most cases the SU(2) gauge group was studied but some SU(3) results, which are qualitatively similar to the SU(2) ones, are given in [156].

The initial conditions used in the simulations [65, 66, 155, 156, 160, 161, 162] are quite similar while the techniques of discretization are different. The initial field amplitudes have a GAUSSIAN white noise distribution, whereas the momentum distribution of the hard particles is strongly anisotropic. For example in the classical simulation [66] the initial parton momentum distribution is chosen as

$$f(\mathbf{p}) \sim \delta(p_x) e^{-\sqrt{p_y^2 + p_z^2}/p_{\text{hard}}}, \quad (4.26)$$

with $p_{\text{hard}} = 10$ GeV. The results turn out to be insensitive to the specific form of the momentum distribution. If the parton distribution function is written in the form (4.1), the results are shown [63, 65] to only depend on the strength of the anisotropy parameterized by ξ and the DEBYE mass m_D (Eq. (3.20)) of the corresponding isotropic system.

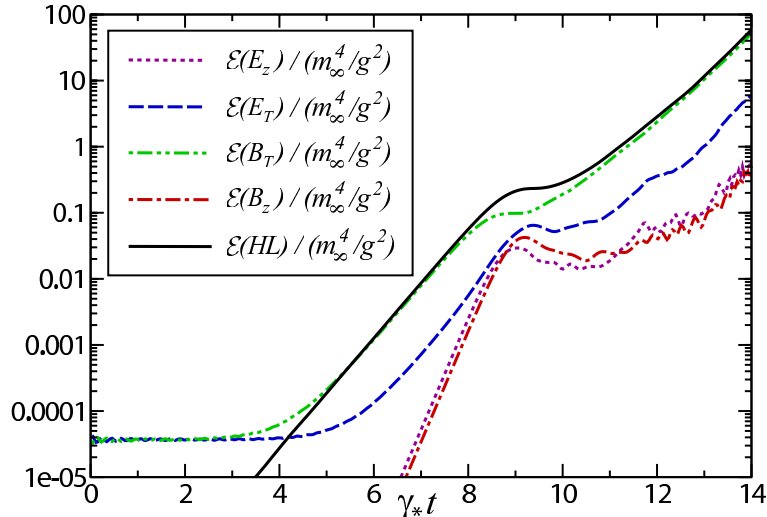


Figure 4.4: Time evolution of the (scaled) energy density (split into various electric and magnetic components) which is carried by the chromo-dynamic field. The simulation is 1+1 dimensional and the gauge group is SU(2). The parton momentum distribution is squeezed along the z axis. The solid line corresponds to the total energy transferred from the particles. γ_* is the growth rate of the fastest growing unstable mode. The figure is taken from [65].

The results from the HL-simulation in 1+1 dimensions are shown in Fig. 4.4, taken from [65]. One observes an exponential growth of the energy density stored in the fields, which is dominated by chromo-magnetic fields which are transverse to the direction of the momentum deficit (B_T). Fig. 4.5, taken from [66], shows results of the classical simulation on a 1+1 dimensional lattice of physical size $L = 40$ fm. As in Fig. 4.4 the amount of field energy grows exponentially and again the magnetic contribution dominates. The Abelian (U(1)) and non-Abelian (SU(2)) results are remarkably similar to each other, which means that the Abelianization, mentioned in Section 4.4.2, appears to be very efficient in 1+1 dimensions.

The results of the 1+3 dimensional simulations [155, 156] are qualitatively different from the 1+1 dimensional simulations. As seen in Figs. 4.6 and 4.7, taken from [155] and [156] respectively, the growth of the field energy density is exponential only for some time; then it becomes linear. It appears that the behavior changes when the field amplitude becomes of the order k/g , where k is the characteristic field wave vector. Then, the non-Abelian effects start to be important. The regime of linear growth of the magnetic energy, shown in Figs. 4.6 and 4.7, was studied in more detail in [160]. There it was found that when the exponential growth of the magnetic energy ends, the long-wavelength modes associated with the instability stop growing, but they *cascade* energy towards the ultraviolet in the form of plasmon excitations. This way a quasi-stationary state with a power-law distribution k^{-2} of the plasmon mode population is created. This phenomenon was argued to be very similar to the KOLMOGOROV wave turbulence, where long-wavelength modes transfer their energy to shorter ones without dissipation. In the classical simulation [162], when the field strength

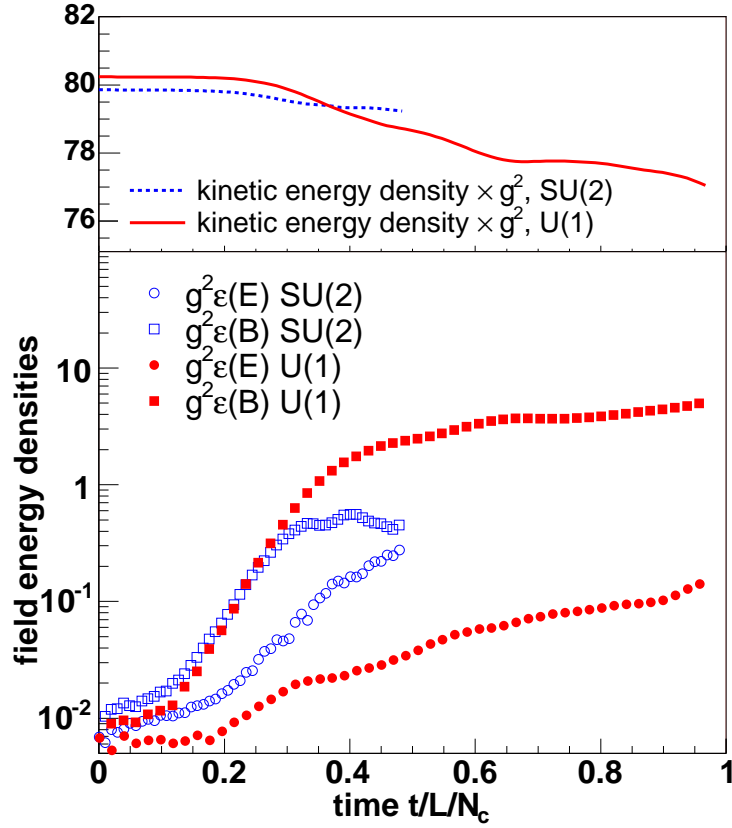


Figure 4.5: Time evolution of the kinetic energy of particles (upper panel) and of the energy of electric and magnetic fields (lower panel) in GeV/fm^3 for the U(1) and SU(2) gauge groups. The figure is taken from [66].

is large enough, the energy drained from the particles by the instability does not build up exponentially in magnetic fields but instead returns isotropically to the ultraviolet, not via the quasi-stationary process, as argued in [160], but via a rapid *avalanche*.

The 1+1 dimensional classical simulation [66] nicely shows the effect of isotropization due to the action of the LORENTZ force. In Fig. 4.8, taken from [66], there are shown the diagonal components of the energy-momentum tensor

$$T^{\mu\nu} = \int \frac{d^3p}{(2\pi)^3} \frac{p^\mu p^\nu}{E_p} f(\mathbf{p}). \quad (4.27)$$

The initial momentum distribution is given by Eq.(4.26), such that $T^{xx} = 0$ at $t = 0$. Fig. 4.8 shows that T^{xx} grows exponentially, but full isotropy, which requires $T^{xx} = (T^{yy} + T^{zz})/2$, is not achieved. So far, all mentioned numerical studies have been dealing with quark-gluon systems of constant volume. In [163, 164] a system that expands boost-invariantly in one direction is treated and it is shown numerically as well as analytically that the expansion slows down the growth of the unstable modes, even if the system is highly anisotropic. The field amplitude grows like an exponential with the exponent pro-

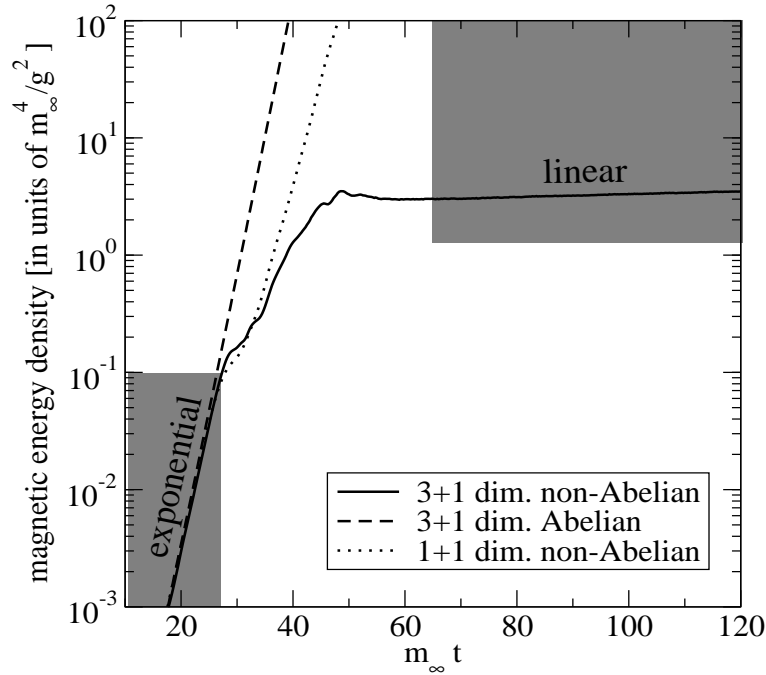


Figure 4.6: Time evolution of the (scaled) chromo-magnetic energy density in the 1+3 dimensional simulation. The Abelian result and that of 1+1 dimensions are also shown. The figure is taken from [155].

portional to \sqrt{t} . Further quantitative analysis of the effect of expansion on the instability growth is necessary, since it may turn out that they are irrelevant for heavy-ion collisions in the case that they grow too slowly to compete with the expansion.

Unstable parton systems under conditions close to those realized in heavy-ion collisions have recently been studied in [165, 166, 167]. The system was described in terms of the Color Glass Condensate approach [168] where small x partons of large occupation numbers, which dominate the wave functions of incoming nuclei, are treated as classical YANG-MILLS fields. In these simulations the hard modes of the classical fields play the role of particles. The instabilities, identified as the WEIBEL modes, appear to be generated when the system of YANG-MILLS fields expands into vacuum.

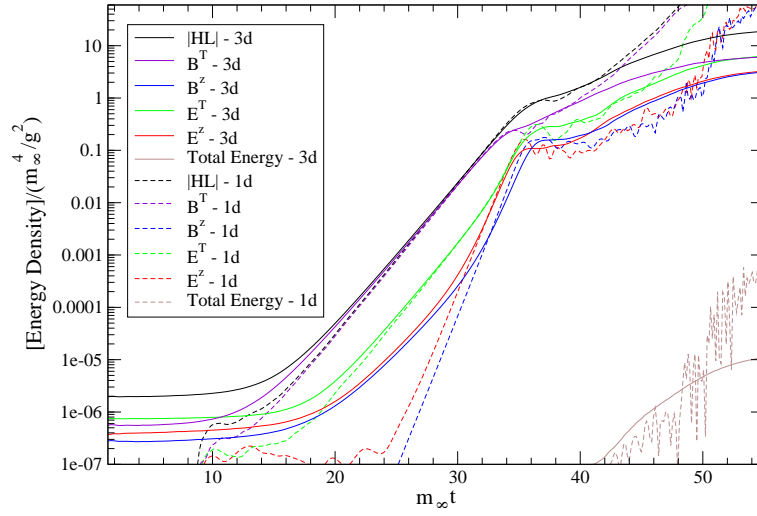


Figure 4.7: Time evolution of the (scaled) energy density (split into various electric and magnetic components) of the chromo-dynamic field in the 1+1 and 1+3 simulations. ‘HL’ denotes the total energy contributed by hard particles. The figure is taken from [156].

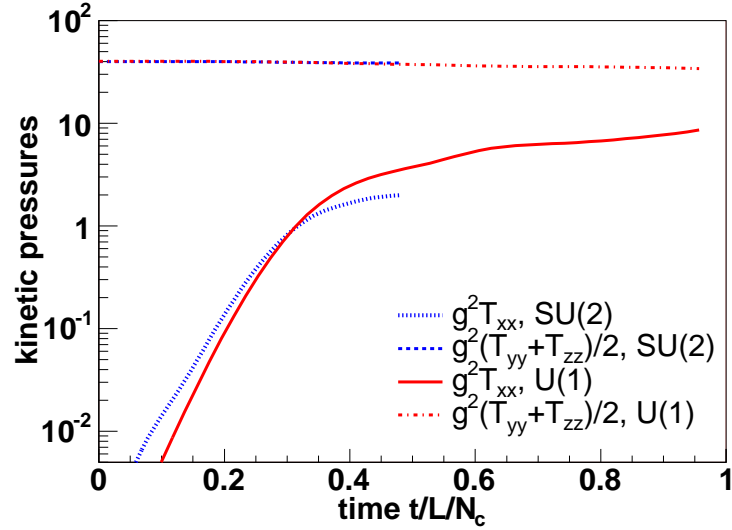


Figure 4.8: Temporal evolution of the energy-momentum tensor components T^{xx} and $(T^{yy} + T^{zz})/2$. The Abelian and non-Abelian results are shown. The figure is taken from [66].

5 A model approach to the inclusion of collisions

Sehr leicht zerstreut der Zufall was er sammelt.

Torquato Tasso. Erster Aufzug. Erster Auftritt. Leonore.
Johann Wolfgang von Goethe (1749-1832)

As pointed out already in Section 4.4, collisions, being responsible for the dissipation, are needed to drive the system towards equilibrium, even if instabilities speed up isotropization. All calculations so far have been carried out at leading order in perturbation theory, such that collisions among the hard particles that enter at higher orders in g could be neglected when concentrating on collective modes with soft momenta of the order gT . However, in heavy-ion collision experiments at the RHIC and LHC the couplings expected are of the order $\alpha_s \sim 0.2 - 0.3$ and higher order terms will be important. Hence, collisions can not simply be neglected and their effect on the system's evolution, particularly on the collective modes, has to be investigated.

In this chapter we give a first quantitative estimate of how the collisions affect the dispersion relations of the collective modes and the growth of instabilities in particular. To achieve this, we introduce a model for the inclusion of collisions based on the VLASOV equations for QCD combined with a BHATNAGAR-GROSS-KROOK (BGK)-type collision term [169].¹ We will deal with anisotropic systems with momentum distributions of the kind (4.1), introduced and discussed in Chapter 4. We concentrate on the case in which the direction of anisotropy is parallel to the wave vector of the regarded collective mode, because in this case the growth rate of the magnetic instability is maximal (see Sections 4.3 and 4.4) and analytic expressions for the structure functions can be found.

5.1 Structure functions and dispersion relations

In the effectively Abelian limit, discussed in Section 3.1, the equation of motion holds for each color channel separately. We now include a BGK-type collision term [169] on the right hand side of Eq. (3.4), which becomes

$$V \cdot \partial_X \delta f_a^i(p, X) + g\theta_i V_\mu F_a^{\mu\nu}(X) \partial_\nu^{(p)} f^i(\mathbf{p}) = C_a^i(p, X), \quad (5.1)$$

with

$$C_a^i(p, X) = -\nu \left[f_a^i(p, X) - \frac{N_a^i(X)}{N_{\text{eq}}^i} f_{\text{eq}}^i(|\mathbf{p}|) \right], \quad (5.2)$$

¹This chapter is based on the work published in [170].

where $f_a^i(p, X) = f^i(\mathbf{p}) + \delta f_a^i(p, X)$. This term describes how collisions equilibrate the system within a time proportional to ν^{-1} . We will assume that the collision rate ν is independent of momentum and particle species, however, these assumptions are easily relaxed. Note that these collisions are not color-rotating. The particle numbers are given by

$$N_a^i(X) = \int_{\mathbf{p}} f_a^i(p, X), \quad N_{\text{eq}}^i = \int_{\mathbf{p}} f_{\text{eq}}^i(|\mathbf{p}|) = \int_{\mathbf{p}} f^i(\mathbf{p}). \quad (5.3)$$

The difference between the BGK collisional kernel (5.2) and the conventional relaxation-time approximation (RTA) is the multiplication of the second term in brackets by the ratio of the density over the equilibrium density. RTA simply takes the difference of the distribution function and the equilibrium distribution function implicitly setting this ratio to one. The advantage of the BGK kernel over an RTA kernel lies in the fact that the number of particles is instantaneously conserved by the BGK collisional-kernel [171], i.e., that

$$\int_{\mathbf{p}} C_a^i(p, X) = 0. \quad (5.4)$$

This simply states that the collisions can only occur if a particle is present and that only the momentum of the particles will change as a result, not the particle number. This condition is violated by RTA.

The inclusion of a BGK collisional kernel allows for simulation of the effect of binary collisions with substantial momentum transfer and is merely an approximation for collisions between the hard charged particles in a hot quark-gluon plasma. However, it is a reasonable way to yield a first quantitative answer to the question of how collisions among hard particles affect the collective modes of QCD. The effects of such a collision term on the dispersion relations in the ultra-relativistic case for an isotropic system were investigated in [172]. For now the collision rate ν is taken to be a free parameter and we postpone the estimation of its magnitude to the discussions in Section 5.4.

Using (5.3) we can write

$$\begin{aligned} V \cdot \partial_X \delta f_a^i(p, X) + g\theta_i V_\mu F_a^{\mu\nu}(X) \partial_\nu^{(p)} f^i(\mathbf{p}) = \\ - \nu \left[f^i(\mathbf{p}) + \delta f_a^i(p, X) - \left(1 + \frac{\int_{\mathbf{p}} \delta f_a^i(p, X)}{N_{\text{eq}}^i} \right) f_{\text{eq}}^i(|\mathbf{p}|) \right]. \end{aligned} \quad (5.5)$$

Solving for $\delta f_a^i(p, X)$ and FOURIER-transforming as in (3.5) and (3.6) leads to the result for the linearized induced current by each particle species i . From Eq. (5.5) we immediately get

$$\begin{aligned} (-i\omega + i\mathbf{v} \cdot \mathbf{k} + \nu) \delta f^i(p, K) = -g\theta_i V_\mu F^{\mu\nu}(K) \partial_\nu^{(p)} f^i(\mathbf{p}) + \\ + \nu (f_{\text{eq}}^i(\mathbf{p}) - f^i(\mathbf{p})) + \nu \frac{f_{\text{eq}}^i(\mathbf{p})}{N_{\text{eq}}} \int_{\mathbf{p}'} \delta f^i(p', K), \end{aligned} \quad (5.6)$$

where $\delta f^i(p, K)$ and $F^{\mu\nu}(K)$ are the FOURIER-transforms of $\delta f_a^i(p, X)$ and $F^{\mu\nu}(X)$, respectively. This yields

$$\delta f^i(p, K) = \frac{-ig\theta_i V_\mu F^{\mu\nu}(K) \partial_\nu^{(p)} f^i(\mathbf{p}) + i\nu (f_{\text{eq}}^i(\mathbf{p}) - f^i(\mathbf{p})) + i\nu f_{\text{eq}}^i(\mathbf{p}) \left(\int_{\mathbf{p}'} \delta f^i(p', K) \right) / N_{\text{eq}}}{\omega - \mathbf{v} \cdot \mathbf{k} + i\nu}. \quad (5.7)$$

Defining

$$\delta f_0^i(p, K) = \left(-ig\theta_i V_\mu F^{\mu\nu}(K) \partial_\nu^{(p)} f^i(\mathbf{p}) + i\nu(f_{\text{eq}}^i(\mathbf{p}) - f^i(\mathbf{p})) \right) D^{-1}(K, \mathbf{v}, \nu), \quad (5.8)$$

with $D(K, \mathbf{v}, \nu) = \omega - \mathbf{k} \cdot \mathbf{v} + i\nu$ we can write

$$\begin{aligned} \delta f^i(p, K) &= \delta f_0^i(p, K) + i\nu D^{-1}(K, \mathbf{v}, \nu) \frac{f_{\text{eq}}^i(\mathbf{p})}{N_{\text{eq}}} \int_{\mathbf{p}'} \delta f_0^i(p', K) \\ &\quad + i\nu D^{-1}(K, \mathbf{v}, \nu) \frac{f_{\text{eq}}^i(\mathbf{p})}{N_{\text{eq}}} \frac{i\nu}{N_{\text{eq}}} \int_{\mathbf{p}'} f_{\text{eq}}^i(\mathbf{p}') D^{-1}(K, \mathbf{v}', \nu) \int_{\mathbf{p}''} \delta f_0^i(p'', K) \\ &\quad + \dots \end{aligned} \quad (5.9)$$

Using the shorthand notation

$$\eta(K) = \int_{\mathbf{p}} \delta f_0^i(p, K), \quad (5.10)$$

and

$$\lambda(K, \nu) = \frac{i\nu}{N_{\text{eq}}} \int_{\mathbf{p}} f_{\text{eq}}^i(\mathbf{p}) D^{-1}(K, \mathbf{v}, \nu), \quad (5.11)$$

we get

$$\begin{aligned} \delta f^i(p, K) &= \delta f_0^i(p, K) + i\nu D^{-1}(K, \mathbf{v}, \nu) \frac{f_{\text{eq}}^i(\mathbf{p})}{N_{\text{eq}}} \eta(K) (1 + \lambda + \lambda^2 + \dots) \\ &= \delta f_0^i(p, K) + i\nu D^{-1}(K, \mathbf{v}, \nu) \frac{f_{\text{eq}}^i(\mathbf{p})}{N_{\text{eq}}} \eta(K) \frac{1}{1 - \lambda}. \end{aligned} \quad (5.12)$$

Using

$$J_{\text{ind } a}^{\mu i}(K) = g \int_{\mathbf{p}} V^\mu \delta f_a^i(p, K), \quad (5.13)$$

we find the final result for the current:

$$\begin{aligned} J_{\text{ind } a}^{\mu i}(K) &= g^2 \int_{\mathbf{p}} V^\mu \partial_{(p)}^\beta f^i(\mathbf{p}) \mathcal{M}_{\gamma\beta}(K, V) D^{-1}(K, \mathbf{v}, \nu) A_a^\gamma(K) + g\nu \mathcal{S}^i(K, \nu) \\ &\quad + g \frac{i\nu}{N_{\text{eq}}^i} \int_{\mathbf{p}} V^\mu f_{\text{eq}}^i(|\mathbf{p}|) D^{-1}(K, \mathbf{v}, \nu) \\ &\quad \times g \left[\int_{\mathbf{p}'} \partial_{(p')}^\beta f^i(\mathbf{p}') \mathcal{M}_{\gamma\beta}(K, V') D^{-1}(K, \mathbf{v}', \nu) A_a^\gamma(K) + g\nu \mathcal{S}^i(K, \nu) \right] \mathcal{W}_i^{-1}(K, \nu), \end{aligned} \quad (5.14)$$

with

$$\mathcal{M}_{\gamma\beta}(K, V) := g_{\gamma\beta}(\omega - \mathbf{k} \cdot \mathbf{v}) - V_\gamma K_\beta, \quad (5.15)$$

$$D(K, \mathbf{v}, \nu) := \omega + i\nu - \mathbf{k} \cdot \mathbf{v}, \quad (5.16)$$

$$\mathcal{S}^i(K, \nu) := \theta_i \int_{\mathbf{p}} V^\mu [f^i(\mathbf{p}) - f_{\text{eq}}^i(|\mathbf{p}|)] D^{-1}(K, \mathbf{v}, \nu), \quad (5.17)$$

and

$$\mathcal{W}_i(K, \nu) := 1 - \frac{i\nu}{N_{\text{eq}}^i} \int_{\mathbf{p}} f_{\text{eq}}^i(|\mathbf{p}|) D^{-1}(K, \mathbf{v}, \nu). \quad (5.18)$$

The total induced current is given by $J_{\text{ind } a}^\mu(K) = 2N_c J_{\text{ind } a}^{g\mu}(K) + N_f [J_{\text{ind } a}^{q\mu}(K) + J_{\text{ind } a}^{\bar{q}\mu}(K)]$. It can be simplified due to the fact that the integrals over f_{eq}^i in Eq. (5.14) are independent of the particle species:

$$\begin{aligned} \frac{1}{N_{\text{eq}}^i} \int_{\mathbf{p}} f_{\text{eq}}^i(|\mathbf{p}|) D^{-1}(K, \mathbf{v}, \nu) &= \int \frac{d\Omega}{4\pi} D^{-1}(K, \mathbf{v}, \nu), \\ \frac{1}{N_{\text{eq}}^i} \int_{\mathbf{p}} V^\mu f_{\text{eq}}^i(|\mathbf{p}|) D^{-1}(K, \mathbf{v}, \nu) &= \int \frac{d\Omega}{4\pi} V^\mu D^{-1}(K, \mathbf{v}, \nu), \end{aligned} \quad (5.19)$$

where $d\Omega = \sin\theta d\theta d\varphi$. Assuming equal distributions for quarks and antiquarks, the full linearized induced current reads

$$\begin{aligned} J_{\text{ind } a}^\mu(K) &= g^2 \int_{\mathbf{p}} V^\mu \partial_{(p)}^\beta f(\mathbf{p}) \mathcal{M}_{\gamma\beta}(K, V) D^{-1}(K, \mathbf{v}, \nu) A_a^\gamma + 2N_c g\nu \mathcal{S}^g(K, \nu) \\ &\quad + g^2 (i\nu) \int \frac{d\Omega}{4\pi} V^\mu D^{-1}(K, \mathbf{v}, \nu) \\ &\quad \quad \times \int_{\mathbf{p}'} \partial_{(p')}^\beta f(\mathbf{p}') \mathcal{M}_{\gamma\beta}(K, V') D^{-1}(K, \mathbf{v}', \nu) \mathcal{W}^{-1}(K, \nu) A_a^\gamma \\ &\quad + 2N_c g^2 (i\nu^2) \int \frac{d\Omega}{4\pi} V^\mu D^{-1}(K, \mathbf{v}, \nu) \mathcal{S}^g(K, \nu) \mathcal{W}^{-1}(K, \nu), \end{aligned} \quad (5.20)$$

where $\mathcal{W}(K, \nu) = 1 - i\nu \int \frac{d\Omega}{4\pi} D^{-1}(K, \mathbf{v}, \nu)$ and $f(\mathbf{p})$ as in Eq. (3.8). The self energy is obtained from Eq. (5.20) as in Section 3.1 via

$$\Pi_{ab}^{\mu\nu}(K) = \frac{\delta J_{\text{ind } a}^\mu(K)}{\delta A_\nu^b(K)}, \quad (5.21)$$

resulting in

$$\begin{aligned} \Pi_{ab}^{\mu\nu}(K) &= \delta_{ab} g^2 \int_{\mathbf{p}} V^\mu \partial_\beta^{(p)} f(\mathbf{p}) \mathcal{M}^{\nu\beta}(K, V) D^{-1}(K, \mathbf{v}, \nu) \\ &\quad + \delta_{ab} g^2 (i\nu) \int \frac{d\Omega}{4\pi} V^\mu D^{-1}(K, \mathbf{v}, \nu) \\ &\quad \quad \times \int_{\mathbf{p}'} \partial_\beta^{(p')} f(\mathbf{p}') \mathcal{M}^{\nu\beta}(K, V') D^{-1}(K, \mathbf{v}', \nu) \mathcal{W}^{-1}(K, \nu), \end{aligned} \quad (5.22)$$

which is diagonal in color and can be shown to be transverse, i.e., $K_\mu \Pi^{\mu\nu} = K_\nu \Pi^{\mu\nu} = 0$. We will from now on omit the color indices of $\Pi^{\mu\nu}$. The terms in the induced current involving \mathcal{S}_ν drive the distribution into an isotropic equilibrium shape. They represent a parity conserving current and thus create a zero average electromagnetic field and therefore do not contribute to instability growth.

So far in this section, the distribution function $f(\mathbf{p})$ in Eq. (5.22) has not yet been specified. We now assume that $f(\mathbf{p})$ is obtained from an isotropic distribution function by the rescaling of one direction in momentum space using (4.1):

$$f(\mathbf{p}) = \sqrt{1 + \xi} f_{\text{iso}}(\mathbf{p}^2 + \xi(\mathbf{p} \cdot \hat{\mathbf{n}})^2), \quad (5.23)$$

for an arbitrary isotropic distribution function $f_{\text{iso}}(|\mathbf{p}|)$. As in Section 4.1 we are able to perform the radial part of the integrations involving $f(\mathbf{p})$ in Eq. (5.22) by changing variables to $\tilde{p}^2 = p^2(1 + \xi(\mathbf{v} \cdot \hat{\mathbf{n}})^2)$. The result is

$$\begin{aligned} \Pi^{ij}(K) &= m_D^2 \sqrt{1 + \xi} \int \frac{d\Omega}{4\pi} v^i \frac{v^l + \xi(\mathbf{v} \cdot \hat{\mathbf{n}})n^l}{(1 + \xi(\mathbf{v} \cdot \hat{\mathbf{n}})^2)^2} \left[\delta^{jl}(\omega - \mathbf{k} \cdot \mathbf{v}) + v^j k^l \right] D^{-1}(K, \mathbf{v}, \nu) \\ &+ (i\nu) m_D^2 \sqrt{1 + \xi} \int \frac{d\Omega'}{4\pi} (v')^i D^{-1}(K, \mathbf{v}', \nu) \\ &\times \int \frac{d\Omega}{4\pi} \frac{v^l + \xi(\mathbf{v} \cdot \hat{\mathbf{n}})n^l}{(1 + \xi(\mathbf{v} \cdot \hat{\mathbf{n}})^2)^2} \left[\delta^{jl}(\omega - \mathbf{k} \cdot \mathbf{v}) + v^j k^l \right] D^{-1}(K, \mathbf{v}, \nu) \mathcal{W}^{-1}(K, \nu), \end{aligned} \quad (5.24)$$

where m_D^2 is given by Eq. (3.20):

$$m_D^2 = -\frac{g^2}{2\pi^2} \int_0^\infty d\tilde{p} \tilde{p}^2 \frac{df_{\text{iso}}(\tilde{p}^2)}{d\tilde{p}}. \quad (5.25)$$

We apply the same tensor decomposition as in the collision free case (see Section 4.1). Since the growth rate of the filamentation instability is the largest when the wave vector is parallel to the direction of the anisotropy, i.e., $\mathbf{k} \parallel \hat{\mathbf{n}}$, we concentrate on this particular case. Then

$$\mathbf{k} \cdot \mathbf{v} = k \hat{\mathbf{n}} \cdot \mathbf{v} = k \cos \theta, \quad (5.26)$$

and γ and $\tilde{n}^2 = 1 - (\mathbf{k} \cdot \hat{\mathbf{n}})^2$ in Eq. (4.9) vanish identically. To determine the poles of the propagator (4.7), and hence the dispersion relations, we are now left with two separate equations for the α - and β -mode, respectively:

$$\begin{aligned} k^2 - \omega^2 + \alpha &= 0, \\ \beta - \omega^2 &= 0. \end{aligned} \quad (5.27)$$

Applying the projections (4.4) to the self energy (5.24) we determine α and β . The appearing integrals can be performed analytically and the final results simplify to:

$$\begin{aligned} \alpha(\omega, k, \xi, \nu) &= \frac{m_D^2}{4} \frac{\sqrt{1 + \xi}}{k(1 + \xi z^2)^2} \times \\ &\times \left\{ (k(z^2 - 1) - iz\nu)(1 + \xi z^2) - (z^2 - 1)(kz(1 + \xi) - i\nu) \ln \left[\frac{z + 1}{z - 1} \right] \right. \\ &\quad \left. - \frac{i}{\sqrt{\xi}} [z\nu(1 + (3 + z^2(1 - \xi))\xi) \right. \\ &\quad \left. + ik(1 - \xi + z^2(1 + \xi(6 + z^2(\xi - 1) + \xi)))] \arctan \sqrt{\xi} \right\}, \end{aligned} \quad (5.28)$$

$$\begin{aligned} \beta(\omega, k, \xi, \nu) &= m_D^2 \sqrt{1 + \xi} k(kz - i\nu)^2 \times \\ &\times \left\{ -2\sqrt{\xi}(1 + z^2\xi) + (1 + \xi) \left(2z\sqrt{\xi} \ln \left[\frac{z + 1}{z - 1} \right] + 2(z^2\xi - 1) \arctan \sqrt{\xi} \right) \right\} \\ &\times \left(2\sqrt{\xi}(1 + z^2\xi)^2 k^2 \left(2k - i\nu \ln \left[\frac{z + 1}{z - 1} \right] \right) \right)^{-1}, \end{aligned} \quad (5.29)$$

where we abbreviate $z = (\omega + i\nu)/k$.

5.2 Stable modes

The dispersion relations for all modes are given by the solutions $\omega(k)$ of Eqs. (5.27). These solutions are found numerically for different values of the collision rate ν . The results for the stable transverse (α -) mode are shown in Figs. 5.1 and 5.2 for two anisotropic distributions, $\xi = 1$ and $\xi = 10$, together with the result for the isotropic case ($\xi = 0$). Note that the finite collision rate causes ω_α to become complex with a negative imaginary part corresponding to damping of these types of modes. The effect of collisions on the stable longitudinal

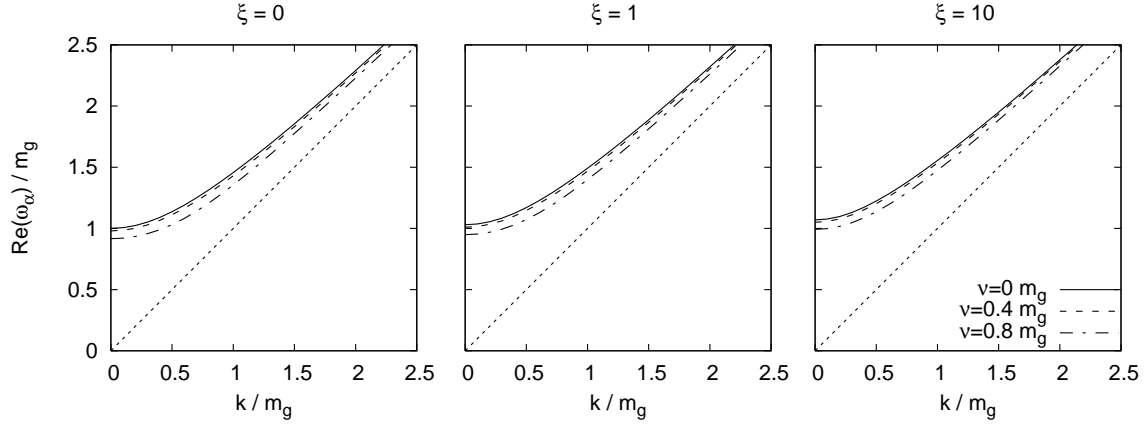


Figure 5.1: Real part of the dispersion relation for the stable α -mode for an anisotropy parameter of $\xi = \{0, 1, 10\}$ and different collision rates in units of $m_g = m_D/\sqrt{3}$.

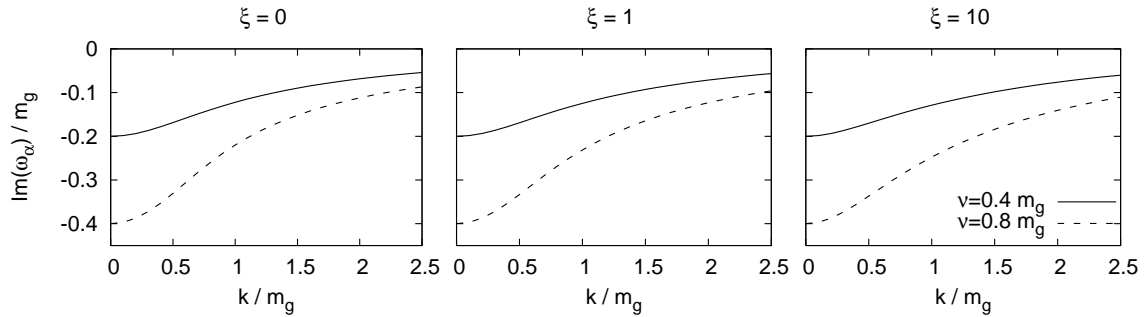


Figure 5.2: Imaginary part of the dispersion relation for the stable α -mode for an anisotropy parameter of $\xi = \{0, 1, 10\}$ and different collision rates in units of $m_g = m_D/\sqrt{3}$.

(β -) modes is more significant. The results are presented in Figs. 5.3 and 5.4. We find that for finite ν the dispersion becomes spacelike ($\text{Re}(\omega) < k$) at large k in contrast to the collisionless case, in which $\text{Re}(\omega) > k$ always holds. This behavior is responsible for the fact that the solution vanishes from the physical RIEMANN sheet above some finite k . This occurs precisely when the solution for ω_β reaches the cut between $-k$ and k at $-i\nu$.

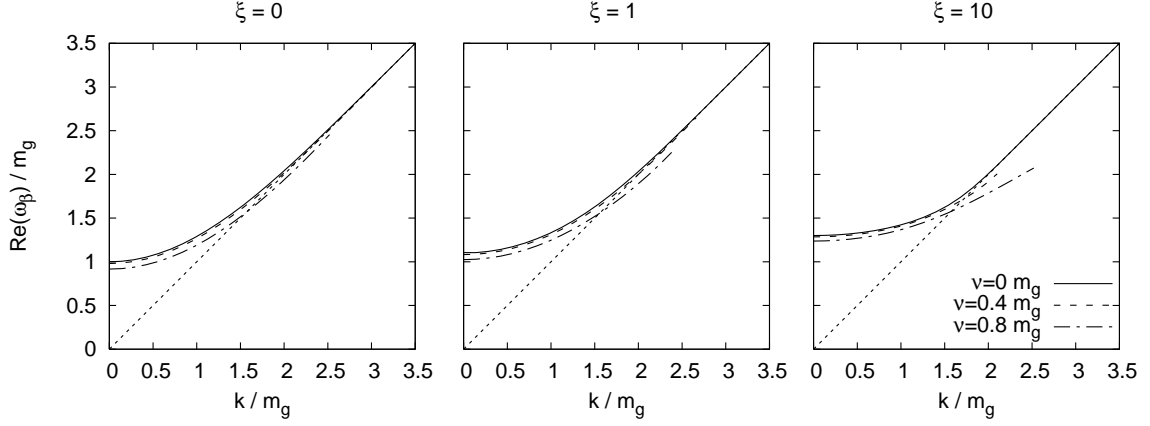


Figure 5.3: Real part of the dispersion relation for the stable β -mode for an anisotropy parameter of $\xi = \{0, 1, 10\}$ and different collision rates in units of $m_g = m_D/\sqrt{3}$. Note that for finite ν there is a maximal k beyond which there is no solution. It vanishes when ω crosses the cut in the complex plane, which extends from $-k$ to $+k$ at $-i\nu$ (cf. Fig 5.4).

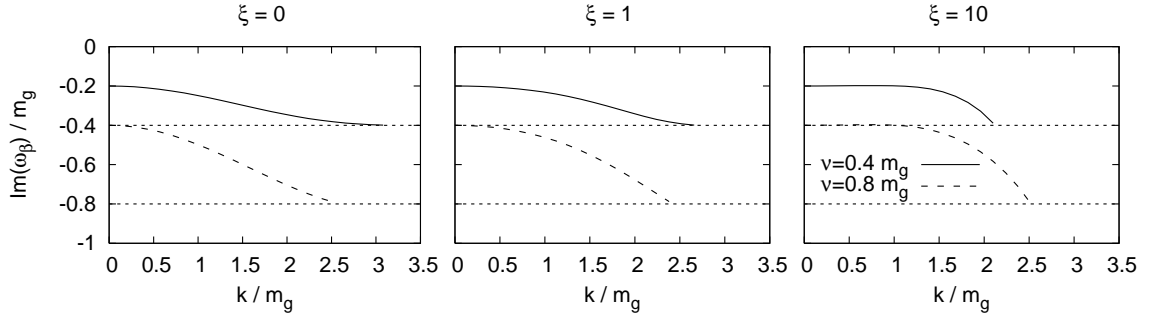


Figure 5.4: Imaginary part of the dispersion relation for the stable β -mode for an anisotropy parameter of $\xi = \{0, 1, 10\}$ and different collision rates in units of $m_g = m_D/\sqrt{3}$. The solution vanishes, when ω crosses the cut in the complex plane, which extends from $-k$ to $+k$ at $-i\nu$ (indicated by the straight dotted line).

It is however possible to find solutions on the unphysical RIEMANN sheets by replacing the logarithm in the structure function with its usual analytic continuation [142]:

$$\ln\left(\frac{z+1}{z-1}\right) = \ln\left(\left|\frac{z+1}{z-1}\right|\right) + i\left[\arg\left(\frac{z+1}{z-1}\right) + 2\pi N\right], \quad (5.30)$$

where N specifies the sheet number. The continuation of the solution to the lower RIEMANN sheets is shown in Figs. 5.5 and 5.6 for a collision rate of $\nu = 0.8 m_g \approx 0.46 m_D$ and different anisotropy parameters ξ . For smaller anisotropies the solution is found to converge to the light cone in an oscillating manner, while the imaginary part of ω oscillates around $\pm\nu$. Between $\xi = 2$ and $\xi = 3$ (for $\nu \approx 0.46 m_D$) this behavior changes qualitatively to the one shown in the case $\xi = 10$. With increasing k the real part of ω moves away from the light cone, while the imaginary part drops to large negative values with the solution remaining on the $N = -1$ RIEMANN sheet, such that these modes are strongly damped.

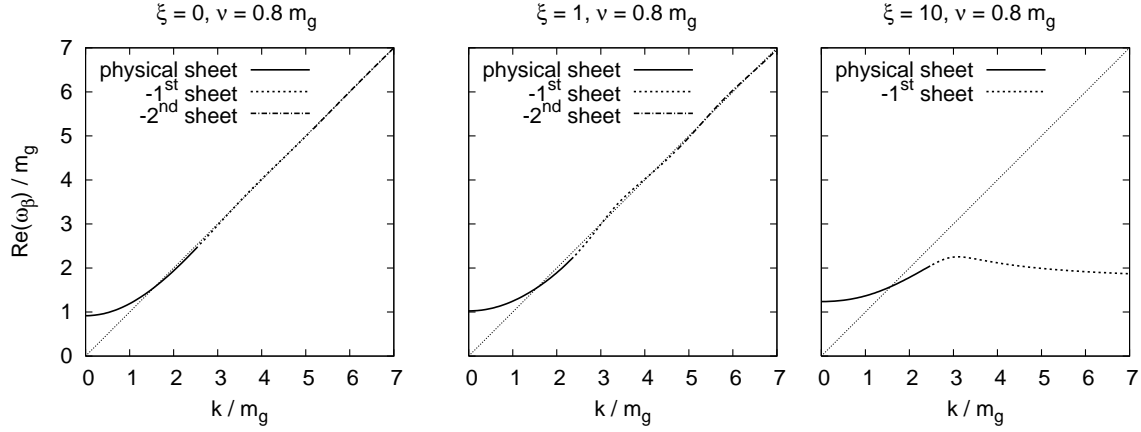


Figure 5.5: Real part of the dispersion relation for the stable β -mode for an anisotropy parameter of $\xi = \{0, 1, 10\}$ and $\nu = 0.8 m_g$. It is shown how the solution continues on lower RIEMANN sheets.

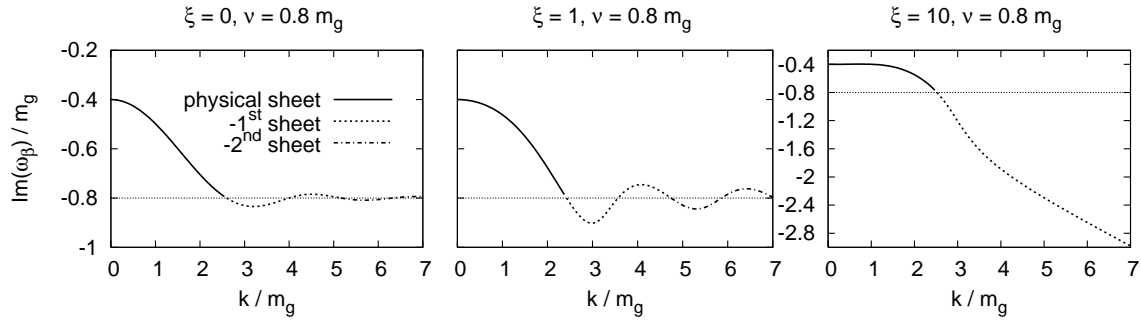


Figure 5.6: Imaginary part of the dispersion relation for the stable β -mode for an anisotropy parameter of $\xi = \{0, 1, 10\}$ and $\nu = 0.8 m_g$. It is shown how the solution continues on lower RIEMANN sheets. Note the different scale for the third plot.

5.3 Unstable modes

We now investigate how the inclusion of collisions affects the growth rates of the instabilities, found for the collisionless case in Section 4.3 and discussed in Section 4.4. Qualitatively one expects a decrease of the growth rates because the particles, which move perpendicular to \mathbf{k} (the particles moving in the z -direction in Fig. 4.3), can scatter with other particles and will no longer be trapped in this direction. Other particles can gain a momentum close to perpendicular to \mathbf{k} and form a new contribution to the instability. However, since the collision term tends to randomize the momentum distribution, the growth of δf and the magnetic field is prevented. In order to describe this effect quantitatively, we solve Eq. (5.27) for purely imaginary ω and vary the collision rate ν . The solution $\omega(k) = i\Gamma(k)$ gives the growth rate $\Gamma(k)$. In the case that $\hat{\mathbf{n}} \parallel \mathbf{k}$ solutions like that only exist for the transverse (α -) mode. The one with $\Gamma > 0$ corresponds to the filamentation instability. Results for different values of the collision rate ν are shown in Fig. 5.7 for $\xi = 1$ and in Fig. 5.8 for

$\xi = 10$. The qualitatively expected effect is nicely reproduced. The growth rate decreases with an increasing collision rate as does the maximal wave number for an unstable mode. One can see that in the case where $\xi = 1$ already for ν being around 20% of the DEBYE mass, growth has completely turned into damping and no instability can evolve. For $\xi = 10$ the collision rate ν has to be slightly larger than 30% of the DEBYE mass in order to prevent growth of a collective mode.

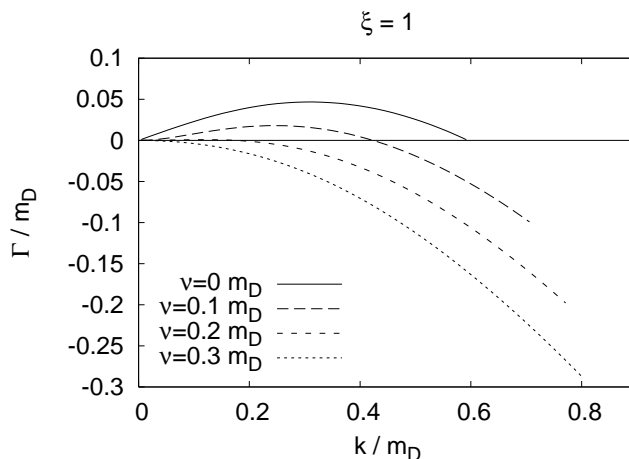


Figure 5.7: Dependence of the growth rate Γ of the unstable transverse (α -) mode on the collision rate ν , for an anisotropy parameter $\xi = 1$.

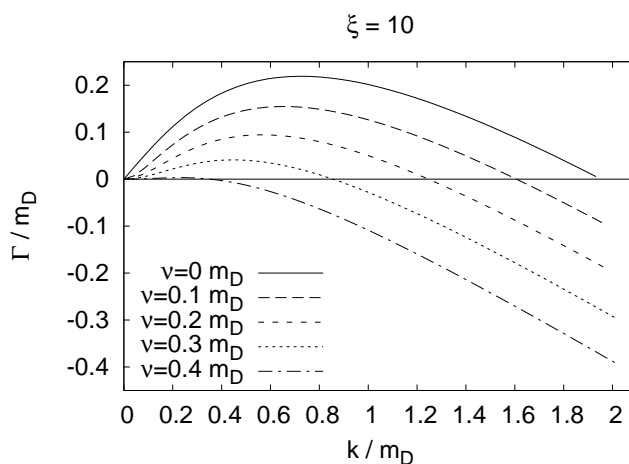


Figure 5.8: Dependence of the growth rate Γ of the unstable transverse (α -) mode on the collision rate ν , for an anisotropy parameter $\xi = 10$.

In order to find the wave number $k_{\max}(\xi, \nu)$ at which the unstable mode spectrum termi-

nates, we take the limit $\omega \rightarrow 0$ to obtain

$$m_\alpha^2 = \lim_{\omega \rightarrow 0} \alpha = -\frac{m_D^2}{8} ik \frac{\sqrt{1+\xi}}{\sqrt{\xi}(k^2 - \nu^2 \xi)^2} \times \left\{ -2ik\sqrt{\xi}(k^2 - \nu^2 \xi) - 2\nu(k^2 + \nu^2)\xi^{3/2} \ln\left(1 - \frac{2k}{k - i\nu}\right) - 2ik[k^2(\xi - 1) + \nu^2 \xi(\xi + 3)] \arctan(\sqrt{\xi}) \right\}. \quad (5.31)$$

One of the solutions to the equation

$$k^2 + m_\alpha^2 = 0, \quad (5.32)$$

which is just the limit $\omega \rightarrow 0$ of the first of the Eqs. (5.27), is k_{\max} . Results for different ξ and ν are shown in Figs. 5.9 and 5.10. We find that for a given anisotropy parameter ξ , there exists a critical collision rate, above which instabilities can not occur. This is also true for the limit $\xi \rightarrow \infty$, as we will show in the following. Taking $\xi \rightarrow \infty$, Eq. (5.31) becomes

$$m_\alpha^2(\xi \rightarrow \infty) = -\frac{\pi}{8} m_D^2 \frac{k^2}{\nu^2}, \quad (5.33)$$

which together with Eq. (5.32) gives

$$k^2(\nu^2 - \frac{\pi}{8} m_D^2) = 0. \quad (5.34)$$

Apart from the result $k = 0$, this is solved by

$$\nu_{\max}(\xi \rightarrow \infty) = \sqrt{\frac{\pi}{8}} m_D \approx 0.6267 m_D = \Gamma_{\max}(\xi \rightarrow \infty), \quad (5.35)$$

the critical collision rate, above which even in the extremely anisotropic limit $\xi = \infty$ no instability can occur.

This is also visible in the plot of the growth rate $\Gamma_{\xi \rightarrow \infty}$, shown in Fig. 5.11. For $\nu = \nu_{\max}(\xi \rightarrow \infty)$ the growth rate becomes zero for all k , and for larger ν only damping occurs. In this case ($\xi = \infty$) the value of the maximal collision rate equals that of the maximal growth rate in the collisionless limit. This simply means that the instability vanishes completely at the point where the collisions damp at the same rate at which the instability grows. Note however that this relation is more complicated in general as shown in Fig. 5.12, where the dependence of the maximal growth rate on the collision rate is plotted. In order to make the instability vanish completely for any $\xi < \infty$, a collision rate larger than the maximal growth rate of the instability in the collisionless limit is needed.

5.4 Discussions

So far the collisional frequency ν has been taken to be arbitrary. Because the inclusion of a BGK collisional term is a phenomenological model for the equilibration of a system and cannot be derived from first principles this makes it difficult to fix the magnitude of ν . However, since as treated here the underlying framework of BOLTZMANN-VLASOV is

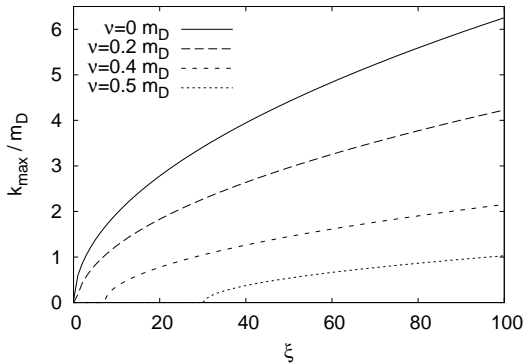


Figure 5.9: k_{\max} of the maximally unstable mode as a function of the anisotropy parameter ξ for different values of ν . For given ν , the momentum anisotropy parameter must be above the critical value for instabilities to occur.

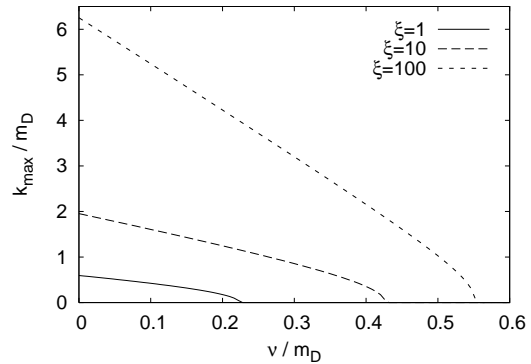


Figure 5.10: k_{\max} of the maximally unstable mode as a function of the collision rate ν for given anisotropy parameter ξ . There exist ξ -dependent critical collision rates $\nu_{\max}(\xi)$ above which instabilities can not exist.

implicitly perturbative, we can attempt to fix ν perturbatively. However, even this is non-trivial since within non-Abelian theories there are at least two possible collisional frequencies to be considered [173, 174, 59, 175, 176]: (1) the frequency for hard-hard scatterings which is parametrically $\nu_{\text{hard}} \sim \alpha_s^2 \log \alpha_s^{-1}$ and (2) the frequency for hard-soft scattering which is parametrically $\nu_{\text{soft}} \sim \alpha_s \log \alpha_s^{-1}$.

The hard-hard scatterings correspond to interactions which change the momentum of a hard particle by $\mathcal{O}(p_{\text{hard}})$ and therefore represent truly momentum-space isotropizing interactions. On the other hand the hard-soft scatterings correspond to changes in momentum which are order $\mathcal{O}(gp_{\text{hard}})$. These small angle scatterings occur rather frequently and it turns out that after traversing one hard scattering mean free path, $\lambda_{\text{hard}} \sim \nu_{\text{hard}}^{-1}$, the typical deflection of the particle is also $\mathcal{O}(1)$.² The physics of small-angle scattering by the soft-background is precisely what is captured by the hard-loop treatment. However, the hard-loop framework does not explicitly take into account that ν_{soft} is also the frequency at which there are color-rotating interactions of the hard particles themselves. One would expect that color-rotation of the hard particles to have a larger effect on the growth of instabilities than the momentum-space isotropization via hard-hard scattering. That being said, the form of the BGK scattering kernel does not mix color channels and in that sense cannot be used to describe the physics of color-rotation of the hard particles. For this reason one is lead to the conclusion that when using the BGK kernel the appropriate damping rate is $\nu \sim \nu_{\text{hard}} \sim \alpha_s^2 \log \alpha_s^{-1}$. This conclusion for the parametric dependence of ν is also supported by looking at the leading order result for the shear viscosity [177].

Even with this conclusion it is hard to say anything quantitative about ν since the overall coefficient and the coefficient in the logarithm are not specified by such a parametric relation. One could hope that previous calculations contained in [177] of parton interaction rates could be of some use. Unfortunately, for a purely gluonic plasma it was found

²This, in the end, is the source of the logarithm in ν_{hard} above.

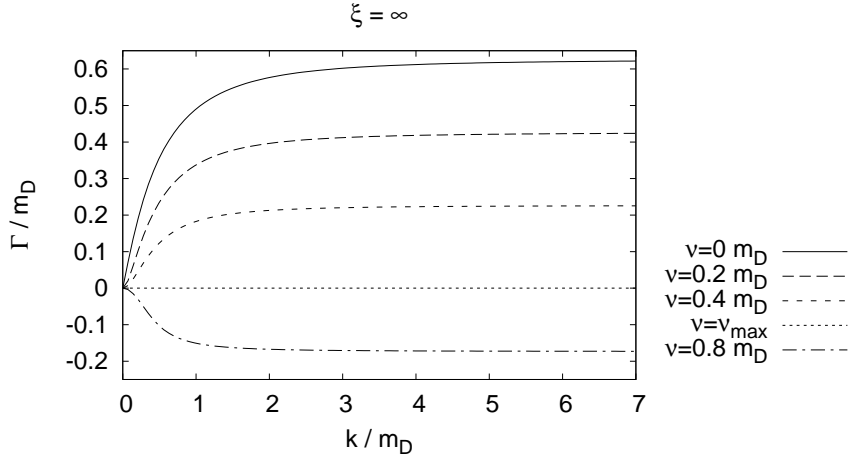


Figure 5.11: Dependence of the growth rate Γ of the unstable transverse ($\alpha-$) mode on the collision rate ν , for the extremely anisotropic limit $\xi = \infty$.

$\nu = 5.2 \alpha_s^2 T \log(0.25 \alpha_s^{-1})$, which clearly cannot be trusted for the values of α_s which are relevant for heavy-ion collisions ($\alpha_s \sim 0.2 - 0.4$) since ν becomes negative for large α_s . We note here that the negativity of this result at large couplings most likely stems from the strict perturbative expansion of the integrals involved failing when the hard and soft scales become comparable in magnitude. Similar erroneous negative values also occur in the perturbative expressions for heavy-quark collisional energy loss [178] when extrapolated to large coupling. A corrected calculational method which yields positive-definite results for the heavy-quark energy loss was detailed in Refs. [179, 180].

Ideally, one would revisit the calculation of the interaction rate and improve upon the techniques used where necessary. Short of such a calculation one cannot say with certainty what the numerical value of ν should be and the best we can do is to play “games”. For instance, one could insert a one into the logarithm appearing in ν similar to what other authors have done [87] to obtain $\nu \sim 5.2 \alpha_s^2 T \log(1 + 0.25 \alpha_s^{-1}) \sim 0.1 - 0.2 m_D$ for $\alpha_s = 0.2 - 0.4$. Using this admittedly specious expression for large-coupling one can expand and obtain $\lim_{\alpha_s \rightarrow \infty} \nu/m_D \sim 0.37 \alpha_s^{1/2}$. Note that in the case $N_f = 2$ both ν and m_D increase; however, the ratio of these two scales is still in the range quoted for $N_f = 0$. The range, $\nu = 0.1 - 0.2 m_D$, places us well below the threshold needed to turn off instabilities in the case of extremely anisotropic distribution functions but does imply (see Fig. 5.12) that for moderately small anisotropies, $\xi \sim 1$, and large coupling that it is possible for collisional damping to eliminate the unstable modes from the spectrum completely. Of course, in the limit of asymptotically small couplings the ratio ν/m_D approaches zero and the collisionless results hold to very good approximation. In the opposite limit of strong coupling the estimates here are at best guesswork and it is indeed possible that the ratio ν/m_D is larger than the range we have quoted. For example, the recent work of PESHIER [181, 182] implies that ν/m_D could be as large as 0.5; however, this number results from a fit of a model assumption to lattice data and is not directly comparable to the collisional widths considered here since in their description the gluon width was assumed to be parametrically

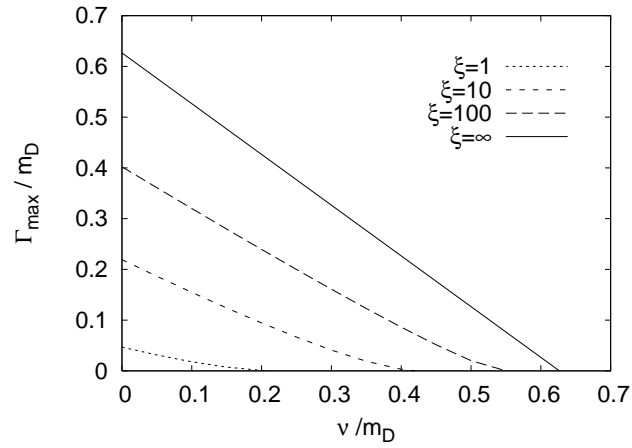


Figure 5.12: The maximal growth rate of the instability as a function of the collision rate ν .

given by ν_{soft} .

Additionally, we have to mention the caveat that all the estimates above rely on full equilibrium thermal field theory calculations. For the very initial state of the matter created in an ultra-relativistic heavy-ion collision the system is clearly not in equilibrium and it is not clear how this estimate will change as a result. However, it is of crucial importance to attempt to estimate the scattering rate in a non-equilibrium setting.

6 Wong-Yang-Mills simulation including collisions

Willst du dich am Ganzen erquicken,
so mußt du das Ganze im Kleinsten erblicken.

Gott, Gemüt und Welt.
Johann Wolfgang von Goethe (1749-1832)

In this chapter we introduce the real time lattice calculations that we use to simulate coupled particle-field evolution in classical $SU(N)$ gauge theories. Because occupation numbers are large in the infrared, the classical field approximation becomes reasonable. The physics is non-perturbative but in an essentially classical way, which gives us hope that analysis of the analogous classical field theory at finite temperature can help understand at leading order the quantum system of interest. We derive the WONG-YANG-MILLS equations and prove their equivalence to the unlinearized VLASOV equation for a microscopic distribution function. Then we describe the update algorithm used to solve the coupled system of WONG-YANG-MILLS equations with emphasis on the numerical method of current smearing. Finally we introduce a new component to the simulation, elastic binary particle collisions with large momentum exchange, i.e., momentum exchange larger than that mediated by the fields. For an isotropic plasma we show that in this scheme particle momentum diffusion is independent of the lattice spacing a , if we adjust initial energy densities of fields and particles appropriately. The numerical implementation is based on a code developed by KRASNITZ and NARA and previously used in [183, 184, 185, 186, 187, 188, 66, 162].

6.1 The Wong equations

The classical transport theory for non-Abelian plasmas has been established by HEINZ and ELZE [189, 122, 190, 109]. We have given a particular derivation of the VLASOV equations in Chapter 2 based on the approach by BLAIZOT and IANCU [110, 111]. In this section we will derive the WONG equations [191] (see also [192, 193]) and show their equivalence to the previously derived VLASOV equation in its non-linearized form in Section 6.2. For the numerical simulation with test particles the WONG equations, together with the YANG-MILLS equation for the soft gluon fields, are the natural choice because they describe the evolution of a microscopic system of individual particles. Let us start with the classical equations of motion in electrodynamics. The WONG equations are then just the extension to chromodynamics. Ignoring the dynamical effects of the spin of the particles, as they are typically small, in electrodynamics we have for particle i :

$$\dot{\mathbf{x}}_i(t) = \mathbf{v}_i(t), \tag{6.1}$$

i.e., the change of position of particle i is given by its velocity $\mathbf{v}_i(t)$. The change of the particle's momentum is given by the LORENTZ force

$$\dot{\mathbf{p}}_i(t) = \mathbf{F}_{\text{Lorentz}} = e(\mathbf{E}(t) + \mathbf{v}_i(t) \times \mathbf{B}(t)), \quad (6.2)$$

where e is the electric charge of the particle, and \mathbf{E} and \mathbf{B} are the electric and magnetic field, respectively. If the particle has a non-Abelian $SU(N)$ color charge q^a , with $a = 1, 2, \dots, N^2 - 1$, then the term corresponding to the LORENTZ force term is given by

$$\dot{\mathbf{p}}_i(t) = gq_i^a(t)(\mathbf{E}^a(t) + \mathbf{v}_i(t) \times \mathbf{B}^a(t)). \quad (6.3)$$

As already indicated in Eq. (6.3), q_i^a is now a time dependent quantity because the color vector \vec{q}_i^1 may be rotated in color space by the color-electric and color-magnetic fields $\vec{\mathbf{E}}$ and $\vec{\mathbf{B}}$. Hence we need to find another equation of motion describing the time evolution of $\vec{q}_i(t)$. Using that the charge and current densities generated by a particle with color charge \vec{q}_i are given by

$$\vec{\rho}(t) = g\vec{q}_i(t)\delta(\mathbf{x} - \mathbf{x}_i(t)), \quad (6.4)$$

$$\vec{\mathbf{J}}(t) = g\vec{q}_i(t)\mathbf{v}_i(t)\delta(\mathbf{x} - \mathbf{x}_i(t)), \quad (6.5)$$

we can write

$$\begin{aligned} \dot{\vec{\rho}} &= \frac{d}{dt}(g\vec{q}_i(t)\delta(\mathbf{x} - \mathbf{x}_i(t))) \\ &= g\dot{\vec{q}}_i(t)\delta(\mathbf{x} - \mathbf{x}_i(t)) + g\vec{q}_i(t)\dot{\mathbf{x}}_i(t)\frac{\partial\delta(\mathbf{x} - \mathbf{x}_i(t))}{\partial\mathbf{x}_i(t)} \\ &= g\dot{\vec{q}}_i(t)\delta(\mathbf{x} - \mathbf{x}_i(t)) + g\vec{q}_i(t)\mathbf{v}_i(t)\left(-\frac{\partial\delta(\mathbf{x} - \mathbf{x}_i(t))}{\partial\mathbf{x}}\right) \\ &= g\dot{\vec{q}}_i(t)\delta(\mathbf{x} - \mathbf{x}_i(t)) - \nabla \cdot \vec{\mathbf{J}}, \end{aligned} \quad (6.6)$$

where we used Eqs. (6.1) and (6.5). Equation (6.6) can be written as

$$g\dot{\vec{q}}_i(t)\delta(\mathbf{x} - \mathbf{x}_i(t)) = \dot{\vec{\rho}} + \nabla \cdot \vec{\mathbf{J}} = \partial_\mu \vec{J}^\mu, \quad (6.7)$$

with the four-current $\vec{J} = (\vec{\rho}, \vec{\mathbf{J}})$. For a non-Abelian theory GAUSS' law reads

$$\vec{D}_\mu \vec{J}^\mu = 0, \quad (6.8)$$

with the covariant derivative $\vec{D}_\mu = \partial_\mu + ig[\vec{A}_\mu, \cdot]$. Hence

$$g\dot{\vec{q}}_i(t)\delta(\mathbf{x} - \mathbf{x}_i(t)) = \partial_\mu \vec{J}^\mu = \vec{D}_\mu \vec{J}^\mu - ig[\vec{A}_\mu, \vec{J}^\mu]. \quad (6.9)$$

Again using the definition (6.5), we can write

$$\begin{aligned} g\dot{\vec{q}}_i(t)\delta(\mathbf{x} - \mathbf{x}_i(t)) &= -ig[\vec{A}_\mu(t), gv_i^\mu(t)\vec{q}_i\delta(\mathbf{x} - \mathbf{x}_i(t))] \\ \dot{\vec{q}}_i(t) &= -igv_i^\mu(t)[\vec{A}_\mu, \vec{q}_i(t)]. \end{aligned} \quad (6.10)$$

¹Note that we denote color vectors by $\vec{\cdot}$, while spatial three-vectors are always represented by bold characters to avoid confusion between the two.

Equation (6.10) completes WONG's equations. It describes the time evolution of the color charge $\vec{q}_i(t)$, as it is rotated by the fields. From now on we will drop the explicit indication of color vectors $\vec{\cdot}$. The WONG equations are coupled self consistently to the YANG-MILLS equation for the soft gluon fields

$$D_\mu F^{\mu\nu} = J^\nu = g \sum_i q_i v_i^\nu \delta(\mathbf{x} - \mathbf{x}_i(t)), \quad (6.11)$$

with the current that is generated by all particles. Let us once more write down the WONG equations, this time as one set:

$$\dot{\mathbf{x}}_i(t) = \mathbf{v}_i(t), \quad (6.12)$$

$$\dot{\mathbf{p}}_i(t) = g q_i^a(t) (\mathbf{E}^a(t) + \mathbf{v}_i(t) \times \mathbf{B}^a(t)), \quad (6.13)$$

$$\dot{q}_i(t) = -i g v_i^\mu(t) [A_\mu(t), q_i(t)]. \quad (6.14)$$

6.2 The relation between the Wong and the Vlasov equations

In this section we show that the WONG equations are equivalent to the non-linearized VLASOV equation for a microscopic system of individual particles. To do so let us first recall the VLASOV equation (2.74), derived in Section 2.3, and rewrite it in a form that is also often used in the literature (e.g. [189] or [112]), using the color charge q as a variable. Using the covariant derivative $D_\mu = \partial_\mu + ig[A_\mu, \cdot]^2$, we can expand Eq.(2.74) to read

$$V^\mu \partial_\mu n^g(P, X, q) + ig V^\mu [A_\mu(X), n^g(P, X, q)] + g V^\mu F_{\mu\nu} \partial_{(p)}^\nu n^g(P, X, q) = 0. \quad (6.15)$$

Since the distribution function n^g is linear in the color charge, we can write $n^g = f = f^a q^a \equiv \sum_a f^a q^a$, with f^a the components of f in a certain color 'direction'. From now on f shall be the complete gluon distribution function. Note that for the components of the color vector q it holds that $q^a \sim T^a$ up to normalization. With that and after multiplication with $|\mathbf{p}|$ we have

$$\begin{aligned} P^\mu \partial_\mu f(P, X, q) + ig P^\mu A_\mu^b(X) f^a(P, X, q) [q^b, q^a] + g P^\mu q^a F_{\mu\nu}^a \partial_{(p)}^\nu f(P, X, q) &= 0 \\ \Leftrightarrow P^\mu \left[\partial_\mu + g q^a F_{\mu\nu}^a \partial_{(p)}^\nu + g f^{abc} A_\mu^b(X) q^c \partial_{q^a} \right] f(P, X, q) &= 0, \end{aligned} \quad (6.16)$$

where we used that $[q^b, q^a] = i f^{bac} q^c = -i f^{abc} q^c$ and $\partial_{q^a} f = f^a$. This form of the VLASOV equation can now be easily compared to the WONG equations derived in Section 6.1. We shall do this by using the WONG equations together with the collisionless equation of motion for the single particle distribution function $f(t, \mathbf{x}, \mathbf{p}, q)$:

$$\frac{d}{dt} f(t, \mathbf{x}, \mathbf{p}, q) = 0, \quad (6.17)$$

and by replacing the continuous f by a large number of test particles [194]

$$f(\mathbf{x}, \mathbf{p}, q) = \frac{1}{N_{\text{test}}} \sum_i \delta^3(\mathbf{x} - \mathbf{x}_i(t)) (2\pi)^3 \delta^3(\mathbf{p} - \mathbf{p}_i(t)) \delta^{N^2-1}(q - q_i(t)). \quad (6.18)$$

²Note that the signs in front of the force term and the color rotation term in the VLASOV equation will depend on the choice of the sign in this definition - this leads to different sign conventions in e.g. [189] and [112] and this work.

With this distribution function Eq.(6.17) becomes

$$\begin{aligned}
\frac{d}{dt}f(\mathbf{x}, \mathbf{p}, q) &= \frac{1}{N_{\text{test}}} \sum_i \frac{d\mathbf{x}}{dt} \frac{d}{d\mathbf{x}} \delta^3(\mathbf{x} - \mathbf{x}_i(t)) (2\pi)^3 \delta^3(\mathbf{p} - \mathbf{p}_i(t)) \delta^{N^2-1}(q - q_i(t)) \\
&\quad + \frac{d\mathbf{p}}{dt} \delta^3(\mathbf{x} - \mathbf{x}_i(t)) (2\pi)^3 \frac{d}{d\mathbf{p}} \delta^3(\mathbf{p} - \mathbf{p}_i(t)) \delta^{N^2-1}(q - q_i(t)) \\
&\quad + \frac{dq}{dt} \delta^3(\mathbf{x} - \mathbf{x}_i(t)) (2\pi)^3 \delta^3(\mathbf{p} - \mathbf{p}_i(t)) \frac{d}{dq} \delta^{N^2-1}(q - q_i(t)) = 0 \\
\Leftrightarrow &-\frac{1}{N_{\text{test}}} \sum_i \frac{d\mathbf{x}_i(t)}{dt} \frac{d}{d\mathbf{x}_i} \delta^3(\mathbf{x} - \mathbf{x}_i(t)) (2\pi)^3 \delta^3(\mathbf{p} - \mathbf{p}_i(t)) \delta^{N^2-1}(q - q_i(t)) \\
&\quad + \frac{d\mathbf{p}_i(t)}{dt} \delta^3(\mathbf{x} - \mathbf{x}_i(t)) (2\pi)^3 \frac{d}{d\mathbf{p}_i} \delta^3(\mathbf{p} - \mathbf{p}_i(t)) \delta^{N^2-1}(q - q_i(t)) \\
&\quad + \frac{dq_i(t)}{dt} \delta^3(\mathbf{x} - \mathbf{x}_i(t)) (2\pi)^3 \delta^3(\mathbf{p} - \mathbf{p}_i(t)) \frac{d}{dq_i} \delta^{N^2-1}(q - q_i(t)) = 0.
\end{aligned}$$

Now we use the WONG equations (6.12)-(6.14) to write

$$\begin{aligned}
&\frac{1}{N_{\text{test}}} \sum_i (-\mathbf{v}_i(t)) \frac{d}{d\mathbf{x}_i} \delta^3(\mathbf{x} - \mathbf{x}_i(t)) (2\pi)^3 \delta^3(\mathbf{p} - \mathbf{p}_i(t)) \delta^{N^2-1}(q - q_i(t)) \\
&\quad + (-gq_i^a(t)(\mathbf{E}^a(t) + \mathbf{v}_i(t) \times \mathbf{B}^a(t))) \delta^3(\mathbf{x} - \mathbf{x}_i(t)) (2\pi)^3 \frac{d}{d\mathbf{p}_i} \delta^3(\mathbf{p} - \mathbf{p}_i(t)) \delta^{N^2-1}(q - q_i(t)) \\
&\quad + (igv_i^\mu(t)[A_\mu(t), q_i(t)]) \delta^3(\mathbf{x} - \mathbf{x}_i(t)) (2\pi)^3 \delta^3(\mathbf{p} - \mathbf{p}_i(t)) \frac{d}{dq_i} \delta^{N^2-1}(q - q_i(t)) = 0. \quad (6.19)
\end{aligned}$$

For every i we have

$$\begin{aligned}
&V_i^\mu \partial_\mu \delta^3(\mathbf{x} - \mathbf{x}_i(t)) (2\pi)^3 \delta^3(\mathbf{p} - \mathbf{p}_i(t)) \delta^{N^2-1}(q - q_i(t)) \\
&\quad + gq_i^a V_i^\mu F_{\mu\nu}^a \partial_{(p)}^\nu \delta^3(\mathbf{x} - \mathbf{x}_i(t)) (2\pi)^3 \delta^3(\mathbf{p} - \mathbf{p}_i(t)) \delta^{N^2-1}(q - q_i(t)) \\
&\quad + gV_i^\mu f_{abc} A_\mu^b q_i^c \delta^3(\mathbf{x} - \mathbf{x}_i(t)) (2\pi)^3 \delta^3(\mathbf{p} - \mathbf{p}_i(t)) \delta^{N^2-1}(q - q_i(t)) = 0, \quad (6.20)
\end{aligned}$$

where we used that $\mathbf{v} \cdot \nabla_x = V^\mu \partial_\mu$ because $\partial_t f(\mathbf{x}, \mathbf{p}, q) = 0$ for the first part, $-gq_i^a(t)(\mathbf{E}^a(t) + \mathbf{v}_i(t) \times \mathbf{B}^a(t)) \nabla_p = gq_i^a (F_{0k}^a + v_i^j F_{jk}^a) \partial_{(p)}^k = gq_i^a V^\mu F_{\mu\nu}^a \partial_{(p)}^\nu$, because $\partial_{(p)}^0 f(\mathbf{x}, \mathbf{p}, q) = 0$ in the second part, and $igV_i^\mu [A_\mu, q_i] = -gV_i^\mu f_{bac} A_\mu^b q_i^c = gv_i^\mu f_{abc} A_\mu^b q_i^c$ in the last component. Note that the derivatives are written with respect to the variables \mathbf{x} , \mathbf{p} and q now instead of \mathbf{x}_i , \mathbf{p}_i and q_i , which is possible due to the δ -functions and just introduces an overall minus sign, which does not matter. The δ -functions also allow the replacement of V_i^μ with V^μ and q_i with q in every summand and we can use this to rewrite Eq.(6.19) to read

$$P^\mu \left[\partial_\mu + gq^a F_{\mu\nu}^a \partial_{(p)}^\nu + gf^{abc} A_\mu^b(X) q^c \partial_{q^a} \right] f(\mathbf{x}, \mathbf{p}, q) = 0, \quad (6.21)$$

which is just the VLASOV equation (6.16) for the distribution function $f(\mathbf{x}, \mathbf{p}, q)$.

6.3 Numerical methods for solving the Wong-Yang-Mills system

In this section we introduce numerical methods for solving the classical field equations coupled to particles and discuss the implementation of the most important parts of the calculation.

6.3.1 Lattice simulation

The time evolution of the YANG-MILLS field is determined by the standard Hamiltonian method in $A^0 = 0$ gauge [195, 196, 197]. The temporal gauge is particularly useful because it allows for a simple identification of the canonical momentum as the electric field

$$\mathbf{E}^a = -\dot{\mathbf{A}}^a. \quad (6.22)$$

In addition, time-like link variables U , defined below, become simple identity matrices.

The lattice Hamiltonian, which we derive in Appendix D, is given by

$$H_L = \frac{1}{2} \sum_i \mathbf{E}_{L i}^a{}^2 + \frac{1}{2} \sum_{\square} (N_c - \text{ReTr} U_{\square}) + \frac{1}{N_{\text{test } L}} \sum_j |\mathbf{p}_{L j}|, \quad (6.23)$$

here including the particle contribution $1/N_{\text{test } L} \sum_j |\mathbf{p}_{L j}|$. The plaquette is defined by

$$U_{\square} = U_{x,y}(i) = U_x(i)U_y(i + \hat{x})U_x^\dagger(i + \hat{y})U_y^\dagger(i), \quad (6.24)$$

with the link variable

$$U_{\mu}(i) = e^{iagA_{\mu}(i)}. \quad (6.25)$$

The shifts \hat{x} and \hat{y} are one lattice spacing in length and directed into the x - or y - direction, respectively. Please refer to Appendix D for more details. We only point out here that we set $\tau_a = \sigma_a$, the PAULI matrices, without the usual factor of $1/2$, i.e., the commutation relation reads $[\tau^a, \tau^b] = 2\delta^{ab}$. Another factor of $1/2$ is absorbed into the A -field, which has to be taken into account when calculating the physical fields \mathbf{E} and \mathbf{B} from it.

Eq. (6.23) is given in lattice units, which are chosen such that all lattice variables are dimensionless:

$$\mathbf{E}_L^a = \frac{ga^2}{2} \mathbf{E}^a, \quad \mathbf{B}_L^a = \frac{ga^2}{2} \mathbf{B}^a, \quad \mathbf{p}_L = \frac{a}{4} \mathbf{p}, \quad Q_L^a = \frac{1}{2} q^a, \quad N_{\text{test } L} = \frac{1}{g^2} N_{\text{test}}, \quad (6.26)$$

with the lattice spacing a . H_L is hence related to the physical Hamiltonian by $H = 4/(g^2 a) H_L$ (also see Appendix D). To convert lattice variables to physical units we will fix the lattice length L in fm, which will then determine the physical scale for a . All other dimensionful quantities can then be determined by using Eqs. (6.26). The Hamiltonian (6.23) determines the energy density of the system and allows to determine the equations of motion for the fields, e.g.,

$$\frac{d}{dt} \mathbf{E}_L = \{ \mathbf{E}_L, H_L \}, \quad (6.27)$$

with the anti-commutator $\{ \cdot, \cdot \}$.

Our lattice has periodic boundary conditions.

6.3.2 Coordinate and current update

In the simulation we keep track of every particle's position $\mathbf{x}_i(t)$, momentum $\mathbf{p}_i(t)$ and charge $q_i(t)$. Knowing the i -th particle's momentum, its coordinate is updated according to Eq. (6.12) for a time step of length Δt :

$$\mathbf{x}_i(t + \Delta t) = \mathbf{x}_i(t) + \mathbf{v}_i(t + \Delta t/2) \Delta t, \quad (6.28)$$

where $\mathbf{v}_i = \mathbf{p}_i/E_i$, and $E_i = |\mathbf{p}_i|$. Note that the velocity is defined at time $t + \Delta t/2$, i.e., in the middle between the initial and final time (t and $t + \Delta t$). Correspondingly, the momentum update will provide \mathbf{p}_i at time $t + \Delta t/2$.

The update of the current is more involved. We employ smoothed currents as it is common for particle-in-cell (PIC) simulations in Abelian plasma physics [198, 199] in order to avoid numerical noise. Let us explain the method for a two-dimensional Abelian system first. Let us consider an Abelian charge q moving from (x^t, y^t) to $(x^{t+\Delta t}, y^{t+\Delta t})$ and define:

$$x_0 \equiv x^t, \quad x_1 \equiv x^{t+\Delta t} = x^t + v_x^{t+\Delta t/2} \Delta t, \quad (6.29)$$

$$y_0 \equiv y^t, \quad y_1 \equiv y^{t+\Delta t} = y^t + v_y^{t+\Delta t/2} \Delta t, \quad (6.30)$$

and

$$i_{x0} \equiv \text{floor}(x_0), \quad i_{x1} \equiv \text{floor}(x_1), \quad (6.31)$$

$$i_{y0} \equiv \text{floor}(y_0), \quad i_{y1} \equiv \text{floor}(y_1), \quad (6.32)$$

where the i 's are the largest integer values not greater than x or y , respectively. They indicate the cell, the particle is located in. We assume that a particle does not move further than one grid spacing Δx or Δy (or a) in one time step Δt , i.e., $v_x \Delta t < \Delta x$ etc. Let us first consider the case when a particle remains in the same cell during one time step. The charge density at a site (i, j) is obtained by smearing

$$\rho(i, j) = \sum_{n=1}^N q_n S_i(x_n) S_j(y_n), \quad (6.33)$$

where the sum runs over all N particles within the cell and S is a form factor. We use the first-order shape factor defined by

$$S_i(x) := \begin{cases} 1 - |x - i_x| & \text{for } |x - i_x| \leq 1 \\ 0 & \text{for } |x - i_x| > 1 \end{cases} \quad (6.34)$$

For a single particle with charge q and coordinates (x, y) and $\tilde{x} = x - i_x, \tilde{y} = y - i_y$, we have

$$\begin{aligned} \rho(i_x, i_y) &= q(1 - \tilde{x})(1 - \tilde{y}), \\ \rho(i_x + 1, i_y) &= q\tilde{x}(1 - \tilde{y}), \\ \rho(i_x, i_y + 1) &= q(1 - \tilde{x})\tilde{y}, \\ \rho(i_x + 1, i_y + 1) &= q\tilde{x}\tilde{y}. \end{aligned} \quad (6.35)$$

A charge flux can be computed from the start point (x_0, y_0) and end point (x_1, y_1) of the particle movement. Using the procedure described by EASTWOOD [200], we can do this ensuring charge conservation of the assigned current densities. Let us define

$$J_x(i_{x0} + \frac{1}{2}, i_{y0}) \equiv J_x(i_{x0}, i_{y0}) = F_x(1 - W_y), \quad (6.36)$$

$$J_x(i_{x0} + \frac{1}{2}, i_{y0} + 1) \equiv J_x(i_{x0}, i_{y0} + 1) = F_x W_y, \quad (6.37)$$

$$J_y(i_{x0}, i_{y0} + \frac{1}{2}) \equiv J_y(i_{x0}, i_{y0}) = F_y(1 - W_x), \quad (6.38)$$

$$J_y(i_{x0} + 1, i_{y0} + \frac{1}{2}) \equiv J_y(i_{x0} + 1, i_{y0}) = F_y W_x, \quad (6.39)$$

where F_x and F_y represent the charge flux given by

$$F_x = q \frac{x_1 - x_0}{\Delta t}, \quad F_y = q \frac{y_1 - y_0}{\Delta t} \quad (\text{Abelian charge here for simplicity}), \quad (6.40)$$

and W represents the first-order shape-factor corresponding to the linear weighting function defined at the midpoint between the start point and the end point:

$$W_x = \frac{x_1 + x_0}{2} - i_{x0}, \quad W_y = \frac{y_1 + y_0}{2} - i_{y0}. \quad (6.41)$$

Note that the currents are defined not at the lattice sites themselves but halfway between two grid points as indicated in Eqs. (6.36)-(6.39). We shall however omit the $1/2$ in all expressions for clarity as already done in Eqs. (6.36)-(6.39). The meaning of the definitions (6.36) through (6.41) is best explained in a graphical way as done in Fig. 6.1. One can see that the larger the part of the smeared charge that moves across a cell boundary of the reciprocal lattice that is closest to the point where the current is defined, the larger the contribution to this current.

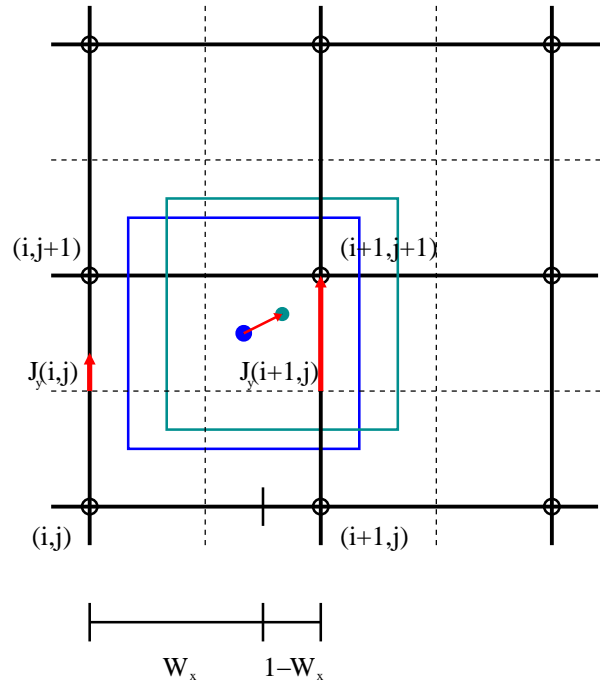


Figure 6.1: The EASTWOOD method for calculating the current with charge conservation. It is shown how the smeared particle charge moves across the reciprocal (dashed) lattice and in the process produces a current proportional to W_x or $1 - W_x$ respectively. The created currents in the x -direction are not shown for clarity.

One can easily see that the lattice continuity equation

$$J_x(i, j) - J_x(i - 1, j) + J_y(i, j) - J_y(i, j - 1) = \frac{\rho^t(i, j) - \rho^{t+\Delta t}(i, j)}{\Delta t}, \quad (6.42)$$

is in fact fulfilled for this procedure. Let us check it for the site $(i_x + 1, i_y + 1)$, considering a single particle moving within cell (i_x, i_y) from (x_0, y_0) to (x_1, y_1) during the time Δt . The total current into and out of cell $(i_x + 1, i_y + 1)$ is

$$J_x(i_x + 1, i_y + 1) - J_x(i_x, i_y + 1) + J_y(i_x + 1, i_y + 1) - J_y(i_x + 1, i_y), \quad (6.43)$$

however, our single particle contributes only to $J_x(i_x, i_y + 1)$ and $J_y(i_x + 1, i_y)$, such that we have

$$\begin{aligned} -J_x(i_x, i_y + 1) - J_y(i_x + 1, i_y) &= -F_x W_y - F_y W_x \\ &= -\frac{q}{\Delta t}(x_1 - x_0) \left(\frac{y_1 + y_0}{2} - i_y \right) \\ &\quad - \frac{q}{\Delta t}(y_1 - y_0) \left(\frac{x_1 + x_0}{2} - i_x \right) \\ &= -\frac{q}{\Delta t}(\tilde{x}_1 - \tilde{x}_0) \left(\frac{\tilde{y}_1 + \tilde{y}_0}{2} \right) - \frac{q}{\Delta t}(\tilde{y}_1 - \tilde{y}_0) \left(\frac{\tilde{x}_1 + \tilde{x}_0}{2} \right) \\ &= \frac{q}{\Delta t}(\tilde{x}_1 \tilde{y}_1 - \tilde{x}_0 \tilde{y}_0) \\ &= \frac{\rho^t(i_x + 1, i_y + 1) - \rho^{t+\Delta t}(i_x + 1, i_y + 1)}{\Delta t}. \end{aligned} \quad (6.44)$$

Now let us consider the case that the particle crosses cell meshes. To implement that case we decompose the particle movement with a special assignment pattern as shown in Figs. 6.2 and 6.3, the so called *zigzag* scheme [201]. If the mesh is crossed in both directions, the particle moves to the lattice site first and in a second step to the final position in the new cell (see Fig. 6.2). If only one mesh is crossed, the particle will first move to the boundary it crosses. The second coordinate (of the intermediate point on the mesh) is taken to be the middle point between the initial and final coordinate in the direction in that no crossing happens (see Fig. 6.3). From there the particle moves to the final position in the second step. If the particle stays in the same cell within one time step, the above procedure is not necessary - however, we formally assume that the movement of the particle is described in two steps as well. That is, in the first step, the particle moves from (x_0, y_0) to $((x_0 + x_1)/2, (y_0 + y_1)/2)$, and in the second step it moves from $((x_0 + x_1)/2, (y_0 + y_1)/2)$ to (x_1, y_1) during the time from t to $t + \Delta t$.

Combining all cases, we can define

$$x_r := \begin{cases} \frac{x_0 + x_1}{2} & \text{for } i_{x0} = i_{x1} \\ \max(i_{x0}, i_{x1}) & \text{for } i_{x0} \neq i_{x1} \end{cases} \quad (6.45)$$

and the analogue for the other directions.

By using (x_r, y_r) (in 2D), a charge flux $q(v_x, v_y)$ is decomposed into (F_{x0}, F_{y0}) and (F_{x1}, F_{y1}) as follows:

$$\begin{aligned} F_{x0} &= q \frac{x_r - x_0}{\Delta t}, & F_{y0} &= q \frac{y_r - y_0}{\Delta t}, \\ F_{x1} &= q \frac{x_1 - x_r}{\Delta t} = qv_x - F_{x0}, & F_{y1} &= q \frac{y_1 - y_r}{\Delta t} = qv_y - F_{y0}. \end{aligned} \quad (6.46)$$

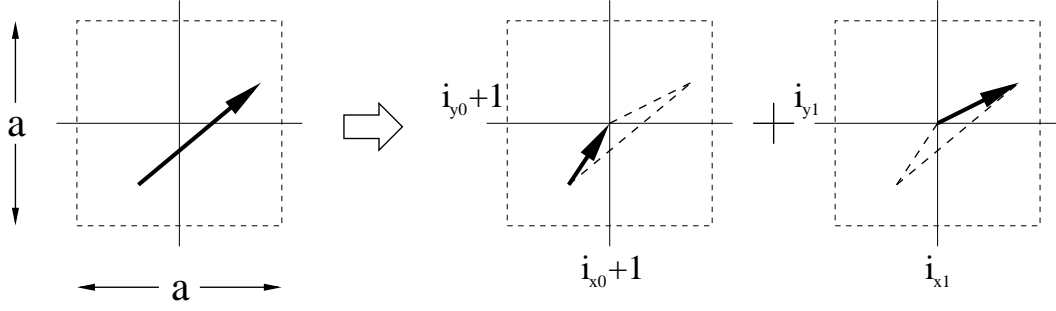


Figure 6.2: Particle trajectory of the two-dimensional zigzag scheme for $i_{x0} \neq i_{x1}$ and $i_{y0} \neq i_{y1}$. One particle moves from (x_0, y_0) to $(i_{x0} + 1, i_{y0} + 1) = (i_{x1}, i_{y1})$ and another particle moves from (i_{x1}, i_{y1}) to (x_1, y_1) during the time from t to $t + \Delta t$. The solid arrows represent particle trajectories. The thin solid lines represent cell meshes.

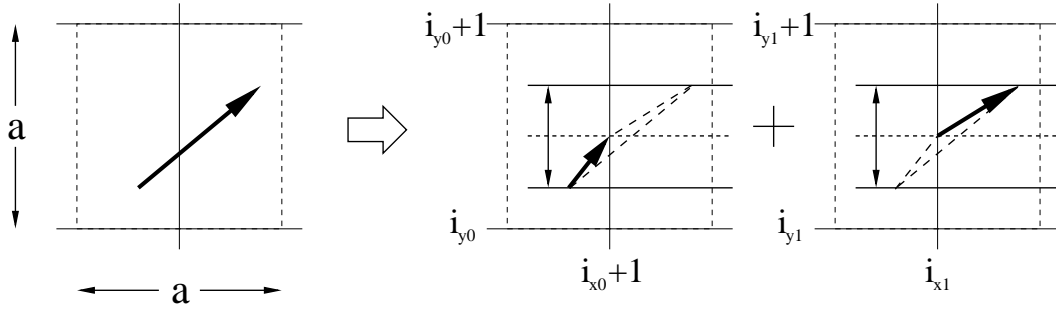


Figure 6.3: Particle trajectory of the two dimensional zigzag scheme for $i_{x0} \neq i_{x1}$ and $i_{y0} = i_{y1}$. One particle moves from (x_0, y_0) to $(i_{x0} + 1, (y_1 + y_0)/2) = (i_{x1}, (y_1 + y_0)/2)$, and another particle moves from $(i_{x1}, (y_1 + y_0)/2)$ to (x_1, y_1) during the time from t to $t + \Delta t$. Here $i_{x0} + 1 = i_{x1}$. The solid arrow represents particle trajectories. The thin solid lines represent cell meshes. Same holds for interchanging x and y .

Now we shall calculate the charge flux at each grid point. Therefore, we apply the shape factors (W) defined at the midpoints between (x_0, y_0) and (x_r, y_r) , and (x_r, y_r) and (x_1, y_1) , respectively, to assign the segments (F_{x0}, F_{y0}) and (F_{x1}, F_{y1}) to the adjacent grid points. The particles exist at the midpoints at time $t + \Delta t/2$ and the first order shape-factors at the midpoints are defined by

$$\begin{aligned} W_{x0} &= \frac{x_0 + x_r}{2} - i_{x0}, & W_{y0} &= \frac{y_0 + y_r}{2} - i_{y0}, \\ W_{x1} &= \frac{x_r + x_1}{2} - i_{x1}, & W_{y1} &= \frac{y_r + y_1}{2} - i_{y1}, \end{aligned} \quad (6.47)$$

Then the segments of the charge flux assigned to the 8 grid points are obtained by the

following procedure:

$$\begin{aligned}
J_x(i_{x0}, i_{y0}) &= F_{x0}(1 - W_{y0}), & J_x(i_{x0}, i_{y0} + 1) &= F_{x0}W_{y0}, \\
J_y(i_{x0}, i_{y0}) &= F_{y0}(1 - W_{x0}), & J_y(i_{x0} + 1, i_{y0}) &= F_{y0}W_{x0}, \\
J_x(i_{x1}, i_{y1}) &= F_{x1}(1 - W_{y1}), & J_x(i_{x1}, i_{y1} + 1) &= F_{x1}W_{y1}, \\
J_y(i_{x1}, i_{y1}) &= F_{y1}(1 - W_{x1}), & J_y(i_{x1} + 1, i_{y1}) &= F_{y1}W_{x1}.
\end{aligned} \tag{6.48}$$

The procedure described above can be directly generalized to three dimensions. It is worth mentioning that in three dimension we have four possible cases, i.e., that the particle remains in the same cell within one time step, that it crosses a cell boundary in one direction, crosses in two directions, or crosses in all three directions. Fig. 6.4 summarizes all these possibilities and describes how the calculation is done.

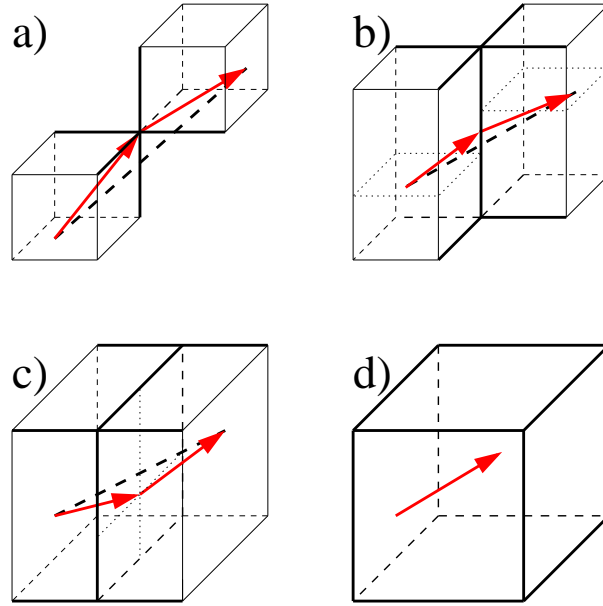


Figure 6.4: Particle trajectories for the 3D zigzag scheme. The solid arrows represent particle trajectories. The thick solid lines represent cell meshes. (a) For $i_{x0} \neq i_{x1}$ and $i_{y0} \neq i_{y1}$ and $i_{z0} \neq i_{z1}$, the particle moves in the first step from (x_0, y_0, z_0) to $(i_{x0} + 1, i_{y0} + 1, i_{z0} + 1) = (i_{x1}, i_{y1}, i_{z1})$, and in the next step from there to (x_1, y_1, z_1) (both steps within the time from t to $t + \Delta t$). (b) For $i_{x0} \neq i_{x1}$ and $i_{y0} \neq i_{y1}$ and $i_{z0} = i_{z1}$, the particle moves from (x_0, y_0, z_0) to $(i_{x0} + 1, i_{y0} + 1, \frac{z_0 + z_1}{2})$ and then to (x_1, y_1, z_1) . (c) For $i_{x0} \neq i_{x1}$ and $i_{y0} = i_{y1}$ and $i_{z0} = i_{z1}$, the particle moves from (x_0, y_0, z_0) to $(i_{x0} + 1, \frac{y_0 + y_1}{2}, \frac{z_0 + z_1}{2})$ and then to (x_1, y_1, z_1) . (d) For $i_{x0} = i_{x1}$ and $i_{y0} = i_{y1}$ and $i_{z0} = i_{z1}$ the particle moves from (x_0, y_0, z_0) to (x_1, y_1, z_1) via $(\frac{x_0 + x_1}{2}, \frac{y_0 + y_1}{2}, \frac{z_0 + z_1}{2})$.

Let us now extend the PIC method with current smearing to the case of a non-Abelian plasma, i.e., let us introduce color and call the method CPIC, colored-particle-in-cell. Again

we consider two dimensions in this discussion for clarity. The currents are now defined by

$$J_x(i_x, i_y) = Q \frac{x_1 - x_0}{\Delta t} (1 - W_y), \quad J_x(i_x, i_y + 1) = Q_y \frac{x_1 - x_0}{\Delta t} W_y, \quad (6.49)$$

$$J_y(i_x, i_y) = Q \frac{y_1 - y_0}{\Delta t} (1 - W_x), \quad J_y(i_x + 1, i_y) = Q_x \frac{y_1 - y_0}{\Delta t} W_x, \quad (6.50)$$

with the W as above. We have to use the parallel transported charges³

$$Q_x \equiv U_x^\dagger(i_x, i_y) Q U_x(i_x, i_y), \quad Q_y \equiv U_y^\dagger(i_x, i_y) Q U_y(i_x, i_y), \quad (6.51)$$

in order to fulfill the lattice covariant continuity equation

$$\begin{aligned} \dot{\rho}(i_x, i_y) = & U_x^\dagger(i_x - 1, i_y) J_x(i_x - 1, i_y) U_x(i_x - 1, i_y) - J_x(i_x, i_y) \\ & + U_y^\dagger(i_x, i_y - 1) J_y(i_x, i_y - 1) U_y(i_x, i_y - 1) - J_y(i_x, i_y). \end{aligned} \quad (6.52)$$

The link variable U_μ was defined in (6.25). For a single particle moving within cell (i_x, i_y) , the continuity equation at the adjacent sites reads

$$\dot{\rho}(i_x, i_y) = -J_x(i_x, i_y) - J_y(i_x, i_y), \quad (6.53)$$

$$\dot{\rho}(i_x + 1, i_y) = U_x^\dagger(i_x, i_y) J_x(i_x, i_y) U_x(i_x, i_y) - J_y(i_x + 1, i_y), \quad (6.54)$$

$$\dot{\rho}(i_x, i_y + 1) = U_y^\dagger(i_x, i_y) J_y(i_x, i_y) U_y(i_x, i_y) - J_x(i_x, i_y + 1). \quad (6.55)$$

This is easiest to understand if you consider the charge density $\rho(i_x, i_y)$ as that within one reciprocal lattice cell around the cite (i_x, i_y) and the currents as those created by a moving charge in the actual lattice cell (i_x, i_y) that influence that charge density. See also Fig. 6.1 to get a better idea.

Eqs. (6.53), (6.54), (6.55) are consistent with the following definitions of the charge densities

$$\rho(i_x, i_y) = Q(1 - \tilde{x})(1 - \tilde{y}), \quad (6.56)$$

$$\rho(i_x, i_y + 1) = Q_y(1 - \tilde{x})\tilde{y}, \quad (6.57)$$

$$\rho(i_x + 1, i_y) = Q_x\tilde{x}(1 - \tilde{y}). \quad (6.58)$$

However, since a particle's color charge depends on its path, so does $\rho(i_x + 1, i_y + 1)$ and we are not able to calculate it from the charge distribution itself. Rather, we directly employ covariant current conservation to determine the increment of charge at site $(i_x + 1, i_y + 1)$ within the time-step. This way, we can satisfy Gauss's law in the non-Abelian case.

We also have to check that $\text{Tr}(Q^2)$ is conserved by this smearing method. This is true when the lattice spacing a is small, as the total charge of a particle is given by

$$Q_0 = Q(1 - x)(1 - y) + Q_x x(1 - y) + Q_y(1 - x)y + [a_p Q_{xy} + (1 - a_p) Q_{yx}] xy, \quad (6.59)$$

where the a_p depend on the path of a particle and $Q_{xy} = U_x^\dagger(i, j + 1) Q_y U_x(i, j + 1)$, $Q_{yx} = U_y^\dagger(i + 1, j) Q_x U_y(i + 1, j)$. If we require that $\text{Tr}(Q_0^2)$ be constant, then the cross terms, for example $\text{Tr}(Q Q_x)$, have to vanish. This is true when a is small, because $\text{Tr}(Q[A, Q]) = 0$:

$$\text{Tr}(Q Q_x) = \text{Tr}(Q(Q + iga[A_x, Q] + \mathcal{O}(a^2))) = \text{Tr}(Q^2) + \mathcal{O}(a^2). \quad (6.60)$$

³We omit the term $[A_z, J_z]$ here, because this term does not appear in 3D and it does not matter in this consideration.

6.3.3 The field updates

The electric fields E live on the links between the lattice sites and so do the U -fields. The B -fields, which can be calculated from the plaquettes according to

$$U_{\square} = U_{xy} = \exp(ia^2 g F_{xy}) = \exp(ia^2 g (-B_z)) \approx \mathbf{1} - ia^2 g B_z^a \sigma^a, \quad (6.61)$$

and analogously for the other two directions, are hence defined within the area enclosed by the plaquette. The time derivative of

$$U(i) = e^{iagA(i)}, \quad (6.62)$$

depends on whether we use a left or right covariant derivative. We will stick to the prescription, where $\dot{A}(i)$ stands on the left:

$$\begin{aligned} \dot{U}(i) &= iag\dot{A}(i)U(i) \\ \Leftrightarrow \dot{U}(i) &= -iagE(i)U(i). \end{aligned} \quad (6.63)$$

So the update of the U -fields is determined by the (color-) electric field. On the lattice, the electric field is updated using the following expression for \dot{E} :

$$\dot{E}^j = -\frac{i}{2a^3 g} \sum_i \left(U_{ij}(x) - U_i^\dagger(x-i)U_{ij}(x-i)U_i(x-i) \right) - J^j, \quad (6.64)$$

where J is the current calculated in the previous subsection, i and j run over the directions x , y and z and the τ_a are the PAULI matrices σ_a . Also note that $(x-i)$ means that from position x , we move one lattice spacing in the $-i$ direction. Let us show that in the continuum limit this becomes the usual expression

$$\dot{E}^j = D_i F^{ij} - J^j = \partial_i F^{ij} + ig[A_i, F^{ij}] - J^j. \quad (6.65)$$

Inserting the continuum limits for the plaquettes (see Eq.(D.39)) and the definitions for the link variables, Eq.(6.64) becomes

$$\begin{aligned} \dot{E}^j &= -\frac{i}{2a^3 g} \sum_i \left(e^{ia^2 g F^{ij}(x)} - e^{-iagA_i(x-i)} e^{ia^2 g F^{ij}(x-i)} e^{iagA_i(x-i)} \right) - J^j \\ &= -\frac{i}{2a^3 g} \sum_i \left(e^{ia^2 g F^{ij}(x)} - e^{-iagA_i(x-i) + ia^2 g F^{ij}(x-i) + \frac{a^3 g^2}{2} [A_i, F^{ij}]} e^{iagA_i(x-i)} \right) - J^j \\ &= -\frac{i}{2a^3 g} \sum_i \left(e^{ia^2 g F^{ij}(x)} - e^{ia^2 g F^{ij}(x-i) + \frac{a^3 g^2}{2} [A_i, F^{ij}] - \frac{a^3 g^2}{2} [F^{ij}, A_i] + \mathcal{O}(a^4)} \right) - J^j \\ &\approx -\frac{i}{2a^3 g} \sum_i \left(ia^2 g F^{ij}(x) - ia^2 g F^{ij}(x-i) - a^3 g^2 [A_i, F^{ij}] \right) - J^j \\ &= \frac{1}{2a} \sum_i \left(F^{ij}(x) - F^{ij}(x-i) + iag[A_i, F^{ij}] \right) - J^j \\ &= \frac{1}{2} \sum_i \left(\frac{F^{ij}(x) - F^{ij}(x-i)}{a} + ig[A_i, F^{ij}] \right) - J^j \\ &\approx \partial_i F^{ij} + ig[A_i, F^{ij}] - J^j. \end{aligned} \quad (6.66)$$

where we used Eq.(D.38) in the first step. The electric field at time $(t + \Delta t)$ follows directly, using

$$E^j(t + \Delta t) = E^j(t) + \Delta t \dot{E}^j(t + \Delta t/2), \quad (6.67)$$

because the U -fields are defined at half time steps. See below. The B -fields do not need an individual update because we can directly obtain them from the updated U -fields via Eq.(6.61). In practice, we use a *leapfrog* algorithm in that the A -fields, and with them the U -fields, are given at time $(t + \Delta t/2)$. From this we can directly update E according to Eq.(6.67). To get the B -field at time $(t + \Delta t)$ U is first updated by half a time step $\Delta t/2$, the B -field is extracted and the particle momentum updated (to $(t + \Delta t/2)$, see Section 6.3.4 below). Then U is evolved by another half time step. The particle coordinates are updated to time $(t + \Delta t)$ using the momentum at time $(t + \Delta t/2)$ and the current at time $(t + \Delta t)$ is calculated.

6.3.4 Momentum update

The momentum update is done in a way that satisfies time reversibility with the so called BUNEMAN-BORIS-method (see [198] and [199]). The procedure is to update the momentum in several steps. We write $\mathbf{E} = gq^a \mathbf{E}^a$ and $\mathbf{B} = gq^a \mathbf{B}^a$. First calculate

$$\mathbf{p}_1(t) = \mathbf{p} \left(t - \frac{\Delta t}{2} \right) + \frac{\Delta t}{2} \mathbf{E}(t), \quad (6.68)$$

i.e., take half a time step just using the electric field. Next define $\mathbf{p}_2(t)$ using

$$\mathbf{p}_2(t) = \mathbf{p} \left(t + \frac{\Delta t}{2} \right) - \frac{\Delta t}{2} \mathbf{E}(t), \quad (6.69)$$

and

$$\begin{aligned} \frac{\mathbf{p}_2(t) - \mathbf{p}_1(t)}{\Delta t} &= \frac{\mathbf{p}_1(t) + \mathbf{p}_2(t)}{2} \times \frac{\mathbf{B}(t)}{e(t)} \\ \Leftrightarrow \mathbf{p}_2(t) - \mathbf{p}_2(t) \times \frac{\mathbf{B}(t)}{e(t)} \frac{\Delta t}{2} &= \mathbf{p}_1(t) + \mathbf{p}_1(t) \times \frac{\mathbf{B}(t)}{e(t)} \frac{\Delta t}{2}. \end{aligned} \quad (6.70)$$

The above expressions make clear that the definition of $\mathbf{p}_2(t)$ is made in order to keep the update time reversible. Let us solve for $\mathbf{p}_2(t)$ using the shorthand $\tilde{\mathbf{B}} \equiv \frac{\mathbf{B}(t)}{e(t)} \frac{\Delta t}{2}$:

$$\begin{aligned} \mathbf{p}_2 - \mathbf{p}_2 \times \tilde{\mathbf{B}} &= \mathbf{p}_1 + \mathbf{p}_1 \times \tilde{\mathbf{B}} \quad | \times \tilde{\mathbf{B}} \\ \Leftrightarrow \mathbf{p}_2 \times \tilde{\mathbf{B}} - (\mathbf{p}_2 \times \tilde{\mathbf{B}}) \times \tilde{\mathbf{B}} &= \mathbf{p}_1 \times \tilde{\mathbf{B}} + (\mathbf{p}_1 \times \tilde{\mathbf{B}}) \times \tilde{\mathbf{B}} \\ \Leftrightarrow \mathbf{p}_2 \times \tilde{\mathbf{B}} + \mathbf{p}_2 \tilde{\mathbf{B}}^2 - \tilde{\mathbf{B}}(\mathbf{p}_2 \cdot \tilde{\mathbf{B}}) &= \mathbf{p}_1 \times \tilde{\mathbf{B}} - \mathbf{p}_1 \tilde{\mathbf{B}}^2 + \tilde{\mathbf{B}}(\mathbf{p}_1 \cdot \tilde{\mathbf{B}}). \end{aligned} \quad (6.71)$$

Now replace $\mathbf{p}_2 \times \tilde{\mathbf{B}}$ using Eq. (6.70):

$$\mathbf{p}_2 \times \tilde{\mathbf{B}} = \mathbf{p}_2 - \mathbf{p}_1 - \mathbf{p}_1 \times \tilde{\mathbf{B}}, \quad (6.72)$$

Then we have

$$\Leftrightarrow \mathbf{p}_2 - \mathbf{p}_1 - \mathbf{p}_1 \times \tilde{\mathbf{B}} + \mathbf{p}_2 \tilde{\mathbf{B}}^2 - \tilde{\mathbf{B}}(\mathbf{p}_2 \cdot \tilde{\mathbf{B}}) = \mathbf{p}_1 \times \tilde{\mathbf{B}} - \mathbf{p}_1 \tilde{\mathbf{B}}^2 + \tilde{\mathbf{B}}(\mathbf{p}_1 \cdot \tilde{\mathbf{B}}). \quad (6.73)$$

Because $\mathbf{p}_2 \cdot \tilde{\mathbf{B}} = (\mathbf{p}_1 + \mathbf{p}_1 \times \tilde{\mathbf{B}} + \mathbf{p}_2 \times \tilde{\mathbf{B}}) \cdot \tilde{\mathbf{B}} = \mathbf{p}_1 \cdot \tilde{\mathbf{B}}$, we can write

$$\Leftrightarrow \mathbf{p}_2(1 + \tilde{\mathbf{B}}^2) = \mathbf{p}_1 + 2\mathbf{p}_1 \times \tilde{\mathbf{B}} + 2\tilde{\mathbf{B}}(\mathbf{p}_1 \cdot \tilde{\mathbf{B}}) - \mathbf{p}_1 \tilde{\mathbf{B}}^2. \quad (6.74)$$

Adding $2(\mathbf{p}_1 \times \tilde{\mathbf{B}}) \times \tilde{\mathbf{B}}$ on both sides yields

$$\mathbf{p}_2(1 + \tilde{\mathbf{B}}^2) + 2(\mathbf{p}_1 \times \tilde{\mathbf{B}}) \times \tilde{\mathbf{B}} = \mathbf{p}_1(1 - \tilde{\mathbf{B}}^2) + 2\mathbf{p}_1 \times \tilde{\mathbf{B}} + 2(\mathbf{p}_1 \times \tilde{\mathbf{B}}) \times \tilde{\mathbf{B}} + 2\tilde{\mathbf{B}}(\mathbf{p}_1 \cdot \tilde{\mathbf{B}}). \quad (6.75)$$

Now define $\mathbf{p}_3 = \mathbf{p}_1 + \mathbf{p}_1 \times \tilde{\mathbf{B}}$ and write:

$$\begin{aligned} &\Rightarrow \mathbf{p}_2(1 + \tilde{\mathbf{B}}^2) + 2\tilde{\mathbf{B}}(\mathbf{p}_1 \cdot \tilde{\mathbf{B}}) - 2\mathbf{p}_1 \tilde{\mathbf{B}}^2 = \mathbf{p}_1(1 - \tilde{\mathbf{B}}^2) + 2\mathbf{p}_3 \times \tilde{\mathbf{B}} + 2\tilde{\mathbf{B}}(\mathbf{p}_1 \cdot \tilde{\mathbf{B}}) \\ &\Leftrightarrow \mathbf{p}_2(1 + \tilde{\mathbf{B}}^2) = \mathbf{p}_1(1 + \tilde{\mathbf{B}}^2) + 2\mathbf{p}_3 \times \tilde{\mathbf{B}} \\ &\Leftrightarrow \mathbf{p}_2(t) = \mathbf{p}_1(t) + \frac{2}{1 + \left(\frac{\mathbf{B}(t) \Delta t}{e(t)}\right)^2} \mathbf{p}_3(t) \times \frac{\mathbf{B}(t) \Delta t}{e(t)} \frac{\Delta t}{2}, \end{aligned} \quad (6.76)$$

where we reintroduced the time t explicitly and replaced $\tilde{\mathbf{B}}$ by its definition. Finally,

$$\mathbf{p} \left(t + \frac{\Delta t}{2} \right) = \mathbf{p}_2(t) + \frac{\Delta t}{2} \mathbf{E}(t), \quad (6.77)$$

is the momentum used to determine the velocity in the coordinate update (6.28).

6.4 Inclusion of binary collisions

After having discussed the collisionless system and explained the numerical methods for solving the equations of motion we now introduce hard collisions, i.e., particle-particle collisions with hard momentum exchange. For a realistic coupling constant g these interactions become important since the higher orders in g at which they contribute are no longer suppressed, as pointed out already in Chapter 5. With the collisions included, our system will be similar to that used in parton cascade simulations [202, 203, 204, 205, 206, 207, 208, 58, 209] with one big advantage. We do not have to cut off (or suppress) the momentum exchange below the DEBYE-mass ($\sim gT$) which is of the order of the temperature in an equilibrium system ($g \sim 1 - 2$), but include softer momentum exchanges via particle-field interactions. This way we are also able to study collective phenomena and their contribution to isotropization and thermalization. In particular, we can study systems far from equilibrium for which the scale corresponding to the DEBYE-mass squared in an isotropic system becomes negative [63]. In this case it can obviously not be used to damp the propagator, i.e., to cut off the momentum exchange in the infrared region, as it is done in the parton cascade simulations. All we need is a separation scale k^* between the field and particle degrees of freedom. We will discuss this separation scale in detail in Section 6.5.1. For now it will serve as a lower bound for the exchanged momenta in the binary elastic particle collisions. All softer momenta will be exchanged via the fields.

6.4.1 Cross section and transition rate

We include collisions using the stochastic method introduced and applied in [210, 211, 58]. This means that we do not interpret the cross section in a geometrical way as done in [202, 203, 204, 205, 206, 207] but determine scattering processes in a stochastic manner by sampling possible transitions in a certain volume per time interval. This collision algorithm can be extended to include the inelastic collision processes $gg \leftrightarrow ggg$ as done in [58, 209], which will be one of the future goals also for our simulation. We introduce collisions by adding the collision term \mathcal{C} to the VLASOV equation (6.16):

$$P_1^\mu \left[\partial_\mu + gq^a F_{\mu\nu}^a \partial_{(p)}^\nu + g f^{abc} A_\mu^b(X) q^c \partial_{q^a} \right] f_1(P_1, X, q_1) = \mathcal{C}, \quad (6.78)$$

with

$$\begin{aligned} \mathcal{C} = & \frac{1}{2E_1} \int \frac{d^3 p_2}{(2\pi)^3 2E_2} \frac{1}{2} \int \frac{d^3 p'_1}{(2\pi)^3 2E'_1} \frac{d^3 p'_2}{(2\pi)^3 2E'_2} f'_1 f'_2 |\mathcal{M}_{1'2' \rightarrow 12}|^2 (2\pi)^4 \delta^{(4)}(p'_1 + p'_2 - p_1 - p_2) \\ & - \frac{1}{2E_1} \int \frac{d^3 p_2}{(2\pi)^3 2E_2} \frac{1}{2} \int \frac{d^3 p'_1}{(2\pi)^3 2E'_1} \frac{d^3 p'_2}{(2\pi)^3 2E'_2} f_1 f_2 |\mathcal{M}_{12 \rightarrow 1'2'}|^2 (2\pi)^4 \delta^{(4)}(p_1 + p_2 - p'_1 - p'_2), \end{aligned} \quad (6.79)$$

with the matrix element \mathcal{M} including all $gg \rightarrow gg$ events shown in Fig. 6.5. The $1/2$ avoids double counting for identical particles.

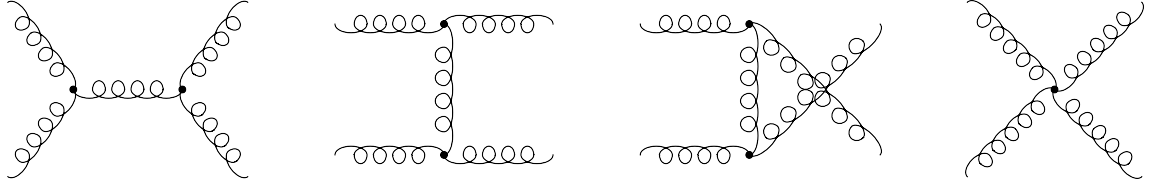


Figure 6.5: Processes contributing to $gg \rightarrow gg$ scattering.

When assuming two particles in a spatial volume element $\Delta^3 x$ with momenta in the range $(\mathbf{p}_1, \mathbf{p}_1 + \Delta^3 p_1)$ and $(\mathbf{p}_2, \mathbf{p}_2 + \Delta^3 p_2)$, the collision rate per unit phase space for such a particle pair follows from Eq. (6.79)

$$\begin{aligned} \frac{\Delta N_{\text{coll}}}{\Delta t \frac{1}{(2\pi)^3} \Delta^3 x \Delta^3 p_1} &= \frac{1}{2E_1} \frac{\Delta^3 p_2}{(2\pi)^3 2E_2} f_1 f_2 \\ &\times \frac{1}{2} \int \frac{d^3 p'_1}{(2\pi)^3 2E'_1} \frac{d^3 p'_2}{(2\pi)^3 2E'_2} |\mathcal{M}_{12 \rightarrow 1'2'}|^2 (2\pi)^4 \delta^{(4)}(p_1 + p_2 - p'_1 - p'_2). \end{aligned} \quad (6.80)$$

Expressing distribution functions as

$$f_i = \frac{\Delta N_i}{\frac{1}{(2\pi)^3} \Delta^3 x \Delta^3 p_i}, \quad i = 1, 2, \quad (6.81)$$

and employing the usual definition of the cross section for massless particles [212]

$$\sigma_{22} = \frac{1}{4s} \int \frac{d^3 p'_1}{(2\pi)^3 2E'_1} \frac{d^3 p'_2}{(2\pi)^3 2E'_2} |\mathcal{M}_{12 \rightarrow 1'2'}|^2 (2\pi)^4 \delta^{(4)}(p_1 + p_2 - p'_1 - p'_2), \quad (6.82)$$

one obtains the absolute collision probability in a unit box $\Delta^3 x$ and unit time Δt

$$P_{22} = \frac{\Delta N_{\text{coll}}}{\Delta N_1 \Delta N_2} = \tilde{v}_{\text{rel}} \sigma_{22} \frac{\Delta t}{\Delta^3 x}. \quad (6.83)$$

$\tilde{v}_{\text{rel}} = s/2E_1 E_2$ denotes the relative velocity⁴, where s is the invariant mass of the particle pair. P_{22} can be any number between 0 and 1.⁵ Whether or not a collision occurs is sampled stochastically as follows: We compare P_{22} with a uniformly distributed random number between 0 and 1. If the random number is less than P_{22} , the collision will occur. Otherwise there will be no collision between the two particles within the present time step. Since we employ N_{test} test particles per particle, we have to scale the cross section by $\sigma \rightarrow \sigma/N_{\text{test}}$, which leads to

$$P_{22} = \tilde{v}_{\text{rel}} \frac{\sigma_{22}}{N_{\text{test}}} \frac{\Delta t}{\Delta^3 x}. \quad (6.84)$$

To determine this probability, we need to calculate the total cross section σ_{22} . It follows from the differential cross section, which can be calculated from the graphs in Fig. 6.5 in perturbative QCD (pQCD) in leading order in the coupling constant α_s . To get an idea of how the calculation works, let us write down the matrix element for the first (s-channel) diagram and then skip directly to the final answer.

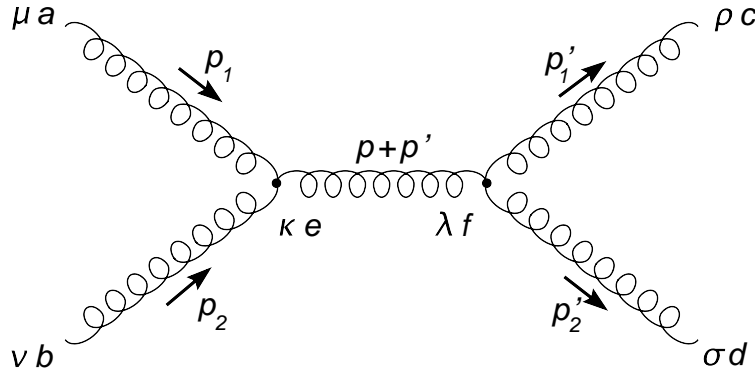


Figure 6.6: s-channel contribution to $gg \rightarrow gg$ scattering.

The vector and color indices of the in- and outgoing gluons as well as that of the intermediate gluon are indicated in Fig. 6.6. Using the appropriate FEYNMAN rules, from this we obtain

⁴Please note that this is not the actual relativistic relative velocity of two particles. Please see Appendix E for a detailed discussion on how \tilde{v}_{rel} relates to the true relative velocity.

⁵In practice one has to choose suitable $\Delta^3 x$ and Δt to make P_{22} less than 1.

for the matrix element

$$\begin{aligned} \mathcal{M}_{12 \rightarrow 1'2'}^{s\text{-channel}} &= \epsilon_1^\mu \epsilon_2^\nu \epsilon_{1'}^{\rho*} \epsilon_{2'}^{\sigma*} \left\{ -gf^{acb} [g_{\mu\kappa}(2P_1 + P_2)_\nu + g_{\kappa\nu}(-P_1 - 2P_2)_\mu + g_{\nu\mu}(P_2 - P_1)_\kappa] \right\} \\ &\quad \times \left\{ -gf^{cdf} [g_{\rho\sigma}(P_2' - P_1')_\lambda + g_{\sigma\lambda}(-2P_2' - P_1')_\rho + g_{\lambda\rho}(2P_1' + P_2')_\sigma] \right\} \\ &\quad \times \left[\frac{-ig^{\kappa\lambda}\delta^{ef}}{(P_1 + P_2)^2} \right], \end{aligned} \quad (6.85)$$

with the gluon polarization vectors ϵ . After writing down the matrix elements for the three other diagrams, adding them together, taking the complex square, summing over final state polarizations and averaging over initial state polarizations, summing over final state gluon colors and averaging over initial state gluon colors one finds [213, 214, 215]

$$\frac{d\sigma}{dt} = \frac{4\pi\alpha_s^2}{s^2} \frac{N^2}{N^2 - 1} \left(3 - \frac{tu}{s^2} - \frac{su}{t^2} - \frac{st}{u^2} \right), \quad (6.86)$$

with N the number of colors. In particular for SU(2) and SU(3) we have

$$\frac{d\sigma}{dt} = \frac{16}{3} \frac{\pi\alpha_s^2}{s^2} \left(3 - \frac{tu}{s^2} - \frac{su}{t^2} - \frac{st}{u^2} \right) \quad \text{for SU(2),} \quad (6.87)$$

$$\frac{d\sigma}{dt} = \frac{9}{2} \frac{\pi\alpha_s^2}{s^2} \left(3 - \frac{tu}{s^2} - \frac{su}{t^2} - \frac{st}{u^2} \right) \quad \text{for SU(3).} \quad (6.88)$$

The invariant MANDELSTAM variables are:

$$\begin{aligned} s &= (P_1 + P_2)^2, \\ t &= (P_1 - P_1')^2, \\ u &= (P_1 - P_2')^2. \end{aligned} \quad (6.89)$$

Some nice relations can be easily derived in the center of mass frame:

$$t = (P_1 - P_1')^2 = (E_1 - E_1')^2 - (\mathbf{p}_1 - \mathbf{p}_1')^2 = \left(\frac{\sqrt{s}}{2} - \frac{\sqrt{s}}{2} \right)^2 - \mathbf{q}^2 = -\mathbf{q}^2, \quad (6.90)$$

with the transferred momentum \mathbf{q} . Furthermore

$$-t = \mathbf{q}^2 = \mathbf{p}_1^2 + \mathbf{p}_1'^2 - 2\mathbf{p}_1 \cdot \mathbf{p}_1' = \frac{s}{4} + \frac{s}{4} - \frac{s}{2} \cos\theta = \frac{s}{2}(1 - \cos\theta). \quad (6.91)$$

Because t is an invariant this holds in every frame. Using (6.91) and $s + t + u = 0$ for the massless case, we can express Eq. (6.87) by q^2 and calculate the total cross section via

$$\sigma_{22} = \int_{k^{*2}}^{\frac{s}{2}} \frac{d\sigma}{dq^2} dq^2. \quad (6.92)$$

The integral can be done analytically and results in the rather lengthy expression

$$\begin{aligned} \sigma_{22} &= \frac{4\pi\alpha_s^2}{9k^{*2}(k^{*2} - s)s^4} \left[-4(k^{*2})^5 + 10(k^{*2})^4s - 42(k^{*2})^3s^2 + 53(k^{*2})^2s^3 + 7k^{*2}s^4 \right. \\ &\quad \left. - 12s^5 + 6k^{*2}(k^{*2} - s)s^3 \log \left(\frac{(k^{*2})^2}{(k^{*2} - s)^2} \right) \right]. \end{aligned} \quad (6.93)$$

6.4.2 Momentum transfer

Now we have all the ingredients to determine whether or not a collision occurs within one time step. However, we also have to calculate the transferred momentum according to the differential cross section $d\sigma/dq^2$. We perform a LORENTZ transformation into the center of mass frame of the colliding particles and then determine the exchanged momentum according to the probability distribution

$$\mathcal{P}(q^2) = \frac{1}{\sigma_{22}} \frac{d\sigma}{dq^2}, \quad (6.94)$$

which satisfies

$$\int_{k^{*2}}^{\frac{s}{2}} \mathcal{P}(q^2) dq^2 = 1. \quad (6.95)$$

To do so, we need to employ the rejection method [216]. That is, we need to find an approximation to (6.94), $\mathcal{P}_{\text{app}}(q^2) > \mathcal{P}(q^2)$, which can be integrated (if possible analytically) and inverted, and is always larger than (6.94). With that distribution we can then employ the transformation method [216] to calculate q^2 . Finally we need to decide (again stochastically) whether to keep that result or to reject it, with the probability depending on the difference between the exact and the approximate distribution. As the approximate distribution we use the small angle scattering limit of the differential cross section (divided by the total cross section) and shift it to make sure that it always lies above the exact probability distribution (6.94). The transformation method is based on the fundamental transformation law for probabilities and the fact that we can generate random deviates with a uniform probability distribution. For these the probability of generating a number between x and $x + dx$, denoted $u(x)dx$, is given by

$$u(x)dx = \begin{cases} dx & \text{for } 0 < x < 1 \\ 0 & \text{otherwise} \end{cases} \quad (6.96)$$

The distribution $u(x)$ is normalized so that

$$\int_{-\infty}^{\infty} u(x)dx = 1. \quad (6.97)$$

Now suppose, we generate a uniform deviate x and take some function $y(x)$ of it. Then the probability distribution of q^2 , denoted $\mathcal{P}_{\text{app}}(q^2)dq^2$ is determined by the fundamental transformation law of probabilities, which is simply

$$|\mathcal{P}_{\text{app}}(q^2)dq^2| = |u(x)dx|, \quad (6.98)$$

or

$$\mathcal{P}_{\text{app}}(q^2) = u(x) \left| \frac{dx}{dq^2} \right|, \quad (6.99)$$

which leads to

$$\int_{k^{*2}}^{q^2} \mathcal{P}_{\text{app}}(q'^2) dq'^2 = \int_0^x u(x') dx' = x, \quad (6.100)$$

with $x < x_{\max}$ and

$$x_{\max} = \int_{k^{*2}}^{\frac{s}{2}} \mathcal{P}_{\text{app}}(q'^2) dq'^2, \quad (6.101)$$

which is larger than one because $\mathcal{P}_{\text{app}}(q^2) > \mathcal{P}(q^2)$ and Eq. (6.95). Defining $F(k^{*2}, q^2) := \int_{k^{*2}}^{q^2} \mathcal{P}_{\text{app}}(q'^2) dq'^2$, we have

$$F(k^{*2}, q^2) = x \Rightarrow q^2 = F^{-1}(k^{*2}, x), \quad (6.102)$$

with F^{-1} being the inverse function to F . This determines the transferred momentum q^2 . However, since we did not use the exact distribution function \mathcal{P} , we need to perform one more step. Having determined a q^2 , we can now easily calculate $\mathcal{P}_{\text{app}}(q^2)$ and $\mathcal{P}(q^2)$. Because $\mathcal{P}_{\text{app}}(q^2) > \mathcal{P}(q^2)$, we compare the ratio of the two with another random number y , which is uniformly distributed on $[0, 1]$, reject the q^2 if

$$y > \frac{\mathcal{P}(q^2)}{\mathcal{P}_{\text{app}}(q^2)}, \quad (6.103)$$

determine a new q^2 and repeat the process until a q^2 is accepted. This makes it obvious why we want the approximate distribution function to be very close to the exact one - if it is not we will have a lot of rejected q^2 and hence longer computation time.

The exchanged transverse (transverse to the straight line connecting the two particles) momentum is related to q^2 and s in the following way

$$q^2 = \frac{s}{2}(1 - \cos \theta) \Rightarrow \theta = \arccos \left(1 - \frac{2}{s}q^2 \right) \quad (6.104)$$

and

$$q_{\perp}^2 = \frac{s}{4} \sin^2 \theta = \frac{s}{4} \sin^2 \left(\arccos \left(1 - \frac{2}{s}q^2 \right) \right). \quad (6.105)$$

In the present status of the simulation the particles do not exchange color in the collisions. As discussed in Section 5.4, this may increase the effect of the collisions on instability growth. The implementation of (classical) color rotation is one of the future projects.

6.5 Momentum space diffusion

Having introduced hard collisions to the system of coupled WONG-YANG-MILLS equations, we now investigate a first observable - the momentum space diffusion of hard particles traversing an isotropic (in momentum space) plasma. We show that when we match the initial energy density in the field modes to that of the particles, the obtained results are approximately independent of the lattice spacing.

6.5.1 The separation scale

We introduced k^* as an infrared cutoff on the exchanged momentum in the hard collisions in Section 6.4. As previously mentioned it will serve as a separation scale between soft

and hard exchanged momenta. The scattering processes in the regime of hard exchanged momentum are described by elastic binary collisions, while the ones in the regime of soft momentum exchange are mediated by the fields. A scattering in the soft regime corresponds to deflection of a particle in the field of the other(s). In order to avoid double counting of scattering processes, k^* should be on the order of the hardest field mode that can be represented on the given lattice, $k^* \simeq \pi/a$.

Physically, the separation scale k^* should be sufficiently small so that the soft field modes below k^* are highly occupied [195] and hence can be described classically. On the other hand, k^* should be sufficiently large to ensure that hard modes can be represented by particles and that collisions are described by (6.79), which is valid only for low occupation numbers, since the Bose term $(1 + f)$ is approximated by 1. Later, when dealing with anisotropic plasmas, unstable modes arise. These should all be located below k^* , i.e., $k_{\max} < k^*$. In practice $g \sim 1$, and we choose k^* to be on the order of the temperature for isotropic systems, and on the order of the hard transverse momentum scale for anisotropic plasmas. At the same time k^* is determined by the largest available field mode, which on a cubic lattice is given by $\sqrt{3}\pi/a$. Obviously, any matching between soft and hard regimes can only be done approximately, because the lattice on which the field modes are defined is cubic, while the momentum space cutoff of the particles is implicitly spherical.

The 'soft' scale in the system, which also sets the scale for the unstable field growth in anisotropic systems, is described by

$$m_\infty^2 = g^2 N_c \int \frac{d^3 p}{(2\pi)^3} \frac{f(\mathbf{p})}{|\mathbf{p}|} \sim g^2 N_c \frac{n_g}{p_h}, \quad (6.106)$$

analogous to the DEBYE mass (3.20). To allow for trustworthy numerical simulations one should have $m_\infty L \gg 1$ and $m_\infty a \ll 1$. The first condition ensures that the relevant soft modes actually fit on the lattice while the latter ensures that the lattice can resolve the wavelength $1/m_\infty$ to good precision.

6.5.2 Initial energy density

We consider a heat-bath of BOLTZMANN distributed particles with a density of $n_g = 10/\text{fm}^3$ and an average particle momentum of $3T = 12 \text{ GeV}$. The reason for not using a completely thermal but under-saturated distribution is of technical nature - we have to fulfill the condition $m_\infty a \ll 1$ and at the same time choose low enough densities and number of lattice sites to keep the computation time within an acceptable range. The rather extreme "temperature" T is also chosen to satisfy the above conditions on $N_s = 32 \cdots 128$ lattices, assuming $L = 15 \text{ fm}$.

For a given lattice (resp. k^*) we take the initial energy density of the thermalized fields to be

$$\varepsilon_{\text{fields}} = \int \frac{d^3 k}{(2\pi)^3} k \hat{f}_{\text{Bose}}(k) \Theta(k^* - k), \quad (6.107)$$

where

$$\hat{f}_{\text{Bose}}(k) = n_g / (2T^3 \zeta(3)) 1 / (e^{k/T} - 1) \quad (6.108)$$

is a Bose distribution normalized to the assumed particle density n_g , and ζ is the RIEMANN zeta function.

The initial field amplitudes are sampled from a Gaussian distribution with a width tuned to the above initial energy density:

$$\langle A_i^a(x) A_j^b(y) \rangle = \frac{4\mu^2}{g^2} \delta_{ij} \delta^{ab} \delta(\mathbf{x} - \mathbf{y}). \quad (6.109)$$

The initial spectrum is then fixed to Coulomb gauge and $A_i \sim 1/k$ (in continuum notation), and also $E_i = 0$. GAUSS's law then implies that the local charge density at time $t = 0$ vanishes. We ensure that any particular initial condition satisfies exact local charge neutrality. The charge smearing algorithm for SU(2) explicitly exploits (covariant) current conservation and hence GAUSS's law is satisfied exactly by construction.

The above procedure ensures that there is not a big jump in the energy density when going from the field to the particle regime. This way we are able to vary the separation scale k^* around the temperature T by varying the lattice spacing. Fig. 6.7 shows the distribution of field modes and particles and the separation momentum k^* at T .

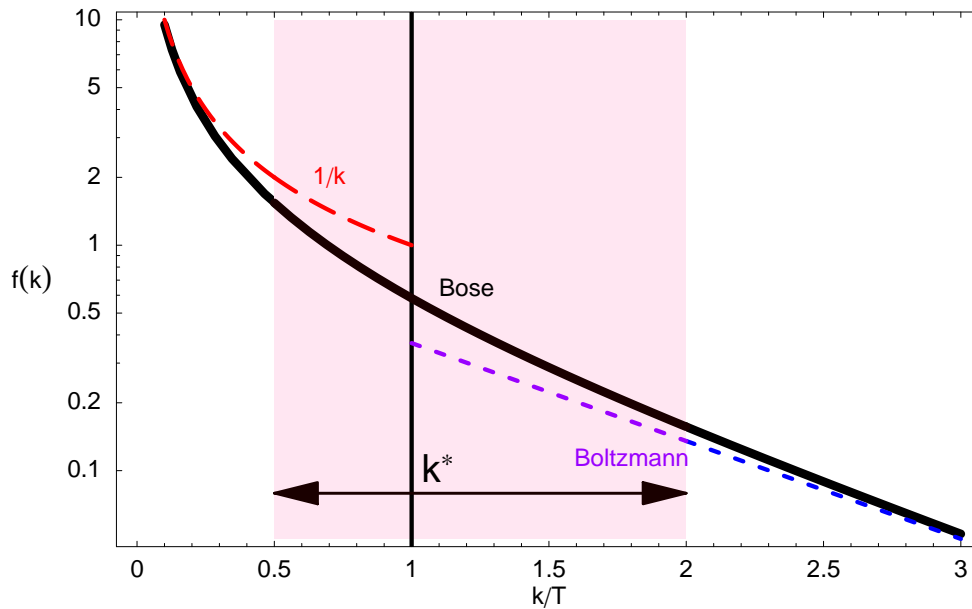


Figure 6.7: BOSE distribution and its low and high-momentum limits, used for the initial fields and particles, respectively. Physically, the separation k^* should lie around the temperature T . The band between $T/2$ and $2T$ roughly indicates the region within which we will vary k^* .

6.5.3 Jet momentum diffusion

Having initialized the background particles and fields, we can now add high-momentum test particles with momentum $p/3T \approx 5$ that are oriented in one direction. We initialize with few enough so that they can not influence the background significantly. Fig. 6.8 shows the setup with background and jet particles. We can now measure the momentum

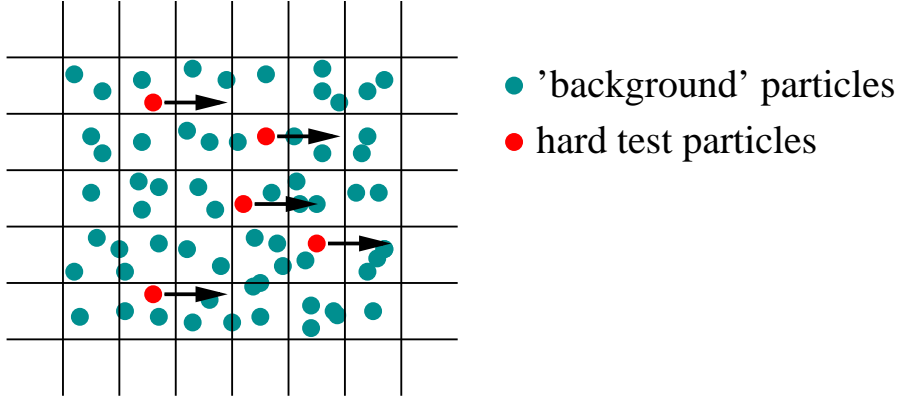


Figure 6.8: Setup for the measurement of momentum diffusion: High energy jets moving in a bath of particles and fields.

broadening $\langle p_{\perp}^2 \rangle(t) = \langle p_x^2 + p_y^2 \rangle(t)$ of the high-energy test particles with initial momentum in the z -direction. First turning off the elastic hard collisions ($\mathcal{C} = 0$) and hence only allowing momentum transfers up to $q = k^*$ via the field interactions leads to a strong lattice (i.e., k^*) dependence of the results. Fig. 6.9 shows the transverse momentum squared of the jets versus time, computed on different lattices. Using half the lattice spacing corresponds to having twice as many available modes. We use $k^* = \sqrt{3}(T/2, T, 2T)$ and a temperature of $T = 4$ GeV as noted above. One can clearly see how the availability of harder modes leads to stronger diffusion on larger lattices.

Now allowing binary collisions with hard momentum exchange in addition to the deflection by the self-consistently generated fields and adjusting energy densities as described in Section 6.5.2 changes the situation drastically. We find that when varying the separation momentum k^* by factors of two in both directions around the central value T (within the band shown in Fig. 6.7) the result for $\langle p_{\perp}^2 \rangle(t)$ is approximately unaffected. For $k^* = T/2$ there are more momentum exchanges described by hard collisions while for $k^* = 2T$ there are more harder field modes present that take care of those interactions. So within the rather wide range $T/2 < k^* < 2T$ we can vary the contribution from field deflections versus that from binary collisions without affecting the result for momentum broadening of the jet particles. Fig. 6.10 shows this result using the same different lattice sizes as in Fig. 6.9.

Figs. 6.9 and 6.10 show that the relative contributions to $\langle p_{\perp}^2 \rangle$ from soft and hard exchanges can depend significantly on k^* , even for $p/k^* = \mathcal{O}(10)$. It is clear, therefore, that transport coefficients obtained in the leading logarithmic (LL) approximation from the pure BOLTZMANN approach (without soft fields) will be rather sensitive to the infrared cutoff k^* . Fitting the difference of Fig. 6.10 and Fig. 6.9 (i.e., the hard contribution) to the LL formula

$$\frac{d\langle p_{\perp}^2 \rangle}{dt} = \frac{C_A}{C_F} \frac{g^4}{8\pi} n_g \log \left(C^2 \frac{p^2}{k^{*2}} \right), \quad (6.110)$$

gives $C \simeq 0.43, 0.41, 0.31$ for $k^*/T = 2\sqrt{3}, \sqrt{3}, 0.5\sqrt{3}$, respectively. For the full calculation $C \simeq 0.61 k^*/(\sqrt{3}T)$.

A related and frequently used transport coefficient is \hat{q} [217]. It is the typical momentum

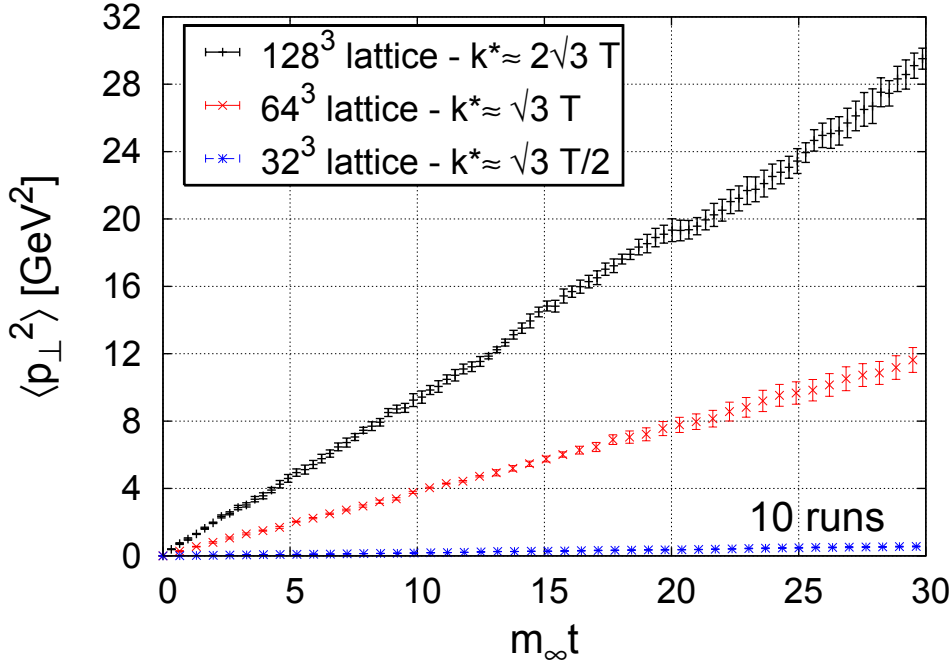


Figure 6.9: Momentum diffusion caused by particle-field interactions only. Additional high-momentum modes on larger lattices cause stronger momentum broadening. $T = 4$ GeV, $g = 2$, $n_g = 10/\text{fm}^3$, $m_{\infty} = 1.4/\text{fm}$.

transfer (squared) per collision divided by the mean-free path λ , which is nothing but $\langle p_{\perp}^2 \rangle(t)/t$. To see this, let us start from the definition of \hat{q}

$$\hat{q} = \frac{1}{\sigma\lambda} \int d^2 p_{\perp} p_{\perp}^2 \frac{d\sigma}{dp_{\perp}^2}. \quad (6.111)$$

The integral is just $\sigma \langle p_{\perp}^2 \rangle_{1 \text{ collision}}$, since

$$\frac{1}{\sigma} \frac{d\sigma}{dp_{\perp}^2}$$

can be seen as a probability distribution for a collision with momentum transfer p_{\perp}^2 to occur. To extract \hat{q} from the accumulated $\langle p_{\perp}^2 \rangle$, shown in Figs. 6.9 and 6.10, we only have to divide by the number of collisions that have occurred up to time t , t/λ . So finally we have

$$\hat{q} = \frac{\langle p_{\perp}^2 \rangle}{t}, \quad (6.112)$$

which is just the slope of the approximately straight lines in Figs. 6.9 and 6.10.

Note that the definition of \hat{q} holds exactly only in the eikonal limit, where the jet does not change its direction. Away from this limit, $\hat{q} = \langle p_{\perp}^2 \rangle/t$ is smaller than the mean momentum transfer squared per collision divided by the mean-free path, because it considers the actual random walk of the particle.

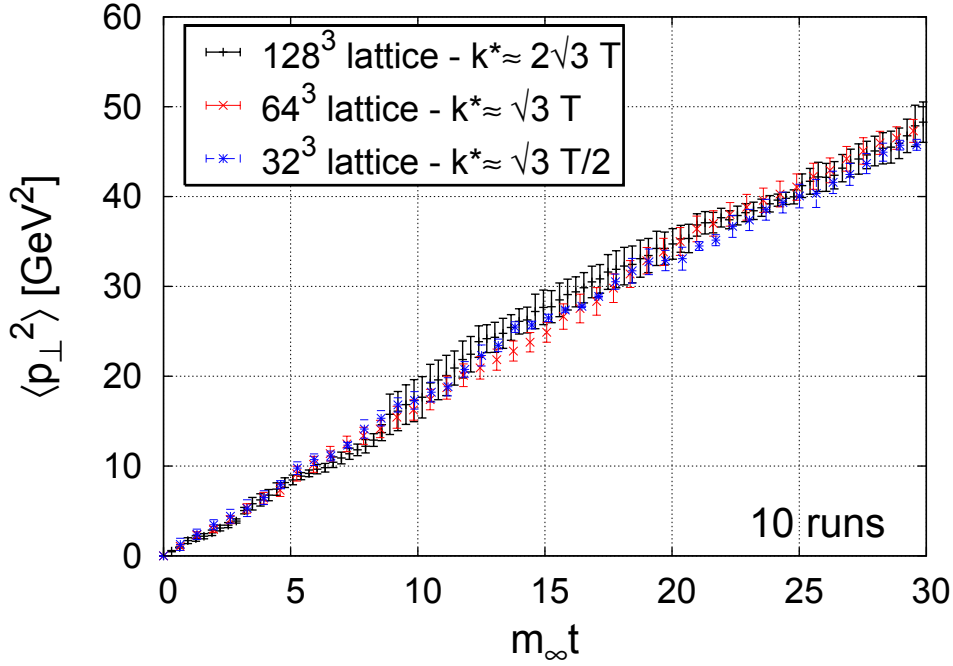


Figure 6.10: Momentum diffusion caused by hard binary collisions and particle-field interactions. $T = 4$ GeV, $g = 2$, $n_g = 10/\text{fm}^3$, $m_{\infty} = 1.4/\text{fm}$.

From Fig. 6.10, $\hat{q} \simeq 2.2$ GeV²/fm for $n_g = 10/\text{fm}^3$ and $p/(3T) \approx 5$. This is the first cut-off independent result for \hat{q} . Its value for \hat{q} is in the range extracted from phenomenological analyses of jet-quenching data from RHIC [218]. As expected from Eq. (6.111) \hat{q} scales with the density of the medium $n = 1/(\sigma\lambda)$, which is demonstrated in Fig. 6.11. Further, it depends on the ratio p/T , but not on T itself as demonstrated in Fig. 6.12.

We can hence scale to physical densities for a QGP created at RHIC, adjust for the different color factors in SU(3), and find $\hat{q} \approx 8$ GeV²/fm, at $T = 400$ MeV, $E_{\text{jet}} \approx 20$ GeV ($p/3T = 16$) in a system of quarks and gluons. Here, we have assumed that the interaction between quarks and gluons is as strong as that among the gluons. Using the small angle approximation for the $qg \rightarrow qg$ cross section one finds that it is a factor of 4/9 smaller than that for the $gg \rightarrow gg$ process. This leads to a modified extrapolated $\hat{q} \approx 5.6$ GeV²/fm.

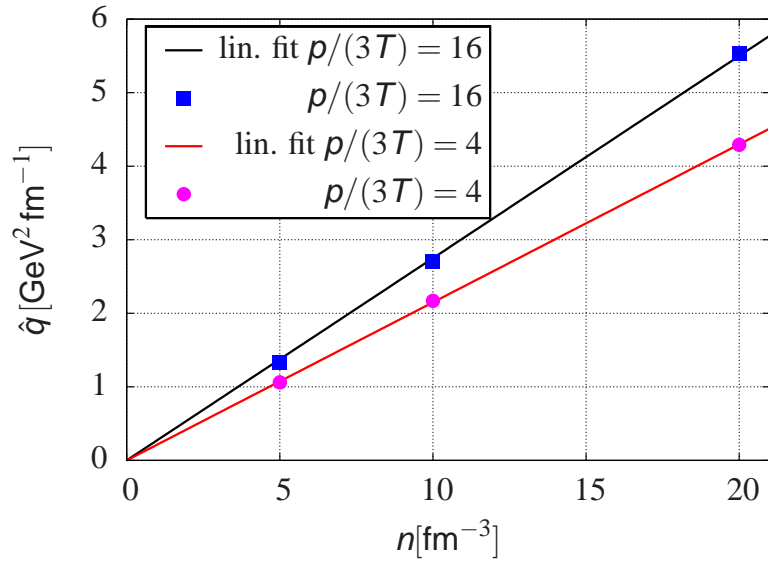


Figure 6.11: \hat{q} as a function of the density n at fixed $T = 4 \text{ GeV}$ and $p/(3T) \in \{4, 16\}$.

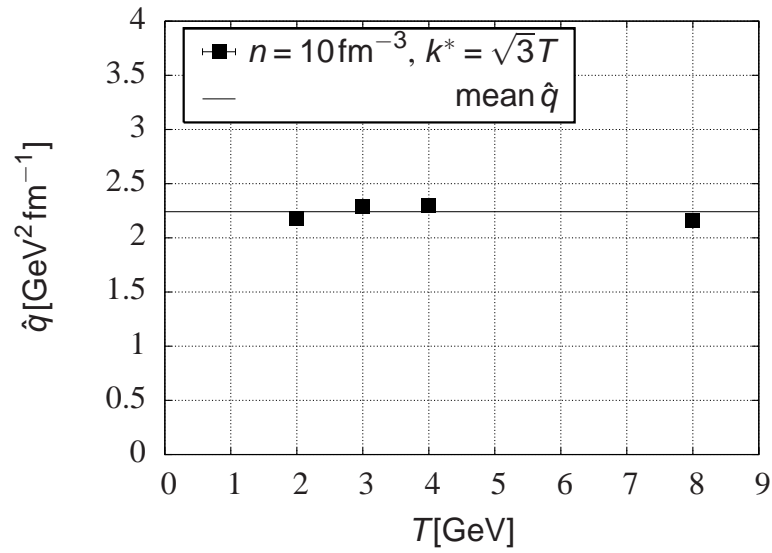


Figure 6.12: \hat{q} as a function of T at fixed $n_g = 10/\text{fm}^3$ and $p/(3T) = 5$.

7 Real-time simulation of plasma instabilities

Es schadet nichts, wenn Starke sich verstärken.

Faust II. Vierter Akt. Auf dem Vorgebirg. Faust.

Johann Wolfgang von Goethe (1749-1832)

So far we have considered particle distributions that are isotropic in momentum space in the simulation. To simulate the early stage of a quark-gluon plasma, created in a heavy-ion collision, we need to initialize with an anisotropic momentum distribution as discussed in Chapter 4.4. In this case, chromo-WEIBEL-instabilities can occur and in the following chapter we will show that in fact they do. We will then concentrate on the effect of collisions on the unstable growth and discuss isotropization. We close the chapter with the discussion of the effect of instabilities on jet propagation and potential observables.¹

The initial momentum distribution for the hard plasma gluons is now taken to be

$$f(\mathbf{p}) = n_g \left(\frac{2\pi}{p_h} \right)^2 \delta(p_z) \exp(-p_\perp/p_h), \quad (7.1)$$

with $p_\perp = \sqrt{p_x^2 + p_y^2}$. This represents a quasi-thermal distribution in two dimensions with average momentum $= 2p_h$. We initialize small-amplitude fields sampled from a Gaussian distribution and set $k^* \approx p_h$, for the reasons discussed in Section 6.5.1. The band of unstable modes is located below k^* .

At the initial time $t = 0$ we randomly sample $N_p = N_{\text{test}} n_g a^3$ particles from the distribution (7.1) at each cell of the lattice. When N_p is not very large it is useful to ensure explicitly that the sum of particle momenta in each cell vanishes, for example by adjusting the momentum of the last particle accordingly.

For the distribution (7.1) the mass scale (6.106) becomes exactly

$$m_\infty^2 = g^2 N_c \frac{n_g}{p_h}. \quad (7.2)$$

As mentioned before in the previous chapter and discussed in detail using the DEBYE mass in Chapters 4 and 5, this quantity sets the scale for the growth rate of unstable field modes in the linear approximation.

7.1 The collisionless limit

In the collisionless limit the chromo-WEIBEL-instability has been studied in detail in [161] and [162] within the WONG-YANG-MILLS-simulation. We will now summarize the most important results and extend the study, showing explicitly the generation of filaments discussed in Section 4.4.1.

¹The main part of this chapter is based on work published in [219].

In the Abelian case, it was found that for fields with weak initial energy density on the order of $0.1m_\infty^4/g^2$ the transverse chromo-magnetic and -electric fields grow, the latter at a slower rate. Modes above $k_z \simeq 12\pi/L$ are stable as opposed to the result in the linear approximation, where for extreme anisotropy the spectrum of unstable modes extends to $k = \infty$ (see Fig. 5.11).

In the non-Abelian $SU(2)$ case initial field energy densities of $\sim 10m_\infty^4/g^2$ and above were studied. In [162] the initial condition was taken to be GAUSSIAN random chromo-electric fields, which were 'low-pass' filtered such that only the lower half of available lattice modes was populated. Fig. 7.1 shows results obtained on various lattices. Runs with an isotropic particle distribution are shown in each panel as an indication of our numerical accuracy (error bars are not indicated for the isotropic runs). The isotropic runs show nearly constant fields over the time interval $t \leq 30m_\infty^{-1}$. From these figures it is observed that after a period of rapid growth both chromo-electric and -magnetic fields settle to an essentially constant energy density.

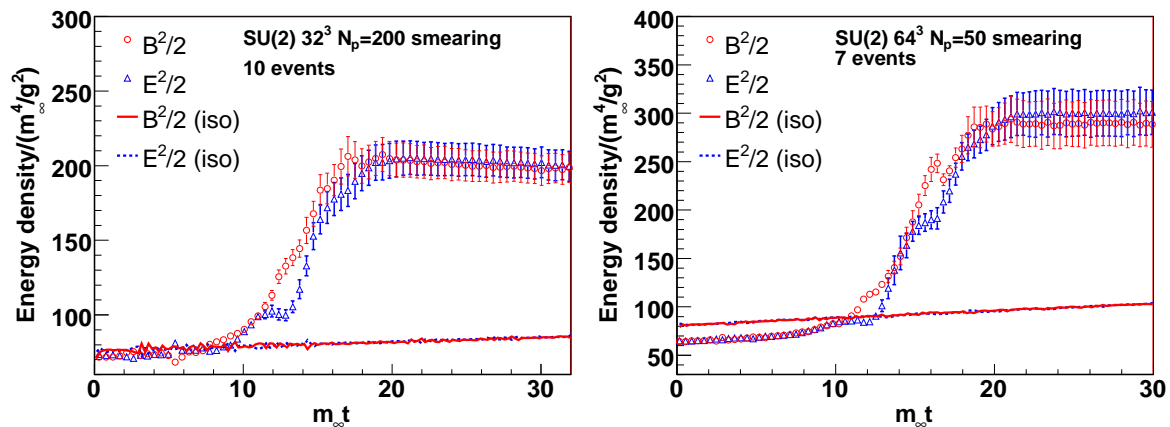


Figure 7.1: Time evolution of the field energy densities for $SU(2)$ gauge group and anisotropic initial particle momentum distributions. Simulation parameters are $L = 5$ fm, $p_h = 16$ GeV, $g^2 n_g = 10/\text{fm}^3$, $m_\infty = 0.1$ GeV. From [162].

Even beyond the hard-loop approximation, the time evolution of non-Abelian fields stronger than $\sim m_\infty^4/g^2$ differs from that in the (effectively Abelian) extreme weak-field limit. In particular, a sustained exponential growth is absent even during the stage where the back-reaction on the particles is weak. For very strong anisotropies a linear analysis predicts that the exponential field growth (in the weak-field situation) can perhaps continue until $B^2 \sim m_\infty^4/g^2/\Delta\theta^2$, with $\Delta\theta^2 = p_z^2/p_\perp^2 \approx \xi^{-1}$ [160]. For the initial condition (7.1), $\Delta\theta^2 = 0$ at $t = 0$ but grows to $\mathcal{O}(10^{-3})$ during the initial transient time with constant fields ($t m_\infty \lesssim 10$ in Fig. 7.1) due to deflection of the particles. However, such strong fields are not seen in our PIC simulations. This may be related to the above-mentioned back-reaction effects which prevent instability of modes near $k_{\text{max}} \sim m_\infty/\Delta\theta$.

The results shown in Fig. 7.1 indicate a sensitivity to hard field modes at the ultra-violet end of the Brillouin zone, $k = \mathcal{O}(a^{-1})$, in contrast to the $U(1)$ simulations and to earlier 1d-3v $SU(2)$ simulations [66, 161, 220]. The energy density contained in the fields at late times increases by a factor of 1.5 when going from a 16^3 to 32^3 to 64^3 lattice with the

same physical size L . Hence, the dynamics of $SU(2)$ instabilities seen here is not dominated entirely by a band of unstable modes in the infrared but clearly involves a cascade of energy from those modes to a harder scale Λ [221]. However, the simulations shown in Fig. 7.1 indicate that $\Lambda(t)$ grows to $\mathcal{O}(a^{-1})$ during the period of rapid growth of the field energy density; otherwise, the final field energy density would not depend on the lattice spacing. Spectra of the field modes also show the avalanching to the UV. After the unstable soft modes have grown, the energy is rapidly transferred to the higher modes [162].

Although energy conservation will eventually stop the growth of the fields as the lattice spacing decreases towards the continuum, it does not solve the following problem. When $\Lambda(t) \sim 1/a$, the hard field modes have reached the momentum scale of the particles, $p_h = \mathcal{O}(a^{-1})$, and so the clean separation of scales is lost, on which our approach is based. In fact, since the occupation number (or phase space density) at that scale is of order 1 or less by construction, it is inappropriate to describe modes at that scale as a classical field. Those perturbative modes should be converted dynamically into particles at a lower scale $\Lambda_{f \rightarrow p} \ll 1/a$ so that the field energy density and the entire coupled field-particle evolution is independent of the artificial lattice spacing. This question will be studied in the future.

We also wish to study the spatial distribution of currents and fields during the unstable growth. We expect to see the filaments discussed in Section 4.4.1 and variation of the fields (i.e., the wavelength of the unstable modes) on a lengthscale given by m_∞^{-1} , which with the used parameters is approximately 0.5 fm. To visualize this directly, we show a cut through the lattice at fixed $y = L/2$ (see Fig. 7.2), i.e., the x - z -plane, at different times in Fig. 7.3. Shown are the current in the x -direction as well as the three color components of the chromo-magnetic field in the y -direction. One can nicely see that filamentation sets in after about $t = 10m_\infty^{-1}$, the time at which the instability starts growing (see Fig. 7.1). Already during the period of growth, which lasts until about $t \approx 18m_\infty^{-1}$, the filaments break and the domains of strong aligned fields become smaller. Finally, at the time when the saturation sets in, we see directly the populated high momentum field modes. The observed structure may however be due to lattice effects, since the saturation depends on the lattice size as discussed above.

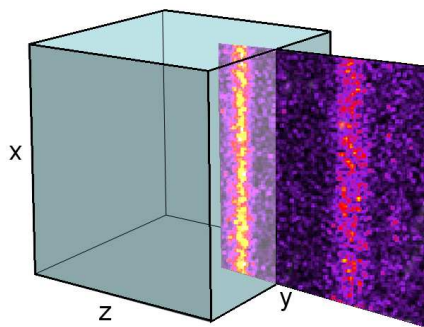


Figure 7.2: The cubic lattice with the pulled out slice we look at.

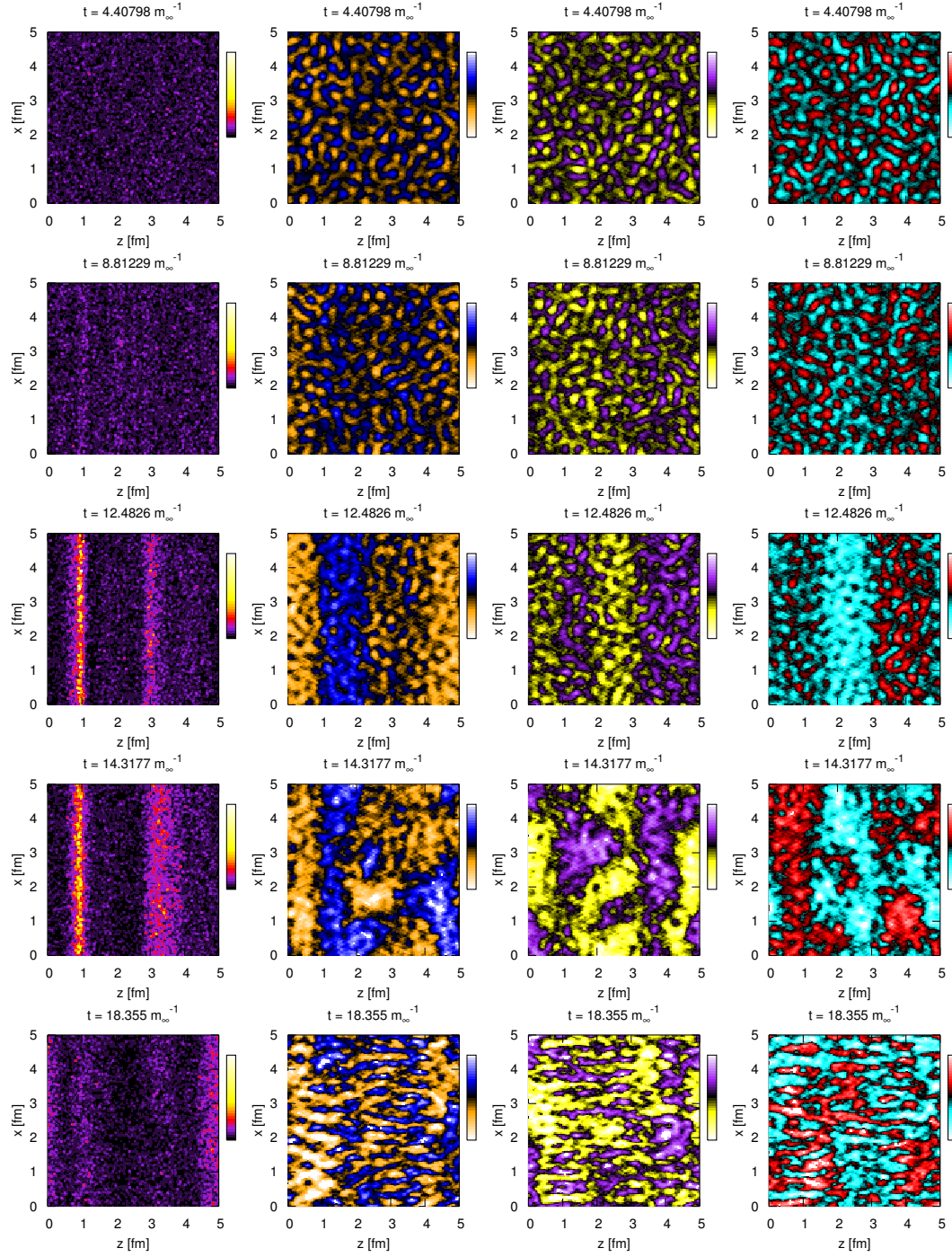


Figure 7.3: Slices in the x - z -plane at fixed $y = L/2$ of the (from left to right) current in the x -direction, J_x , and the three color components of the chromo-magnetic field in the y -direction, B_y^1 , B_y^2 , and B_y^3 . Time is increasing from top to bottom. The filaments are nicely visible in the early stage of the unstable growth in the third row. Please also compare the indicated times to those in Fig. 7.1, which shows the corresponding field energy density vs. time. Simulation parameters are $L = 5$ fm, $p_h = 16$ GeV, $g^2 n_g = 10/\text{fm}^3$, $m_\infty = 0.1$ GeV. The scales are in lattice units and reach from 0 to $5 \cdot 10^{-8}$ for the current and from $-4 \cdot 10^{-3}$ to $4 \cdot 10^{-3}$ for the chromo-magnetic fields.

Comparing to Fig. 4.3 on page 38, which shows the acting forces and resulting filaments, we find a direct correspondence to the structure in the simulation (note that since now the direction of the anisotropy is in the z -direction, x and z in Fig. 4.3 have to switch places - however, of course the argument does not change). This nicely shows that the instability observed in the simulation is indeed due to current filamentation and hence of the WEIBEL kind. Note that in order to compare field amplitudes at different places one would actually have to parallel transport their values. In other words, since we are looking at a quantity that is not gauge invariant, the plots of the B_y -components have to be taken with care. In any case they serve to visualize the qualitative structure of the fields in a very illuminating fashion.

7.2 Instabilities under the influence of collisions

We now study how the inclusion of collisions as described in Section 6.4 affects instability growth in the WONG-YANG-MILLS-simulation. We expect the growth rate to be reduced and the number of unstable modes to decrease from the model calculation in Chapter 5. The decrease of the growth rate is now partly because of the randomizing effect of the collisions, which disturbs the collective behavior, and because of the faster isotropization, which reduces $\xi \simeq \langle p_{\perp}^2 \rangle / \langle p_z^2 \rangle$ more rapidly. With the collision term an explicit dependence on g enters again. Regardless of the large hard momentum scale used, we set $g = 2$ to simulate the 'worst case' for the instability growth with the coupling expected at RHIC energies.

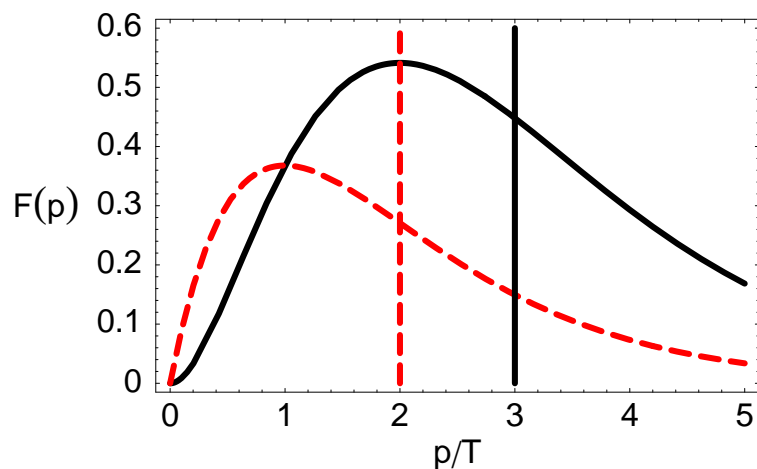


Figure 7.4: Qualitative shape of the quasi thermal particle distribution functions in three and two dimensions. $F(p)$ includes the phase-space factor: $F(p) = p^2 e^{-p/T}$ (3D) (solid black), $F(p) = p e^{-p/T}$ (2D) (dashed red), where in the latter case $T = p_h$. The vertical lines indicate the mean absolute value of the momentum $\langle p \rangle$ of the distribution.

The problem in these simulations is that we cannot match the energy densities of the fields and particles as we had done in the isotropic case. If we did that, the initial field amplitude would be too large to see any unstable growth at all. However, it may well be the case in the

experimental situation, which is strongly out of equilibrium, that the distribution functions are far from their equilibrium shape, such that a matching of the energy densities based on equilibrium distribution functions would not make much sense. We initialize weaker fields than the matching would demand, but choose the separation scale k^* to lie around the hard momentum scale p_h of the distribution (7.1). Since we have a two-dimensional distribution the average momentum is $2p_h$ as opposed to $3T$ for the three dimensional BOLTZMANN distribution. The most probable momentum is at p_h as opposed to $2T$ (see Fig. 7.4). Using the previous arguments for choosing the separation scale to lie around the temperature, we should in fact shift this value closer to $p_h/2$, because the distribution changed its shape. We will do the calculation for $k^* \approx 0.9p_h$ and $k^* \approx 1.7p_h$, and note that the more physical choice is $0.9p_h$. We realize different values for k^* by employing different lattice sizes for the same set of physical parameters.

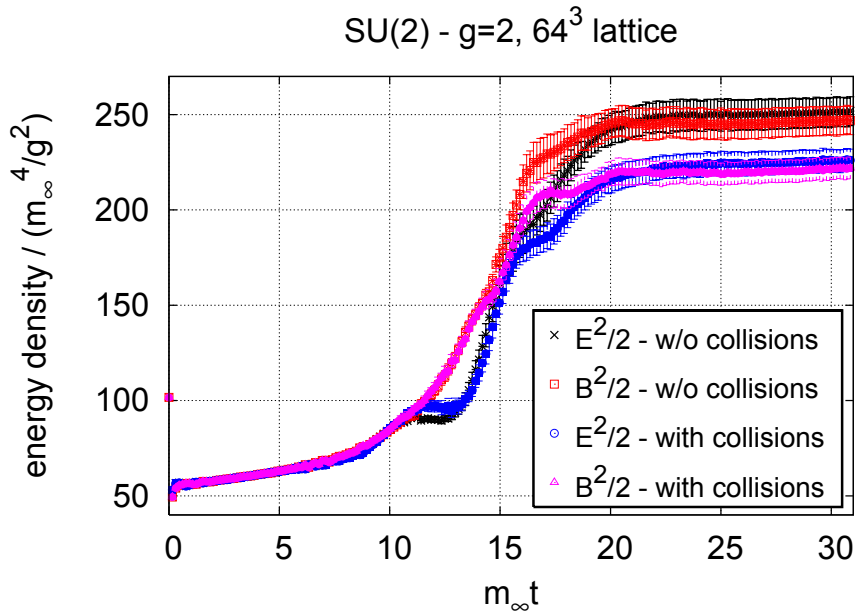


Figure 7.5: The effect of collisions with momentum exchange above $k^* \approx 1.7p_h$ (below that scatterings are mediated by the fields). Shown are calculations with (lower curves) and without collisions.

Figs. 7.5 and 7.6 show the results for a 64^3 ($k^* \approx 1.7p_h$) and a 32^3 ($k^* \approx 0.9p_h$), respectively. The reduction of the saturated value lies between about a factor of 0.6 ($k^* \approx 0.9p_h$) and 0.89 ($k^* \approx 1.7p_h$). The growth rate is reduced approximately by a factor 0.85 or 0.95 respectively. This result is obtained from assuming an exponential behavior between 10 and 20 $m_\infty t$. The comparison to the results in Chapter 5 is complicated by the fact that the anisotropy of the system is dynamically changing and the anisotropy parameter ξ evolves from initially ∞ down to about 60 at the time when the instability growth saturates. From Fig. 5.12 we can read off that for the estimated realistic growth rate of $\nu \approx 0.15m_D$, a reduction by 20% is to be expected when the anisotropy stays at the extreme limit. Hence we find that the two approaches lead to compatible results: the reduction of instability

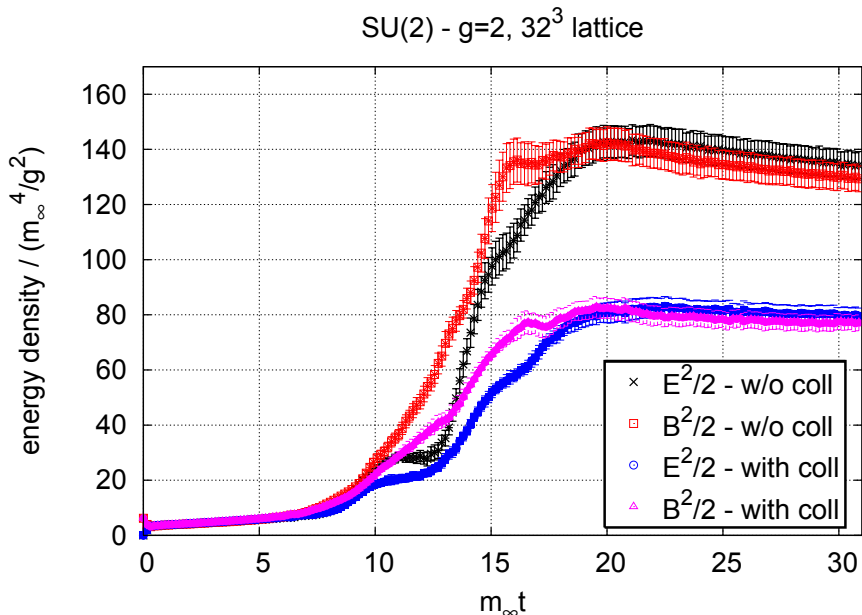


Figure 7.6: The effect of collisions with momentum exchange above $k^* \approx 0.9 p_h$ (below that scatterings are mediated by the fields). Shown are calculations with (lower curves) and without collisions.

growth by the collisions is present, but small enough for the instabilities to still play an important role in isotropization and equilibration of the QGP, even if the coupling is not infinitely small and collisions can not be neglected.

7.3 Isotropization

It is interesting to see, at not infinitesimally small coupling, whether the instability still dominates the isotropization when collisions are included. For the choice $g = 2$, which we chose in spite of the high temperature to get a contribution of the collisions comparable to the physical situation in heavy ion collisions, we find that the unstable growth still dominates the isotropization when we start with the extremely anisotropic initial distribution (7.1). This is shown in Figs. 7.7 and 7.8, where we plot the quantity $\langle p_z^2 \rangle / \langle p_x^2 + p_y^2 \rangle$ as a measure of the isotropy of the hard particle distribution. We can relate it to the previously used ξ , defined in Chapter 4, via $\xi = \langle p_\perp^2 \rangle / \langle p_z^2 \rangle - 1$. It starts out at 0 ($\xi = \infty$), because initially the particles do not have any longitudinal (z -direction) momentum at all. First, we just find a linear rise of this quantity, caused mainly by the hard collisions with momentum exchange above the separation scale k^* . The weak initial fields do not contribute much, at least for $k^* \approx p_h$ on the 64^3 -lattice. During the time of unstable field growth, however, the isotropization happens much faster than with collisions alone. The isotropizing effect of the domains of strong chromo-electro-magnetic fields dominates. These domains are visible in Fig. 7.3, and we will discuss them in more detail in Sec. 7.4, where we investigate the

effect of the created strong turbulent fields on jet momentum broadening. The phenomenon, leading to the faster isotropization of the complete hard particle distribution, is of course the same.

In Fig. 7.7 the purely collisional contribution has been extrapolated from the early times when no unstable growth was present. Fig. 7.8 also shows the result obtained on a 128^3 lattice, which corresponds to using $k^* \approx 3.4 p_h$. The rather few collisions with high momentum exchange above $3.4 p_h$ do not change much for the isotropization when we compare to the collisionless case with only particle-field interactions. For the more sensible choice $k^* \approx 1.7 p_h$ the difference is more significant, as expected.

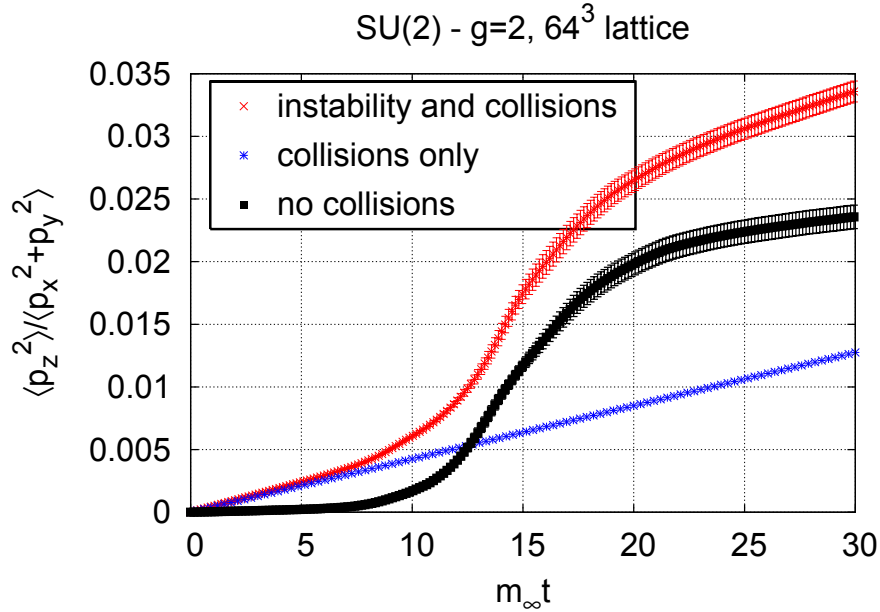


Figure 7.7: Isotropization with time in the case of instability growth and collisions (red cross), particle-field interactions only (black square) and collisions only, extrapolated from the early stage where the particle-field contribution is negligible (blue star).

In summary, the collective field-particle interaction, particularly the instability, dominates the isotropization process compared to the contribution of binary collisions at coupling $g = 2$. When including hard splittings and $gg \leftrightarrow ggg$ processes as in [58], this result is likely to be modified and the instability could be less dominating, or not be the most important process at all. This scenario will have to be studied in the future, leading to the most complete simulation of isotropization and thermalization so far.

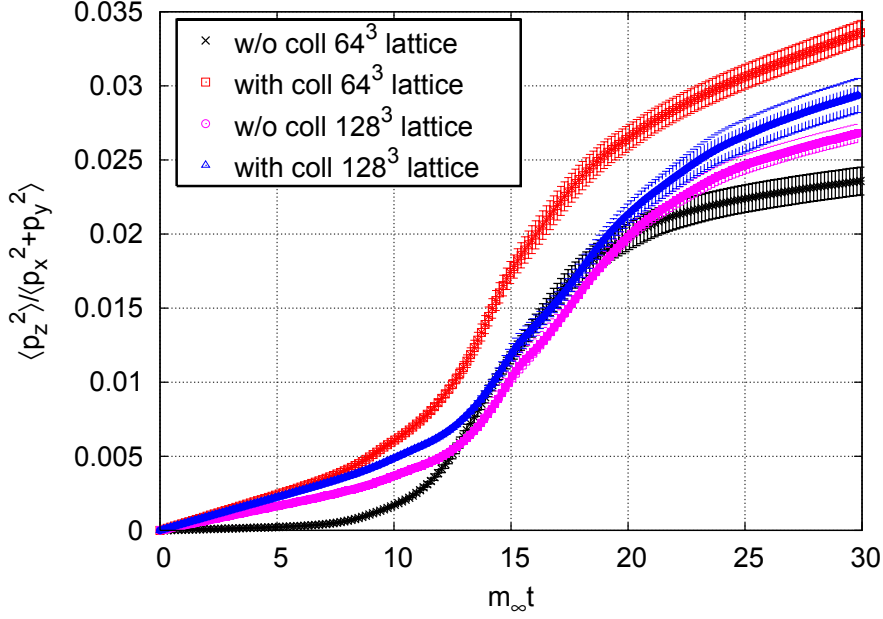


Figure 7.8: Isotropization with time in the case of instability growth with and without collisions on two different lattices. The 64^3 -lattice corresponds to $k^* = 1.7 p_h$, the 128^3 -lattice to $k^* = 3.4 p_h$. In the latter case one can nicely see that the additional high momentum field modes act just like the hard binary collisions in the case of the 64^3 lattice. The few additional large momentum transfer collisions above $k^* = 3.4 p_h$ do not contribute much to the isotropization, as seen from the small difference between the pink (circle) and blue (triangle) curve.

7.4 Collective effects on jet propagation

Let us now investigate the effect of the instability on momentum broadening of jets, including the effect of collisions.

The initial momentum distribution for the hard plasma gluons is again taken to be of the form (7.1). We add additional high momentum particles with $p_x = 12 p_h$ and $p_x = 6 p_h$, respectively, to investigate the broadening in the y and z directions via the variances [222]

$$\kappa_\perp(p_x) := \frac{d}{dt} \langle (\Delta p_\perp)^2 \rangle, \quad (7.3)$$

$$\kappa_z(p_x) := \frac{d}{dt} \langle (\Delta p_z)^2 \rangle. \quad (7.4)$$

In our case $\langle \Delta p_\perp^2 \rangle = \langle p_y^2 \rangle$ and $\langle \Delta p_z^2 \rangle = \langle p_z^2 \rangle$. Since for our initial jet profile we have $\langle (\Delta p_\perp)_0^2 \rangle = \langle (\Delta p_z)_0^2 \rangle$, the ratio κ_z/κ_\perp can be roughly associated with the ratio of jet correlation widths in azimuth and rapidity [223]:

$$\sqrt{\frac{\kappa_z}{\kappa_\perp}} \approx \frac{\langle \Delta \eta \rangle}{\langle \Delta \phi \rangle}. \quad (7.5)$$

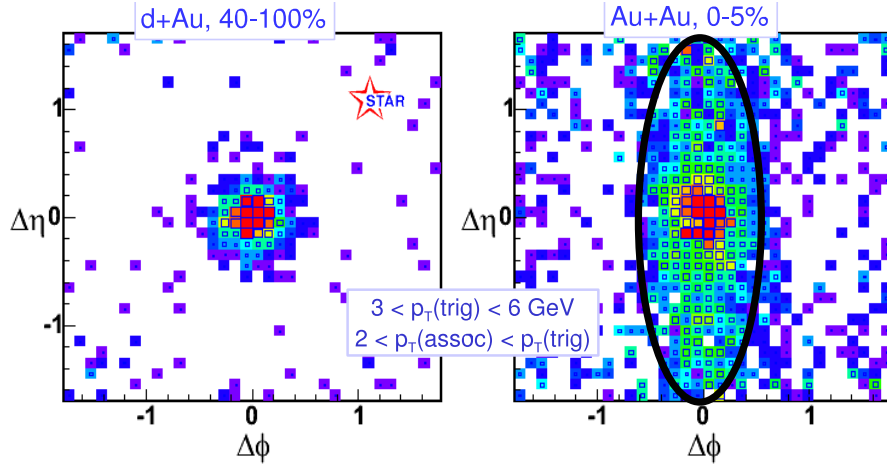


Figure 7.9: Dihadron correlation functions in azimuth $\Delta\phi$ and space-time rapidity $\Delta\eta$, for d+Au and central Au+Au at $\sqrt{s} = 200$ GeV (figure courtesy J. Putschke (STAR), Proceedings of Hard Probes 2006). For comparison, on the right plot an ellipse with eccentricity $e \simeq \frac{\sqrt{8}}{3}$ which corresponds to a ratio $\sqrt{\kappa_z/\kappa_\perp} \sim 3$ is shown [223].

Experimental data on dihadron correlation functions for central Au+Au collisions at $\sqrt{s} = 200$ GeV [224] are consistent with $\langle\Delta\eta\rangle/\langle\Delta\phi\rangle \approx 3$ [223] as is shown in Fig. 7.9. So our result can not quite quantitatively explain the measured ratio. Photon-jet correlation measurements should provide additional insight in the future.

Fig. 7.10 shows the time evolution of $\langle p_\perp^2 \rangle$ and of $\langle p_z^2 \rangle$. The strong growth of the soft fields sets in at about $t \simeq 10 m_\infty^{-1}$ and saturates around $t \simeq 20 m_\infty^{-1}$ due to the finite lattice spacing, as discussed above, as can be seen in Fig. 7.1. Outside of this time interval the ratio $\kappa_z/\kappa_\perp \approx 1$. During the period of instability, however,

$$\frac{\kappa_z}{\kappa_\perp} \approx 2.3, \quad (7.6)$$

for both jet energies shown in Fig. 7.10. We find approximately the same ratio for denser plasmas ($n_g = 20/\text{fm}^3$ and $n_g = 40/\text{fm}^3$). Reducing the number of lattice sites and scaling p_h down to 8 GeV in order to still have the separation scale k^* lie around this scale, gives $\kappa_z/\kappa_\perp \approx 2.1$. However, these latter runs are rather far from the continuum limit and lattice artifacts are significant.

Initially $\xi \equiv \langle p_\perp^2 \rangle / \langle p_z^2 \rangle$ is infinite. However, due to collisions and the backreaction of the fields on the hard particles we find that $\xi \approx 30$ at $t \approx 20 m_\infty^{-1}$. This puts our measured ratio for κ_z/κ_\perp in the same range as those calculated in [223] for heavy quarks to leading-log accuracy, where $\kappa_z/\kappa_\perp \simeq 3.6$ was obtained for $\xi = 10$ and velocity $v = 0.95$. We emphasize that all of these estimates apply to the early pre-equilibrium stage before hydrodynamic evolution sets in.

The explanation for the larger broadening along the beam axis is as follows. In the Abelian case the instability generates predominantly transverse magnetic fields which deflect the particles in the z -direction [225]. In the non-Abelian case, however, on three-dimensional lattices transverse magnetic fields are much less dominant (see, e.g. Fig. 5 in [162]) although

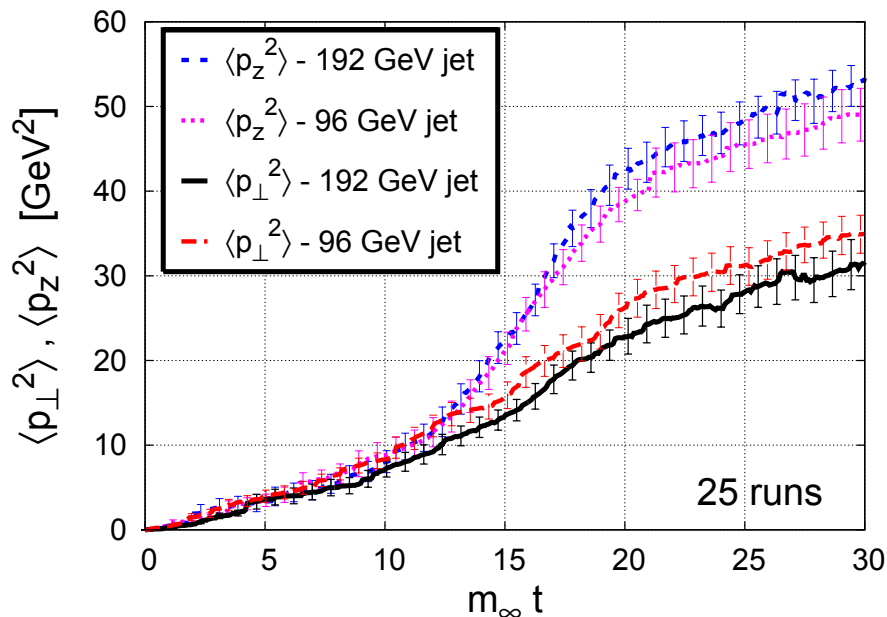


Figure 7.10: Momentum broadening of a jet in the directions transverse to its initial momentum. p_z is directed along the beam axis, p_{\perp} is transverse to the beam. Anisotropic plasma, 64^3 lattice.

they do form larger coherent domains in the transverse plane at intermediate times than E_{\perp} , Fig. 7.11. This is also shown directly in Figs. 7.12 and 7.13. We see that the transverse chromo-magnetic fields form the most coherent domains. The upper right plot in Fig. 7.12 shows that the transverse chromo-magnetic field is directed in the same direction over the whole system, while the upper plots of Fig. 7.13 show that for the transverse component of the chromo-electric field the formation of domains is less pronounced. The opposite behavior is found for the longitudinal components, where the effect is less visible, however.

Longitudinal fields and locally non-zero Chern-Simons number $\sim \text{Tr } \mathbf{E} \cdot \mathbf{B}$ emerge as well. However, the transverse magnetic fields dominate during the time of unstable growth as can be seen in Fig. 7.14. Furthermore, Fig. 7.15 makes it more apparent that also $E_z > B_z$, aside from $B_{\perp} > E_{\perp}$. Hence, the field configurations are such that particles are deflected preferentially in the longitudinal z -direction, which helps restore isotropy.

A third contribution to p_z broadening in an expanding plasma, not considered explicitly here, is due to a longitudinal collective flow field which “blows” the jet fragments to the side [226]. This mechanism is also available for collision dominated plasmas with (nearly) isotropic momentum distribution. However, rather strong flow gradients seem to be required to reproduce the observed broadening of midrapidity jets (the flow velocity has to vary substantially *within* the narrow jet cone). In contrast, color fields will naturally deflect particles with lower momentum by larger angles ($\Delta p \sim E, B$): the jet profile broadens even if the induced radiation is exactly collinear. It is therefore important to determine, experimentally, whether the asymmetric broadening is related to the *macroscopic* collective flow or to an anisotropy of the plasma in the local rest frame.

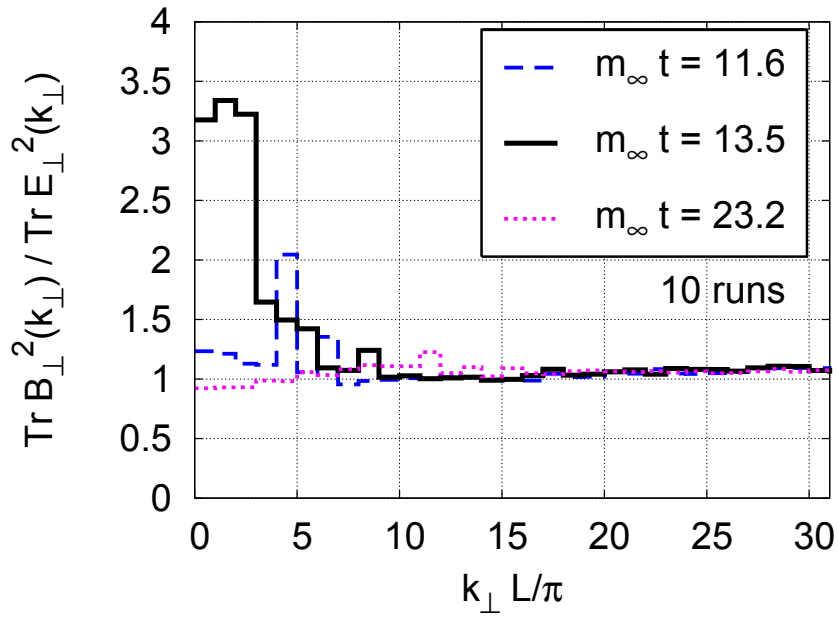


Figure 7.11: Ratios of fourier transforms of the field energy densities (integrated over k_z) at various times; the gauge potentials were transformed to Coulomb gauge.

In summary, we have shown that the collective effects appearing in the anisotropic QGP, as produced in a heavy-ion collision can lead to jet broadening, which is stronger in the longitudinal direction than in azimuth and thereby offer an explanation for the experimentally observed near-side “ridge”, shown in Fig. 7.9.

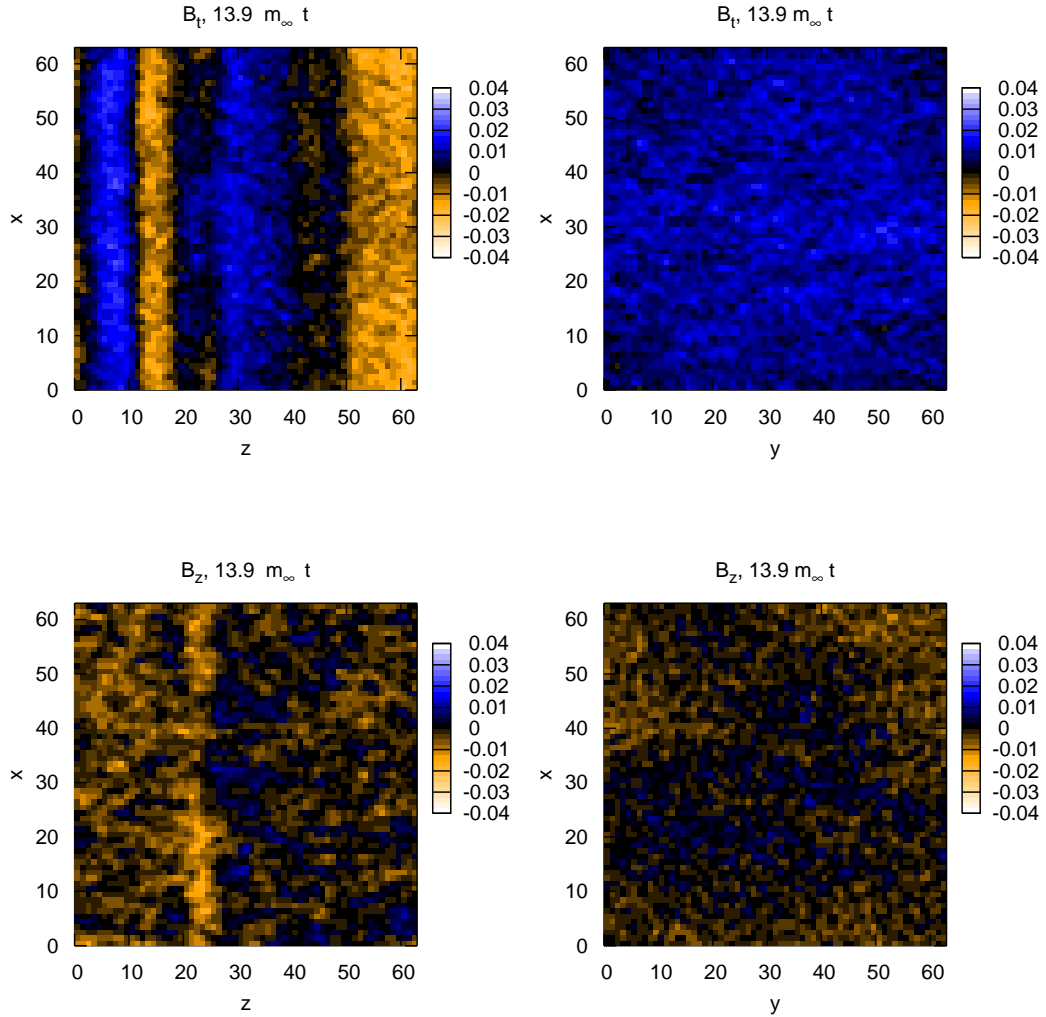


Figure 7.12: Transverse (upper panel) and longitudinal (lower panel) components of the chromo-magnetic field. The position in the third dimension, which is not shown in the plots, is always fixed to 32. We see strong formation of domains in the transverse component, which spread over the whole range in the transverse direction (x - y -plane) - see upper right plot.

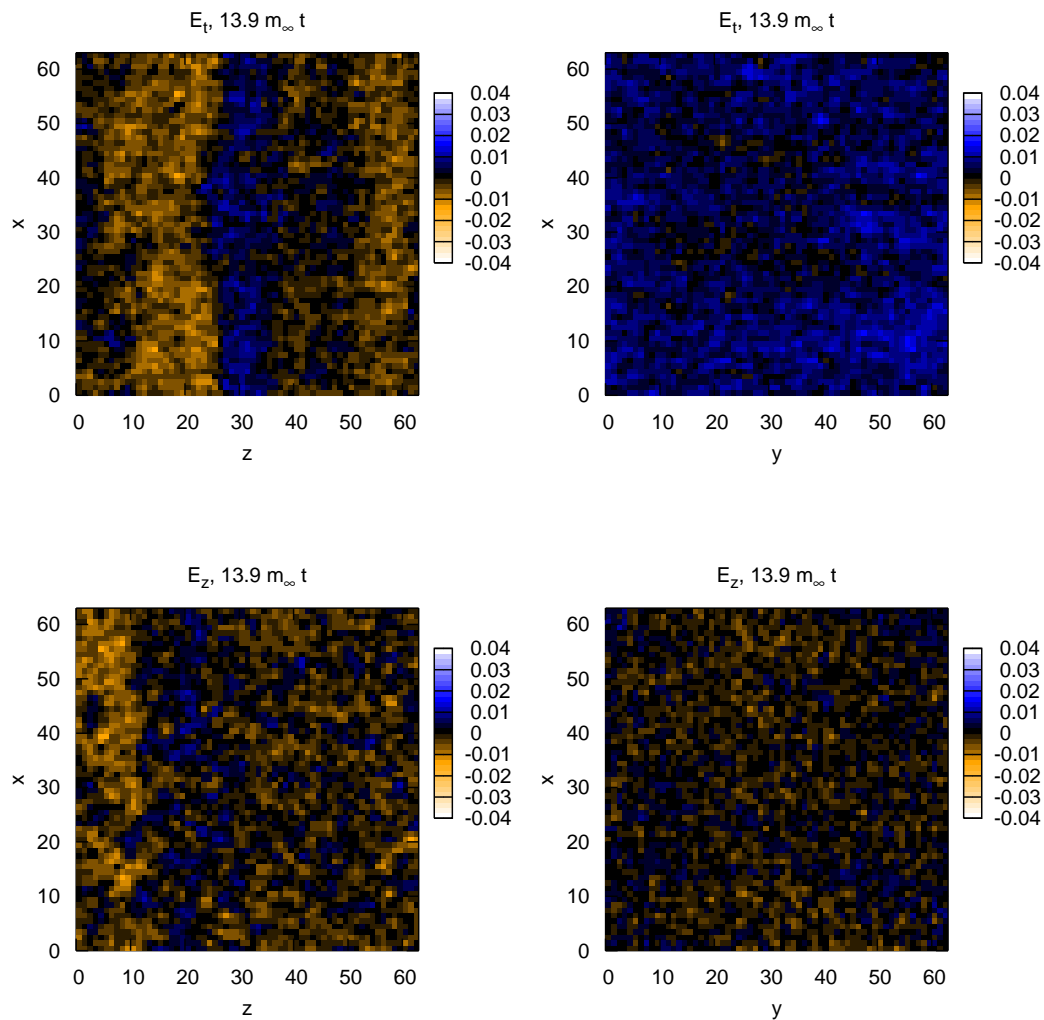


Figure 7.13: Transverse (upper panel) and longitudinal (lower panel) components of the chromo-electric field. The position in the third dimension, which is not shown in the plots, is always fixed to 32. The formation of domains is less pronounced than for the transverse chromo-magnetic field.

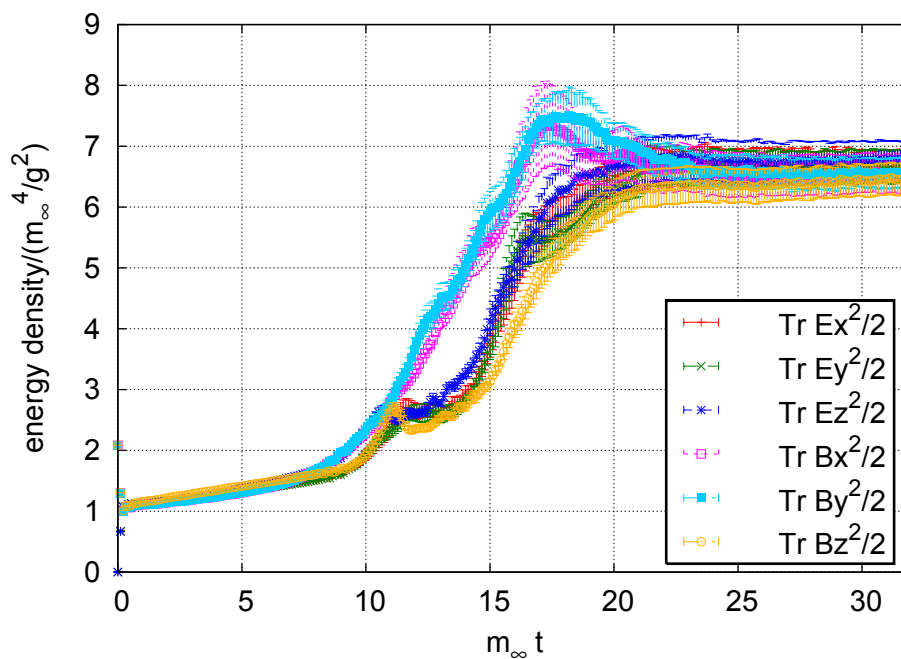


Figure 7.14: Energy density in the different field components.

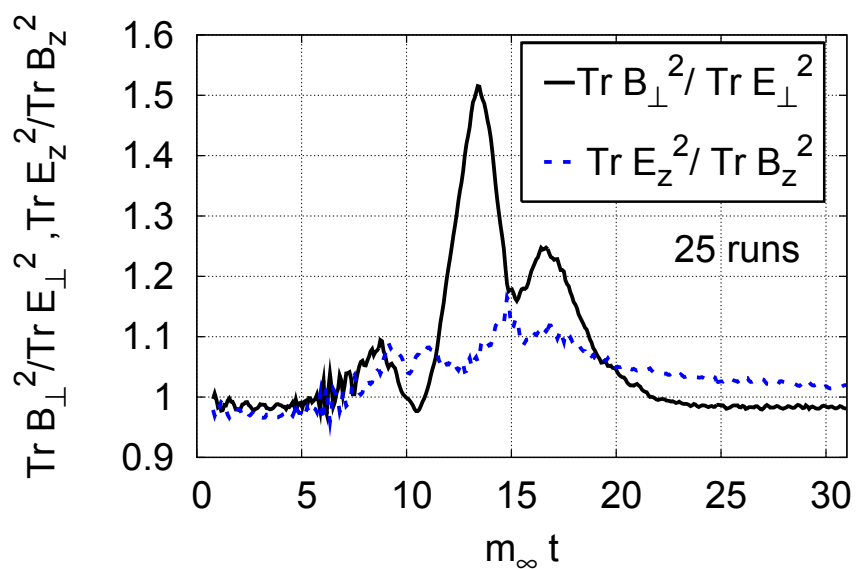


Figure 7.15: Ratios of field energy densities.

8 Fermionic collective modes of an anisotropic quark-gluon plasma

After having discussed the gluonic collective modes of the quark-gluon plasma in great detail, we now turn to the fermionic modes and concentrate on the investigation of whether they can be unstable too. We show analytically for two special cases as well as numerically for the general case that there are no fermionic instabilities. This result is similar to the case of the fermionic collective modes in a two-stream system [227], where it was also found that fermionic instabilities do not exist.

The absence of unstable fermionic modes is expected on physical grounds due to the fact that fermion exclusion precludes the condensation of modes; however, it could be possible that, through pairing, fermions could circumvent this as has been predicted [228, 229, 230, 231, 232] and demonstrated [233] in superfluid condensation of cold fermionic atoms. However, this would require a description in terms of fermionic bound or composite states which are not included at the level of hard loops so we do not expect to find any fermionic condensate-like instabilities using this approximation. This is verified via an explicit contour integration of the inverse hard-loop quark propagator for the two special cases in which we can obtain analytic expressions for the self-energy. The special cases considered analytically are (a) the case when the wave vector of the collective mode is parallel to the anisotropy direction with arbitrary oblate anisotropy and (b) for all angles of propagation in the limit of an infinitely oblate anisotropy.¹

8.1 Quark self-energy in an anisotropic system

The integral expression for the retarded quark self-energy for an anisotropic system has been obtained previously [125] and is given by

$$\Sigma(K) = \frac{C_F}{4} g^2 \int_{\mathbf{p}} \frac{f(\mathbf{p})}{|\mathbf{p}|} \frac{P \cdot \gamma}{P \cdot K}, \quad (8.1)$$

where $C_F \equiv (N_c^2 - 1)/2N_c$, and $f(\mathbf{p}) \equiv 2(n(\mathbf{p}) + \bar{n}(\mathbf{p})) + 4n_g(\mathbf{p})$. To obtain Eq. (8.1) one computes the leading-order quark self-energy diagram, assuming that (a) the quarks are massless, (b) the external fermion momentum is soft, $k_0 \sim k \sim g p_{\text{hard}}$, (c) the momentum carried by the internal lines is hard, $p_0 \sim p \sim p_{\text{hard}}$, and (d) the distribution function f is symmetric in momentum space, $f(\mathbf{p}) = f(-\mathbf{p})$. The hard scale p_{hard} can be identified with the temperature T in the case of thermal equilibrium but represents an arbitrary scale present in the non-equilibrium system, e.g. the nuclear saturation scale Q_s .

¹This chapter is based on the work published in [234]

To simplify the calculation we follow Ref. [63] and again choose a distribution function $f(\mathbf{p})$ given by

$$f(\mathbf{p}) = f_\xi(\mathbf{p}) = N(\xi) f_{\text{iso}} \left(\sqrt{\mathbf{p}^2 + \xi(\mathbf{p} \cdot \hat{\mathbf{n}})^2} \right). \quad (8.2)$$

Again, note that the appearance of $N(\xi)$ is not relevant for our considerations, but it allows for an easier comparison of systems with different strong anisotropies. Without it, every calculation in this section works analogously up to constant multiplicative factors. Here we use $N(\xi) = \sqrt{1 + \xi}$. Using Eq. (8.2) and performing the change of variables

$$\tilde{p}^2 = p^2 (1 + \xi(\mathbf{v} \cdot \hat{\mathbf{n}})^2), \quad (8.3)$$

we obtain

$$\Sigma(K) = m_q^2 \sqrt{1 + \xi} \int \frac{d\Omega}{4\pi} (1 + \xi(\hat{\mathbf{p}} \cdot \hat{\mathbf{n}})^2)^{-1} \frac{P \cdot \gamma}{P \cdot K}, \quad (8.4)$$

where

$$m_q^2 = \frac{g^2 C_F}{8\pi^2} \int_0^\infty dp p f_{\text{iso}}(p). \quad (8.5)$$

We then decompose the self-energy into four contributions

$$\Sigma(K) = \gamma^0 \Sigma_0 + \boldsymbol{\gamma} \cdot \boldsymbol{\Sigma}. \quad (8.6)$$

The fermionic collective modes are determined by finding all four-momenta for which the determinate of the inverse propagator vanishes

$$\det S^{-1} = 0, \quad (8.7)$$

where

$$\begin{aligned} iS^{-1}(P) &= \gamma^\mu p_\mu - \Sigma, \\ &\equiv \gamma^\mu A_\mu. \end{aligned} \quad (8.8)$$

with $A(K) = (k_0 - \Sigma_0, \mathbf{k} - \boldsymbol{\Sigma})$. Using the fact that $\det(\gamma^\mu A_\mu) = (A^\mu A_\mu)^2$ and defining $A_s^2 = \mathbf{A} \cdot \mathbf{A}$ we obtain

$$A_0 = \pm A_s. \quad (8.9)$$

In practice, we can define the z -axis to be in the $\hat{\mathbf{n}}$ direction and use the azimuthal symmetry to restrict our consideration to the $x-z$ plane. In this case we need only three functions instead of four

$$\begin{aligned} \Sigma_0(w, k, \theta_n, \xi) &= \frac{1}{2} m_q^2 \sqrt{1 + \xi} \int_{-1}^1 dx \frac{R(w - k \cos \theta_n x, k \sin \theta_n \sqrt{1 - x^2})}{1 + \xi x^2}, \\ \Sigma_x(w, k, \theta_n, \xi) &= \frac{1}{2} m_q^2 \sqrt{1 + \xi} \int_{-1}^1 dx \frac{\sqrt{1 - x^2} S(w - k \cos \theta_n x, k \sin \theta_n \sqrt{1 - x^2})}{1 + \xi x^2}, \\ \Sigma_z(w, k, \theta_n, \xi) &= \frac{1}{2} m_q^2 \sqrt{1 + \xi} \int_{-1}^1 dx \frac{x R(w - k \cos \theta_n x, k \sin \theta_n \sqrt{1 - x^2})}{1 + \xi x^2}, \end{aligned} \quad (8.10)$$

where

$$\begin{aligned} R(a,b) &= \left(\sqrt{a+b+i\epsilon} \sqrt{a-b+i\epsilon} \right)^{-1}, \\ S(a,b) &= \frac{1}{b} [aR(a,b) - 1]. \end{aligned} \quad (8.11)$$

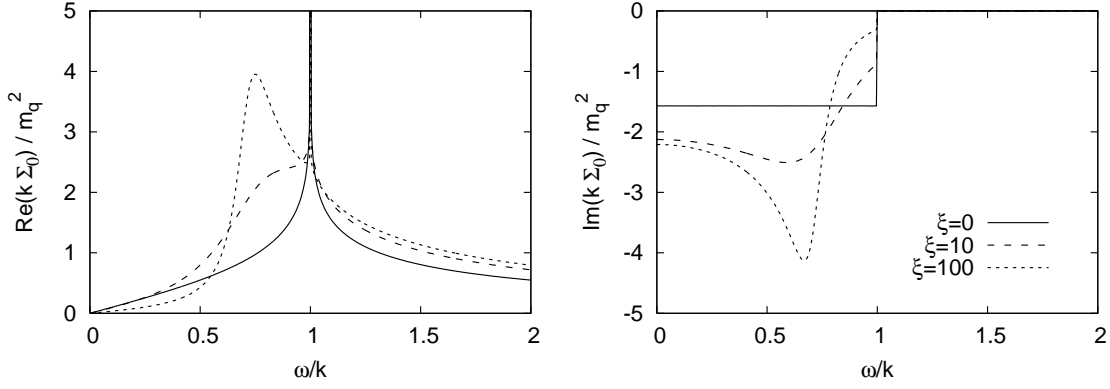


Figure 8.1: Real and imaginary part of Σ_0 as a function of ω/k for $\theta_n = \pi/4$ and $\xi = \{0, 10, 100\}$.

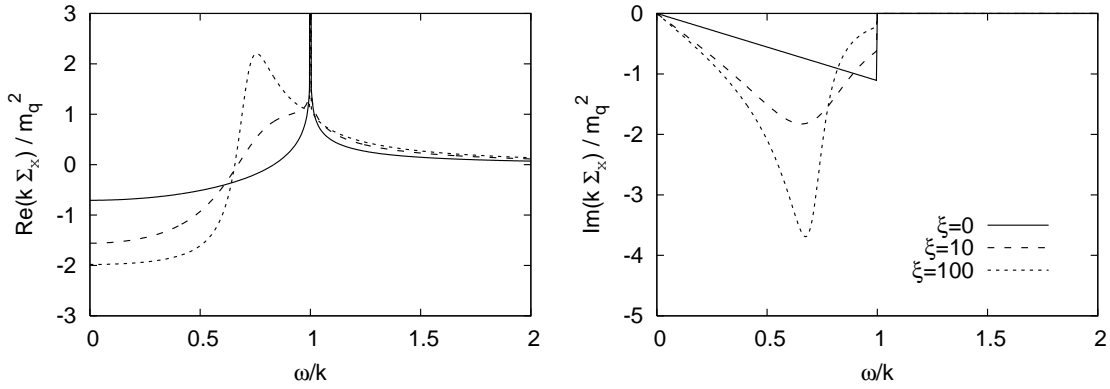


Figure 8.2: Real and imaginary part of Σ_x as a function of ω/k for $\theta_n = \pi/4$ and $\xi = \{0, 10, 100\}$.

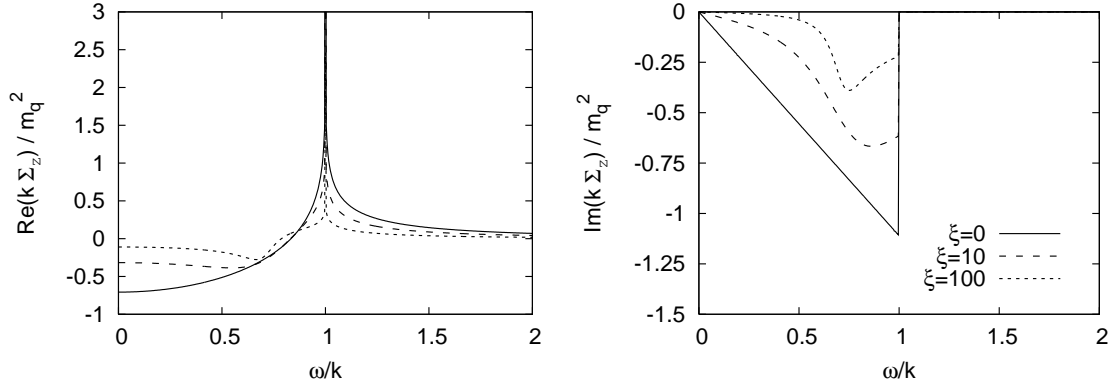


Figure 8.3: Real and imaginary part of Σ_z as a function of ω/k for $\theta_n = \pi/4$ and $\xi = \{0, 10, 100\}$.

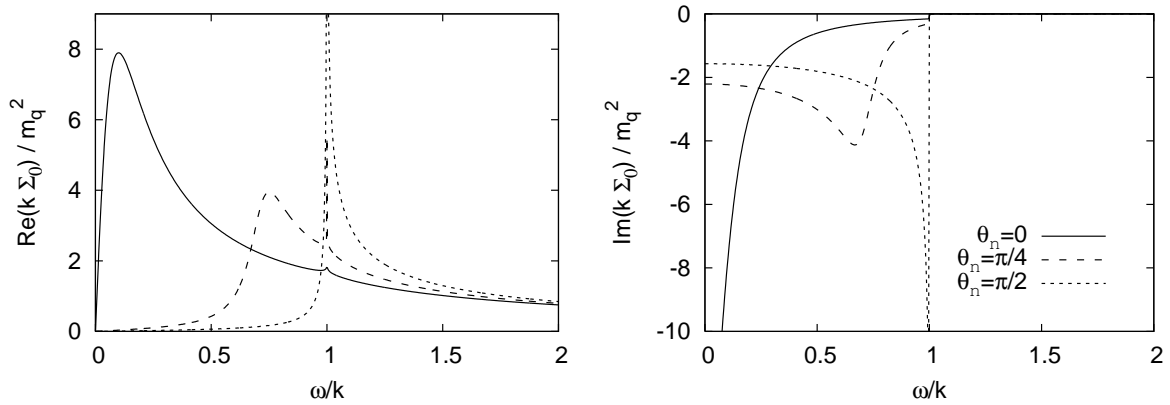


Figure 8.4: Real and imaginary part of Σ_0 as a function of ω/k for $\xi = 100$ and $\theta_n = \{0, \pi/4, \pi/2\}$.

In Figs. 8.1 through 8.3 we plot the real and imaginary parts of the quark self-energies Σ_0 , Σ_x , and Σ_z for $\xi = \{0, 10, 100\}$. From these Figures we see that the spacelike quark self-energy is strongly affected by the presence of an anisotropy with a peak appearing at $\omega/k = \sin \theta_n$ for strong anisotropies. To further illustrate this in Fig. 8.4 we have plotted Σ_0 for $\xi = 100$ and $\theta_n = \{0, \pi/4, \pi/2\}$. From this Figure we see that there is a large directional dependence of the spacelike quark self-energy. Note that this could have a measurable impact on quark-gluon plasma photon production during the early stages of evolution since screening of infrared divergences in leading order photon production amplitudes requires as input the hard-loop fermion propagator for spacelike momentum. We return to this point in Chapter 9 and calculate photon emission from an anisotropic quark-gluon plasma. Assuming the necessary measurements of the rapidity dependence of the thermal photon spectrum could be performed, photon emission could provide an excellent measure of the degree of momentum-space anisotropy in the partonic distribution functions at early stages of a heavy-ion collision.

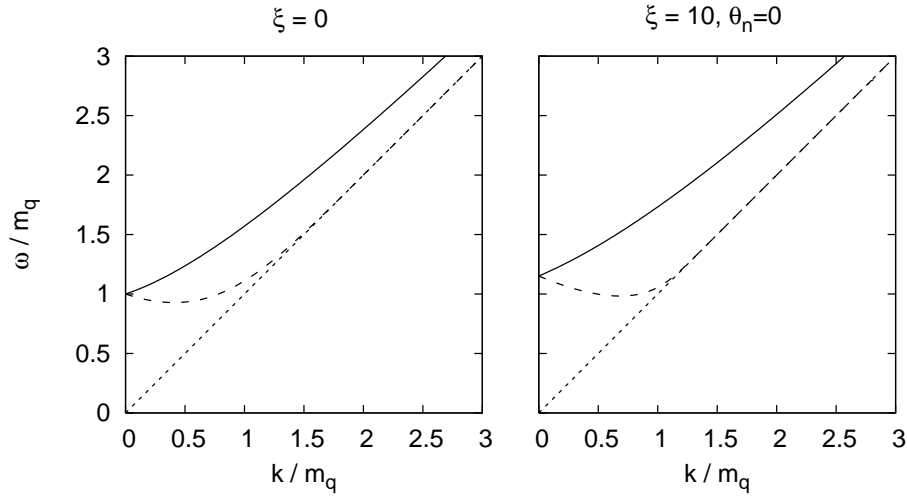


Figure 8.5: Fermionic dispersion relations for the isotropic case and the case $\xi = 10$ and $\theta_n = 0$.

For general ξ and θ_n we have to evaluate the integrals given in Eq. (8.10) numerically. To find the collective modes we then numerically solve the fermionic dispersion relations given by Eq. (8.9). As in the isotropic case, for real timelike momenta ($|\omega| > |k|$, $\text{Im}(\omega/k) = 0$) there are two stable quasiparticle modes which result from choosing either plus or minus in Eq. (8.9).² The results for the isotropic case ($\xi = 0$) and the case where $\xi = 10$ are shown in Fig. 8.5

8.2 Analytical investigation

We have looked for modes in the upper- and lower-half planes and numerically we find none. In the following we explicitly count the number of modes using complex contour integration and demonstrate that there are no unstable collective modes in two special cases.

8.2.1 Special case: $\mathbf{k} \parallel \hat{\mathbf{n}}$

Let us consider the special case where the momentum of the collective mode is in the direction of the anisotropy $\mathbf{k} \parallel \hat{\mathbf{n}}$, i.e., $\theta_n = 0$. In this case the integrals in Eq. (8.10) can

²Note that there are four solutions to the dispersion relations since each solution exists at both positive and negative ω .

be evaluated analytically. Σ_x becomes zero, while the other components read

$$\begin{aligned}\Sigma_0(\omega, k, \theta_n = 0, \xi) &= \frac{1}{2}m_q^2 \frac{\sqrt{1+\xi}}{\xi\omega^2 + k^2} \left[2\sqrt{\xi}\omega \arctan \sqrt{\xi} + k \ln \left(\frac{\omega+k}{\omega-k} \right) \right] \\ \Sigma_z(\omega, k, \theta_n = 0, \xi) &= \frac{1}{2}m_q^2 \frac{\sqrt{1+\xi}}{\xi\omega^2 + k^2} \left[-2\frac{1}{\sqrt{\xi}}k \arctan \sqrt{\xi} + \omega \ln \left(\frac{\omega+k}{\omega-k} \right) \right].\end{aligned}\quad (8.12)$$

Eq. (8.9) simplifies to

$$\omega - \Sigma_0 = \pm(k - \Sigma_z). \quad (8.13)$$

Nyquist analysis

We now show analytically for this special case that unstable modes do not exist. This is done by a NYQUIST analysis of the following function:

$$f_{\mp}(\omega, k, \xi) = \omega - \Sigma_0(\omega, k, \xi) \mp [k - \Sigma_z(\omega, k, \xi)]. \quad (8.14)$$

In practice, that means that we evaluate the contour integral

$$\frac{1}{2\pi i} \oint_C dz \frac{f'_{\mp}(z)}{f_{\mp}(z)} = N - P, \quad (8.15)$$

which gives the numbers of zeros N minus the number of poles P of f_{\mp} in the region encircled by the closed path C . In Eq. (8.15) and in the following, we write the functions f_{\mp} in terms of $z = \omega/k$ and for clarity do not always state the explicit dependence of f_{\mp} on k and ξ . Choosing the path depicted in Fig. 8.6, which excludes the logarithmic cut for real z with $z^2 < 1$ of the function (8.14), leads to $P = 0$ and the left hand side of Eq. (8.15) equals the number of modes N . Evaluation of the respective pieces of the contour C for each f_- and f_+ leads to

$$N_{\mp} = 1 + 0 + 0 + 1 = 2, \quad (8.16)$$

such that for the total number we get is $N = N_- + N_+ = 4$, which corresponds to the stable modes (two for positive ω and two for negative ω). The four contributions in (8.16) are the following:

1. The first 1 results from integration along the large circle at $|z| \gg 1$.
2. The first zero is the contribution from the path connecting the large circle with the contour around $z = \pm 1$.
3. The second zero stems from the two small half-circles around $z = \pm 1$
4. The last 1 is obtained from integration along the straight lines running infinitesimally above and below the cut between $z = -1$ and $z = 1$. See below for details on this integration.

The last contribution can be evaluated using

$$\int_{-1+i\epsilon}^{1+i\epsilon} dz \frac{f'_{\mp}(z)}{f_{\mp}(z)} = \ln \frac{f_{\mp}(1+i\epsilon)}{f_{\mp}(-1+i\epsilon)} + 2\pi i n, \quad (8.17)$$

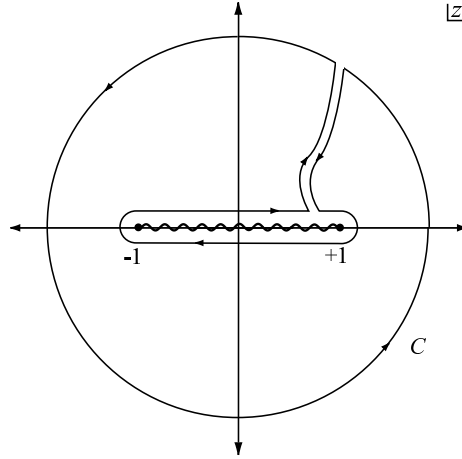


Figure 8.6: Contour C in the complex z -plane used for the Nyquist analysis.

for the line above and the corresponding expression for the line below the cut. n is the number of times the function f_{\mp} crosses the logarithmic cut located on the real axis, running from zero to minus infinity. This cut is due to the appearance of the logarithm on the right hand side of Eq. (8.17). In the sum of the line integrations above and below the cut diverging contributions from the first part on the right hand side of Eq. (8.17) cancel and we are left with a contribution of $2\pi i$ for each function. Furthermore it is necessary to show that neither f_- nor f_+ crosses the cut. The proof is given in some detail for f_- and is performed analogously for f_+ . From Eq. (8.14) we find for f_- :

$$f_-(z, k, \xi) = z - 1 + \frac{\sqrt{1+\xi}}{2(1+\xi x^2)} \frac{1}{k^2} \left[-2 \left(z + \frac{1}{\xi} \right) \sqrt{\xi} \arctan \sqrt{\xi} + (z-1) \ln \left(\frac{z+1}{z-1} \right) \right]. \quad (8.18)$$

We want to study whether this function crosses the real axis in the range $\text{Re}[z] \in [-1, 1]$ for $\text{Im}[z] \rightarrow 0$, i.e., whether the imaginary part of f_- changes sign in that range. On the straight line infinitesimally above the cut the imaginary part of f_- is given by

$$\text{Im} \left[\lim_{\epsilon \rightarrow 0} f_-(x + i\epsilon, k, \xi) \right] = -\frac{\pi}{2} \frac{\sqrt{1+\xi}(x-1)}{k^2(1+\xi x^2)}, \quad (8.19)$$

for real x . It is only zero for $x = 1$, which means that the function f_- can not cross but merely touch the cut within the limits of the integration. On the straight line below the cut we get the same result (8.19) with a minus sign. For f_+ , we find that the imaginary part in the regarded range only becomes zero for $x = -1$, which means that the logarithmic cut is not crossed within $[-1, 1]$ either. Hence we have proved for the case $\mathbf{k} \parallel \hat{\mathbf{n}}$ that there are no more solutions than the four stable modes. In particular we have shown that unstable fermionic modes can not exist.

8.2.2 Large- ξ limit

In the extremely anisotropic case where $\xi \rightarrow \infty$ the self-energies for arbitrary angle θ_n can be calculated explicitly. The distribution function (8.2) becomes [235]

$$\lim_{\xi \rightarrow \infty} f_\xi(\mathbf{p}) = \delta(\hat{\mathbf{p}} \cdot \hat{\mathbf{n}}) \int_{-\infty}^{\infty} dx f_{\text{iso}}\left(p\sqrt{1+x^2}\right). \quad (8.20)$$

With $\hat{\mathbf{n}}$ in the z -direction this implies that \mathbf{p} lies in the x - y -plane only. As in Section 8.1, due to azimuthal symmetry, we consider the case where \mathbf{k} lies in the x - z -plane only. Using (8.20) we obtain from Eqs. (8.10)

$$\begin{aligned} \Sigma_0(\omega, k, \theta_n) &= \frac{\pi}{2} m_q^2 \frac{1}{\sqrt{\omega + k \sin \theta_n} \sqrt{\omega - k \sin \theta_n}}, \\ \Sigma_x(\omega, k, \theta_n) &= \frac{\pi}{2k \sin \theta_n} m_q^2 \left(\frac{\omega}{\sqrt{\omega + k \sin \theta_n} \sqrt{\omega - k \sin \theta_n}} - 1 \right). \end{aligned} \quad (8.21)$$

Since p_z is always zero, Σ_z vanishes. Eq. (8.9) now becomes

$$\omega - \Sigma_0 = \pm \sqrt{(k_x - \Sigma_x)^2 + k_z^2}. \quad (8.22)$$

Nyquist analysis

Again, we only find four stable modes and will now show analytically that these are the only solutions in the large ξ -limit for arbitrary angle θ_n . The cut resulting from the complex square roots in (8.21) can be chosen to lie between $z = -\sin \theta_n$ and $z = \sin \theta_n$ on the real axis. The NYQUIST analysis can then be performed analogously to that in Section 8.2.1 with the contour in Fig. 8.6 adjusted such that the inner path still runs infinitesimally close around the cut. Using this path in the evaluation of Eq. (8.15) for the functions

$$f_{\mp}(\omega, k, \theta_n) = \omega - \Sigma_0 \mp \sqrt{(k_x - \Sigma_x)^2 + k_z^2}, \quad (8.23)$$

we find the number of solutions to Eq. (8.22) to be

$$N_{\mp} = 1 + 0 + \frac{1}{4} + \frac{1}{4} + \frac{1}{2} = 2, \quad (8.24)$$

so that again there are $N = N_+ + N_- = 4$ solutions, which are the known stable modes. The decomposition in (8.24) is done as follows:

1. The first contribution to N_{\mp} comes from integration along the large outer circle at $|z| \gg 1$.
2. The zero stems from the paths connecting the outer and the inner circle.
3. The two contributions of $1/4$ result from integrations along the small circles around $-\sin \theta_n$ and $\sin \theta_n$.
4. The last contribution of $1/2$ comes from integration along the straight lines running infinitesimally close above and below the cut. We discuss this part in further detail below.

The last contribution can be obtained using Eq. (8.17). For the evaluation of the limit $\epsilon \rightarrow 0$ it is essential to note that the f_{\mp} behave like $\ln \epsilon$ or $1/(\ln \epsilon)$ (depending on which function is evaluated on which line) and are both negative as $\epsilon \rightarrow 0$. This results in a contribution of $+i\pi$ for each function and integration, because in all cases the imaginary part of both functions can be shown to be positive in the regarded limit. All other contributions, including the diverging parts $\pm \ln(-\ln \epsilon)$ cancel in the sum of the results from the upper and lower line.

Again, we need to show that the functions f_{\mp} do not cross the logarithmic cut for $z \in [-\sin \theta_n, \sin \theta_n]$, i.e., that $n = 0$ in Eq. (8.17). It is possible to find an analytic expression for the imaginary part of f_{\mp} using

$$\text{Im} \sqrt{x + iy} = \frac{1}{\sqrt{2}} \text{sgn}(y) \sqrt{\sqrt{x^2 + y^2} - x}, \quad (8.25)$$

for the imaginary part of the square root appearing in (8.23) with real x and y . Then the only solutions to

$$\text{Im} f_{\mp}(z) = 0 \quad (8.26)$$

are found analytically to be $\text{Re}(z) = \sin \theta_n$ and $\text{Re}(z) = -\sin \theta_n$ for f_- and f_+ respectively. This means that the cut is not crossed during the integration along the straight lines and that the contribution from this piece is in fact $1/2$.

8.3 Summary

In this chapter we have extended the exploration of the collective modes of an anisotropic quark-gluon plasma by studying the quark collective modes. Specifically, we derived integral expressions for the quark self-energy for arbitrary anisotropy and evaluated these numerically using the momentum-space rescaling (8.2). In the direct numerical calculation we found only real timelike fermionic modes and no unstable modes. Additionally using complex contour integration we have proven analytically in the cases (a) when the wave vector of the collective mode is parallel to the anisotropy direction with arbitrary oblate anisotropy and (b) for all angles of propagation in the limit of an infinitely oblate anisotropy that there are no fermionic unstable modes.

9 Photon production from an anisotropic quark-gluon plasma

Wo viel Licht ist, ist starker Schatten - doch wär's mir
willkommen. Wollen sehn, was es gibt.

*Götz von Berlichingen, Erster Aufzug.
Jagsthausen. Götzens Burg. Götz.*
Johann Wolfgang von Goethe (1749-1832)

In this chapter we calculate photon production from a quark-gluon plasma which is anisotropic in momentum space including the COMPTON scattering, $q(\bar{q})g \rightarrow q(\bar{q})\gamma$, and annihilation, $q\bar{q} \rightarrow g\gamma$, processes. We show that for a quark-gluon plasma which has a momentum-space anisotropy the photon production rate has an angular dependence which is peaked transverse to the beamline. Convolving this with a model for the fireball evolution, we calculate the total photon yield and compare to other contributions like prompt photons and those from jet fragmentation. We discuss to which extent and under which circumstances the results can be used to experimentally determine the degree of momentum-space isotropy of a quark-gluon plasma produced in relativistic heavy-ion collisions.¹

9.1 Medium photon production rate

To lowest order photons are produced via annihilation and COMPTON scattering processes

$$q + \bar{q} \rightarrow g + \gamma, \quad (9.1)$$

$$q(\bar{q}) + g \rightarrow q(\bar{q}) + \gamma. \quad (9.2)$$

We do not include the bremsstrahlung contribution which in an equilibrium plasma also contributes at leading order in the coupling constant due to enhancements from collinear photon radiation [89, 90, 91, 92]. This contribution has been omitted because it is currently not known how to resolve the problem that the presence of unstable modes causes unregulated singularities to appear in matrix elements which involve soft gluon exchange. Recent work [223] has suggested that these singularities could be shielded by next-to-leading order (NLO) corrections to the gluonic polarization tensor, however, the detailed evaluation of these NLO corrections has not been performed to date. Absent explicit calculation, our naive expectation would be that these NLO corrections would yield similar angular dependence as the annihilation and COMPTON scattering contributions since they are also peaked at nearly collinear angles.

¹This chapter is based on the work published in [236]

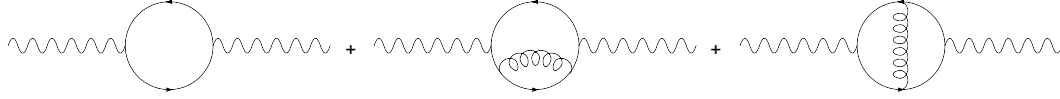


Figure 9.1: One- and two-loop contributions to the photon self energy in QCD

In a thermal medium the production rate is given by [237, 238, 95, 87]

$$E \frac{dR}{d^3q} = -\frac{2}{(2\pi)^3} \text{Im} \Pi_{\mu}^{\mu} \frac{1}{e^{E/T} - 1}, \quad (9.3)$$

with the retarded photon self energy $\Pi_{\mu\nu}$. It is valid to all orders in the strong interaction α_s and to leading order in e^2 , as in its derivation it was assumed that the produced photons do not interact with the medium after they have been produced. For an anisotropic system, we adopt the KELDysh formulation of quantum field theory, which is appropriate for systems away from equilibrium [239, 240, 241]. In this formalism both propagators and self energies have a 2×2 matrix structure. The components (12) and (21) of the self-energy matrices are related to the emission and absorption probability of the particle species under consideration [241, 242, 243]. Due to the almost complete lack of photon absorbing back reactions, the rate of photon emission can be expressed as [244]

$$E \frac{dR}{d^3q} = \frac{i}{2(2\pi)^3} \Pi_{12\mu}^{\mu}(Q), \quad (9.4)$$

from the trace of the (12)-element $\Pi_{12} = \Pi^{<}$ of the photon-polarization tensor.

If the photon self energy is approximated by carrying out a loop expansion to some finite order then Eq. (9.3) is equivalent to a description in terms of relativistic kinetic theory. Generally, when \mathcal{M} is the amplitude for a reaction of m particles to n particles plus one photon then the contribution of this reaction to the differential photon production rate is given by

$$\mathcal{N} \int d\Phi (2\pi)^4 \delta(p_{\text{in}}^{\mu} - p_{\text{out}}^{\mu}) |\mathcal{M}|^2, \quad (9.5)$$

with the phase space $d\Phi$ given by a factor of $d^3p/(2p(2\pi)^3)$ for each particle, a BOSE-EINSTEIN or FERMI-DIRAC distribution for each particle in the initial state and a BOSE enhancement or PAULI suppression factor for each particle in the final state. The overall degeneracy factor depends on the specific reaction. Expanding the self energy up to L loops is equivalent to computing the contribution from all reactions with $m+n \leq L+1$, with each amplitude calculated to order g^{L-1} . In our case this can be seen when applying cutting rules to the loop diagrams shown in Fig. 9.1, which yields graphs corresponding to the following processes: Cutting the one-loop diagram gives zero for an on-shell photon since the process $q\bar{q} \rightarrow \gamma$ has no phase space. Certain cuts of the two-loop diagrams give order g^2 corrections to this nonexistent reaction. Other cuts correspond to the reactions $q\bar{q} \rightarrow g\gamma$, $qg \rightarrow q\gamma$ and $\bar{q}g \rightarrow \bar{q}\gamma$, the annihilation and COMPTON scattering processes discussed above and shown in Figs. 9.2 and 9.3. Following the prescription (9.5), we find the contributions of these

processes to the rate to be

$$E \frac{dR_i}{d^3q} = \mathcal{N} \int_{\mathbf{k}_1} f_1(\mathbf{k}_1) \int_{\mathbf{k}_2} f_2(\mathbf{k}_2) \int_{\mathbf{k}_3} (1 \pm f_3(\mathbf{k}_3)) (2\pi)^4 \delta^{(4)}(K_1 + K_2 - Q - K_3) |\overline{\mathcal{M}_i}|^2, \quad (9.6)$$

with $\int_{\mathbf{k}_i} = \int d^3k_i / (2k_i (2\pi)^3)$. The f_i are the appropriate distribution functions (BOSE-EINSTEIN or FERMI-DIRAC in equilibrium) and there is either a BOSE enhancement or PAULI blocking term depending on the nature of the strongly interacting particle in the final state, as mentioned above. Putting in the right distribution functions, the appropriate matrix element, and the correct degeneracy factor \mathcal{N} yields the annihilation and COMPTON scattering contribution.

Let us calculate \mathcal{N} : For the annihilation process we have a quark and an anti-quark in the initial state, which leads to a color degeneracy of $3 \cdot 3 = 9$, furthermore, we have to multiply by 4 for the spin degeneracy, and summing over u and d quarks yields a factor of

$$\sum_q e_q^2 = \left(\frac{1}{3}\right)^2 + \left(\frac{2}{3}\right)^2 = \frac{5}{9}.$$

This makes an \mathcal{N} of $9 \cdot 4 \cdot 5/9 = 20$. For the COMPTON scattering part we have a quark and a gluon in the initial state, meaning that we have to multiply by $3 \cdot 8 = 24$, we take times 4 for initial spins/helicities and times 2 for both quark and anti quark scattering, and again have a factor of $5/9$ from the sum over the squares of the quark charges. This yields an \mathcal{N} of $24 \cdot 4 \cdot 2 \cdot 5/9 = 320/3$.

9.1.1 Cross sections

We now calculate the cross sections for the two processes (9.1,9.2) in vacuum, giving the matrix elements needed to compute (9.6). We have to evaluate the FEYNMAN diagrams shown in Figs. 9.2 and 9.3

We go through the calculation of the COMPTON scattering process in detail and give the result of the analogous calculation of the annihilation diagram.

QED case

For simplicity let us first consider the QED process

$$\gamma e^- \rightarrow \gamma e^-, \quad (9.7)$$

which apart from the color factors that we shall discuss later is equivalent to the process (9.2). We set the electron mass to zero as we shall do with the quark masses. Then, using the FEYNMAN rules for QED (see [245]), the amplitudes of the two diagrams in Fig. 9.3 read:

$$-i\mathcal{M}_1 = \bar{u}^{(s')}(K_3) \left[\varepsilon_\mu (ie\gamma^\mu) \frac{i(\not{K}_1 - \not{Q})}{(K_1 - Q)^2} (ie\gamma^\nu) \varepsilon_\nu'^* \right] u^{(s)}(K_1), \quad (9.8)$$

$$-i\mathcal{M}_2 = \bar{u}^{(s')}(K_3) \left[\varepsilon_\nu'^* (ie\gamma^\nu) \frac{i(\not{K}_1 + \not{K}_2)}{(K_1 + K_2)^2} (ie\gamma^\mu) \varepsilon_\mu \right] u^{(s)}(K_1), \quad (9.9)$$

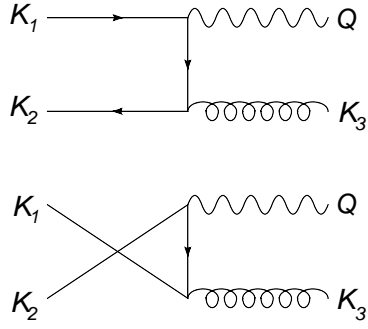


Figure 9.2: Annihilation diagram with momentum labels. All four-momenta indicated flow to the right so that $K_1 + K_2 = Q + K_3$.

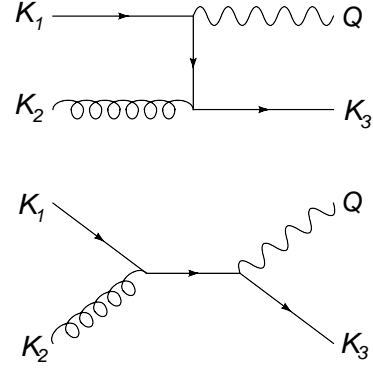


Figure 9.3: COMPTON diagrams for hard photon production with momentum labels. All four-momenta indicated flow to the right so that $K_1 + K_2 = Q + K_3$. Anti-quark graphs are not shown but are included in the calculation.

where u is the positive energy four-spinor solution of the DIRAC equation with spin index $s = \{1, 2\}$, $\bar{u} = u^\dagger \gamma^0$ and ε^μ is the polarization vector of the free photon, which appears in the solutions $A^\mu = \varepsilon^\mu(\mathbf{q})e^{-iqx}$ to the (free) MAXWELL equation $\square^2 A^\mu = 0$. e is the electron charge. The ingoing electron is assigned the four-momentum K_1 and spin s , the outgoing electron has four-momentum K_3 and spin s' according to Fig. 9.3. The ingoing and outgoing photons have four-momentum K_2 and Q and the polarization vector ε and ε' , respectively.

The invariant MANDELSTAM variables are:

$$\begin{aligned} s &= (K_1 + K_2)^2 = 2 K_1 \cdot K_2 = 2 Q \cdot K_3 \\ t &= (K_1 - Q)^2 = -2 K_1 \cdot Q = -2 K_2 \cdot K_3 \\ u &= (K_1 - K_3)^2 = -2 K_1 \cdot K_3 = -2 K_2 \cdot Q. \end{aligned} \quad (9.10)$$

With these definitions the invariant amplitudes can be written as

$$\mathcal{M}_1 = \frac{1}{t} \varepsilon_\nu'^* \varepsilon_\mu e^2 \bar{u}^{(s')}(K_3) \gamma^\mu (\not{K}_1 - \not{Q}) \gamma^\nu u^{(s)}(K_1), \quad (9.11)$$

$$\mathcal{M}_2 = \frac{1}{s} \varepsilon_\nu'^* \varepsilon_\mu e^2 \bar{u}^{(s')}(K_3) \gamma^\nu (\not{K}_1 + \not{K}_2) \gamma^\mu u^{(s)}(K_1). \quad (9.12)$$

We want to determine the unpolarized cross section and therefore have to average $|\mathcal{M}_1 + \mathcal{M}_2|^2$ over initial electron spins and photon polarizations and sum over the final ones. Because we are dealing with real photons we can make the replacement [245]

$$\sum_{\text{transverse}} \varepsilon_\alpha^* \varepsilon_\beta \rightarrow -g_{\alpha\beta}, \quad (9.13)$$

where the sum is over the physical transverse polarizations, and a similar one for the outgoing

polarizations. This yields for the squared s-channel amplitude:

$$\overline{|\mathcal{M}_2|^2} = \frac{e^4}{4s^2} \sum_{s,s'} \left[\bar{u}^{(s')}(K_3) \gamma^\nu (\not{K}_1 + \not{K}_2) \gamma^\mu u^{(s)}(K_1) \right] \left[\bar{u}^{(s)}(K_1) \gamma_\mu (\not{K}_1 + \not{K}_2) \gamma_\nu u^{(s')}(K_3) \right], \quad (9.14)$$

where the factor 1/4 comes from averaging over the two initial electron spins and two initial photon polarizations. In the next step we calculate the spin sum in (9.14), using the spinor completeness relation [245, 246]:

$$\sum_{s=1,2} u^{(s)}(K_1) \bar{u}^{(s)}(K_1) = \not{K}_1 + m \xrightarrow{m=0} \not{K}_1 \quad (9.15)$$

We find

$$\begin{aligned} \overline{|\mathcal{M}_2|^2} &= \frac{e^4}{4s^2} \text{Tr} [\not{K}_3 \gamma^\nu (\not{K}_1 + \not{K}_2) \gamma^\mu \not{K}_1 \gamma_\mu (\not{K}_1 + \not{K}_2) \gamma_\nu] \\ &= \frac{e^4}{4s^2} \text{Tr} [\gamma_\nu \not{K}_3 \gamma^\nu (\not{K}_1 + \not{K}_2) \gamma^\mu \not{K}_1 \gamma_\mu (\not{K}_1 + \not{K}_2)] \\ &= \frac{e^4}{4s^2} \text{Tr} [(-2) \not{K}_3 (\not{K}_1 + \not{K}_2) (-2) \not{K}_1 (\not{K}_1 + \not{K}_2)] \\ &= \frac{e^4}{s^2} \text{Tr} [\not{K}_3 \not{K}_2 \not{K}_1 \not{K}_2], \end{aligned}$$

where we used the cyclic invariance of the trace in the first step, the relation $\gamma_\nu \gamma^\mu \gamma^\nu = -2\gamma^\mu$ in the second, and the fact that $\not{K} \not{K} = 0$ in the third. Using

$$\text{Tr}(\not{a} \not{b} \not{c} \not{d}) = 4 [(a \cdot b)(c \cdot d) - (a \cdot c)(b \cdot d) + (a \cdot d)(b \cdot c)],$$

we can further write

$$\begin{aligned} \overline{|\mathcal{M}_2|^2} &= 8 \frac{e^4}{s^2} (K_2 \cdot K_3)(K_1 \cdot K_2) \\ &= 2e^4 \left(-\frac{t}{s} \right). \end{aligned} \quad (9.16)$$

Similarly we obtain

$$\overline{|\mathcal{M}_1|^2} = 2e^4 \left(-\frac{s}{t} \right), \quad (9.17)$$

$$\overline{\mathcal{M}_1 \mathcal{M}_2^*} = 0, \quad (9.18)$$

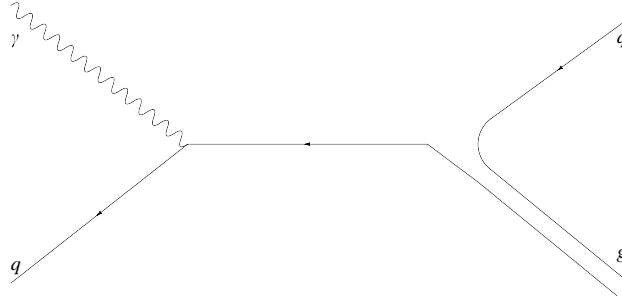
such that the full spin-averaged squared matrix element is given by

$$\overline{|\mathcal{M}|^2} = \overline{|\mathcal{M}_1 + \mathcal{M}_2|^2} = -32\pi^2 \alpha^2 \left(\frac{t}{s} + \frac{s}{t} \right), \quad (9.19)$$

using $\alpha = e^2/(4\pi)$.

The calculation for the annihilation process is completely analogous and yields

$$\overline{|\mathcal{M}|^2} = 32\pi^2 \alpha^2 \left(\frac{u}{t} + \frac{t}{u} \right). \quad (9.20)$$

Figure 9.4: Color lines for $gq \rightarrow q\gamma$

QCD case

The result for the spin averaged squared matrix elements in QCD follows directly from the ones in QED on (1) substitution of $\alpha \rightarrow e_q^2 \alpha_s$ because we now have one photon and one gluon vertex each with a quark charge e_q (the summation over both u and d quarks will be done later), and (2) the multiplication with a color factor, which we shall now derive. One way to determine the color factor is simply to count all possible color combinations, sum them up and then divide by the number of possibilities for the color configuration in the initial state. An easy way to do this is by counting the color lines in Fig. 9.4. There are two, and the same holds for all other diagrams considered here. Each line can take on three colors such that we have 9 possibilities of combining them. However we have to subtract one possibility, which corresponds to the SU(3) color singlet state of the gluon. This singlet does not carry color and cannot mediate between color charges. Hence we are left with 8 possibilities. This we have to divide by a factor of two which comes from the (unfortunate) historical definition of α_s [245]. For the COMPTON scattering diagram we have a quark and a gluon in the initial state, which means that for averaging over color we have to divide by 3 for the colors of the quark and by 8 for all possible color combinations of the gluon. This leads to the spin and color averaged matrix element

$$\overline{|\mathcal{M}|^2} = -32\pi^2 e_q^2 \alpha_s \frac{1}{6} \left(\frac{t}{s} + \frac{s}{t} \right). \quad (9.21)$$

The annihilation diagram has two quarks in the initial state, which means that we have to divide by 9, 3 for each quark, when we want to average over initial colors. This yields

$$\overline{|\mathcal{M}|^2} = 32\pi^2 e_q^2 \alpha_s \frac{4}{9} \left(\frac{u}{t} + \frac{t}{u} \right). \quad (9.22)$$

Alternatively one can perform the summation over initial and final states by taking the trace over the squared matrix element. Each diagram includes a gluon vertex yielding a factor of $-igt^a \gamma^\mu$. This means the color trace is to be taken over $t^a t^a$ giving

$$\text{Tr}(t^a t^a) = C_2(N) \text{Tr}(\mathbf{1}) = \frac{N^2 - 1}{2N} \cdot 3 = 4, \quad (9.23)$$

with the quadratic CASIMIR operator C_2 and $N = 3$ for SU(3). What is left to do is dividing by the number of color combinations in the initial state for averaging and we get the same results as above.

9.2 Infrared divergence and Braaten-Yuan method

The matrix elements (9.21) and (9.22) have poles at t and/or $u = 0$, which causes infrared divergent production rates (9.6). Many-body effects have to be included in the calculation to account for the screening of these divergences. This is done by first excluding the contribution from soft momentum exchange $p < p^*$, with the cutoff on p^* , and separately calculating the soft contribution $p < p^*$ by using HL-resummed propagators instead of bare ones. This cures the infrared divergence and in the limit $g \rightarrow 0$ the sum of hard and soft contributions becomes independent of the cutoff p^* . This procedure has first been used for the calculation of the rate of energy loss of a hot plasma from the PRIMAKOFF production of axions by BRAATEN and YUAN in [247]. For the calculation of high energy medium photon production from an isotropic QGP the method has been applied by BAIER et.al [248] and KAPUSTA et.al in [87]. We will summarize their results in Sec. 9.2.4 and compare to our more general result in the limit that the anisotropy, characterized by the parameter ξ , goes to zero.

9.2.1 Hard contribution

Annihilation Diagrams

From (9.6), (9.22) and remembering that $\mathcal{N} = 20$ we find the rate of photon production from the quark annihilation diagram shown in Fig. 9.2 to be

$$E \frac{dR_{\text{ann}}}{d^3q} = 64\pi^3 \frac{5}{9} \alpha_s \alpha \int_{\mathbf{k}_1} \frac{f_q(\mathbf{k}_1)}{k_1} \int_{\mathbf{k}_2} \frac{f_q(\mathbf{k}_2)}{k_2} \int_{\mathbf{k}_3} \frac{1 + f_g(\mathbf{k}_3)}{k_3} \times \delta^{(4)}(K_1 + K_2 - Q - K_3) \left[\frac{u}{t} + \frac{t}{u} \right], \quad (9.24)$$

where we have assumed that the distribution function for quarks and anti-quarks is the same, $f_q = f_{\bar{q}}$, which allows us to simplify Eq. (9.24) by combining the two terms in square brackets after interchanging K_1 and K_2 in the second term. This operation casts the second term into the exact same form as the first so that we simply pick up a factor of 2.

As discussed earlier we will be confronted with an infrared divergence and hence begin by first changing variables in the first integration to $P \equiv K_1 - Q$ and introduce the infrared cutoff p^* on the integration over the exchanged three-momentum p . We also split the zero and vector components of the delta function as $\delta^{(4)}(P + K_2 - K_3) = \delta(\omega + k_2 - k_3) \delta^{(3)}(\mathbf{p} + \mathbf{k}_2 - \mathbf{k}_3)$ where $\omega \equiv |\mathbf{p} + \mathbf{q}| - q$. We then use the vector part of the delta function to perform the \mathbf{k}_3 integration. Doing this and relabelling $\mathbf{k}_2 \rightarrow \mathbf{k}$ in order to simplify the notation we obtain

$$E \frac{dR_{\text{ann}}}{d^3q} = 16 \frac{5}{9} \alpha_s \alpha \int_{\mathbf{p}} \frac{f_q(\mathbf{p} + \mathbf{q})}{|\mathbf{p} + \mathbf{q}|} \int_{\mathbf{k}} \frac{f_q(\mathbf{k})}{k} \frac{1 + f_g(\mathbf{p} + \mathbf{k})}{|\mathbf{p} + \mathbf{k}|} \times \delta(\omega + k - |\mathbf{p} + \mathbf{k}|) \Theta(p - p^*) \left[\frac{u}{t} \right]. \quad (9.25)$$

To proceed further we choose spherical coordinates with the anisotropy vector $\hat{\mathbf{n}}$ defining the z -axis. Exploiting the azimuthal symmetry about the z -axis we also choose \mathbf{q} to lie in

the $x-z$ plane. It is then possible to reexpress the remaining delta function as

$$\delta(\omega+k-|\mathbf{p}+\mathbf{k}|) = \frac{|\mathbf{p}+\mathbf{k}|}{pk \sin \theta_p \sin \theta_k |\sin(\phi_i - \phi_p)|} \sum_i \delta(\phi_k - \phi_i), \quad (9.26)$$

where ϕ_i are defined through the transcendental equation

$$\cos(\phi_i - \phi_p) = \frac{\omega^2 - p^2 + 2k(\omega - p \cos \theta_p \cos \theta_k)}{2pk \sin \theta_p \sin \theta_k}. \quad (9.27)$$

Eq. (9.26) can be made more explicit using $\sin^2(\phi_i - \phi_p) = 1 - \cos^2(\phi_i - \phi_p)$ yielding

$$\delta(\omega+k-|\mathbf{p}+\mathbf{k}|) = 2|\mathbf{p}+\mathbf{k}| \chi^{-1/2} \Theta(\chi) \sum_{i=1}^2 \delta(\phi_k - \phi_i), \quad (9.28)$$

with

$$\chi \equiv 4p^2 k^2 \sin^2 \theta_k \sin^2 \theta_p - [\omega^2 - p^2 + 2k(\omega - p \cos \theta_p \cos \theta_k)]^2 \quad (9.29)$$

and where we have indicated that there are two solutions to Eq. (9.27) when $\chi > 0$. Making these substitutions and expanding out the phase-space integrals explicitly gives

$$\begin{aligned} E \frac{dR_{\text{ann}}}{d^3q} &= \frac{5}{9} \alpha_s \alpha \sum_{i=1}^2 \int_{p^*}^{\infty} dp p^2 \int_{-1}^1 d \cos \theta_p \int_0^{2\pi} d\phi_p \frac{f_q(\mathbf{p}+\mathbf{q})}{|\mathbf{p}+\mathbf{q}|} \\ &\times \int_0^{\infty} dk k \int_{-1}^1 d \cos \theta_k f_q(\mathbf{k}) [1 + f_g(\mathbf{p}+\mathbf{k})] \chi^{-1/2} \Theta(\chi) \left[\frac{u}{t} \right] \Bigg|_{\phi_k=\phi_i}, \end{aligned} \quad (9.30)$$

with $t = \omega^2 - p^2$, $u = (k - q)^2 - (\mathbf{k} - \mathbf{q})^2$, and recalling $\omega = |\mathbf{p} + \mathbf{q}| - q$.

Compton Scattering Diagrams

Again assuming $f_{\bar{q}} = f_q$ the rate of photon production from the Compton scattering diagrams shown in Fig. 9.3 can be expressed as

$$\begin{aligned} E \frac{dR_{\text{com}}}{d^3q} &= -128\pi^3 \frac{5}{9} \alpha_s \alpha \int_{\mathbf{k}_1} \frac{f_q(\mathbf{k}_1)}{k_1} \int_{\mathbf{k}_2} \frac{f_g(\mathbf{k}_2)}{k_2} \int_{\mathbf{k}_3} \frac{1 - f_q(\mathbf{k}_3)}{k_3} \\ &\times \delta^{(4)}(K_1 + K_2 - Q - K_3) \left[\frac{s}{t} + \frac{t}{s} \right], \end{aligned} \quad (9.31)$$

where we have again assumed massless quarks, and the MANDELSTAM variables are defined by $s \equiv (K_1 + K_2)^2$ and $t \equiv (K_1 - Q)^2$. Performing a change of variables to $P \equiv K_1 - Q$, redefining $K_2 \rightarrow K$, and evaluating the delta function as in the annihilation case above gives

$$\begin{aligned} E \frac{dR_{\text{com}}}{d^3q} &= -\frac{5}{9} \alpha_s \alpha \sum_{i=1}^2 \int_{p^*}^{\infty} dp p^2 \int_{-1}^1 d \cos \theta_p \int_0^{2\pi} d\phi_p \frac{f_q(\mathbf{p}+\mathbf{q})}{|\mathbf{p}+\mathbf{q}|} \\ &\times \int_0^{\infty} dk k \int_{-1}^1 d \cos \theta_k f_g(\mathbf{k}) [1 - f_q(\mathbf{p}+\mathbf{k})] \chi^{-1/2} \Theta(\chi) \left[\frac{s}{t} + \frac{t}{s} \right] \Bigg|_{\phi_k=\phi_i}, \end{aligned} \quad (9.32)$$

where here $t = \omega^2 - p^2$, $s = (\omega + q + k)^2 - (\mathbf{p} + \mathbf{q} + \mathbf{k})^2$, and recalling $\omega = |\mathbf{p} + \mathbf{q}| - q$.

Total Hard Contribution

The total photon production from processes which have a hard momentum exchange is given by the sum of Eqs. (9.30) and (9.32).

$$E \frac{dR_{\text{hard}}}{d^3q} = E \left(\frac{dR_{\text{ann}}}{d^3q} + \frac{dR_{\text{com}}}{d^3q} \right) \quad (9.33)$$

To evaluate the five-dimensional integrals in Eqs. (9.30) and (9.32) we use monte-carlo integration.

The total hard contribution (9.33) has a logarithmic infrared divergence as $p^* \rightarrow 0$. This logarithmic infrared divergence will be cancelled by a corresponding ultraviolet divergence in the soft contribution so that in the limit $g \rightarrow 0$ there will be no dependence of the total (soft + hard) rate on the separation scale p^* . In the next section we present the calculation of the soft part which we will then combine with the hard result to obtain the total photon production rate.

9.2.2 Soft contribution

We now turn to the calculation of the previously excluded infrared divergent contribution from soft momentum exchange. The infrared divergence in the photon production rate is caused by a diverging differential cross section when the momentum transfer goes to zero. Long-ranged forces are usually screened by many-body effects at finite temperature. In the high temperature limit these effects can be included by using the HL-resummed propagators instead of free ones. This way we will be able to derive an infrared finite result. The rate for the soft part is given by Eq. (9.4):

$$E \frac{dR_{\text{soft}}}{d^3q} = \frac{i}{2(2\pi)^3} \Pi_{\mu}^{<\mu}(Q), \quad (9.34)$$

from the trace of the (12)-element $\Pi^{<} = \Pi_{12}$ of the photon-polarization tensor. After the

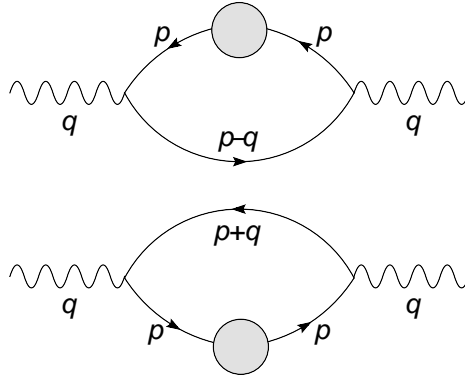


Figure 9.5: The photon polarization tensor $\Pi^{<}$ for soft momentum $p \sim gT$. The blob indicates the hard-loop resummed quark propagator.

replacement of free propagators with the HL-resummed ones, the photon polarization tensor is calculated from the FEYNMAN graphs in Fig. 9.5, resulting in

$$i\Pi_{12\mu}^{\mu}(Q) = e^2 \frac{5}{9} N_c \int \frac{d^4 p}{(2\pi)^4} \text{Tr} [\gamma^{\mu} iS_{12}^*(P)|_{HL} \gamma_{\mu} iS_{21}(P-Q) + \gamma^{\mu} iS_{12}(P+Q) \gamma_{\mu} iS_{21}^*(P)|_{HL}] , \quad (9.35)$$

where $e_q^2 = 5/9$ comes from the sum over quark charges. S_{12} and S_{21} are the free fermion propagators for massless quarks, to be read off the matrix propagator

$$S(K) = \not{K} \left[\left(\begin{array}{cc} \frac{1}{K^2+i\epsilon} & 0 \\ 0 & \frac{-1}{K^2-i\epsilon} \end{array} \right) + 2\pi i \delta(K^2) \left(\begin{array}{cc} f_F(K) & -\theta(-k_0) + f_F(K) \\ -\theta(k_0) + f_F(K) & f_F(K) \end{array} \right) \right] , \quad (9.36)$$

with the general fermion distribution function $f_F(K)$, and propagators with a HL subscript are the full propagators in the hard-loop approximation. These satisfy a fluctuation dissipation relation given by (see Appendix F on the validity of this expression in our framework)

$$S_{12/21}^*(P)|_{HL} = S_{\text{ret}}^*(P)|_{HL} \Sigma_{12/21}(P) S_{\text{adv}}^*(P)|_{HL} . \quad (9.37)$$

The HL resummed retarded propagator reads

$$S_{\text{ret}}^*(P)|_{HL} = \frac{1}{\not{P} - \Sigma(P)} , \quad (9.38)$$

where $\Sigma(P)$ is the retarded self-energy given in Eq.(8.1). The advanced propagator follows analogously with the advanced self-energy. Note that Eq.(9.37) is equivalent to the expression for $S_{12/21}^*$ in [244] (see [249]). To one loop order Σ_{12} is given by

$$\Sigma_{12}(P) = 2ig^2 C_F \int \frac{d^4 k}{(2\pi)^4} S_{12}(K) \Delta_{12}(P-K) , \quad (9.39)$$

where Δ_{12} is the (12)-element of the matrix boson propagator given by

$$\Delta(K) = \left(\begin{array}{cc} \frac{1}{K^2-m^2+i\epsilon} & 0 \\ 0 & \frac{-1}{K^2-m^2-i\epsilon} \end{array} \right) - 2\pi i \delta(K^2 - m^2) \left(\begin{array}{cc} f_B(K) & \theta(-k_0) + f_B(K) \\ \theta(k_0) + f_B(K) & f_B(K) \end{array} \right) . \quad (9.40)$$

With the anisotropic distribution function (8.2) Σ_{12} can be evaluated in the hard-loop approximation to read

$$\begin{aligned} \Sigma_{12}^{\mu}(P) = & i \frac{g^2 C_F}{(2\pi)^2} \int d\tilde{k} \int_0^{2\pi} d\phi \int_{-1}^{+1} dx \frac{\tilde{k}^2}{(1+\xi x^2)^{3/2}} \\ & \times \left[\frac{k^{\mu}}{k} \Big|_{k_0=k} \delta(g_-) N(\xi) f_F^{\text{iso}}(\tilde{k}) \left(N(\xi) f_B^{\text{iso}}(\tilde{k}) + 1 \right) \right. \\ & \left. + \frac{k^{\mu}}{k} \Big|_{k_0=-k} \delta(g_+) N(\xi) f_B^{\text{iso}}(\tilde{k}) \left(N(\xi) f_F^{\text{iso}}(\tilde{k}) - 1 \right) \right] , \end{aligned} \quad (9.41)$$

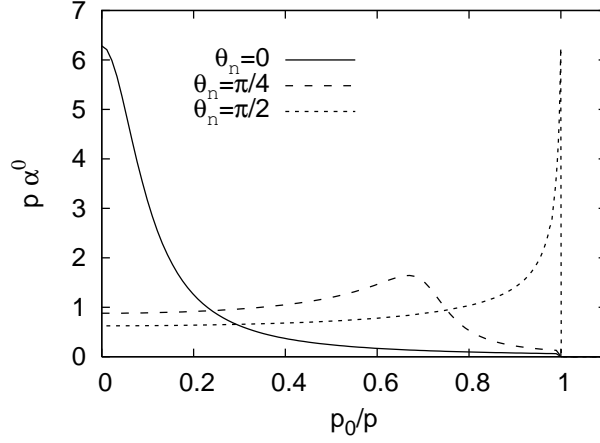


Figure 9.6: θ_n -dependent part α^0 of the self-energy Σ_{12}^0 . $\theta_n \in \{0, \pi/4, \pi/2\}$ and $\xi = 100$.

where

$$g_{\pm} = 2 \frac{\tilde{k}}{\sqrt{1+\xi x^2}} \left[\pm p_0 + p \left(\sin \theta_n \sqrt{1-x^2} \cos \phi + \cos \theta_n x \right) \right] \quad (9.42)$$

and we chose \mathbf{p} to lie in the $x-z$ -plane and used the change of variables (8.3) for k . Note that in the hard-loop limit one can ignore the quark masses and hence they have been explicitly set to zero above. The term k^μ/k does not depend on k and is given by $(\pm 1, \sin \theta \cos \phi, \sin \theta \sin \phi, \cos \theta)$. Evaluation of the δ -function leads to

$$-i\Sigma_{12}^\mu(P, \theta_n, \xi) = A \alpha^\mu(P, \theta_n, \xi) + B \beta^\mu(P, \theta_n, \xi), \quad (9.43)$$

with

$$\begin{aligned} \alpha^\mu &= \int d\phi \sum_i \frac{k^\mu}{k} \Big|_{k_0=k} \left| \frac{(1-x_i^2)^{1/2}}{(1-x_i^2)^{1/2}(p \cos \theta_n + p_0 \xi x_i) - p \sin \theta_n x_i (1+\xi) \cos \phi} \right| \theta(1-x_i^2), \\ \beta^\mu &= \int d\phi \sum_i \frac{k^\mu}{k} \Big|_{k_0=-k} \left| \frac{(1-\tilde{x}_i^2)^{1/2}}{(1-\tilde{x}_i^2)^{1/2}(p \cos \theta_n - p_0 \xi \tilde{x}_i) - p \sin \theta_n \tilde{x}_i (1+\xi) \cos \phi} \right| \theta(1-\tilde{x}_i^2), \end{aligned} \quad (9.44)$$

where the x_i and \tilde{x}_i are solutions to $\frac{\tilde{k}}{\sqrt{1+\xi x^2}} \left[-p_0 + p \left(\sin \theta_n \sqrt{1-x^2} \cos \phi + \cos \theta_n x \right) \right] = 0$ and $\frac{\tilde{k}}{\sqrt{1+\xi x^2}} \left[p_0 + p \left(\sin \theta_n \sqrt{1-x^2} \cos \phi + \cos \theta_n x \right) \right] = 0$, respectively, and

$$A = \frac{g^2 C_F}{8\pi^2} \int dk k N(\xi) f_F^{\text{iso}}(k) (N(\xi) f_B^{\text{iso}}(k) + 1), \quad (9.45)$$

$$B = \frac{g^2 C_F}{8\pi^2} \int dk k N(\xi) f_B^{\text{iso}}(k) (N(\xi) f_F^{\text{iso}}(k) - 1). \quad (9.46)$$

There can be $N \in \{0, 1, 2\}$ solutions for both x_i and \tilde{x}_i , depending on the parameters p, p_0, θ_n and ϕ . Note that $\frac{k^\mu}{k}$ is also given in terms of the x_i . It is easily verified that

$$\alpha^\mu(P, \theta_n, \xi) = -\beta^\mu(P, \theta_n, \xi), \quad (9.47)$$

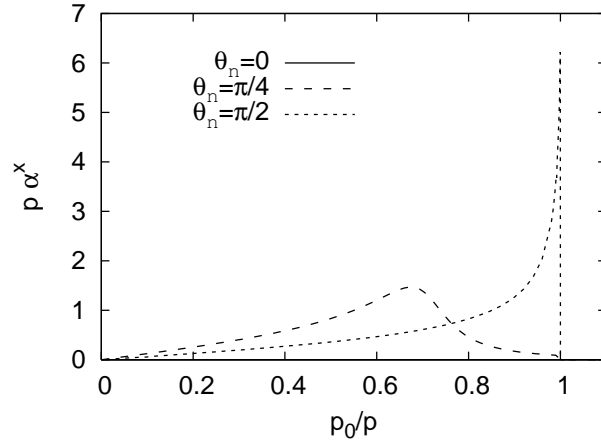


Figure 9.7: θ_n -dependent part α^x of the self-energy Σ_{12}^x . $\theta_n \in \{0, \pi/4, \pi/2\}$ and $\xi = 100$. For $\theta_n = 0$ $\alpha^x = 0$.

such that Eq. (9.43) greatly simplifies to read

$$-i\Sigma_{12}^\mu(P, \theta_n, \xi) = (A - B) \alpha^\mu(P, \theta_n, \xi), \quad (9.48)$$

where

$$A - B = \frac{g^2 C_F}{8\pi^2} N(\xi) \left[\int_0^\infty dk k (f_B^{\text{iso}}(k) + f_F^{\text{iso}}(k)) \right] = \frac{1}{4} m_q^2 N(\xi), \quad (9.49)$$

assuming equal quark and anti-quark distributions. We did not present the analogous explicit calculation of Σ_{21} , but find for it the same result as for Σ_{12} with A and B interchanged. We also verified that Σ_{12} and Σ_{21} fulfill the general relation

$$\Sigma_{21} - \Sigma_{12} = 2i \text{Im} \Sigma, \quad (9.50)$$

with the retarded self-energy Σ given in Sec. 8.1. Furthermore, since Σ_{21} is given by Eq. (9.48) with A and B interchanged it follows within the hard-loop approximation that with the form of the anisotropic distribution function assumed here it always holds that

$$\Sigma_{12} = -\Sigma_{21}, \quad (9.51)$$

which can be seen as a high-temperature limit of the KUBO-MARTIN-SCHWINGER (KMS) relation in equilibrium, but also holds for finite ξ and hence for non-equilibrium systems. Note that in equilibrium the relation (9.51) does not contradict the usual KMS-relation, but is an approximation to it. In equilibrium, the KMS-relation is given by

$$\Sigma_{12}(P) = -e^{-p_0/T} \Sigma_{21}(P), \quad (9.52)$$

with the temperature T . In our case the soft momentum p is of the order gT , such that an expansion of the exponential gives 1 as in Eq. (9.51) plus terms that are suppressed by higher orders of g . Eqs.(9.50) and (9.51) show that in order to calculate the hard-loop

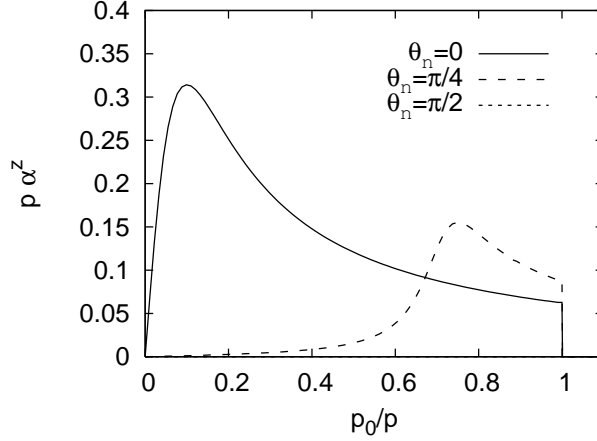


Figure 9.8: θ_n -dependent part α^z of the self-energy Σ_{12}^z . $\theta_n \in \{0, \pi/4, \pi/2\}$ and $\xi = 100$. For $\theta_n = \pi/2$ $\alpha^z = 0$.

photon production rate from an anisotropic plasma one need only know the retarded self-energy. We plot the functions α for an anisotropy parameter of $\xi = 100$ and different angles θ_n in Figs. 9.6, 9.7 and 9.8 to emphasize the strong angular dependence once more.

Now that we have calculated Σ_{12} and Σ_{21} and expressed it in terms of the retarded self energy:

$$\Sigma_{12} = -\Sigma_{21} = -i \text{Im}\Sigma, \quad (9.53)$$

we can rewrite Eq. (9.37) to find

$$i S_{12}^*|_{HL} = -i S_{21}^*|_{HL} = \Lambda_{\alpha\beta\gamma}(P) \gamma^\alpha \gamma^\beta \gamma^\gamma, \quad (9.54)$$

where

$$\Lambda_{\alpha\beta\gamma}(P) = \frac{P_\alpha - \Sigma_\alpha(P)}{(P - \Sigma(P))^2} \text{Im} \Sigma_\beta(P) \frac{P_\gamma - \Sigma_\gamma^*(P)}{(P - \Sigma^*(P))^2}, \quad (9.55)$$

with the complex conjugate of the self energy Σ^* . With that Eq. (9.35) becomes

$$i \Pi_{12\mu}^\mu(Q) = e^2 \frac{5}{9} N_c \int \frac{d^4 p}{(2\pi)^4} \text{Tr} \left[\gamma^\mu \Lambda_{\alpha\beta\gamma}(P) \gamma^\alpha \gamma^\beta \gamma^\gamma \gamma_\mu i S_{21}(P - Q) \right. \\ \left. - \gamma^\mu i S_{12}(P + Q) \gamma_\mu \Lambda_{\alpha\beta\gamma}(P) \gamma^\alpha \gamma^\beta \gamma^\gamma \right]. \quad (9.56)$$

In the HL approximation and assuming a \mathbf{k} dependent distribution function that satisfies $f(\mathbf{k}) = f(-\mathbf{k})$, we can write for the free propagator

$$i S_{21}(P - Q) = S_{21\nu}(P - Q) \gamma^\nu = -2\pi (\not{P} - \not{Q}) \delta((P - Q)^2) f_F(P - Q) \\ \simeq -2\pi (\not{P} - \not{Q}) \frac{1}{2q} \delta(p_0 - p(\hat{\mathbf{p}} \cdot \hat{\mathbf{q}})) f_F(\mathbf{q}), \quad (9.57)$$

$$i S_{12}(P + Q) = S_{12\nu}(P - Q) \gamma^\nu = -2\pi (\not{P} + \not{Q}) \delta((P - Q)^2) f_F(P + Q) \\ \simeq -2\pi (\not{P} + \not{Q}) \frac{1}{2q} \delta(p_0 - p(\hat{\mathbf{p}} \cdot \hat{\mathbf{q}})) f_F(\mathbf{q}), \quad (9.58)$$

where the θ -functions could be neglected in both cases because $q_0 \gg p_0$.

To evaluate the trace in Eq. (9.56), we use its cyclic invariance and the identities

$$\gamma^\mu \gamma^\alpha \gamma^\beta \gamma^\gamma \gamma_\mu = \gamma_\mu \gamma^\alpha \gamma^\beta \gamma^\gamma \gamma^\mu = -2\gamma^\gamma \gamma^\beta \gamma^\alpha, \quad (9.59)$$

$$\text{Tr} \left[\gamma^\gamma \gamma^\beta \gamma^\alpha \gamma^\nu \right] = 4 \left(g^{\gamma\beta} g^{\alpha\nu} - g^{\gamma\alpha} g^{\beta\nu} + g^{\gamma\nu} g^{\beta\alpha} \right). \quad (9.60)$$

This, together with Eqs. (9.57) and (9.58), leads to the expression

$$i\Pi_{12\mu}^\mu(Q) = -e^2 \frac{5}{9} N_c \frac{8f_F(\mathbf{q})}{q} \int \frac{d^3p}{(2\pi)^3} Q_\nu \tilde{\Lambda}^\nu(P), \quad (9.61)$$

where

$$\tilde{\Lambda}^\nu(P) = (\Lambda^{\nu\alpha}_\alpha(P) - \Lambda_\alpha^{\nu\alpha}(P) + \Lambda_\alpha^{\alpha\nu}(P))_{p_0=p(\hat{\mathbf{p}} \cdot \hat{\mathbf{q}})}. \quad (9.62)$$

This can be further simplified when realizing that $Q_\nu \tilde{\Lambda}^\nu = \text{Im} (Q_\nu S_{\text{ret}}^{*\nu}|_{HL})$ [250]². The final expression then becomes

$$i\Pi_{12\mu}^\mu(Q) = -e^2 \frac{5}{9} N_c \frac{8f_F(\mathbf{q})}{q} \int^{p^*} \frac{d^3p}{(2\pi)^3} \text{Im} (Q_\nu S_{\text{ret}}^{*\nu}|_{HL}(P)), \quad (9.63)$$

where the ultra-violet cutoff p^* is imposed on the radial part of the integral.

9.2.3 Total contribution

The total photon rate is found by adding the hard (9.33) and soft (9.34) rates

$$E \frac{dR}{d^3q} = E \left(\frac{dR_{\text{hard}}}{d^3q} + \frac{dR_{\text{soft}}}{d^3q} \right). \quad (9.64)$$

In the following sections we will discuss its dependence on the cutoff p^* and compare to previously found analytic results [87, 248] in the isotropic limit.

As in the previous chapters we now choose the anisotropic distribution functions to be given by isotropic distributions that are squeezed or stretched along one direction in momentum space, i.e.,

$$f_i(\mathbf{k}, \xi, p_{\text{hard}}) = f_{i,\text{iso}} \left(\sqrt{\mathbf{k}^2 + \xi(\mathbf{k} \cdot \hat{\mathbf{n}})^2}, p_{\text{hard}} \right),$$

where $i \in \{q, g\}$, p_{hard} is a hard momentum scale which appears in the distribution functions, $\hat{\mathbf{n}}$ is the direction of the anisotropy, and $\xi > -1$ is a parameter reflecting the strength and type of the anisotropy [63].

In the following we will suppress the explicit dependence on ξ and p_{hard} . We specialize to the case $\xi > 0$ which is the relevant one for heavy-ion collisions after times $\tau \gtrsim 0.2$ fm/c. For the arbitrary isotropic distribution functions, $f_{i,\text{iso}}$, which are contracted along the z -axis, we choose BOSE-EINSTEIN and FERMI-DIRAC distributions in the case of gluons and quark/anti-quarks, respectively.

²I thank A. Ipp for pointing this out to me.

Using these distribution functions we are able to reproduce the equilibrium results, which have been obtained previously [248, 87] by taking the limit $\xi \rightarrow 0$.

9.2.4 The isotropic limit

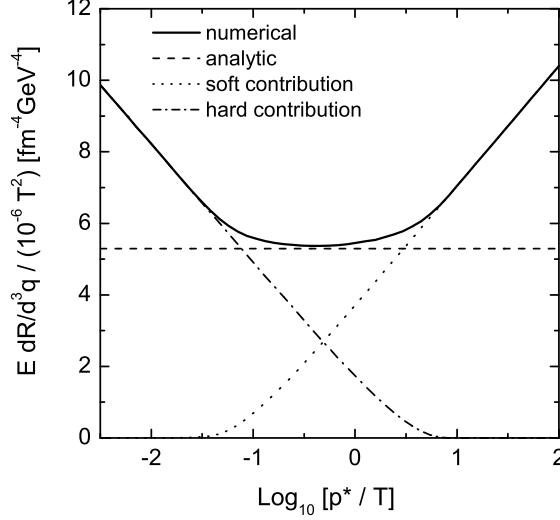


Figure 9.9: Full photon rate for $\xi = 0$ and $g = 0.1$ as a function of the cutoff p^* compared to the totally cutoff independent analytic approximation Eq. (9.67). Around the geometrical mean of the hard and soft momentum scale, $\sqrt{g}T$, the rate is nearly independent of the cutoff.

In the case of isotropic quark/anti-quark and gluon distribution functions, Eqs. (9.24) and (9.31) can be further simplified by transforming to s - and t - variables as explained in [85]. This has been done in [248] and Eq. (9.33) becomes

$$E \frac{dR_{\text{hard}}}{d^3q} \simeq \frac{5}{9} \alpha \alpha_s T^2 e^{-E/T} \left[\ln \frac{ET}{p^{*2}} + \frac{3}{2} + \frac{\ln 2}{3} - \gamma + \frac{\zeta'(2)}{\zeta(2)} \right], \quad (9.65)$$

where T is now the temperature of the equilibrated system, γ is EULER's constant and ζ is the RIEMANN zeta function:

$$\frac{\zeta'(2)}{\zeta(2)} \simeq -0.57$$

They also calculated the soft part using hard thermal loop quark self energies in a calculation analogous to ours in Sec. 9.2.2, but assuming equilibrium. The result is

$$E \frac{dR_{\text{soft}}}{d^3q} \simeq \frac{5}{9} \alpha \alpha_s T^2 e^{-E/T} \left[\ln \frac{p^{*2}}{m_q^2} - 1.31 \right], \quad (9.66)$$

with m_q^2 as defined in (8.5). When adding (9.65) and (9.66) the p^{*2} under the logarithms cancel exactly and the result is independent of the cutoff:

$$E \frac{dR}{d^3q} \simeq \frac{5}{9} \alpha \alpha_s T^2 e^{-E/T} \ln \left(\frac{0.23 E}{\alpha_s T} \right), \quad (9.67)$$

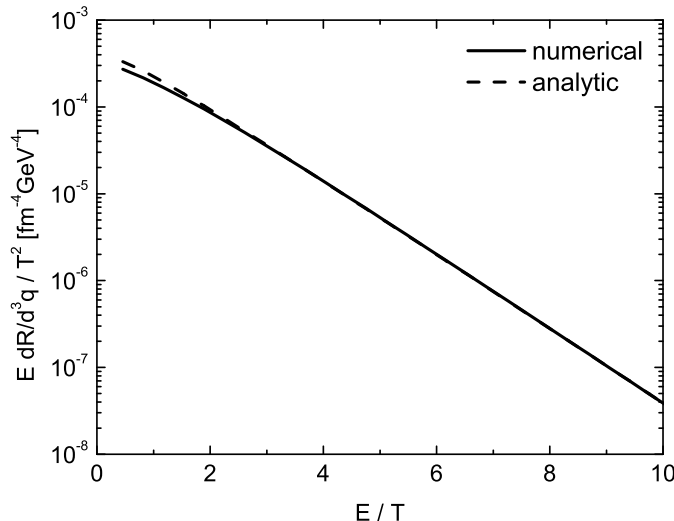


Figure 9.10: Full photon rate for $\xi = 0$ and $g = 0.1$ as a function of E/T compared to the analytic expression Eq. (9.67). The cutoff dependence is smaller than the width of the full line.

which holds in the limit of arbitrarily small gauge coupling g and cutoff p^* , as well as $E > T$.

We will now compare the limiting case of vanishing anisotropy of the rate (9.64) to (9.67) as a consistency check. First let us focus on the case of small coupling, choosing $g = 0.1$, and explore the cutoff dependence of the numerically calculated rate (9.64). It is shown together with the comparison to the analytic approximation given by (9.67) in Fig. 9.9. We find that around the intermediate scale \sqrt{gT} , which is the geometrical mean of the soft momentum scale gT and the hard momentum scale T , the rate develops a plateau close to the analytic result. This is due to a cancellation of the p^* -dependent parts in the soft and the hard contribution in this regime: The same cancellation that happens in the analytic result for all values of p^* . Outside the plateau the rate rises logarithmically with p^* . A very similar behavior has been found in the investigation of the energy loss of a heavy fermion in a QED- or QCD-plasma by ROMATSCHKE and STRICKLAND [179, 180]. To get a feeling for the cutoff dependence, we evaluate the rate at the minimum p_{\min}^* , which we determine numerically and at two more values, half the value at the minimum, $0.5p_{\min}^*$, and twice that value, $2p_{\min}^*$. This choice for the variation of p^* is completely arbitrary - one could as well choose a smaller value. However, we decided to be conservative and use a factor of two. The E/T -dependence of the numerical result compared to the analytic one is shown in Fig. 9.10. The cutoff dependence for the case of small coupling, $g = 0.1$ is smaller than the width of the line and hence does not show up as a band in the plot.

Next, we move on to a more realistic coupling of $g = 2$ and do the same as before, i.e., explore the cutoff dependence of the rate (Fig. 9.11) and plot the rate versus E/T , varying the cutoff by factors of two around the minimal value (Fig. 9.12). Both figures show that the cutoff dependence increases with increasing coupling g , which can be expected since our theory is only precise for small couplings. However, the BRAATEN-YUAN-Method provides a

good means to measure the uncertainty of the final results caused by applying perturbation theory to systems with large coupling.

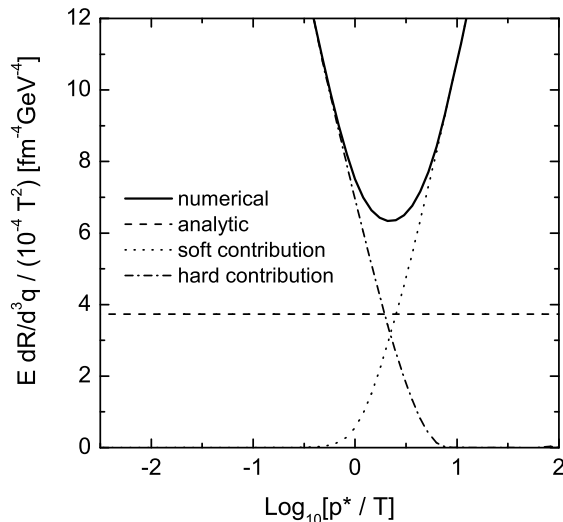


Figure 9.11: Full photon rate for $\xi = 0$ and $g = 2$ as a function of the cutoff p^* compared to the totally cutoff independent analytic approximation Eq. (9.67). The plateau is now merely a minimum, because its width decreases with increasing coupling. Also, the difference to the approximate analytic result increases.

9.3 Results for the anisotropic case

In Fig. 9.13 we plot the dependence of the total anisotropic photon production rate as a function of photon energy, E , for three different photon propagation angles assuming $\xi = 10$ and $\alpha_s = 0.3$. The shaded bands indicate our estimated theoretical uncertainty which is determined by varying the hard-soft separation scale p^* by a factor of two around its central value which is parametrically $p^* \sim \sqrt{g} p_{\text{hard}}$. We have scaled everywhere by the arbitrary hard-momentum scale p_{hard} which appears in the quark and gluon distribution functions. This scale will be, in general, time dependent with its value set to the nuclear saturation scale, Q_s , at the earliest times and to the plasma temperature at late times. For RHIC $Q_s \sim 1.4\text{--}2$ GeV and expected initial plasma temperatures are $T_o \sim 300\text{--}400$ MeV. As can be seen from this Figure there is a clear dependence of the spectrum on photon angle with the difference increasing as the energy of the photon increases.

To compare the angular dependence at different ξ in Fig. 9.14 we show the dependence of the photon production rate on angle at a fixed photon energy $E/p_{\text{hard}} = 5$ and $\alpha_s = 0.3$. As can be seen from Fig. 9.14 the difference between the forward and transverse production rates increases as ξ increases. To summarize the effect we define the photon anisotropy parameter, $\mathcal{R}_\gamma \equiv (dR/d^3q|_{\theta_q=0}) / (dR/d^3q|_{\theta_q=\pi/2})$. This ratio is one at all energies if the plasma is isotropic. For anisotropic plasmas it increases as the anisotropy of the system and/or the energy of the photon increases. Due to the limited experimental rapidity acceptance one

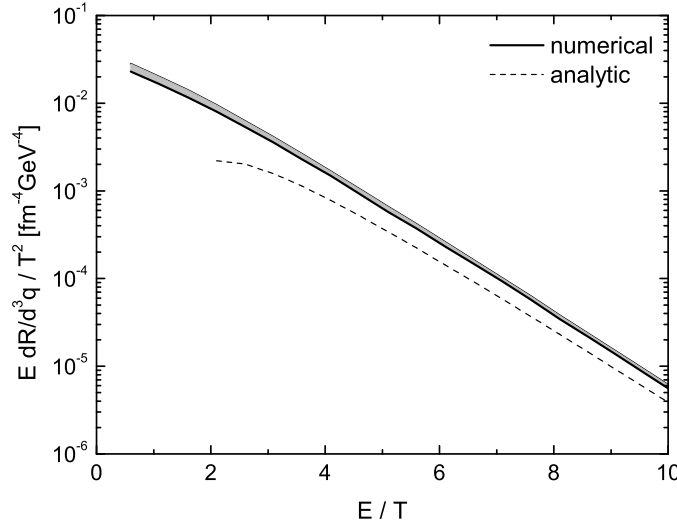


Figure 9.12: Full photon rate for $\xi = 0$ and $g = 2$ as a function of E/T compared to the analytic expression Eq. (9.67). The grey band indicates the uncertainty of the result with the variation of the cutoff p^* by factors of two around the value at the minimum.

could define this ratio at a lower angle, e.g. $\pi/4$. However, the ability to resolve anisotropies increases as the sensitivity to forward angles increases so the best experiment would be to compare the most forward photons possible with transverse photon emission.

\mathcal{R}_γ	$\xi = 0$	$\xi = 1$	$\xi = 10$
$E/p_{\text{hard}} = 5$	1	4.7	$2 \cdot 10^2$
$E/p_{\text{hard}} = 10$	1	34	$3 \cdot 10^4$

Table 9.1: Photon anisotropy parameter \mathcal{R}_γ for different photon energies and anisotropy parameters assuming $\alpha_s = 0.3$.

9.4 Total photon yield

In order to quantify the effect of an evolving anisotropic distribution function on experimental observables, we apply the space time model introduced in [251] and [252]. This model allows to interpolate between the hydrodynamical and the free streaming limit, when performing the integral over the space-time volume

$$E \frac{dN}{d^3q} = \left. \frac{dN}{d^2q_\perp dy} \right|_{\text{CM}} = \pi R_A^2 \int_{\tau_0}^{\tau_f} d\tau \tau \int_{-y_{\text{nucl}}}^{y_{\text{nucl}}} d\eta E \left. \frac{dR}{d^3q} \right|_{\text{LR}}, \quad (9.68)$$

where q_\perp is the transverse momentum of the photon, $y = 1/2 \ln[(E + q_z)/(E - q_z)]$ its rapidity, and $\eta = 1/2 \ln[(t + z)/(t - z)]$ its space-time rapidity. $\tau = \sqrt{t^2 - z^2}$ is proper time, and $R_A \approx 1.2A^{1/3}$ is the radius of the nucleus in the transverse plane. $y_{\text{nucl}} =$

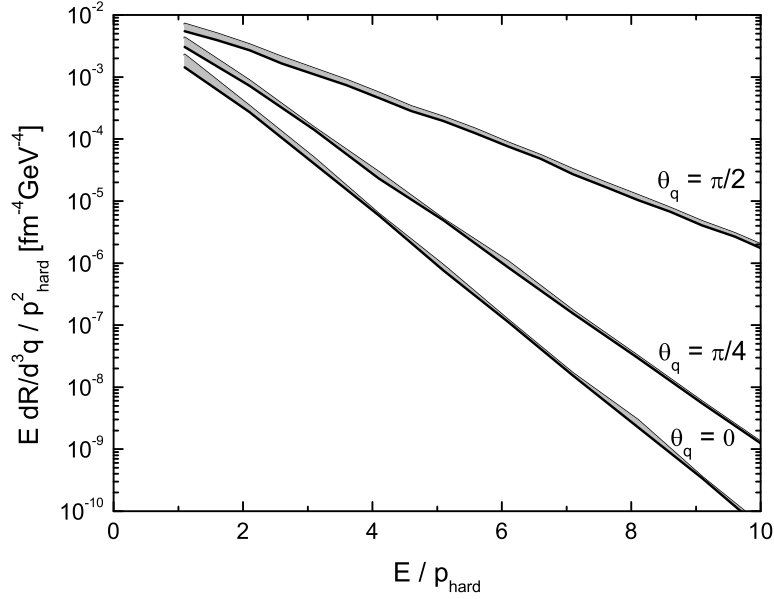


Figure 9.13: Photon rate for $\xi = 10$ and $\alpha_s = 0.3$ as a function of energy for three different photon angles, $\theta_q = \{0, \pi/4, \pi/2\}$, corresponding to rapidities $y = \{\infty, 0.88, 0\}$, respectively.

$\arccos(\sqrt{s}/(2A\text{GeV}))$ is the center-of-mass rapidity of the projectiles. Note that the final yield is evaluated in the center of mass (CM) frame, while the differential rate is calculated in the local rest (LR) frame of the emitting fluid cell, such that the photon energy in the local rest-frame is given by $E_{\text{LR}} = q_{\perp} \cosh(y - \eta)$, while its longitudinal momentum reads $q_z = q_{\perp} \sinh(y - \eta)$. We neglect transverse expansion of the system, because we are interested in the early time behavior for which it is negligible compared to the longitudinal expansion [253].

One limit that the space-time evolution can have is the hydrodynamical expansion, for which the system is assumed to be isotropic already at the partonic formation time $\tau_0 = \tau_{\text{iso}}$, and stay isotropic throughout the evolution: $\xi(\tau) = 0$. τ_0 is the time after the coherence effects in the nuclear wave functions can be ignored. Using 1+1 dimensional BJORKEN expansion, the temperature drops like $T(\tau) = T_0(\tau_0/\tau)^{1/3}$, with the initial temperature T_0 . Another limit is the free-streaming case, in which the distribution function is a solution to the collisionless BOLTZMANN equation

$$p \cdot \partial_x f(p, x) = 0. \quad (9.69)$$

We assume that it is initially isotropic at time $\tau = \tau_0$ and then by longitudinal expansion becomes more and more anisotropic, such that we have

$$f(p, x)_{\text{f.s.}} = f\left(\frac{p_{\perp}}{T_0} \sqrt{1 + \frac{\tau^2}{\tau_0^2} \sinh^2(y - \eta)}\right), \quad (9.70)$$

where the initial temperature represents the hard momentum scale and is equal to the one used in the hydrodynamic expansion. The anisotropy parameter ξ can be expressed via the

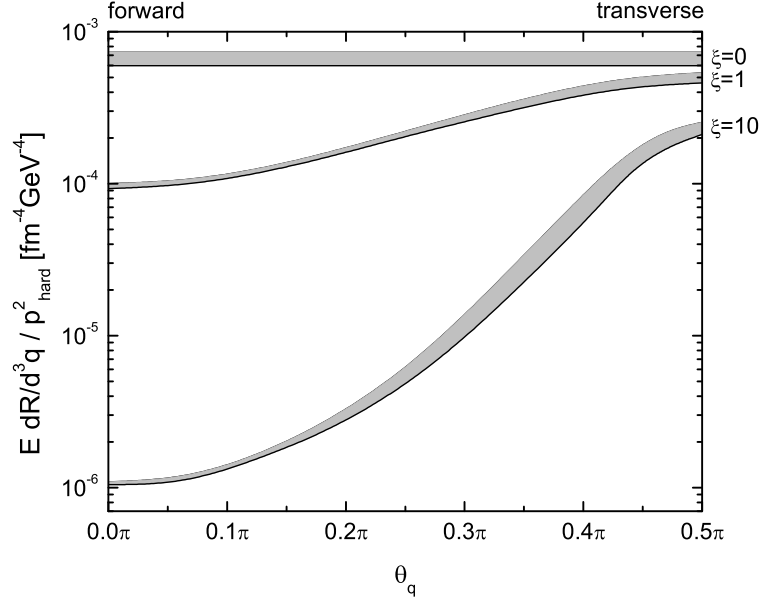


Figure 9.14: Photon rate for $\xi = \{0, 1, 10\}$ as a function of the photon angle, θ_q , for $E/p_{\text{hard}} = 5$ and $\alpha_s = 0.3$.

transverse and longitudinal parton momentum by

$$\xi = \frac{\langle p_{\perp}^2 \rangle}{2 \langle p_L^2 \rangle} - 1. \quad (9.71)$$

Using the nuclear saturation scale Q_s , and $\tau_0 \sim Q_s^{-1}$, $\langle p_{\perp}^2 \rangle \sim Q_s^2$, and $\langle p_L^2 \rangle \sim \tau^{-2}$, we find for the free streaming limit

$$\xi(\tau) = \frac{\tau^2}{\tau_0^2} - 1. \quad (9.72)$$

Given that we start with an isotropic distribution, this poses an upper bound on the anisotropy parameter, due to causality. The temperature stays constant and isotropization is never reached: $\tau_{\text{iso}} \rightarrow \infty$.

The interpolating model, described in detail in [251] and [252], introduces the following time dependencies of the hard momentum scale and the anisotropy parameter:

$$p_{\text{hard}}(\tau) = T_0 (\mathcal{R}(a_{\text{iso}}^2 - 1))^{\lambda/4} \left(\frac{a_{\text{iso}}}{a}\right)^{\lambda/3}, \quad (9.73a)$$

$$\xi(\tau) = a^{2(1-\lambda)} - 1, \quad (9.73b)$$

where $\lambda(\tau, \tau_0, \tau_{\text{iso}}, \gamma) \equiv \{\tanh[\gamma(\tau - \tau_{\text{iso}})/\tau_0] + 1\}/2$, with the free parameter γ , which sets the width of the transition, $\mathcal{R}(\xi) = [1/(\xi + 1) + \arctan\sqrt{\xi}/\sqrt{\xi}]/2$, $a \equiv \tau/\tau_0$ and $a_{\text{iso}} \equiv \tau_{\text{iso}}/\tau_0$. Then the energy density behaves as follows

$$\mathcal{E}(\tau) = \mathcal{E}_{\text{f.s.}}(\tau) (\mathcal{R}(a_{\text{iso}}^2 - 1))^\lambda \left(\frac{a_{\text{iso}}}{a}\right)^{4\lambda/3}, \quad (9.74)$$

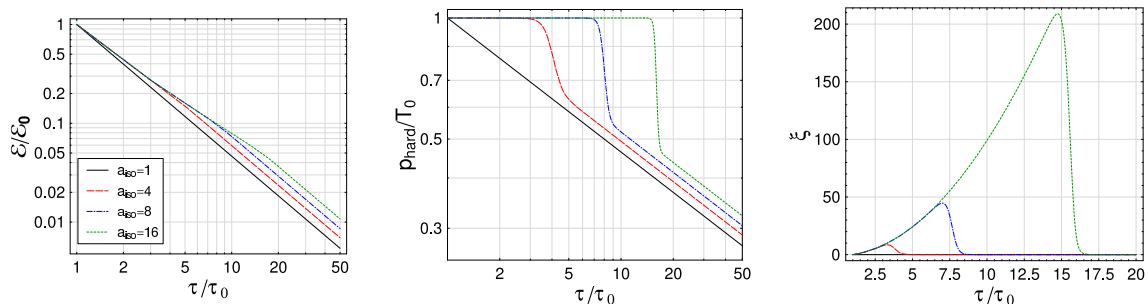


Figure 9.15: Model energy density (left), hard momentum scale (middle), and anisotropy parameter (right) for four different isotropization times $\tau_{\text{iso}} \in \{0.1, 0.4, 0.8, 1.6\}$ fm/c assuming $\tau_0 = 0.1$ fm/c. The transition width is taken to be $\gamma = 2$. Initial energy density and τ_0 are for LHC. [251]

where $\mathcal{E}_{\text{f.s.}} \sim \tau^{-1}$. In the limit $\tau \ll \tau_{\text{iso}}$ the system behaves as in the free streaming limit, while for $\tau \gg \tau_{\text{iso}}$ it expands hydrodynamically. Fig. 9.15 shows the time dependence of \mathcal{E} , p_{hard} , and ξ assuming $\gamma = 2$ for different values of τ_{iso} .

Implementing the model like this leads to different multiplicities in the hydrodynamical phase for different τ_{iso} . However, what is measured in experiments is the multiplicity of particles, such that we should have this quantity fixed to be able to compare different model realizations as discussed in [252]. To guarantee the same multiplicity in the hydrodynamical phase for different τ_{iso} , we modify the time dependence of the hard momentum scale in the following way:

$$p_{\text{hard}}(\tau) = T_0 \frac{[\mathcal{R}(a_{\text{iso}}^2 - 1)]^{\lambda/4}}{[\mathcal{R}(a_{\text{iso}}^2 - 1)]^{1/4}} \left(\frac{a_{\text{iso}}}{a}\right)^{\lambda/3} \left(\frac{1}{a_{\text{iso}}}\right)^{1/3} \quad (9.75)$$

Fig. 9.16 shows the modified ansatz (9.75), which leads to the same multiplicity in the hydrodynamical phase, but, as a consequence, a different initial hard momentum scale and energy density for different τ_{iso} .

We now present results for the expected photon yields at mid-rapidity for Pb-Pb collisions at full LHC beam energy of $\sqrt{s} = 5.5$ TeV. The critical temperature is chosen to be $T_C = 160$ MeV, which sets τ_f , the time at which all emission from the QGP-phase stops. The initial time is $\tau_0 = 0.11$ fm/c and the initial temperature $T_0 = 0.845$ GeV. The same values as used in [93] and [14] to allow for a comparison. Fig. 9.17 shows the results for fixed initial conditions and parametrization (9.73), with $\tau_{\text{iso}} = \tau_0 = 0.11$ fm/c, representing pure hydrodynamical evolution and $\tau_{\text{iso}} = 2$ fm/c including an evolving anisotropic stage for 1.89 fm/c before the system becomes isotropic and continues to expand hydrodynamically. We find that mainly due to the constant initial hard momentum scale the photon yield increases in the second scenario (red squares in Fig. 9.17). Compared to the pure hydrodynamical evolution (black circles in Fig. 9.17) the increase is approximately a factor of 6 at $q_t = 5$ GeV. The yield even lies above the sum from all contributions considered by [14], which apart from the thermal QGP contributions includes those from jet-photon conversion and the hadron gas phase. However, it should be compared to the sum of all contributions without the thermal QGP part (purple triangles in Fig. 9.17, because it replaces the thermal calculation (neglecting bremsstrahlung as discussed above). This way we find it to be the

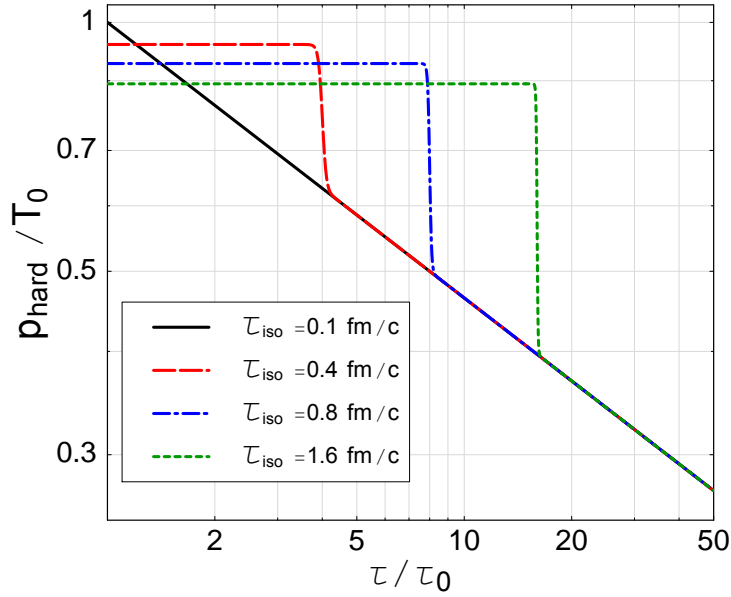


Figure 9.16: Modification of the time dependence of the hard momentum scale for four different isotropization times $\tau_{\text{iso}} \in \{0.1, 0.4, 0.8, 1.6\}$ fm/c assuming $\tau_0 = 0.1$ fm/c and transition width $\gamma = 2$. τ_0 is for LHC.

dominating contribution in the range $1 \text{ GeV} < q_t < 8 \text{ GeV}$. Assuming that the background, mainly coming from pion decays, can be subtracted efficiently, one can extract information about the anisotropy of the system from photon yields.

Fixing the initial multiplicity in the hydrodynamical phase leads to very similar results in the two scenarios of pure hydrodynamical evolution and for an isotropization time of 2 fm/c. This is mainly due to the now adjusted initial hard momentum scale that goes down for later τ_{iso} (see Fig. 9.16). The most realistic scenario lies somewhere between the two presented parametrizations. The soft particles, which are responsible for the main part of the entropy production, isotropize earlier while the hard particles remain anisotropic longer and dominate the high momentum photon production. Hence, $\tau_{\text{iso}}(p_{\text{soft}})$ should be used for fixing the initial multiplicity, while $\tau_{\text{iso}}(p \geq p_{\text{soft}}) > \tau_{\text{iso}}(p_{\text{soft}})$ should be used in the calculation of the yield. In addition, modifications to the free streaming parametrization of ξ follow from calculations in [254, 221].

9.5 Conclusions

We showed that the differential high-energy medium photon production rate is sensitive to quark-gluon plasma momentum-space anisotropies with the sensitivity increasing with photon energy. In order to translate this behavior into an experimental observable, we applied a phenomenological model that takes into account the evolution of the momentum-space anisotropy of the parton distribution functions, and calculated the photon yield. For the

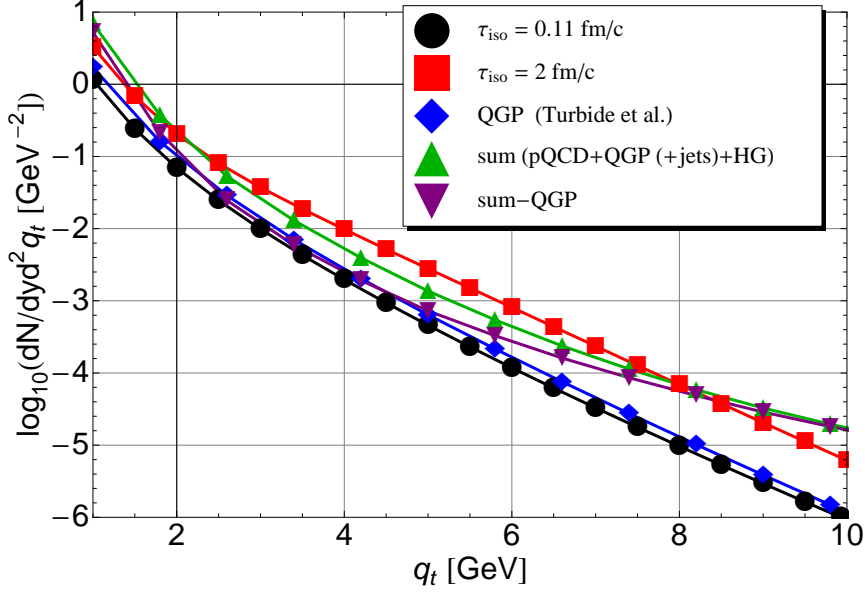


Figure 9.17: Photon yield for fixed initial conditions. $\sqrt{s} = 5.5$ TeV, $T_0 = 845$ MeV, $y_\gamma = 0$. The calculations for $\tau_{\text{iso}} = \tau_0 = 0.11$ fm/c (Hydrodynamic case) and $\tau_{\text{iso}} = 2$ fm/c are compared to the results from Turbide et al. [14] where the thermal QGP result (also with $\tau_{\text{iso}} = \tau_0 = 0.11$ fm/c) additionally contains leading order bremsstrahlung and inelastic pair annihilation contributions. The sum contains all contributions from prompt photons (including jet fragmentation), jet bremsstrahlung, thermal QGP, jet-photon conversion, and the hadron gas phase. The last line shows the sum without the thermal QGP contribution.

same initial hard momentum scale and energy density, the scenario with an initial anisotropy lead to an approximately 6 times larger yield above $q_t = 4$ GeV, as compared to the scenario with instantaneous isotropization and a purely hydrodynamical evolution. Fixing the initial multiplicity of the hydrodynamical phase reduced this enhancement dramatically, since the initial energy density and hard momentum scale were reduced for a larger isotropization time. However, since the isotropization time should be a function of the particle momenta, the correct answer should lie somewhere between the two simplified scenarios. In addition, other observables might help to remove the ambiguity in the plasma initial conditions at $\tau \sim Q_s^{-1}$.

In summary, we found that although the strong dependence on the system's anisotropy of the rate is reduced significantly when integrating over the space-time evolution of the system, there is still an effect on the observable photon yield. Of course, extracting those differences of factors of 2–6 in the photon yield, is a daunting task experimentally, especially due to the large background from decay photons that we have not shown here.

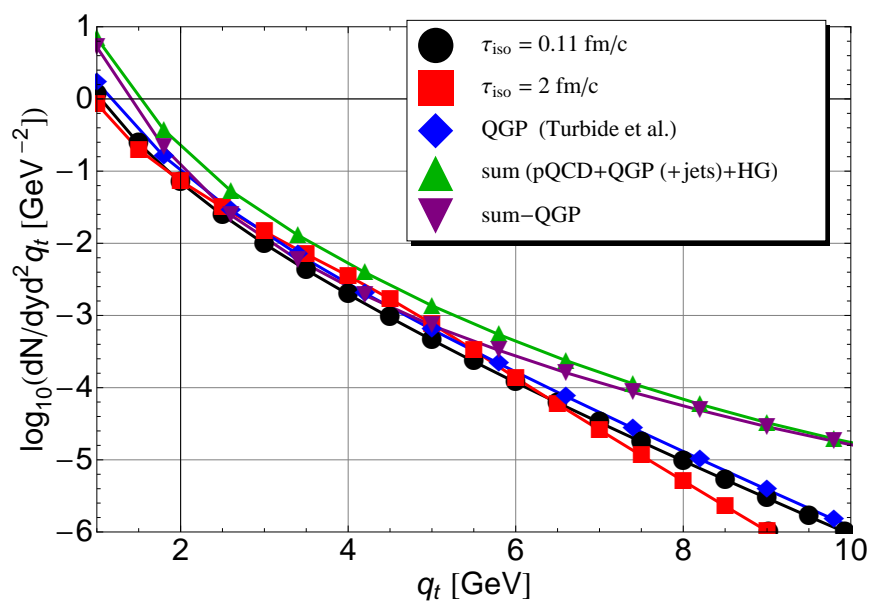


Figure 9.18: Same as Fig. 9.17 but for fixed initial multiplicity in the hydrodynamic phase. Again the last three curves are results obtained by Turbide et al. [14].

10 Conclusions and Outlook

Wie alles sich zum Ganzen webt,
Eins in dem andern wirkt und lebt!

Faust. Eine Tragödie, Nacht. Faust.
Johann Wolfgang von Goethe (1749-1832)

In this work, we have investigated the collective modes of the pre-equilibrium quark-gluon plasma, as created in heavy-ion collisions. We concentrated particularly on the unstable modes, the so-called chromo-WEIBEL-instabilities, which could provide an explanation for the fast isotropization and thermalization of the QGP. After having derived the framework of kinetic theory for non-Abelian plasmas, we reviewed the extension to anisotropic systems, in which plasma instabilities are generically present. To answer the question, whether plasma instabilities can actually contribute significantly to isotropization and equilibration during the early stage of a heavy-ion collision, we studied the effect of collisions among the particles, which are expected to reduce the growth rate of the unstable modes due to their randomizing effect. At infinitely small coupling, instabilities dominate and collisions among the particles are parametrically suppressed. However, at couplings present in heavy-ion collision experiments, they become important. Additionally, the equilibration due to instabilities only happens indirectly, because the instabilities driven isotropization is a mean-field reversible process, which does not produce entropy. Collisions, being responsible for the dissipation are needed to reach the equilibrium state of maximum entropy. We investigated the effect of collisions on the unstable modes in a model calculation introducing a BGK-collision-term (similar to the relaxation time approximation) in the hard-loop limit, as well as in a classical real-time lattice calculation beyond the hard-loop limit, which allows to simulate the full dynamics of the system. In both cases it turns out that the randomizing effect of the collisions slows down the growth of the unstable modes. Furthermore, it was shown that there exists an upper limit of the collisional frequency beyond which the instabilities cease to exist. However, they are still present for a reasonable estimate of the collision rate in heavy-ion collisions, and were shown to continue to dominate the isotropization of the system in the numerical simulation.

The introduction of hard binary collisions to the colored-particle-in-cell simulation of the WONG-YANG-MILLS system lead to a new kind of parton-cascade including particle-field interactions in addition to the usually present collision term. With this advance the simulation does not have to implicitly rely on assumptions from equilibrium physics, such as thermal DEBYE-screening, to regulate infrared problems encountered in the existing cascade codes. This way one can study non-equilibrium dynamics, for which the screening mass can become imaginary, because the soft momentum exchanges are mediated by the self-consistently generated fields and do not have to be screened artificially. This also means that the simulations are capable of describing collective phenomena like plasma instabilities, which is impossible in usual parton-cascade simulations.

In the simulation, interactions with momentum exchange below the separation momentum are mediated by the fields, whereas higher momentum scatterings are described by the collision term. A physically sensible choice for the separation scale is the temperature (or hard momentum scale for a non-equilibrium system), because below the temperature occupation numbers are large and the description of the degrees of freedom by classical fields becomes valid. Above the temperature, occupation numbers are small and the used collision term describes the interactions more appropriately. We showed that the momentum space diffusion of high transverse momentum particles is independent of the lattice spacing, and hence the separation scale between the field and particle description, when matching the energy densities of the fields and particles appropriately. This lead to the first cutoff independent estimate for the transport coefficient \hat{q} . Another important result is that the contribution from low momentum exchange scatterings, mediated by the fields, is not negligible (contributes about 25%) when the separation momentum is of the order of the temperature.

Extending the investigation of hard probes to pre-equilibrium situations, we studied the effect of plasma instabilities on jet propagation. Interestingly, the domains of growing fields turn out to bend transversely directed particles stronger along the beam direction than in the transverse plane. The reason is the creation of large domains of strong chromo-electromagnetic fields, with $B_{\perp} > E_{\perp}$ and $E_z > B_z$, which cause the observed broadening. This is not obvious for a non-Abelian plasma, because as opposed to electromagnetic plasmas all field components grow during instability evolution. This finding provides a possible explanation (or at least a contribution to the full effect) for the experimental observation that high-energy jets traversing the plasma perpendicular to the beam axis experience much stronger broadening in rapidity than in azimuth.

In the future, the extended CPIC-simulation will be used to further the understanding of energy deposition of jets in the medium and study medium reponse to the jets. In addition, one can study the shear-viscosity to entropy ratio of the simulated system, a measure that is used to determine whether the system is strongly coupled or not.

To complete our investigation of unstable modes in the hard-loop limit, we extended the exploration of the collective modes of an anisotropic quark-gluon plasma by studying the quark collective modes. Specifically, we derived integral expressions for the quark self-energy for arbitrary anisotropy and evaluated these numerically. In the direct numerical calculation only real time-like fermionic modes and no unstable modes were found. Additionally, using complex contour integration, we have proven analytically for the cases when the wave vector of the collective mode is parallel to the anisotropy direction with arbitrary oblate distributions, and for all angles of propagation in the limit of an infinitely oblate distribution, that there are no fermionic instabilities.

Since we want to determine the the role of instabilities for equilibration in heavy-ion collisions, the knowledge of the momentum-space anisotropy is particularly important. This is due to the observation that the growth rate depends strongly on the degree of anisotropy. Therefore, we turned to the possible experimental determination of the system's anisotropy using photon production. Electromagnetic probes are sensitive to the early phases of a heavy-ion collision because of their long mean free path, which allows them to leave the created medium without further interaction. This may provide an undistorted signal of the momentum-space anisotropies in the quark and gluon distribution functions. It turned out that the differential high-energy medium photon production rate is highly sensitive to quark-

gluon plasma momentum-space anisotropies with the sensitivity increasing with photon energy. However, the strong dependence on the system's anisotropy of the rate is reduced significantly when integrating over the space-time evolution of the system. Principally, the photon yield could provide a means to extract the system's anisotropy, however, extracting the differences of factors of 2 – 6 in the yield is a daunting task experimentally, especially due to the large background.

The next step towards a complete description of photon production from an anisotropic quark-gluon plasma should be the determination of additional photon sources, like that from jet-medium interaction, in the presence of a momentum-space anisotropy.

Appendices

A Gauge covariance of the Coulomb type gauge fixing term

We show that the COULOMB type gauge fixing term

$$G^a \equiv [D_i[A], a^i]^a = \partial^i a_i^a - g f^{abc} A_i^b a^{ic} \quad (\text{A.1})$$

transforms covariantly under infinitesimal gauge transformations of the various gauge fields:

$$\begin{aligned} A_\mu &\rightarrow h A_\mu h^\dagger - \frac{i}{g} h \partial_\mu h^\dagger, \\ a_\mu &\rightarrow h a_\mu h^\dagger, \end{aligned} \quad (\text{A.2})$$

with

$$h(x) = \exp(i\theta^a(x)T^a) = 1 + i\theta^a(x)T^a + \mathcal{O}(\theta^2). \quad (\text{A.3})$$

That is,

$$\begin{aligned} A_i^b &\rightarrow A_i^b - \frac{1}{g} \partial_i \theta^b(x) + f^{bde} A_i^d \theta^e(x), \\ a_i^a &\rightarrow a_i^a - f^{abc} \theta^b(x) a_i^c. \end{aligned} \quad (\text{A.4})$$

Under these transformations the gauge fixing term (A.1) transforms into

$$\begin{aligned} \partial^i a_i^a - g f^{abc} A_i^b a^{ic} &\rightarrow \partial^i a_i^a - f^{abc} \partial^i (\theta^b(x) a_i^c) - g f^{abc} A_i^b a^{ic} + f^{abc} (\partial_i \theta^b(x)) a^{ic} \\ &\quad - g f^{abc} f^{bde} A_i^d \theta^e(x) a^{ic} + g f^{abc} f^{cde} A_i^b \theta^d(x) a^{ie} + \mathcal{O}(\theta^2) \\ &= \partial^i a_i^a - g f^{abc} A_i^b a^{ic} - f^{abc} \theta^b(x) \partial^i a_i^c \\ &\quad - g f^{aec} f^{ebd} A_i^b \theta^d(x) a^{ic} + g f^{abe} f^{edc} A_i^b \theta^d(x) a^{ic} + \mathcal{O}(\theta^2), \end{aligned} \quad (\text{A.5})$$

where we renamed color indices in the second step. If this result is equal to

$$h G h^\dagger, \quad (\text{A.6})$$

we have shown that G transforms covariantly under the gauge transformations (A.2). Using (A.3) we can write (A.6) as

$$\begin{aligned} \partial^i a_i^a T^a + i\theta^b(x) \partial^i a_i^c [T^b, T^c] - g f^{abc} A_i^b a^{ic} T^a + i g f^{ebc} \theta^d(x) A_i^b a^{ic} [T^e, T^d] + \mathcal{O}(\theta^2) \\ = \partial^i a_i^a T^a - g f^{abc} A_i^b a^{ic} T^a - f^{abc} \theta^b(x) \partial^i a_i^c T^a - g f^{ebc} f^{aed} \theta^d(x) A_i^b a^{ic} T^a + \mathcal{O}(\theta^2). \end{aligned} \quad (\text{A.7})$$

Using the Jacobi identity

$$f^{bec} f^{ade} + f^{aec} f^{dbe} + f^{dec} f^{bae} = 0, \quad (\text{A.8})$$

we can rewrite the last term in Eq. (A.7) to read

$$-g f^{ebc} f^{aed} \theta^d(x) A_i^b a^{ic} T^a = -g f^{aec} f^{ebd} A_i^b \theta^d(x) a^{ic} T^a + g f^{abe} f^{edc} A_i^b \theta^d(x) a^{ic} T^a, \quad (\text{A.9})$$

and have thereby shown that the right hand sides of Eqs. (A.5) and (A.7) are equivalent and hence that

$$G \rightarrow h G h^\dagger. \quad (\text{A.10})$$

B Experimental evidence of the Weibel instability in plasma physics

To stress that plasma instabilities are not merely theoretical ideas but can be observed experimentally outside heavy-ion physics, we quote recent results in plasma physics showing experimental evidence for the occurrence of WEIBEL-like instabilities.

In measurements of energetic electron beams generated from ultrahigh intensity laser interactions the beams have been shown to be unstable to filamentation instabilities in the regime where the beam density approaches the density of the background plasma. [255, 256]

Development of laser systems producing pulses focused to extreme intensities made possible the exploration of relativistic plasma physics in the laboratory. When such high intensity laser pulses are focused into a plasma, very energetic electrons, ions, and gamma rays can be observed. One of the most exciting applications for these exotic laser-produced plasmas is in the context of fast ignition [257, 258] for inertial confinement fusion. In this scheme, a high power laser generates a short pulse, high current electron beam at the edge of a cold, highly compressed plasma of deuterium and tritium. This electron beam is then used to spark a burn wave able to propagate throughout the fuel - consequently generating fusion energy. Since current laser systems are unable to generate electron beams with sufficient current density to be useful for fast ignition the propagation of electron beams produced by state-of-the-art laser systems in lower density plasmas has been studied [255].

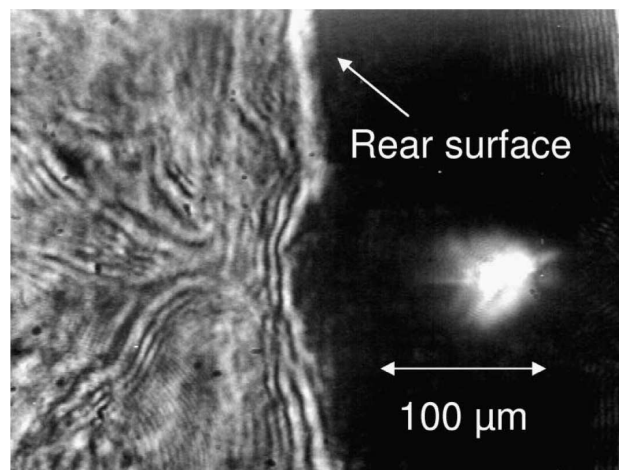


Figure B.1: Shadowgraph at later times in helium (300 ps after the main interaction) Target is 50 μm thick Mylar. The filamentation is likely the result of a WEIBEL-like instability. Picture taken from [255]

Fig. B.1 shows the propagation path of an electron beam exiting a $50\ \mu\text{m}$ Mylar target into a low density helium plasma. The probe image shown is taken at late time (300 ps after the pulse). In this experiment the electron beam remains collimated over about $50\ \mu\text{m}$ upon entering the gas plasma after which it filaments. This was observed for distances of the order of $100\ \mu\text{m}$ which is about an order of magnitude larger than the electron plasma wavelength. Clearly such structures cannot be the result of energy deposition by radiation or by neutral plasma “jets” - but rather of the beam of electrons produced during the interaction. Also no significant proton or ion acceleration was observed at the rear of the target during these experiments so this is unlikely to have contributed to the observed structure. These data were also taken before shock breakout at the rear of the target which occurs several nanoseconds later. Consequently, the observed filamentation in Fig. B.1 is likely the result of a WEIBEL-like instability [152] which is observed after the beam has propagated some distance in the plasma. The WEIBEL- instability is observed as a filamentation of the electron beam due to variations in the plasma return current and will grow until the filament charge density exceeds that of the return current.

This is the most direct observation of the WEIBEL-instability, which in a similar form is expected to be relevant for the evolution of the quark-gluon plasma, as discussed in Section 4.4.

C Abelianization

We explain the phenomenon of ‘‘Abelianization’’ as described by ARNOLD and LENAGHAN in [159]. At linear order in the hard-loop approximation unstable growth continues indefinitely. However, it is possible that the self interactions of the soft fields stop the instability growth. To see how this can happen, we analyze the effective potential energy without linearization in the gauge field A^μ . The hard-loop effective action for anisotropic distribution functions f is given by [154]

$$S_{\text{eff}} = - \int_x \frac{1}{4} F^a{}_{\mu\nu} F^{a\mu\nu} - cg^2 \int_x \int_{\mathbf{p}} \frac{f(\mathbf{p})}{p} F^a{}_{\alpha\mu}(x) \left(\frac{v^\mu v^\nu}{(v \cdot D)^2} \right)_{ab} F^b{}_{\nu}{}^\alpha(x). \quad (\text{C.1})$$

The PENROSE criterion for instabilities is fulfilled when the potential energy defined by the static limit ($\omega \rightarrow 0$) of the effective action has an unstable direction. When we start with an oblate momentum distribution f for that $p_z \ll p_x, p_y$ then the spectrum of unstable modes typically has $k_z \ll k_\perp$, see [64]. That means, they vary more rapidly with z than with x or y . Let us therefore consider gauge field configurations that only depend on z :

$$\mathbf{A} = \mathbf{A}(z), \quad (\text{C.2})$$

for which we will now simplify (C.1). First rewrite (C.1) as

$$S_{\text{eff}} = - \int_x \frac{1}{4} F^a{}_{\mu\nu} F^{a\mu\nu} - cg^2 \int_x \int_{\mathbf{p}} \frac{f(\mathbf{p})}{p} W_\alpha^a W^{a\alpha}, \quad (\text{C.3})$$

where $W_\alpha = W_\alpha(x, \mathbf{v}) = \frac{v^\mu}{v \cdot D} F_{\mu\alpha}(x)$, using the anti-symmetry of $\mathbf{v} \cdot \mathbf{D}$. For static configurations $\mathbf{A}(\mathbf{x})$ in $A_0 = 0$ gauge, we obtain the effective potential

$$V_{\text{eff}} = \int_{\mathbf{x}} \frac{1}{4} F_{ij}^a F_{ij}^a + cg^2 \int_{\mathbf{x}} \int_{\mathbf{p}} \frac{f(\mathbf{p})}{p} W_k^a W_k^a, \quad (\text{C.4})$$

where

$$W_k = W_k(\mathbf{x}, \mathbf{v}) = \frac{v_i}{\mathbf{v} \cdot \mathbf{D}} F_{ik}(\mathbf{x}). \quad (\text{C.5})$$

Let us now specialize to $\mathbf{A} = \mathbf{A}(z)$, and use that

$$v \cdot D \left(A^\alpha - \frac{n^\alpha v \cdot A}{n \cdot v} \right) = v^\nu F_\nu{}^\alpha, \quad (\text{C.6})$$

which holds when $A = A(n \cdot x)$ for some constant four-vector n [259]. Now apply $(v \cdot D)^{-1}$ to both sides of (C.6) to get

$$W^\alpha = A^\alpha - \frac{n^\alpha v \cdot A}{n \cdot v}, \quad (\text{C.7})$$

which in our case ($\mathbf{n} = \mathbf{e}_z$) becomes

$$W_k = A_k - \delta_{kz} \frac{\mathbf{v} \cdot \mathbf{A}}{v_z}. \quad (\text{C.8})$$

Substituting this into the effective potential, we find that the second term is quadratic in $\mathbf{A}(z)$, meaning that it must be the same as in the linear approximation. Using the result of the linear theory we have

$$V_{\text{eff}} = \int_{\mathbf{x}} \frac{1}{4} F_{ij}^a F_{ij}^a + \int_{\mathbf{x}} \frac{1}{2} A_i^a \Pi_{ij} A_j^a, \quad (\text{C.9})$$

where Π is the self energy of the linearized theory. In \mathbf{k} space the second part can be written as

$$\int_{\mathbf{k}} \frac{1}{2} A_i^a(\mathbf{k})^* \Pi_{ij}(0, \hat{\mathbf{k}}) A_j^a(\mathbf{k}). \quad (\text{C.10})$$

Since the Fourier transform of $\mathbf{A} = \mathbf{A}(z)$ has support only for \mathbf{k} 's proportional to $\hat{\mathbf{e}}_z$, we can replace $\Pi^{ij}(0, \hat{\mathbf{k}})$ by the matrix of constants $\Pi_{ij}(0, \hat{\mathbf{e}}_z)$. The effective potential for $\mathbf{A} = \mathbf{A}(z)$ is then local in \mathbf{x} and may be written as

$$V[\mathbf{A}(z)] = \int_{\mathbf{x}} \left[\frac{1}{4} F_{ij}^a F_{ij}^a + \frac{1}{2} A_i^a \Pi_{ij}(0, \hat{\mathbf{e}}_z) A_j^a \right]. \quad (\text{C.11})$$

The first term contains cubic and quartic interactions, while the second term, representing the effects of hard particles, is quadratic in \mathbf{A} as in the linearized theory. In order to study the stability of the system, we consider the effective potential for the low momentum modes $k \rightarrow 0$:

$$\begin{aligned} \mathcal{V} &= -\frac{1}{4} g^2 [A_i, A_j]^a [A_i, A_j]^a + \frac{1}{2} A_i^a \Pi_{ij}(0, \hat{\mathbf{e}}_z) A_j^a, \\ &= \frac{1}{4} g^2 f^{abc} f^{ade} A_i^b A_j^c A_i^d A_j^e + \frac{1}{2} A_i^a \Pi_{ij}(0, \hat{\mathbf{e}}_z) A_j^a, \end{aligned} \quad (\text{C.12})$$

Let us now assume $f(\mathbf{p})$ to be axially symmetric about the z -axis and $\Pi_{ij}(0, \mathbf{e}_z)$ to have a negative eigenvalue, which is the case for oblate distributions. Using the transversality of the hard-loop self-energy ($K_\mu \Pi^{\mu\nu} = 0$) and its symmetry, we find $\Pi^{iz} = \Pi^{zi} = 0$. Then we choose the other two eigenvectors to lie along the x - and y -axis and find

$$\mathcal{V} = \frac{1}{4} g^2 f^{abc} f^{ade} A_i^b A_j^c A_i^d A_j^e - \frac{1}{2} \mu^2 (A_x^a A_x^a + A_y^a A_y^a), \quad (\text{C.13})$$

where

$$\mu^2 \equiv -\Pi_{xx}(0, \hat{\mathbf{e}}_z) = -\Pi_{yy}(0, \hat{\mathbf{e}}_z) > 0. \quad (\text{C.14})$$

\mathcal{V} is unbounded below. In particular for an Abelian configuration, which is one for that all components A_i of \mathbf{A} commute (e.g. $A_i^a = A_i \delta^{a1}$), the quartic term vanishes, leaving $\mathcal{V} = -\frac{1}{2} \mu^2 (A_x^a A_x^a + A_y^a A_y^a)$, which goes to $-\infty$ as A increases. Note that this argument only holds as long as A is small enough such that the assumption $\delta f \ll f$ is fulfilled. The unstable growth of Abelian configurations should stop when A gets as large as the scale p_{hard}/g .

To visualize the topography of \mathcal{V} for non-Abelian configurations we make some simplifying restrictions to \mathbf{A} : (i) assume \mathbf{A} to lie in an $SU(2)$ subgroup of color $SU(3)$ and (ii) take $A_z = 0$. With (i) we can replace the f^{abc} by ε^{abc} , use $\varepsilon^{abc}\varepsilon^{ade} = \delta_{bd}\delta_{ce} - \delta_{be}\delta_{cd}$, and get

$$\mathcal{V} = \frac{1}{4}g^2 \left[(A_i^b A_i^b)^2 - A_i^b A_j^c A_i^c A_j^b \right] - \frac{1}{2}\mu^2 (A_x^a A_x^a + A_y^a A_y^a). \quad (\text{C.15})$$

To make use of the symmetries we rewrite (C.15) in the form

$$\mathcal{V} = \frac{1}{4}g^2 \left\{ \left[\text{tr} \left(\mathcal{A}^\top \mathcal{A} \right) \right]^2 - \text{tr} \left[\left(\mathcal{A}^\top \mathcal{A} \right)^2 \right] \right\} - \frac{1}{2}\mu^2 \text{tr} \left(\mathcal{A}^\top P^{(xy)} \mathcal{A} \right), \quad (\text{C.16})$$

with

$$\mathcal{A} = \begin{pmatrix} A_x^1 & A_x^2 & A_x^3 \\ A_y^1 & A_y^2 & A_y^3 \\ A_z^1 & A_z^2 & A_z^3 \end{pmatrix}, \quad P^{(xy)} = \begin{pmatrix} 1 & & \\ & 1 & \\ & & 0 \end{pmatrix}, \quad (\text{C.17})$$

where the latter is the projector on the x - y -plane. \mathcal{V} is symmetric under spatial rotations

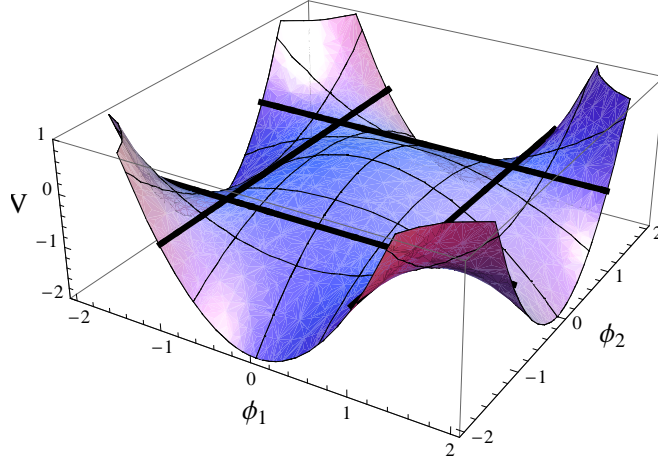


Figure C.1: Depiction of the potential $V(\phi_1, \phi_2)$ of (C.19). The ϕ_1 and ϕ_2 axis are in units of μ/g , and the values of V are in units of μ^4/g^2 . There is a local maximum with $\mathcal{V} = 0$ at the origin. The four straight lines in the plots correspond to the equipotential $V = -\mu^4/2g^2$, and the four intersection points of those lines are saddle points corresponding to static, unstable, non-Abelian configurations.

in the x - y -plane and color rotations. Together we can write that it is symmetric under the rotation $\mathcal{A} \rightarrow \mathcal{R}\mathcal{A}\mathcal{C}^\top$, where \mathcal{C} is a color rotation for the adjoint representation of $SU(2)$, represented by any 3×3 real, orthogonal matrix with $\det \mathcal{C} = 1$. \mathcal{R} is a 3×3 real, orthogonal matrix, representing spatial rotations in the x - y -plane. We can assume without loss of generality that \mathcal{A} is symmetric, since this can always be achieved by a color rotation. Restriction to $A_z = 0$ makes \mathcal{A}_{ia} zero except for $i = x, y$ and $a = 1, 2$. Then we can

diagonalize \mathcal{A} in its 2×2 subspace by a simultaneous space and color rotation $\mathcal{A} \rightarrow \mathcal{R}\mathcal{A}\mathcal{R}^\top$. So we have for $k \rightarrow 0$

$$A_i^a = \phi_1 \delta_{ix} \delta_{a1} + \phi_2 \delta_{iy} \delta_{a2}, \quad (\text{C.18})$$

and the potential becomes

$$\mathcal{V}(\phi_1, \phi_2) = \frac{1}{2} g^2 \phi_1^2 \phi_2^2 - \frac{1}{2} \mu^2 (\phi_1^2 + \phi_2^2). \quad (\text{C.19})$$

This potential is depicted in Fig. C.1. The Abelian configurations correspond to the ϕ_1 axis ($\phi_2 = 0$) and the ϕ_2 axis ($\phi_1 = 0$). The static non-Abelian solutions are indicated by the intersection points of the four straight lines in the figure. At these points, the amplitude of the gauge field is $A \sim \mu/g$. Recalling that unstable modes typically have $k_{\text{soft}} \sim \mu$, this corresponds to the non-Abelian scale $A \sim k_{\text{soft}}/g$. However, these solutions are unstable to rolling down and subsequently growing in amplitude along one of the axes. The picture suggests that, if we start from A near zero, the system might possibly at first roll toward one of these configurations with $A \sim k_{\text{soft}}/g$, but its trajectory would eventually roll away, growing along either the $\pm\phi_1$ or $\pm\phi_2$ axis until the effective action breaks down at $A \sim p_{\text{hard}}/g$. This effect of unstable growth of the gauge fields towards an Abelian configuration is called ‘‘Abelianization’’.

D Hamiltonian formulation of lattice gauge theory

We present the derivation of the Hamiltonian formulation of lattice gauge theory based on the work by KOGUT and SUSSKIND [260] using simple correspondences to the rigid rotator in three dimensions.

D.1 Fermion fields on a lattice

Although we restrict our investigations to pure gauge field dynamics, we now start with the lattice formulation for fermion fields for generality. We denote a link between two lattice sites by (\mathbf{r}, \hat{m}) , where \mathbf{r} denotes the position on the lattice, and \hat{m} points in one of the 6 directions emanating from that site. Defining the two-component spinor $\Psi(r)$, we can write down the discrete Hamiltonian that reproduces the DIRAC theory in the continuum:

$$H = a^{-1} \sum_{r,n} \Psi^\dagger(r) \frac{\boldsymbol{\sigma} \cdot \mathbf{n}}{i} \Psi(r+n) + m_0 \sum_r (-1)^r \Psi^\dagger(r) \Psi(r), \quad (\text{D.1})$$

with lattice spacing a .

The transformation of the fermion field under *global* gauge transformations reads

$$\Psi'(r) = e^{i\boldsymbol{\tau} \cdot \boldsymbol{\alpha}/2} \Psi(r) \equiv V \Psi(r), \quad (\text{D.2})$$

where $\boldsymbol{\tau}$ is a vector of generators of the group and the parameter $\boldsymbol{\alpha}$ the analog of a vector of rotation angles. The Hamiltonian (D.1) is invariant under such transformations. However, under *local* transformations

$$\Psi'(r) = e^{i\boldsymbol{\tau} \cdot \boldsymbol{\alpha}(r)/2} \Psi(r) \equiv V(r) \Psi(r), \quad (\text{D.3})$$

this is not the case, since H in (D.1) contains products of fields at separated points. Note that without loss of generality we concentrate on the invariance under spatially dependent gauge transformations. Then we can set the time component of the vector potential to zero when the gauge field enters the theory. To compensate the lack of local invariance, we introduce a gauge field $\tilde{\mathbf{A}}$ and place it on each link. Furthermore, on each link we define a unitary transformation:

$$U(r, m) = \exp \left(\frac{i}{2} \boldsymbol{\tau} \cdot \tilde{\mathbf{A}}(r, m) \right). \quad (\text{D.4})$$

To place the gauge field on the link is natural because it transports color information between lattice points. The two indices of the matrix $U(r, m)^i_j$ can be identified with the two ends of the link m .

A gauge transformation acts on U like

$$U'(r, m) = V(r)U(r, m)V^{-1}(r + m). \quad (\text{D.5})$$

We can now use U to convert non-gauge-invariant products of spatially separated fields to gauge-invariant products as initially intended. For example the non-gauge-invariant product

$$\Psi^\dagger(r)\Psi(r + m) \rightarrow \Psi^\dagger(r)V^{-1}(r)V(r + m)\Psi(r + m) \quad (\text{D.6})$$

is rewritten as

$$\begin{aligned} \Psi^\dagger(r)U(r, m)\Psi(r + m) &\rightarrow \Psi^\dagger(r)V^{-1}(r)V(r)U(r, m)V^{-1}(r + m)V(r + m)\Psi(r + m) \\ &= \Psi^\dagger(r)U(r, m)\Psi(r + m), \end{aligned} \quad (\text{D.7})$$

which is gauge-invariant. The gauge transformations acting on the ends of the link undo the gauge transformations of the fermion fields.

Let us render the Hamiltonian gauge-invariant:

$$H = a^{-1} \sum_{r, m} \Psi^\dagger(r) \frac{\boldsymbol{\sigma} \cdot \mathbf{m}}{i} U(r, m) \Psi(r + m), \quad (\text{D.8})$$

where we dropped the mass term, which is not affected by the changes. To check whether the continuum limit is correctly reproduced we first write

$$\begin{aligned} H &= a^3 \sum_{r, m} \Psi^\dagger(r) \frac{\boldsymbol{\sigma} \cdot \mathbf{m}}{i a} e^{i\boldsymbol{\tau} \cdot \tilde{\mathbf{A}}(r, m)/2} \left(1 - e^{-i\boldsymbol{\tau} \cdot \tilde{\mathbf{A}}(r, m)/2}\right) \Psi'(r + m) \\ &\quad + a^3 \sum_{r, m} \Psi^\dagger(r) \frac{\boldsymbol{\sigma} \cdot \mathbf{m}}{i a} \Psi'(r + m), \end{aligned} \quad (\text{D.9})$$

with $\Psi'(r) = a^{-3/2}\Psi(r)$. To take the continuum limit, we have to assume that $(1 - e^{-i\boldsymbol{\tau} \cdot \tilde{\mathbf{A}}(r, m)/2})$ tends to 0 as $a \rightarrow 0$. Then we can expand the exponential in H :

$$\begin{aligned} H &= a^3 \sum_{r, m} \Psi^\dagger(r) \frac{\boldsymbol{\sigma} \cdot \mathbf{m}}{i a} \left(i \frac{1}{2} \boldsymbol{\tau} \cdot \tilde{\mathbf{A}}(r, m)\right) \Psi'(r + m) \\ &\quad + a^3 \sum_{r, m} \Psi^\dagger(r) \frac{\boldsymbol{\sigma} \cdot \mathbf{m}}{i a} \Psi'(r + m). \end{aligned} \quad (\text{D.10})$$

For $a \rightarrow 0$,

$$\Psi^\dagger(r) \frac{\boldsymbol{\sigma} \cdot \mathbf{m}}{i a} \Psi'(r + m) \rightarrow \bar{\Psi}'(r) \gamma_i \partial_i \Psi'(r), \quad (\text{D.11})$$

the well known kinetic energy term. Reintroducing the mass term, the full continuum Hamiltonian reads

$$H = \int_r \left[\bar{\Psi}'(r) i \gamma_i \partial_i \Psi'(r) - \bar{\Psi}'(r) \gamma_i \frac{\tilde{\mathbf{A}}_i(r)}{a} \cdot \frac{\boldsymbol{\tau}}{2} \Psi'(r) + m_0 \bar{\Psi}'(r) \Psi'(r) \right], \quad (\text{D.12})$$

which we recognize as the one for usual YANG-MILLS gauge theory when identifying

$$\tilde{\mathbf{A}}_i(r) = ag\mathbf{A}_i(r), \quad (\text{D.13})$$

with the vector potential \mathbf{A} and the coupling constant g .

D.2 Gauge field on a lattice and analogy to the rigid rotator

In YANG-MILLS theory the local degree of freedom, $U(r, m)$, is an element of the group. The $SU(2)$ algebra is isomorphic to that of $SO(3)$, the group of rotations in three-dimensional space. This is fortunate, since, being a non-Abelian compact group, the topology of the configuration space at a link is closed and nontrivial. We use this correspondence to the quantum rigid rotator to gain some insight of the nature of the gauge-field degree of freedom.

A configuration of the rigid rotator is specified by a rotation from the space-fixed to the body-fixed axes. It may be represented in the form

$$U_j = \exp(i\mathbf{T}_j \cdot \boldsymbol{\Omega}) \quad (\text{D.14})$$

with $T_{j\alpha}$, ($\alpha = 1, 2, 3$) being the representation matrices of the generators of the rotation group for angular momentum j . $j = 1/2$ corresponds to 2×2 matrices, the defining representation of $SU(2)$ ¹, $j = 1$ to 3×3 matrices, $j = 3/2$ to 4×4 matrices and so on. We define lower indices of matrices and vectors to refer to space-fixed axes, and upper indices to refer to body-fixed axes. So V_i are the components of a vector in the space-fixed frame and $(U_1)^l{}_i V_i = V^l$ the corresponding body components. Remembering that we associated the two indices of U in the YANG-MILLS theory with the two ends of a link, we find a first correspondence: Rotation from a space fixed to a body fixed coordinate system for the rigid rotator corresponds to a ‘rotation’ from the beginning of a link to its end. Simultaneous body and space rotations correspond to global gauge transformations, while separate body and space rotations correspond to local gauge transformations. The body (upper) index corresponds to the final end of a link, the space (lower) index to the beginning end of a link. The angular velocity of the rigid rotator is

$$\boldsymbol{\omega} = \frac{d}{dt} \boldsymbol{\Omega}. \quad (\text{D.15})$$

The angular momentum \mathbf{J} , which is the generator of space rotations, is given by $I\boldsymbol{\omega}$, where I is the moment of inertia of the rigid body. The Hamiltonian reads

$$H = \frac{\mathbf{J}^2}{2I} = \frac{1}{2} I \boldsymbol{\omega}^2. \quad (\text{D.16})$$

The action of a rotation of the space-axes on U is given by left multiplication of the appropriate rotation matrix, say V . Similarly, that of a rotation of the body-axes relative to the body is given by right multiplication. Considering a spherical rotator (only a spherical rotator has invariance under rotation of the body-axes), we find that invariance under separate space and body rotations for the rigid rotator corresponds to local gauge invariance in the YANG-MILLS theory. The Hamiltonian (D.16) is invariant under individual body and space rotations. In fact, with $\mathcal{J} = U_1 \mathbf{J}$, the generator of body rotations, (D.16) may be written as

$$H = \frac{\mathcal{J}^2}{2I}. \quad (\text{D.17})$$

¹This representation is responsible for the name SU , an acronym for “Special Unitary”. Exponentiating the generators of the $j = 1/2$ representation to get the representation of the finite group elements gives the most general 2×2 unitary matrices with determinant 1. The “special” means that the determinant is equal to 1 instead of being a complex number of absolute value 1.

The body- (space-) fixed angular momenta, $\mathcal{J}(\mathbf{J})$, correspond to the generators of gauge transformations in the YANG-MILLS theory that rotate only one end of the link. Let us denote these operators as Q_- and Q_+ , where the $-$ ($+$) indicates the beginning (end) of a link. By correspondence to

$$\mathcal{J}^\alpha = (U_1)^\alpha_\beta J_\beta, \quad (\text{D.18})$$

we find

$$Q_+^\alpha = (U_1)^\alpha_\beta (Q_-)_\beta. \quad (\text{D.19})$$

We can further identify the total color carried by a link with the difference $Q = Q_+ - Q_-$. Another important correspondence can be drawn from the expressions for rotations (D.4) and (D.14):

$$\Omega \rightarrow \tilde{\mathbf{A}}, \quad (\text{D.20})$$

and hence

$$\dot{\Omega} = \omega = \mathbf{J}/I \rightarrow \dot{\tilde{\mathbf{A}}}. \quad (\text{D.21})$$

D.3 Gauge-invariant space of states

We have now shown the correspondence between a link in the YANG-MILLS theory with a rigid rotator in three dimensions. Evidently the space of states of the YANG-MILLS theory is the product of an infinite number of rigid rotators. The physical states are drawn from the space of gauge-invariant states.

An arbitrary gauge transformation can be built from individual gauge transformations at the points of the lattice. Therefore it suffices to consider only a gauge transformation at a single lattice site i . This gauge transformation affects all of the six links that emanate from site i . Thus, the generator G must be equal to the sum of the generators Q_+ over the six links

$$G(r) = \sum_m Q_+(r, m). \quad (\text{D.22})$$

In (D.21) we showed that \mathbf{J}/I corresponds to $\dot{\tilde{\mathbf{A}}}$. Hence, by the correspondence between \mathbf{J} and Q_+ , Q_+ is proportional to $\dot{\tilde{\mathbf{A}}}$. Accordingly, the generator $G(r)$ may be written as

$$G(r) = \text{const} \times \sum_m \dot{\tilde{\mathbf{A}}}(r, m). \quad (\text{D.23})$$

The time derivative of the vector potential can be identified with the component of the non-Abelian electric field at position r in direction m . The sum of electric fields emanating from a single lattice site is the lattice analog of $\nabla \cdot \mathbf{E}$ at site r . Because \mathbf{E} varies from $Q_-(r, m)$ to $Q_+(r, m)$ along a link, there is an additional contribution to the lattice analog of $\nabla \cdot \mathbf{E}$, which is associated with the links: $Q_+(r, m) - Q_-(r, m)$, the charge carried by the links. So

$$G(r) = (\nabla \cdot \mathbf{E})(r) - \frac{1}{2} \sum_m Q(r, m). \quad (\text{D.24})$$

The gauge-invariance of the physical sector is defined by $G(r)|\Psi\rangle = 0$. Identifying $\frac{1}{2} \sum_m Q(r, m)$ as the local color density ρ_G (G for gluons), this constraint becomes the familiar

$$\nabla \cdot \mathbf{E} = \rho_G. \quad (\text{D.25})$$

Defining $|0\rangle_G$ as the gauge-invariant state given by the product over all lattice sites of the individual gauge field ground states, we can construct the full gauge-invariant space of states by acting on $|0\rangle_G$ with any product of components of $U_{1/2}(r, m)$

$$\prod_{r, m \in \{s\}} U_{1/2}(r, m)^i_l |0\rangle_G. \quad (\text{D.26})$$

The set $\{s\}$ may contain any link any number of times. Note that (D.26) describes a gauge-invariant state only if the color indices at each point are contracted to form a local singlet. Indices associated with different lattice sites may not be contracted, because they do not transform identically under local gauge transformations. Let us give some examples:

$$U_{1/2}(r, m)^i_l |0\rangle \quad (\text{D.27})$$

is not a gauge-invariant state because it has uncontracted indices.

$$U_{1/2}(1)^i_j U_{1/2}(2)^j_k U_{1/2}(3)^k_l U_{1/2}(4)^l_i |0\rangle, \quad (\text{D.28})$$

where the numbers 1, 2, 3 and 4 refer to the links shown in Fig. D.1, is gauge-invariant. However, if the contractions do not involve the same lattice site, the object would not be

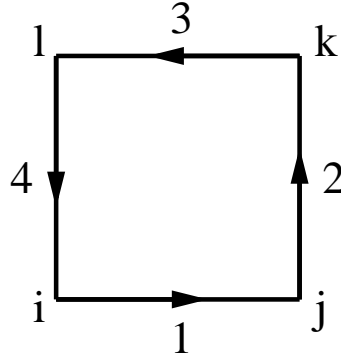


Figure D.1: Graphical representation of the gauge-invariant operator $\text{Tr} U_{1/2}(1)U_{1/2}(2)U_{1/2}(3)U_{1/2}(4)$.

gauge-invariant as in this example:

$$U_{1/2}(1)^i_j U_{1/2}(3)^j_k U_{1/2}(2)^k_l U_{1/2}(4)^l_i |0\rangle. \quad (\text{D.29})$$

When we include the fermion field Ψ some more gauge-invariant objects can be constructed. We can construct a gauge-invariant state by considering the lowest eigenstate of the gauge-invariant charge-conjugation-invariant operator

$$\sum_r (-1)^r \Psi^\dagger(r) \Psi(r) |0\rangle_F, \quad (\text{D.30})$$

where the state $|0\rangle_{\text{F}}$ is a product of fermion vacua over all lattice sites. The product state $|0\rangle = |0\rangle_{\text{F}}|0\rangle_{\text{G}}$ is gauge-invariant. In addition to the gauge-invariant operators formed from closed paths (e.g. D.28) we can now form gauge-invariant operators from paths with ends. For example, considering a path Γ beginning at site r and ending at site s , we can form the gauge-invariant object

$$U(\Gamma, \Sigma) = \Psi^\dagger(r) \Sigma U_{1/2}(r, n) U_{1/2}(r+n, m) \cdots U_{1/2}(s-l, l) \Psi(s), \quad (\text{D.31})$$

where Σ is any 2×2 spin matrix. Physically the lines between occupied sites represent electric flux. To see this recall from above that the operator $Q_+(r, m)$ is proportional to the electric field at site r and points in direction m . On all links where there is no $U_{1/2}(r, m)$, $Q_+(r, m)$ gives zero, while on the links through which a line Γ_j has passed, $Q_+^2(r, m)$ gives $j(j+1)$ (again in analogy to the rigid rotator). Hence, one can think of the lines as containing electric flux of magnitude $\sqrt{j(j+1)}$.

Now that the fermions have been added again, the generator of gauge transformations at point r must include the additional operator $\Psi^\dagger(r) \frac{1}{2} \boldsymbol{\tau} \Psi(r)$, which generates color rotations of Ψ . The full gauge-invariance condition on the space of states becomes

$$\left(\sum_m Q_+^\alpha(r, m) - \Psi^\dagger(r) \frac{1}{2} \boldsymbol{\tau}^\alpha \Psi(r) \right) \left| \right\rangle = 0, \quad (\text{D.32})$$

which is again analogous to the condition

$$\boldsymbol{\nabla} \cdot \mathbf{E} = \rho_{\text{G}} + \rho_{\text{F}}, \quad (\text{D.33})$$

where ρ_{G} and ρ_{F} are the color densities of the gauge and fermion fields.

D.4 The gauge-field Hamiltonian

To give the field $\tilde{\mathbf{A}}$ some non-trivial dynamics we must add a pure gauge-field term to the Hamiltonian H . This term must be built from gauge-invariant operators to keep H gauge-invariant. So H may contain objects like $U(\Gamma)$ with any closed path Γ . In addition, gauge-invariant operators can be built from the $Q_\pm(r, m)$. Note that in particular $Q_+^2 (= Q_-^2)$ is the analog of J^2 for the rigid rotator. Since J^2 commutes with space and body rotations, Q_+^2 commutes with left and right gauge transformations and is therefore gauge-invariant. Since Q_+^2 does not commute with U , its appearance in the Hamiltonian will generate non-trivial dynamics. In analogy to the Hamiltonian for the rigid rotator let us include

$$\sum_{r, m} Q_+^2(r, m) / (2I) \quad (\text{D.34})$$

in the Hamiltonian, where I is a constant. (D.34) represents the energy of an assembly of uncoupled rotators. We have already mentioned that Q_+ is proportional to the color electric field. To get the correct continuum limit, the constant I in (D.34) has to be $I = a/g^2$, such that (D.34) becomes

$$\frac{a}{2g^2} \sum_{r, m} \dot{A}^2(r, m) = \frac{a^3}{2} \sum_{r, m} \dot{A}^2(r, m) = \frac{a^3}{2} \sum_{r, m} E^2(r, m), \quad (\text{D.35})$$

where we used that $\dot{\tilde{\mathbf{A}}} = Q_+/I$ and $\tilde{\mathbf{A}}_i = ag\mathbf{A}_i$. In the continuum limit this turns into

$$\frac{1}{2} \int d^3x E^2. \quad (\text{D.36})$$

To make the pure YANG-MILLS theory non-trivial we have to include terms that couple different links using the operators $U(\Gamma)$. Obviously there is a great deal of arbitrariness involved in the choice of the Γ . Following WILSON [261], we pick the simplest object $U_{\square} := U(\Gamma)$ that reproduces the continuum YANG-MILLS theory in the limit $a \rightarrow 0$, with Γ shown in Fig. D.2. Please note that from this point on we stick to the conventions of the main text and set the τ^a to the PAULI matrices without a factor of two and absorb another factor of 2 into A , such that $U(r, x)$ becomes $e^{iagA_x(r)} = e^{iagA_x^a(r)\sigma^a}$.

$$\begin{aligned} U_{\square} &= U(r, x)U(r+x, y)U^{\dagger}(r+y, x)U^{\dagger}(r, y) \\ &= e^{iagA_x(r)}e^{iagA_y(r+x)}e^{-iagA_x(r+y)}e^{-iagA_y(r)} \\ &= e^{iagA_x(r)}e^{iagA_y(r)+ia^2g\partial_x A_y(r)}e^{-iagA_x(r)-ia^2g\partial_y A_x(r)}e^{-iagA_y(r)} \end{aligned} \quad (\text{D.37})$$

where $A_x = A_x^a \tau^a$ etc.

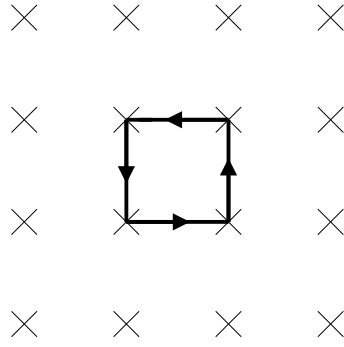


Figure D.2: The simplest gauge-invariant closed loop, the so called plaquette U_{\square} . The crosses denote lattice sites.

Let us determine the continuum limit of U_{\square} . Using

$$e^x e^y \simeq e^{x+y+\frac{1}{2}[x,y]}, \quad (\text{D.38})$$

we can write

$$\begin{aligned} U_{\square} &= \exp \left(iagA_x(r) + iagA_y(r) + ia^2g\partial_x A_y(r) - \frac{a^2g^2}{2}[A_x(r), A_y(r)] + \mathcal{O}(a^3) \right) \\ &\quad \times \exp \left(-iagA_x(r) - iagA_y(r) - ia^2g\partial_y A_x(r) - \frac{a^2g^2}{2}[A_x(r), A_y(r)] + \mathcal{O}(a^3) \right) \\ &\approx \exp [ia^2g(\partial_x A_y(r) - \partial_y A_x(r) + ig[A_x(r), A_y(r)])] \\ &= \exp (ia^2gF_{xy}(r)) , \end{aligned} \quad (\text{D.39})$$

with the spatial components F_{xy} of the field tensor. Realizing that

$$\text{Re Tr}(U_{\square}(r)) \xrightarrow{a \rightarrow 0} \text{Re Tr} \left(1 + ia^2 g F_{xy} - a^4 \frac{g^2}{2} F_{xy}^2 + \dots \right) = N_c - \frac{a^4 g^2}{2} \text{Re Tr}(F_{xy}^2), \quad (\text{D.40})$$

we can identify the lattice version of the color magnetic field contribution to the Hamiltonian to be

$$\frac{2}{ag^2} \sum_{\square} (N_c - \text{Re Tr} U_{\square}), \quad (\text{D.41})$$

where the sum runs over all plaquettes \square , which includes all directions of the B-field (B_x^2 , B_y^2 and B_z^2 , where B_z is shown in the example path above) at every site. The prefactor is chosen to reproduce the correct continuum limit, which reads

$$\sum_{i \leq j} \frac{2}{ag^2} \frac{a^4 g^2}{2} \text{Tr} F_{ij}^2 = 2a^3 F_{ij}^a F_{ij}^a = \frac{1}{2} \int d^3 x B^2. \quad (\text{D.42})$$

where you should note that we are sticking to our convention $[\tau^a, \tau^b] = 2\delta^{ab}$ instead of $[\tau^a, \tau^b] = 1/2 \delta^{ab}$, and that F_{ij} is half the conventional F_{ij} . B is then the usual physical B-field.

Adding the two pieces that correspond to the continuum terms $\frac{1}{2} \int d^3 x E^2$ and $\frac{1}{2} \int d^3 x B^2$, we find the lattice version of the Hamiltonian to be

$$\frac{a^3}{2} \sum_{r,m} E^2(r,m) + \frac{2}{ag^2} \sum_{\square} (N_c - \text{Re Tr} U_{\square}), \quad (\text{D.43})$$

which we can rewrite to lattice units using $\mathbf{E}_L^a = ga^2/2 \mathbf{E}^a$

$$H = \frac{2}{ag^2} \sum_{r,m} E_L^2(r,m) + \frac{2}{ag^2} \sum_{\square} (N_c - \text{Re Tr} U_{\square}). \quad (\text{D.44})$$

This form allows us to rescale and write

$$H_L = \frac{1}{2} \sum_i E_L^2(r,m) + \frac{1}{2} \sum_{\square} (N_c - \text{Re Tr} U_{\square}) = \frac{g^2 a}{4} H, \quad (\text{D.45})$$

the field part of the KOGUT-SUSSKIND-Hamiltonian used in this work. The first sum goes over all (spatial) links, the second one over all (spatial) plaquettes. Note again that the lattice is just a spatial one whereas time is continuous. Of course for actual calculations, time will be discretized. As opposed to the usual lattice formulation the Hamiltonian formulation derived above allows for realtime simulations. We only consider pure gauge field simulations in this work, but for completeness let us give the fermionic contribution to the Hamiltonian as well:

$$H_F = a^{-1} \sum \Psi^\dagger(r) \frac{\boldsymbol{\sigma} \cdot \mathbf{n}}{i} U(r,n) \Psi(r+n) + m_0 \sum (-1)^r \Psi^\dagger(r) \Psi(r). \quad (\text{D.46})$$

E The relativistic relative velocity

We derive the relativistic relative velocity of two particles and point out that \tilde{v}_{rel} in Section 6.4.1 is not the actual relative velocity. The argument is based on [262].

Let us consider two particles with velocities \mathbf{v}_1 and \mathbf{v}_2 and go to a system in that $\mathbf{v}_2 = 0$. In this system the number of collisions per time dt and volume dV is given by

$$d\nu = \sigma v_{\text{rel}} n_1 n_2 dV dt, \quad (\text{E.1})$$

which is a LORENTZ invariant. σ is the total cross section for a collision and n_1 and n_2 are the particle densities. The probability for two particles to collide is

$$P = \sigma v_{\text{rel}} \frac{dt}{dV}, \quad (\text{E.2})$$

such that

$$d\nu = P n_1 n_2 dV dV = P \Delta N_1 \Delta N_2, \quad (\text{E.3})$$

with N_1 and N_2 the number of particles of species 1 and 2 within the volume dV . Since $d\nu$ is an invariant and so are $n_1 dV$ and $n_2 dV$, P is invariant as well. We shall now derive a general expression for the invariant $d\nu$, which so far we have only expressed in the system where $\mathbf{v}_2 = 0$. In all systems $d\nu$ shall be given by

$$d\nu = A n_1 n_2 dV dt, \quad (\text{E.4})$$

where A is equal to σv_{rel} in the system where $\mathbf{v}_2 = 0$. Since $dV dt$ is invariant, $A n_1 n_2$ has to be invariant too. Let us rewrite the condition that $A n_1 n_2$ is invariant in terms of the energies of the particles: n transforms as

$$n = \frac{n_0}{\sqrt{1-v^2}}, \quad (\text{E.5})$$

because $n dV$ is invariant and dV transforms as $dV = dV_0 \sqrt{1-v^2}$, where n_0 and dV_0 are given in the rest frame of the particle. Because $E = \gamma m = 1/\sqrt{1-v^2} m$, we can write

$$n = n_0 \frac{E}{m}. \quad (\text{E.6})$$

This means that if $A n_1 n_2$ is invariant, so is $A E_1 E_2$. Now we may as well demand that $A E_1 E_2 / P_{1\mu} P_2^\mu$ is invariant, since we just divided by another invariant $P_{1\mu} P_2^\mu$. In the rest frame of particle 2 we have $E_2 = m_2$ and $\mathbf{p}_2 = 0$, such that

$$A \frac{E_1 E_2}{P_{1\mu} P_2^\mu} = A. \quad (\text{E.7})$$

Furthermore, in this rest frame, $A = \sigma v_{\text{rel}}$, such that in an arbitrary frame it has to hold that

$$A = \sigma v_{\text{rel}} \frac{P_{1\mu} P_2^\mu}{E_1 E_2}. \quad (\text{E.8})$$

Again going to the rest frame of particle 2, we can calculate the invariant

$$P_{1\mu} P_2^\mu = \frac{m_1}{\sqrt{1 - v_{\text{rel}}^2}} m_2, \quad (\text{E.9})$$

which leads to

$$v_{\text{rel}} = \sqrt{1 - \frac{m_1^2 m_2^2}{(P_{1\mu} P_2^\mu)^2}} = \sqrt{1 - \frac{m_1^2 m_2^2}{(E_1 E_2 - \mathbf{p}_1 \cdot \mathbf{p}_2)^2}}. \quad (\text{E.10})$$

Now using $\mathbf{p} = m\mathbf{v}/\sqrt{1 - v^2}$ and $E = m/\sqrt{1 - v^2}$, this becomes

$$\begin{aligned} v_{\text{rel}} &= \sqrt{1 - \frac{(1 - v_1^2)(1 - v_2^2)}{(1 - \mathbf{v}_1 \cdot \mathbf{v}_2)^2}} = \sqrt{\frac{(1 - \mathbf{v}_1 \cdot \mathbf{v}_2)^2 - (1 - v_1^2)(1 - v_2^2)}{(1 - \mathbf{v}_1 \cdot \mathbf{v}_2)^2}} \\ &= \frac{\sqrt{1 - 2\mathbf{v}_1 \cdot \mathbf{v}_2 + (\mathbf{v}_1 \cdot \mathbf{v}_2)^2 - (1 - v_1^2)(1 - v_2^2)}}{1 - \mathbf{v}_1 \cdot \mathbf{v}_2} \\ &= \frac{\sqrt{-2\mathbf{v}_1 \cdot \mathbf{v}_2 + (\mathbf{v}_1 \cdot \mathbf{v}_2)^2 - v_1^2 v_2^2 + v_1^2 + v_2^2}}{1 - \mathbf{v}_1 \cdot \mathbf{v}_2} \\ &= \frac{\sqrt{(\mathbf{v}_1 - \mathbf{v}_2)^2 + (\mathbf{v}_1 \cdot \mathbf{v}_2)^2 - v_1^2 v_2^2}}{1 - \mathbf{v}_1 \cdot \mathbf{v}_2} = \frac{\sqrt{(\mathbf{v}_1 - \mathbf{v}_2)^2 - (v_1^2 v_2^2 (1 - \cos^2 \phi))}}{1 - \mathbf{v}_1 \cdot \mathbf{v}_2} \\ &= \frac{\sqrt{(\mathbf{v}_1 - \mathbf{v}_2)^2 - (v_1^2 v_2^2 (\sin^2 \phi))}}{1 - \mathbf{v}_1 \cdot \mathbf{v}_2} = \frac{\sqrt{(\mathbf{v}_1 - \mathbf{v}_2)^2 - (\mathbf{v}_1 \times \mathbf{v}_2)^2}}{1 - \mathbf{v}_1 \cdot \mathbf{v}_2}. \end{aligned} \quad (\text{E.11})$$

This is the correct expression for the relative velocity, which is bounded from above by 1. To see how on the other hand \tilde{v}_{rel} is defined, let us plug Eq. (E.10) into (E.8) and then A into (E.4). We get

$$d\nu = \sigma \sqrt{1 - \frac{m_1^2 m_2^2}{(P_{1\mu} P_2^\mu)^2}} \frac{P_{1\mu} P_2^\mu}{E_1 E_2} n_1 n_2 dV dt = \sigma \frac{\sqrt{(P_{1\mu} P_2^\mu)^2 - m_1^2 m_2^2}}{E_1 E_2} n_1 n_2 dV dt. \quad (\text{E.12})$$

In the massless limit $m_1, m_2 \rightarrow 0$, we have

$$d\nu = \sigma \frac{P_{1\mu} P_2^\mu}{E_1 E_2} n_1 n_2 dV dt, \quad (\text{E.13})$$

which can be expressed as

$$d\nu = \sigma \frac{s}{2E_1 E_2} n_1 n_2 dV dt, \quad (\text{E.14})$$

using the MANDELSTAM variable

$$\begin{aligned} s &= (P_1 + P_2)^2 = (E_1 + E_2)^2 - (\mathbf{p}_1 + \mathbf{p}_2)^2 \\ &= E_1^2 + E_2^2 + 2E_1 E_2 - \mathbf{p}_1^2 - \mathbf{p}_2^2 - 2\mathbf{p}_1 \cdot \mathbf{p}_2 \\ &= 2(E_1 E_2 - \mathbf{p}_1 \cdot \mathbf{p}_2) = 2P_{1\mu} P_2^\mu, \end{aligned} \quad (\text{E.15})$$

because $\mathbf{p}^2 = E^2$. One may now define $\tilde{v}_{\text{rel}} = \frac{s}{2E_1 E_2}$ and write

$$d\nu = \sigma \tilde{v}_{\text{rel}} n_1 n_2 dV dt, \quad (\text{E.16})$$

however, one should keep in mind that

$$\tilde{v}_{\text{rel}} = v_{\text{rel}} \frac{P_{1\mu} P_2^\mu}{E_1 E_2}, \quad (\text{E.17})$$

is not the true relative velocity, which is given by (E.10) or (E.11). \tilde{v}_{rel} is not even less than 1, i.e., can be larger than the speed of light. The difference is just that we have absorbed the factor $P_{1\mu} P_2^\mu / E_1 E_2$ into \tilde{v}_{rel} .

F Validity of the equilibrium fluctuation dissipation relation in the hard-loop limit

In this appendix we argue that Eq. (9.37) is valid for a non-equilibrium system within the hard-loop- (HL-) framework. This is necessary because GREINER and LEUPOLD showed in [263] and [249] that it does not hold in a general non-equilibrium system. As BAIER et al. did in [244], we resum in the following way, using the self energy calculated from *free* propagators):

$$D = D_0 + D_0 \Sigma D_0 + D_0 \Sigma D_0 \Sigma D_0 + \dots = D_0 + D_0 \Sigma D. \quad (\text{F.1})$$

With the definitions $\Gamma_0(\vec{p}, p_0) := \frac{i}{2p_0} [\Sigma^>(\vec{p}, p_0) - \Sigma^<(\vec{p}, p_0)]$ and $\text{Re}\Sigma := \text{Re}\Sigma^{\text{ret}} = \text{Re}\Sigma^{\text{av}}$ we end up with

$$D^{\text{ret}} = D_0^{\text{ret}} + D_0^{\text{ret}} \Sigma^{\text{ret}} D^{\text{ret}} = \frac{1}{p^2 - m^2 - \text{Re}\Sigma + ip_0 \Gamma_0}, \quad (\text{F.2})$$

$$D^{\text{av}} = D_0^{\text{av}} + D_0^{\text{av}} \Sigma^{\text{av}} D^{\text{av}} = \frac{1}{p^2 - m^2 - \text{Re}\Sigma - ip_0 \Gamma_0}, \quad (\text{F.3})$$

$$D^< = D^{\text{ret}} \Sigma^< D^{\text{av}} = (-2i) \frac{p_0 \Gamma_0}{(p^2 - m^2 - \text{Re}\Sigma)^2 + p_0^2 \Gamma_0^2} \frac{\Sigma^<}{\Sigma^> - \Sigma^<}. \quad (\text{F.4})$$

The quantity

$$n_\Sigma(\vec{p}, p_0) := \frac{\Sigma^<}{\Sigma^> - \Sigma^<} \quad (\text{F.5})$$

appearing in the emerging fluctuation dissipation relation has to be interpreted as the ‘occupation number’ demanded by the self energy parts [249]. If the equilibrium KMS conditions (9.52) apply for the self energy part, then $n_\Sigma(\vec{p}, p_0) \xrightarrow{\text{KMS}} n_B(p_0)$ becomes just the BOSE distribution function. In the limit $g \rightarrow 0$ this factor is just 1/2 (cf. Eq.(9.51) and the discussion thereafter). Generally $D^<$ has to be proportional to some non-equilibrium distribution function f :

$$D^<(\vec{x}, t; p) \approx (-2i) \frac{p_0 \Gamma(\vec{x}, t; p)}{(p^2 - m^2(\vec{x}, t) - \text{Re}\Sigma(\vec{x}, t; p))^2 + p_0^2 \Gamma^2(\vec{x}, t; p)} f(\vec{x}, t; \vec{p}), \quad (\text{F.6})$$

which it is not in all cases, when one uses the resummation (F.1). GREINER and LEUPOLD argue that the reason for this is that the self energy parts $\Sigma^<$ and $\Sigma^>$ should also evolve with time, and do not in this scheme. They should depend on the *evolving* distribution function and not persistently on the initial one which enters Σ in (F.1). Thus the resummation of (F.1) does not cover all relevant contributions. Speaking more technically, the self energy operators must also be evaluated consistently by the fully dressed and temporally evolving

one-particle propagators. To get the correct description for every possible non-equilibrium situation, one would need to apply the appropriate (quantum) transport equations with the difference to the resummation of (F.1) that the propagators entering into the self-energy operators are then the fully dressed ones. Unfortunately, the full quantum transport equations are generally hard to solve and thus are not so much of practical use.

However, when we use squeezed equilibrium distributions as we do in Chapter 9, the same arguments as those for the equilibrium case hold and the resummation (F.1) and in particular Eq. (F.4) is valid. To make this more explicit, we can rewrite the expression (F.5) using $\Sigma_{12} = -\Sigma_{21}$, which holds for all self energies in the HL-limit, now for the case of Fermions:

$$n_{\Sigma}(\vec{p}, p_0) := \frac{\Sigma^{<}}{\Sigma^{<} - \Sigma^{>}} = \frac{\Sigma^{<}}{\Sigma^{<} + \Sigma^{<}} = \frac{1}{2} \quad (\text{F.7})$$

This is equivalent to writing f to order $\mathcal{O}(1)$:

$$f(\mathbf{p}, \xi) = \frac{1}{e^{\sqrt{\mathbf{p}^2 + \xi(\mathbf{n} \cdot \mathbf{p})^2/p_{\text{hard}}} + 1}} \rightarrow \frac{1}{2}, \quad (\text{F.8})$$

because all components of \mathbf{p} are of order gp_{hard} . This shows that at leading order in the coupling constant g (and for $g \rightarrow 0$), the fluctuation dissipation relation is valid for the hard loop self energies Σ and hence can be used in the derivation of the soft contribution to the production rate as done in Section 9.2.2.

Bibliography

- [1] G. Baym, *Rhic: From dreams to beams in two decades*, *Nucl. Phys.* **A698** (2002) XXIII–XXXII, [[hep-ph/0104138](https://arxiv.org/abs/hep-ph/0104138)].
- [2] D. J. Gross and F. Wilczek, *Ultraviolet behavior of non-abelian gauge theories*, *Phys. Rev. Lett.* **30** (1973) 1343–1346.
- [3] H. D. Politzer, *Reliable perturbative results for strong interactions?*, *Phys. Rev. Lett.* **30** (1973) 1346–1349.
- [4] E. V. Shuryak, *Theory of hadronic plasma*, *Sov. Phys. JETP* **47** (1978) 212–219.
- [5] E. V. Shuryak, *Quark-gluon plasma and hadronic production of leptons, photons and pions*, *Phys. Lett.* **B78** (1978) 150.
- [6] E. V. Shuryak, *Quantum chromodynamics and the theory of superdense matter*, *Phys. Rept.* **61** (1980) 71–158.
- [7] O. K. Kalashnikov and V. V. Klimov, *Phase transition in quark - gluon plasma*, *Phys. Lett.* **B88** (1979) 328.
- [8] J. I. Kapusta, *Quantum chromodynamics at high temperature*, *Nucl. Phys.* **B148** (1979) 461–498.
- [9] “Bevalac Synchrotron. The Bevalac started life as the Bevatron in 1954 (the “Bev” in “Bevatron” standing for “billion electron volts” - BeV). At the time, it was the world’s largest particle accelerator, capable of accelerating a beam of protons and charging the particles to 6.2 BeV. In 1974, at the age of 20, the Bevatron was at the end of its useful life for research. It was ”saved” when a proposal to convert it to a heavy ion accelerator was acted on - this would allow it to accelerate all elements on the periodic table to relativistic energies. The SuperHILAC linear accelerator located 550 ft. up the hill above the Bevatron was linked, replacing the Bevatron’s own linear accelerator. This linkage renamed the Bevatron to the Bevalac. The first beams were produced on August 1, 1974. The Bevalac ceased operations when the beam was turned off for the last time on February 21, 1993.”
<http://www.uer.ca/locations/show.asp?locid=21423>.
- [10] “Alternating Gradient Synchrotron. The name of the AGS, running since 1960, is derived from the concept of alternating gradient focusing, in which the field gradients of the accelerator’s 240 magnets are successively alternated inward and outward, permitting particles to be propelled and focused in both the horizontal and vertical plane at the same time. Capable of accelerating 25 trillion protons with every pulse, and heavy ions such as gold and iron, the AGS is used by 850 users

from 180 institutions from around the world annually. The AGS receives protons from Brookhaven's 200 million electron-volt (MeV) linear accelerator (LINAC). The AGS Booster, constructed in 1991, further augmented the capabilities of the AGS, enabling it to accelerate protons and heavy ions to much higher energies than before. Even now, the applications for the AGS continue to be expanded with the construction of the NASA Space Radiation Laboratory. Among its other duties, the AGS is now used as an injector for the Relativistic Heavy Ion Collider (RHIC)."
<http://www.bnl.gov/bnlweb/facilities/AGS.asp>.

- [11] "Super Proton Synchrotron. The Super Proton Synchrotron is the second largest machine in CERN's accelerator complex. Measuring nearly 7 km in circumference, it takes particles from the Proton Synchrotron (PS) and accelerates them to provide beams for the Large Hadron Collider (LHC), the COMPASS experiment and the CNGS project. When it switched on in 1976, the SPS became the workhorse of CERN's particle physics programme. Research using SPS beams has probed the inner structure of protons, investigated nature's preference for matter over antimatter, looked for matter as it might have been in the first instants of the Universe and searched for exotic forms of matter. A major highlight came in 1983 with the Nobel-prize-winning discovery of W and Z particles made with the SPS running as a proton-antiproton collider. The SPS has 1317 conventional (room temperature) electromagnets, including 744 dipoles to bend the beams round the ring, and it operates at up to 450 GeV. It has handled many different kinds of particles - sulphur and oxygen nuclei, electrons, positrons, protons and antiprotons."
<http://info.web.cern.ch/public/en/Research/SPS-en.html>.
- [12] "Relativistic Heavy Ion Collider. The Relativistic Heavy Ion Collider (RHIC) achieved its first successful operation in the summer of 2000, capping ten years of development. However, the history of RHIC stretches back more than 30 years beginning with an idea for a machine called the Intersecting Storage Accelerator (ISA). When single ring accelerators like the Alternating Gradient Synchrotron propel protons against a stationary target to investigate nuclear properties, much of the usable energy in the reaction is lost, carried away in the forward motion of the incident proton. This limits the energy which can be practically achieved by a single ring accelerator. It was recognized by early accelerator physicists that much higher reaction energies could be achieved by colliding two accelerated beams head-on. Using this technique, the energy released can equal the sum total carried in each beam. The idea of using storage rings for a colliding beam accelerator was considered at a summer study held at Brookhaven in 1963. Such technology was considered feasible at that time, though it was decided that no construction would take place since it was felt that storage rings lacked the versatility of a single proton accelerator of the same equivalent energy. The idea was revived in 1970 by John Blewett and this time, it was greeted with enthusiasm. A group called the Fitch committee recommended that Brookhaven apply its pioneering development work in superconducting magnets to build two proton intersecting storage rings. This was the beginning of the ISABELLE project. In 1981 technical problems were encountered in the fabrication of the superconducting magnets which would power

the machine, causing Brookhaven to replace the ISABELLE proposal with a different machine design called the Colliding Beam Accelerator (CBA). Due to the change in machine plans, the HEPAP voted in 1983 to discontinue construction of the CBA in favor of a new machine to be built in Texas called the Superconducting Supercollider (SSC) (which would ironically be abandoned itself a decade later). Physicists at Brookhaven persevered, continuing to push for an advanced accelerator design. In 1984, the first proposal was submitted for the machine now known as RHIC. RHIC's main function is to search for a state of matter called the quark-gluon plasma. It was considered very cost-effective to build RHIC at Brookhaven because of the existing accelerator infrastructure which could be used to inject protons and heavy ions into the machine as well as the fact that a tunnel (originally excavated for ISABELLE/CBA) was already completed. Brookhaven received funding to proceed with the construction of RHIC in 1991.”
http://www.bnl.gov/bnlweb/history/RHIC_history.asp.

- [13] “Large Hadron Collider. The Large Hadron Collider (LHC) is being built in a circular tunnel 27 km in circumference. The tunnel is buried around 50 to 175 m underground. It straddles the Swiss and French borders on the outskirts of Geneva. It is planned to circulate the first beams in May 2008. First collisions at high energy are expected mid-2008 with the first results from the experiments soon after. The LHC is designed to collide two counter rotating beams of protons or heavy ions. Proton-proton collisions are foreseen at an energy of 7 TeV per beam. The beams move around the LHC ring inside a continuous vacuum guided by magnets. The magnets are superconducting and are cooled by a huge cryogenics system. The cables conduct current without resistance in their superconducting state. The beams will be stored at high energy for hours. During this time collisions take place inside the four main LHC experiments.” <http://lhc.web.cern.ch/lhc/>.
- [14] S. Turbide, C. Gale, S. Jeon, and G. D. Moore, *Energy loss of leading hadrons and direct photon production in evolving quark-gluon plasma*, *Phys. Rev.* **C72** (2005) 014906, [[hep-ph/0502248](#)].
- [15] T. D. Lee and G. C. Wick, *Vacuum stability and vacuum excitation in a spin 0 field theory*, *Phys. Rev.* **D9** (1974) 2291.
- [16] J. C. Collins and M. J. Perry, *Superdense matter: Neutrons or asymptotically free quarks?*, *Phys. Rev. Lett.* **34** (1975) 1353.
- [17] G. Baym and S. A. Chin, *Can a neutron star be a giant mit bag?*, *Phys. Lett.* **B62** (1976) 241–244.
- [18] B. A. Freedman and L. D. McLerran, *Fermions and gauge vector mesons at finite temperature and density. 3. the ground state energy of a relativistic quark gas*, *Phys. Rev.* **D16** (1977) 1169.
- [19] G. Chapline and M. Nauenberg, *Asymptotic freedom and the baryon-quark phase transition*, *Phys. Rev.* **D16** (1977) 450.

- [20] “The Nobel Prize in Physics 2004.”
http://nobelprize.org/nobel_prizes/physics/laureates/2004/.
- [21] S. Bethke, *Experimental tests of asymptotic freedom*, *Prog. Part. Nucl. Phys.* **58** (2007) 351–386, [hep-ex/0606035].
- [22] **Particle Data Group** Collaboration, W. M. Yao *et al.*, *Review of particle physics*, *J. Phys.* **G33** (2006) 1–1232.
- [23] “The sun fact sheet.”
<http://nssdc.gsfc.nasa.gov/planetary/factsheet/sunfact.html>.
- [24] “The proposed project FAIR (Facility for Antiproton and Ion Research) is an international accelerator facility of the next generation. It builds on the experience and technological developments already made at the existing GSI facility, and incorporates new technological concepts. At its heart is a double ring facility with a circumference of of 1100 meters. A system of cooler-storage rings for effective beam cooling at high energies and various experimental halls will be connected to the facility .” <http://www.gsi.de/fair/>.
- [25] For a complete list of RHIC publications see Spires and use “FIND CN BRAHMS OR CN PHOBOS OR CN STAR OR CN PHENIX AND PS PUBLISHED”.
<http://www.slac.stanford.edu/spires/>.
- [26] C. R. Allton *et al.*, *The equation of state for two flavor qcd at non-zero chemical potential*, *Phys. Rev.* **D68** (2003) 014507, [hep-lat/0305007].
- [27] F. Karsch, E. Laermann, and A. Peikert, *The pressure in 2, 2+1 and 3 flavour qcd*, *Phys. Lett.* **B478** (2000) 447–455, [hep-lat/0002003].
- [28] F. Karsch, *Lattice qcd at high temperature and density*, *Lect. Notes Phys.* **583** (2002) 209–249, [hep-lat/0106019].
- [29] **MILC** Collaboration, C. W. Bernard *et al.*, *The equation of state for two flavor qcd at $n(t) = 6$* , *Phys. Rev.* **D55** (1997) 6861–6869, [hep-lat/9612025].
- [30] S. Gupta, *The quark gluon plasma: Lattice computations put to experimental test*, *Pramana* **61** (2003) 877–888, [hep-ph/0303072].
- [31] Z. Fodor and S. D. Katz, *Critical point of qcd at finite t and μ , lattice results for physical quark masses*, *JHEP* **04** (2004) 050, [hep-lat/0402006].
- [32] F. Csikor *et al.*, *The qcd equation of state at finite t/μ on the lattice*, *Prog. Theor. Phys. Suppl.* **153** (2004) 93–105, [hep-lat/0401022].
- [33] Y. Aoki, Z. Fodor, S. D. Katz, and K. K. Szabo, *The qcd transition temperature: Results with physical masses in the continuum limit*, *Phys. Lett.* **B643** (2006) 46–54, [hep-lat/0609068].
- [34] M. Cheng *et al.*, *The transition temperature in qcd*, *Phys. Rev.* **D74** (2006) 054507, [hep-lat/0608013].

-
- [35] M. Gyulassy and L. McLerran, *New forms of qcd matter discovered at rhic*, *Nucl. Phys.* **A750** (2005) 30–63, [nucl-th/0405013].
- [36] Z. Fodor and S. D. Katz, *A new method to study lattice QCD at finite temperature and chemical potential*, *Phys. Lett.* **B534** (2002) 87–92, [hep-lat/0104001].
- [37] P. de Forcrand and O. Philipsen, *The QCD phase diagram for small densities from imaginary chemical potential*, *Nucl. Phys.* **B642** (2002) 290–306, [hep-lat/0205016].
- [38] P. Braun-Munzinger and J. Stachel, *Probing the phase boundary between hadronic matter and the quark-gluon-plasma in relativistic heavy ion collisions*, *Nucl. Phys.* **A606** (1996) 320–328, [nucl-th/9606017].
- [39] O. Philipsen, *Exploring the QCD phase diagram*, 0710.1217.
- [40] M. A. Stephanov, *QCD phase diagram: An overview*, *PoS LAT2006* (2006) 024, [hep-lat/0701002].
- [41] M. G. Alford, *Color superconductivity in ultra-dense quark matter*, *PoS LAT2006* (2006) 001, [hep-lat/0610046].
- [42] P. Braun-Munzinger and J. Wambach, *The Phase Diagram of Strongly-Interacting Matter*, 0801.4256.
- [43] **BRAHMS** Collaboration, I. Arsene *et al.*, *Quark gluon plasma and color glass condensate at rhic? the perspective from the brahms experiment*, *Nucl. Phys.* **A757** (2005) 1–27, [nucl-ex/0410020].
- [44] B. B. Back *et al.*, *The phobos perspective on discoveries at rhic*, *Nucl. Phys.* **A757** (2005) 28–101, [nucl-ex/0410022].
- [45] **STAR** Collaboration, J. Adams *et al.*, *Experimental and theoretical challenges in the search for the quark gluon plasma: The star collaboration’s critical assessment of the evidence from rhic collisions*, *Nucl. Phys.* **A757** (2005) 102–183, [nucl-ex/0501009].
- [46] **PHENIX** Collaboration, K. Adcox *et al.*, *Formation of dense partonic matter in relativistic nucleus nucleus collisions at rhic: Experimental evaluation by the phenix collaboration*, *Nucl. Phys.* **A757** (2005) 184–283, [nucl-ex/0410003].
- [47] B. Muller and J. L. Nagle, *Results from the relativistic heavy ion collider*, *Ann. Rev. Nucl. Part. Sci.* **56** (2006) 93–135, [nucl-th/0602029].
- [48] B. Muller, *From Quark-Gluon Plasma to the Perfect Liquid*, *Acta Phys. Polon.* **B38** (2007) 3705–3730, [0710.3366].
- [49] U. W. Heinz, *Equation of state and collective dynamics*, *J. Phys. Conf. Ser.* **50** (2006) 230–237, [nucl-th/0504011].
- [50] F. Retiere, *Flow in ultra-relativistic heavy ion collisions*, *J. Phys.* **G30** (2004) S827–S834, [nucl-ex/0405024].

- [51] A. M. Poskanzer and S. A. Voloshin, *Methods for analyzing anisotropic flow in relativistic nuclear collisions*, *Phys. Rev.* **C58** (1998) 1671–1678, [nucl-ex/9805001].
- [52] U. W. Heinz, *Thermalization at rhic*, *AIP Conf. Proc.* **739** (2005) 163–180, [nucl-th/0407067].
- [53] P. Arnold, J. Lenaghan, G. D. Moore, and L. G. Yaffe, *Apparent thermalization due to plasma instabilities in quark gluon plasma*, *Phys. Rev. Lett.* **94** (2005) 072302, [nucl-th/0409068].
- [54] E. Shuryak, *A strongly coupled quark-gluon plasma*, *J. Phys.* **G30** (2004) S1221–S1224.
- [55] H. Sorge, *Highly sensitive centrality dependence of elliptic flow: A novel signature of the phase transition in qcd*, *Phys. Rev. Lett.* **82** (1999) 2048–2051, [nucl-th/9812057].
- [56] R. Baier, A. H. Mueller, D. Schiff, and D. T. Son, *'bottom-up' thermalization in heavy ion collisions*, *Phys. Lett.* **B502** (2001) 51–58, [hep-ph/0009237].
- [57] R. Baier, A. H. Mueller, D. Schiff, and D. T. Son, *Does parton saturation at high density explain hadron multiplicities at rhic?*, *Phys. Lett.* **B539** (2002) 46–52, [hep-ph/0204211].
- [58] Z. Xu and C. Greiner, *Thermalization of gluons in ultrarelativistic heavy ion collisions by including three-body interactions in a parton cascade*, *Phys. Rev.* **C71** (2005) 064901, [hep-ph/0406278].
- [59] P. Arnold, D. T. Son, and L. G. Yaffe, *Hot b violation, color conductivity, and $\log(1/\alpha)$ effects*, *Phys. Rev.* **D59** (1999) 105020, [hep-ph/9810216].
- [60] S. Mrowczynski, *Plasma instability at the initial stage of ultrarelativistic heavy ion collisions*, *Phys. Lett.* **B314** (1993) 118–121.
- [61] S. Mrowczynski, *Color collective effects at the early stage of ultrarelativistic heavy ion collisions*, *Phys. Rev.* **C49** (1994) 2191–2197.
- [62] J. Randrup and S. Mrowczynski, *Chromodynamic weibel instabilities in relativistic nuclear collisions*, *Phys. Rev.* **C68** (2003) 034909, [nucl-th/0303021].
- [63] P. Romatschke and M. Strickland, *Collective modes of an anisotropic quark gluon plasma*, *Phys. Rev.* **D68** (2003) 036004, [hep-ph/0304092].
- [64] P. Arnold, J. Lenaghan, and G. D. Moore, *Qcd plasma instabilities and bottom-up thermalization*, *JHEP* **08** (2003) 002, [hep-ph/0307325].
- [65] A. Rebhan, P. Romatschke, and M. Strickland, *Hard-loop dynamics of non-abelian plasma instabilities*, *Phys. Rev. Lett.* **94** (2005) 102303, [hep-ph/0412016].
- [66] A. Dumitru and Y. Nara, *Qcd plasma instabilities and isotropization*, *Phys. Lett.* **B621** (2005) 89, [hep-ph/0503121].

-
- [67] **PHENIX** Collaboration, M. Csanad, *Milestones of the PHENIX experiment at RHIC*, 0712.1435.
- [68] **PHENIX** Collaboration, S. S. Adler *et al.*, *Centrality dependence of direct photon production in $s(NN)^{1/2} = 200\text{-GeV}$ Au + Au collisions*, *Phys. Rev. Lett.* **94** (2005) 232301, [nucl-ex/0503003].
- [69] **STAR** Collaboration, J. Adams *et al.*, *Transverse momentum and collision energy dependence of high $p(T)$ hadron suppression in Au + Au collisions at ultrarelativistic energies*, *Phys. Rev. Lett.* **91** (2003) 172302, [nucl-ex/0305015].
- [70] **PHENIX** Collaboration, H. Busching *et al.*, *Medium effects on high particle production measured with the PHENIX experiment*, *Eur. Phys. J.* **C43** (2005) 303–310.
- [71] I. Vitev and M. Gyulassy, *High- $p(T)$ tomography of $d + Au$ and $Au + Au$ at SPS, RHIC, and LHC*, *Phys. Rev. Lett.* **89** (2002) 252301, [hep-ph/0209161].
- [72] D. d’Enterria, *High $p(T)$ leading hadron suppression in nuclear collisions at $s(NN)^{1/2} = 20\text{-GeV} - 200\text{-GeV}$: Data versus parton energy loss models*, *Eur. Phys. J.* **C43** (2005) 295–302, [nucl-ex/0504001].
- [73] **STAR** Collaboration, C. Adler *et al.*, *Disappearance of back-to-back high $p(t)$ hadron correlations in central au + au collisions at $s(nn)^{1/2} = 200\text{-gev}$* , *Phys. Rev. Lett.* **90** (2003) 082302, [nucl-ex/0210033].
- [74] **PHENIX** Collaboration, S. S. Adler *et al.*, *Modifications to di-jet hadron pair correlations in au + au collisions at $s(nn)^{1/2} = 200\text{-gev}$* , *Phys. Rev. Lett.* **97** (2006) 052301, [nucl-ex/0507004].
- [75] H. G. Baumgardt *et al.*, *Shock waves and mach cones in fast nucleus-nucleus collisions*, *Z. Phys.* **A273** (1975) 359–371.
- [76] H. Stoecker, B. Betz, and P. Rau, *Hydrodynamic flow and jet induced mach shocks at rhic and lhc*, *PoS CPOD2006* (2006) 029, [nucl-th/0703054].
- [77] B. Baeuchle, L. P. Csernai, and H. Stoecker, *Mace – mach cones in heavy ion collisions*, 0710.1476.
- [78] J. Putschke, *Intra-jet correlations of high- p_t hadrons from star*, *J. Phys.* **G34** (2007) S679–684, [nucl-ex/0701074].
- [79] **STAR** Collaboration, J. Adams *et al.*, *Minijet deformation and charge-independent angular correlations on momentum subspace (η , ϕ) in au-au collisions at $s(nn)^{1/2} = 130\text{-gev}$* , *Phys. Rev.* **C73** (2006) 064907, [nucl-ex/0411003].
- [80] K. Kajantie and H. I. Miettinen, *Temperature measurement of quark - gluon plasma formed in high-energy nucleus-nucleus collisions*, *Zeit. Phys.* **C9** (1981) 341.
- [81] F. Halzen and H. C. Liu, *Experimental signatures of phase transition to quark matter in high-energy collisions of nuclei*, *Phys. Rev.* **D25** (1982) 1842.

- [82] K. Kajantie and P. V. Ruuskanen, *Shielding of quark mass singularities in photon emission from hot quark - gluon plasma*, *Phys. Lett.* **B121** (1983) 352.
- [83] B. Sinha, *Universal signals of quark - gluon plasma*, *Phys. Lett.* **B128** (1983) 91–94.
- [84] R. C. Hwa and K. Kajantie, *Diagnosing quark matter by measuring the total entropy and the photon or dilepton emission rates*, *Phys. Rev.* **D32** (1985) 1109.
- [85] G. Staadt, W. Greiner, and J. Rafelski, *Photons from strange quark annihilation in quark - gluon plasma*, *Phys. Rev.* **D33** (1986) 66.
- [86] M. Neubert, *Photon production in ultrarelativistic heavy ion collisions at 200-gev/u*, *Z. Phys.* **C42** (1989) 231–242.
- [87] J. I. Kapusta, P. Lichard, and D. Seibert, *High-energy photons from quark - gluon plasma versus hot hadronic gas*, *Phys. Rev.* **D44** (1991) 2774–2788.
- [88] K. Redlich, R. Baier, H. Nakkagawa, and A. Niegawa, *Dynamical screening and real photon production in a hot quark gluon plasma*, *Nucl. Phys.* **A544** (1992) 511–512.
- [89] P. Aurenche, F. Gelis, R. Kobes, and H. Zaraket, *Bremsstrahlung and photon production in thermal QCD*, *Phys. Rev.* **D58** (1998) 085003, [hep-ph/9804224].
- [90] P. Aurenche, F. Gelis, and H. Zaraket, *Kln theorem, magnetic mass, and thermal photon production*, *Phys. Rev.* **D61** (2000) 116001, [hep-ph/9911367].
- [91] P. Arnold, G. D. Moore, and L. G. Yaffe, *Photon emission from ultrarelativistic plasmas*, *JHEP* **11** (2001) 057, [hep-ph/0109064].
- [92] P. Arnold, G. D. Moore, and L. G. Yaffe, *Photon emission from quark gluon plasma: Complete leading order results*, *JHEP* **12** (2001) 009, [hep-ph/0111107].
- [93] S. Turbide, R. Rapp, and C. Gale, *Hadronic production of thermal photons*, *Phys. Rev.* **C69** (2004) 014903, [hep-ph/0308085].
- [94] H. A. Weldon, *Reformulation of finite temperature dilepton production*, *Phys. Rev.* **D42** (1990) 2384–2387.
- [95] C. Gale and J. I. Kapusta, *Vector dominance model at finite temperature*, *Nucl. Phys.* **B357** (1991) 65–89.
- [96] R. Rapp, G. Chanfray, and J. Wambach, *Medium modifications of the rho meson at cern sps energies*, *Phys. Rev. Lett.* **76** (1996) 368–371, [hep-ph/9508353].
- [97] E. L. Bratkovskaya and W. Cassing, *Dilepton production from aqs to sps energies within a relativistic transport approach*, *Nucl. Phys.* **A619** (1997) 413–446, [nucl-th/9611042].
- [98] S. Leupold, W. Peters, and U. Mosel, *What qcd sum rules tell about the rho meson*, *Nucl. Phys.* **A628** (1998) 311–324, [nucl-th/9708016].

-
- [99] F. Cooper, *Inclusive dilepton production at rhic: A field theory approach based on a non-equilibrium chiral phase transition*, *Phys. Rept.* **315** (1999) 59–81, [hep-ph/9811246].
- [100] R. Rapp and J. Wambach, *Chiral symmetry restoration and dileptons in relativistic heavy-ion collisions*, *Adv. Nucl. Phys.* **25** (2000) 1, [hep-ph/9909229].
- [101] T. Renk, R. A. Schneider, and W. Weise, *Phases of qcd, thermal quasiparticles and dilepton radiation from a fireball*, *Phys. Rev.* **C66** (2002) 014902, [hep-ph/0201048].
- [102] J. Ruppert, T. Renk, and B. Muller, *Mass and width of the rho meson in a nuclear medium from Brown-Rho scaling and QCD sum rules*, *Phys. Rev.* **C73** (2006) 034907, [hep-ph/0509134].
- [103] B. Schenke and C. Greiner, *Dilepton production from hot hadronic matter in nonequilibrium*, *Phys. Rev.* **C73** (2006) 034909, [hep-ph/0509026].
- [104] B. Schenke and C. Greiner, *Dilepton yields from Brown-Rho scaled vector mesons including memory effects*, *Phys. Rev. Lett.* **98** (2007) 022301, [hep-ph/0608032].
- [105] G. E. Brown and M. Rho, *Scaling effective Lagrangians in a dense medium*, *Phys. Rev. Lett.* **66** (1991) 2720–2723.
- [106] T. Hatsuda and S. H. Lee, *QCD sum rules for vector mesons in nuclear medium*, *Phys. Rev.* **C46** (1992) 34–38.
- [107] **CERES** Collaboration, G. Agakichiev *et al.* *Phys. Rev. Lett.* **75** (1995) 1272.
- [108] **NA60** Collaboration, R. Arnaldi *et al.*, *First measurement of the rho spectral function in high- energy nuclear collisions*, *Phys. Rev. Lett.* **96** (2006) 162302, [nucl-ex/0605007].
- [109] H.-T. Elze and U. W. Heinz, *Quark - gluon transport theory*, *Phys. Rept.* **183** (1989) 81–135.
- [110] J. P. Blaizot and E. Iancu, *Kinetic equations for long wavelength excitations of the quark - gluon plasma*, *Phys. Rev. Lett.* **70** (1993) 3376–3379, [hep-ph/9301236].
- [111] J. P. Blaizot and E. Iancu, *Soft collective excitations in hot gauge theories*, *Nucl. Phys.* **B417** (1994) 608–673, [hep-ph/9306294].
- [112] P. F. Kelly, Q. Liu, C. Lucchesi, and C. Manuel, *Classical transport theory and hard thermal loops in the quark - gluon plasma*, *Phys. Rev.* **D50** (1994) 4209–4218, [hep-ph/9406285].
- [113] J.-P. Blaizot and E. Iancu, *The quark-gluon plasma: Collective dynamics and hard thermal loops*, *Phys. Rept.* **359** (2002) 355–528, [hep-ph/0101103].
- [114] E. Lifshitz and L. Pitaevskii, *Physical kinetics*, Pergamon Press, Oxford (1981).
- [115] A. D. Linde, *Infrared Problem in Thermodynamics of the Yang-Mills Gas*, *Phys. Lett.* **B96** (1980) 289.

-
- [116] R. D. Pisarski, *Scattering Amplitudes in Hot Gauge Theories*, *Phys. Rev. Lett.* **63** (1989) 1129.
- [117] E. Braaten and R. D. Pisarski, *Soft amplitudes in hot gauge theories: A general analysis*, *Nucl. Phys.* **B337** (1990) 569.
- [118] B. D. Witt *Phys. Rev.* **162** (1967) 1195.
- [119] B. S. DeWitt, *Quantum field theory in curved space-time*, *Phys. Rept.* **19** (1975) 295–357.
- [120] L. F. Abbott, *The background field method beyond one loop*, *Nucl. Phys.* **B185** (1981) 189.
- [121] T. H. Hansson and I. Zahed, *Electric and magnetic properties of hot gluons*, *Phys. Rev. Lett.* **58** (1987) 2397.
- [122] U. W. Heinz, *Quark - gluon transport theory. part 1. the classical theory*, *Ann. Phys.* **161** (1985) 48.
- [123] H. T. Elze, M. Gyulassy, and D. Vasak, *Transport equations for the qcd quark wigner operator*, *Nucl. Phys.* **B276** (1986) 706–728.
- [124] M. Gyulassy, H. T. Elze, A. Iwazaki, and D. Vasak, *Introduction to quantum chromo transport theory for quark - gluon plasmas*, . LBL-22072.
- [125] S. Mrowczynski and M. H. Thoma, *Hard loop approach to anisotropic systems*, *Phys. Rev.* **D62** (2000) 036011, [[hep-ph/0001164](#)].
- [126] H. A. Weldon, *Covariant calculations at finite temperature: The relativistic plasma*, *Phys. Rev.* **D26** (1982) 1394.
- [127] L. V. Gribov, E. M. Levin, and M. G. Ryskin, *Semihard Processes in QCD*, *Phys. Rept.* **100** (1983) 1–150.
- [128] A. H. Mueller and J.-w. Qiu, *Gluon Recombination and Shadowing at Small Values of x* , *Nucl. Phys.* **B268** (1986) 427.
- [129] J. P. Blaizot and A. H. Mueller, *The Early Stage of Ultrarelativistic Heavy Ion Collisions*, *Nucl. Phys.* **B289** (1987) 847.
- [130] L. D. McLerran and R. Venugopalan, *Computing quark and gluon distribution functions for very large nuclei*, *Phys. Rev.* **D49** (1994) 2233–2241, [[hep-ph/9309289](#)].
- [131] L. D. McLerran and R. Venugopalan, *Gluon distribution functions for very large nuclei at small transverse momentum*, *Phys. Rev.* **D49** (1994) 3352–3355, [[hep-ph/9311205](#)].
- [132] L. D. McLerran and R. Venugopalan, *Green's functions in the color field of a large nucleus*, *Phys. Rev.* **D50** (1994) 2225–2233, [[hep-ph/9402335](#)].

-
- [133] J. Jalilian-Marian, A. Kovner, L. D. McLerran, and H. Weigert, *The intrinsic glue distribution at very small x* , *Phys. Rev.* **D55** (1997) 5414–5428, [[hep-ph/9606337](#)].
- [134] Y. V. Kovchegov, *Non-Abelian Weizsaecker-Williams field and a two-dimensional effective color charge density for a very large nucleus*, *Phys. Rev.* **D54** (1996) 5463–5469, [[hep-ph/9605446](#)].
- [135] J. Jalilian-Marian, A. Kovner, A. Leonidov, and H. Weigert, *The BFKL equation from the Wilson renormalization group*, *Nucl. Phys.* **B504** (1997) 415–431, [[hep-ph/9701284](#)].
- [136] J. Jalilian-Marian, A. Kovner, A. Leonidov, and H. Weigert, *The Wilson renormalization group for low x physics: Towards the high density regime*, *Phys. Rev.* **D59** (1999) 014014, [[hep-ph/9706377](#)].
- [137] L. D. McLerran and R. Venugopalan, *Fock space distributions, structure functions, higher twists and small x* , *Phys. Rev.* **D59** (1999) 094002, [[hep-ph/9809427](#)].
- [138] A. Kovner and J. G. Milhano, *Vector potential versus colour charge density in low- x evolution*, *Phys. Rev.* **D61** (2000) 014012, [[hep-ph/9904420](#)].
- [139] E. Iancu, A. Leonidov, and L. D. McLerran, *Nonlinear gluon evolution in the color glass condensate. I*, *Nucl. Phys.* **A692** (2001) 583–645, [[hep-ph/0011241](#)].
- [140] E. Iancu, A. Leonidov, and L. D. McLerran, *The renormalization group equation for the color glass condensate*, *Phys. Lett.* **B510** (2001) 133–144, [[hep-ph/0102009](#)].
- [141] R. V. Gavai and R. Venugopalan, *Lattice computations of small- x parton distributions in a model of parton densities in very large nuclei*, *Phys. Rev.* **D54** (1996) 5795–5803, [[hep-ph/9605327](#)].
- [142] P. Romatschke and M. Strickland, *Collective modes of an anisotropic quark-gluon plasma. ii*, *Phys. Rev.* **D70** (2004) 116006, [[hep-ph/0406188](#)].
- [143] A. Dumitru, Y. Guo, and M. Strickland, *The heavy-quark potential in an anisotropic (viscous) plasma*, 0711.4722.
- [144] N. Krall and A. Trivelpiece, *Principles of plasma physics*, McGraw-Hill, New York (1973).
- [145] U. W. Heinz, *Quark - gluon transport theory*, *Nucl. Phys.* **A418** (1984) 603c–612c.
- [146] Y. E. Pokrovsky and A. V. Selikhov, *Filamentation in a quark - gluon plasma*, *JETP Lett.* **47** (1988) 12–14.
- [147] Y. E. Pokrovsky and A. V. Selikhov, *Filamentation in quark plasma at finite temperatures*, *Sov. J. Nucl. Phys.* **52** (1990) 146–152.
- [148] Y. E. Pokrovsky and A. V. Selikhov, *Filamentation in the quark-gluon plasma at finite temperatures*, *Sov. J. Nucl. Phys.* **52** (1990) 385–387.

- [149] S. Mrowczynski, *Stream instabilities of the quark - gluon plasma*, *Phys. Lett.* **B214** (1988) 587.
- [150] O. P. Pavlenko, *Dynamical instabilities in quark - gluon plasma with hard jet*, *Sov. J. Nucl. Phys.* **54** (1991) 884–886.
- [151] O. P. Pavlenko, *Filamentation instability of hot quark - gluon plasma with hard jet*, *Sov. J. Nucl. Phys.* **55** (1992) 1243–1245.
- [152] E. Weibel, *Spontaneously growing transverse waves in a plasma due to an anisotropic velocity distribution*, *Phys. Rev. Lett.* **2** (1959) 83–84.
- [153] M. C. Birse, C.-W. Kao, and G. C. Nayak, *Magnetic screening effects in anisotropic qed and qcd plasmas*, *Phys. Lett.* **B570** (2003) 171–179, [hep-ph/0304209].
- [154] S. Mrowczynski, A. Rebhan, and M. Strickland, *Hard-loop effective action for anisotropic plasmas*, *Phys. Rev.* **D70** (2004) 025004, [hep-ph/0403256].
- [155] P. Arnold, G. D. Moore, and L. G. Yaffe, *The fate of non-abelian plasma instabilities in 3+1 dimensions*, *Phys. Rev.* **D72** (2005) 054003, [hep-ph/0505212].
- [156] A. Rebhan, P. Romatschke, and M. Strickland, *Dynamics of quark-gluon plasma instabilities in discretized hard-loop approximation*, *JHEP* **09** (2005) 041, [hep-ph/0505261].
- [157] S. Mrowczynski, *Color filamentation in ultrarelativistic heavy-ion collisions*, *Phys. Lett.* **B393** (1997) 26–30, [hep-ph/9606442].
- [158] T. N. Kato, *Saturation mechanism of the weibel instability in weakly magnetized plasmas*, *Phys. Plasmas* **12** (2005) 080705, [physics/0501110].
- [159] P. Arnold and J. Lenaghan, *The abelianization of qcd plasma instabilities*, *Phys. Rev.* **D70** (2004) 114007, [hep-ph/0408052].
- [160] P. Arnold and G. D. Moore, *Qcd plasma instabilities: The nonabelian cascade*, *Phys. Rev.* **D73** (2006) 025006, [hep-ph/0509206].
- [161] A. Dumitru and Y. Nara, *Numerical simulation of non-abelian particle-field dynamics*, *Eur. Phys. J.* **A29** (2006) 65–69, [hep-ph/0511242].
- [162] A. Dumitru, Y. Nara, and M. Strickland, *Ultraviolet avalanche in anisotropic non-abelian plasmas*, *Phys. Rev.* **D75** (2007) 025016, [hep-ph/0604149].
- [163] P. Romatschke and A. Rebhan, *Plasma instabilities in an anisotropically expanding geometry*, *Phys. Rev. Lett.* **97** (2006) 252301, [hep-ph/0605064].
- [164] A. Rebhan, M. Strickland, and M. Attems, *Instabilities of an anisotropically expanding non-Abelian plasma: 1D+3V discretized hard-loop simulations*, 0802.1714.
- [165] P. Romatschke and R. Venugopalan, *Collective non-abelian instabilities in a melting color glass condensate*, *Phys. Rev. Lett.* **96** (2006) 062302, [hep-ph/0510121].

-
- [166] P. Romatschke and R. Venugopalan, *Signals of a weibel instability in the melting color glass condensate*, *Eur. Phys. J.* **A29** (2006) 71–75, [[hep-ph/0510292](#)].
- [167] P. Romatschke and R. Venugopalan, *The unstable glasma*, *Phys. Rev.* **D74** (2006) 045011, [[hep-ph/0605045](#)].
- [168] E. Iancu and R. Venugopalan, *The color glass condensate and high energy scattering in qcd*, [hep-ph/0303204](#).
- [169] P. L. Bhatnagar, E. P. Gross, and M. Krook, *A model for collision processes in gases. i. small amplitude processes in charged and neutral one-component systems*, *Phys. Rev.* **94** (1954) 511–525.
- [170] B. Schenke, M. Strickland, C. Greiner, and M. H. Thoma, *A model of the effect of collisions on qcd plasma instabilities*, *Phys. Rev.* **D73** (2006) 125004, [[hep-ph/0603029](#)].
- [171] C. Manuel and S. Mrowczynski, *Whitening of the quark-gluon plasma*, *Phys. Rev.* **D70** (2004) 094019, [[hep-ph/0403024](#)].
- [172] M. E. Carrington, T. Fugleberg, D. Pickering, and M. H. Thoma, *Dielectric functions and dispersion relations of ultra-relativistic plasmas with collisions*, *Can. J. Phys.* **82** (2004) 671–678, [[hep-ph/0312103](#)].
- [173] A. Selikhov and M. Gyulassy, *Color diffusion and conductivity in a quark - gluon plasma*, *Phys. Lett.* **B316** (1993) 373–380, [[nucl-th/9307007](#)].
- [174] D. Bodeker, *On the effective dynamics of soft non-abelian gauge fields at finite temperature*, *Phys. Lett.* **B426** (1998) 351–360, [[hep-ph/9801430](#)].
- [175] D. Bodeker, *From hard thermal loops to langevin dynamics*, *Nucl. Phys.* **B559** (1999) 502–538, [[hep-ph/9905239](#)].
- [176] P. Arnold, G. D. Moore, and L. G. Yaffe, *Effective kinetic theory for high temperature gauge theories*, *JHEP* **01** (2003) 030, [[hep-ph/0209353](#)].
- [177] M. H. Thoma, *Parton interaction rates in the quark - gluon plasma*, *Phys. Rev.* **D49** (1994) 451–459, [[hep-ph/9308257](#)].
- [178] E. Braaten and M. H. Thoma, *Energy loss of a heavy quark in the quark - gluon plasma*, *Phys. Rev.* **D44** (1991) 2625–2630.
- [179] P. Romatschke and M. Strickland, *Energy loss of a heavy fermion in an anisotropic qcd plasma*, *Phys. Rev.* **D69** (2004) 065005, [[hep-ph/0309093](#)].
- [180] P. Romatschke and M. Strickland, *Collisional energy loss of a heavy quark in an anisotropic quark-gluon plasma*, *Phys. Rev.* **D71** (2005) 125008, [[hep-ph/0408275](#)].
- [181] A. Peshier, *Hard gluon damping in hot qcd*, *Phys. Rev.* **D70** (2004) 034016, [[hep-ph/0403225](#)].

- [182] A. Peshier and W. Cassing, *The hot non-perturbative gluon plasma is an almost ideal colored liquid*, *Phys. Rev. Lett.* **94** (2005) 172301, [[hep-ph/0502138](#)].
- [183] A. Krasnitz and R. Venugopalan, *Non-perturbative computation of gluon mini-jet production in nuclear collisions at very high energies*, *Nucl. Phys.* **B557** (1999) 237, [[hep-ph/9809433](#)].
- [184] A. Krasnitz and R. Venugopalan, *The initial energy density of gluons produced in very high energy nuclear collisions*, *Phys. Rev. Lett.* **84** (2000) 4309–4312, [[hep-ph/9909203](#)].
- [185] A. Krasnitz, Y. Nara, and R. Venugopalan, *Coherent gluon production in very high energy heavy ion collisions*, *Phys. Rev. Lett.* **87** (2001) 192302, [[hep-ph/0108092](#)].
- [186] A. Krasnitz, Y. Nara, and R. Venugopalan, *Gluon production in the color glass condensate model of collisions of ultrarelativistic finite nuclei*, *Nucl. Phys.* **A717** (2003) 268–290, [[hep-ph/0209269](#)].
- [187] A. Krasnitz, Y. Nara, and R. Venugopalan, *Classical gluodynamics of high energy nuclear collisions: An erratum and an update*, *Nucl. Phys.* **A727** (2003) 427–436, [[hep-ph/0305112](#)].
- [188] A. Krasnitz, Y. Nara, and R. Venugopalan, *Elliptic flow of colored glass in high energy heavy ion collisions*, *Phys. Lett.* **B554** (2003) 21–27, [[hep-ph/0204361](#)].
- [189] U. W. Heinz, *Kinetic theory for nonabelian plasmas*, *Phys. Rev. Lett.* **51** (1983) 351.
- [190] U. W. Heinz, *Quark - gluon transport theory. part 2. color response and color correlations in a quark - gluon plasma*, *Ann. Phys.* **168** (1986) 148.
- [191] S. K. Wong, *Field and particle equations for the classical yang-mills field and particles with isotopic spin*, *Nuovo Cim.* **A65S10** (1970) 689–694.
- [192] D. F. Litim and C. Manuel, *Effective transport equations for non-Abelian plasmas*, *Nucl. Phys.* **B562** (1999) 237–274, [[hep-ph/9906210](#)].
- [193] D. F. Litim and C. Manuel, *Mean field dynamics in non-Abelian plasmas from classical transport theory*, *Phys. Rev. Lett.* **82** (1999) 4981–4984, [[hep-ph/9902430](#)].
- [194] G. F. Bertsch and S. Das Gupta, *A guide to microscopic models for intermediate-energy heavy ion collisions*, *Phys. Rept.* **160** (1988) 189–233.
- [195] J. Ambjorn, T. Askgaard, H. Porter, and M. E. Shaposhnikov, *Sphaleron transitions and baryon asymmetry: A numerical real time analysis*, *Nucl. Phys.* **B353** (1991) 346–378.
- [196] C. R. Hu and B. Muller, *Classical lattice gauge field with hard thermal loops*, *Phys. Lett.* **B409** (1997) 377–381, [[hep-ph/9611292](#)].
- [197] G. D. Moore, C.-r. Hu, and B. Muller, *Chern-simons number diffusion with hard thermal loops*, *Phys. Rev.* **D58** (1998) 045001, [[hep-ph/9710436](#)].

-
- [198] R. W. Hockney and J. Eastwood, *Computer Simulation using Particles*. MacGraw-Hill, New York, 1981.
- [199] C. Birdsall and A. Langdon, *Plasma Physics via Computer Simulation*. MacGraw-Hill, New York, 1985.
- [200] J. Eastwood, *The virtual particle electromagnetic particle-mesh method*, *Computer Physics Communications* **64** (1991) 252–266.
- [201] T. Umeda, Y. Omura, T. Tominaga, and H. Matsumoto, *A new charge conservation method in electromagnetic particle-in-cell simulations*, *Comput. Phys. Comm.* **156** (2003) 73.
- [202] T. Kodama, S. B. Duarte, K. C. Chung, R. Donangelo, and R. A. M. S. Nazareth, *Causality and relativistic effects in intranuclear cascade calculations*, *Phys. Rev. C* **29** (Jun, 1984) 2146–2152.
- [203] G. Kortemeyer, W. Bauer, K. Haglin, J. Murray, and S. Pratt, *Causality violations in cascade models of nuclear collisions*, *Phys. Rev.* **C52** (1995) 2714–2724, [[nucl-th/9509013](#)].
- [204] B. Zhang, M. Gyulassy, and Y. Pang, *Equation of state and collision rate tests of parton cascade models*, *Phys. Rev.* **C58** (1998) 1175–1182, [[nucl-th/9801037](#)].
- [205] S. Cheng *et al.*, *The effect of finite-range interactions in classical transport theory*, *Phys. Rev.* **C65** (2002) 024901, [[nucl-th/0107001](#)].
- [206] G. Welke, R. Malfiet, C. Grégoire, M. Prakash, and E. Suraud, *Collisional relaxation in simulations of heavy-ion collisions using boltzmann-type equations*, *Phys. Rev. C* **40** (Dec, 1989) 2611–2620.
- [207] D. Molnar and M. Gyulassy, *Saturation of elliptic flow at rhic: Results from the covariant elastic parton cascade model mpc*, *Nucl. Phys.* **A697** (2002) 495–520, [[nucl-th/0104073](#)].
- [208] X.-M. Xu, Y. Sun, A.-Q. Chen, and L. Zheng, *Triple-gluon scatterings and early thermalization*, *Nucl. Phys.* **A744** (2004) 347–377.
- [209] Z. Xu and C. Greiner, *Transport rates and momentum isotropization of gluon matter in ultrarelativistic heavy-ion collisions*, *Phys. Rev.* **C76** (2007) 024911, [[hep-ph/0703233](#)].
- [210] P. Danielewicz and G. F. Bertsch, *Production of deuterons and pions in a transport model of energetic heavy ion reactions*, *Nucl. Phys.* **A533** (1991) 712–748.
- [211] A. Lang, H. Babovsky, W. Cassing, U. Mosel, H. Reusch, and K. Weber, *A new treatment of boltzmann-like collision integrals in nuclear kinetic equations*, *J. Comp. Phys.* **106** (1993) 391–396.
- [212] S. de Groot, W. van Leeuwen, and C. van Weert, *Relativistic Kinetic Theory: Principles and Applications*. North Holland, Amsterdam, 1980.

- [213] B. L. Combridge, J. Kripfganz, and J. Ranft, *Hadron production at large transverse momentum and qcd*, *Phys. Lett.* **B70** (1977) 234.
- [214] J. F. Owens, E. Reya, and M. Gluck, *Detailed quantum chromodynamic predictions for high $p(t)$ processes*, *Phys. Rev.* **D18** (1978) 1501.
- [215] Z. Bern, A. De Freitas, and L. J. Dixon, *Two-loop helicity amplitudes for gluon gluon scattering in qcd and supersymmetric yang-mills theory*, *JHEP* **03** (2002) 018, [hep-ph/0201161].
- [216] W. Press, S. Teukolsky, W. Vetterling, and B. Flannery, *Numerical Recipes in C*. Cambridge University Press, 1992.
- [217] R. Baier, Y. L. Dokshitzer, A. H. Mueller, S. Peigne, and D. Schiff, *Radiative energy loss and $p(t)$ -broadening of high energy partons in nuclei*, *Nucl. Phys.* **B484** (1997) 265–282, [hep-ph/9608322].
- [218] A. Majumder, *A comparative study of jet-quenching schemes*, *J. Phys.* **G34** (2007) S377–388, [nucl-th/0702066].
- [219] A. Dumitru, Y. Nara, B. Schenke, and M. Strickland, *Jet broadening in unstable non-abelian plasmas*, 0710.1223.
- [220] Y. Nara, *Isotropization by qcd plasma instabilities*, *Nucl. Phys.* **A774** (2006) 783–786, [nucl-th/0509052].
- [221] P. Arnold and G. D. Moore, *The turbulent spectrum created by non-abelian plasma instabilities*, *Phys. Rev.* **D73** (2006) 025013, [hep-ph/0509226].
- [222] G. D. Moore and D. Teaney, *How much do heavy quarks thermalize in a heavy ion collision?*, *Phys. Rev.* **C71** (2005) 064904, [hep-ph/0412346].
- [223] P. Romatschke, *Momentum broadening in an anisotropic plasma*, *Phys. Rev.* **C75** (2007) 014901, [hep-ph/0607327].
- [224] P. Jacobs, *Jets in nuclear collisions: Status and perspective*, *Eur. Phys. J.* **C43** (2005) 467–473, [nucl-ex/0503022].
- [225] A. Majumder, B. Muller, and S. A. Bass, *Longitudinal broadening of quenched jets in turbulent color fields*, *Phys. Rev. Lett.* **99** (2007) 042301, [hep-ph/0611135].
- [226] N. Armesto, C. A. Salgado, and U. A. Wiedemann, *Low- $p(t)$ collective flow induces high- $p(t)$ jet quenching*, *Phys. Rev.* **C72** (2005) 064910, [hep-ph/0411341].
- [227] S. Mrowczynski, *Quasiquarks in two stream system*, *Phys. Rev.* **D65** (2002) 117501, [hep-ph/0112100].
- [228] H. Stooft *et al.* *Phys. Rev. Lett.* **76** (1996) 10.
- [229] M. Houbiers *et al.* *Phys. Rev.* **A56** (1997) 4864.
- [230] M. Holland *et al.* *Phys. Rev. Lett.* **87** (2001) 120406.

-
- [231] E. Timmermans *et al.* *Phys. Lett.* **A285** (2001) 228.
- [232] Y. Ohashi and A. Griffin *Phys. Rev. Lett.* **89** (2002) 130402.
- [233] J. Kinast, S. Hemmer, M. Gehm, A. Turlapov, and J. Thomas *Phys. Rev. Lett.* **92** (2004) 150402.
- [234] B. Schenke and M. Strickland, *Fermionic collective modes of an anisotropic quark-gluon plasma*, *Phys. Rev.* **D74** (2006) 065004, [hep-ph/0606160].
- [235] P. Romatschke, *Quasiparticle description of the hot and dense quark gluon plasma*, hep-ph/0312152.
- [236] B. Schenke and M. Strickland, *Photon production from an anisotropic quark-gluon plasma*, *Phys. Rev.* **D76** (2007) 025023, [hep-ph/0611332].
- [237] H. A. Weldon, *Simple rules for discontinuities in finite temperature field theory*, *Phys. Rev.* **D28** (1983) 2007.
- [238] L. D. McLerran and T. Toimela, *Photon and dilepton emission from the quark - gluon plasma: Some general considerations*, *Phys. Rev.* **D31** (1985) 545.
- [239] L. Keldysh *Zh. Eks. Teor. Fiz.* **47** (1964) 1515.
- [240] L. Keldysh *Sov. Phys. JETP* **20** (1965) 1018.
- [241] K.-c. Chou, Z.-b. Su, B.-l. Hao, and L. Yu, *Equilibrium and nonequilibrium formalisms made unified*, *Phys. Rept.* **118** (1985) 1.
- [242] S. Mrowczynski and U. W. Heinz, *Towards a relativistic transport theory of nuclear matter*, *Ann. Phys.* **229** (1994) 1–54.
- [243] E. Calzetta and B. L. Hu, *Nonequilibrium quantum fields: Closed time path effective action, wigner function and boltzmann equation*, *Phys. Rev.* **D37** (1988) 2878.
- [244] R. Baier, M. Dirks, K. Redlich, and D. Schiff, *Thermal photon production rate from non-equilibrium quantum field theory*, *Phys. Rev.* **D56** (1997) 2548–2554, [hep-ph/9704262].
- [245] F. Halzen and A. Martin, *Quarks & Leptons*. John Wiley & Sons, New York, 1984.
- [246] M. Peskin and D. Schroeder, *An Introduction to Quantum Field Theory*. Westview Press, 1995.
- [247] E. Braaten and T. C. Yuan, *Calculation of screening in a hot plasma*, *Phys. Rev. Lett.* **66** (1991) 2183–2186.
- [248] R. Baier, H. Nakkagawa, A. Niegawa, and K. Redlich, *Production rate of hard thermal photons and screening of quark mass singularity*, *Z. Phys.* **C53** (1992) 433–438.

- [249] C. Greiner and S. Leupold, *Stochastic interpretation of kadanoff-baym equations and their relation to langevin processes*, *Annals Phys.* **270** (1998) 328–390, [hep-ph/9802312].
- [250] A. Ipp, A. Di Piazza, J. Evers, and C. H. Keitel, *Photon polarization as a probe for quark-gluon plasma dynamics*, 0710.5700.
- [251] M. Martinez and M. Strickland, *Measuring QGP thermalization time with dileptons*, *Phys. Rev. Lett.* **100** (2008) 102301, [0709.3576].
- [252] M. Martinez and M. Strickland *forthcoming*.
- [253] J.-Y. Ollitrault, *Relativistic hydrodynamics*, 0708.2433.
- [254] D. Bodeker, *The impact of QCD plasma instabilities on bottom-up thermalization*, *JHEP* **10** (2005) 092, [hep-ph/0508223].
- [255] M. Tatarakis, F. N. Beg, E. L. Clark, A. E. Dangor, R. D. Edwards, R. G. Evans, T. J. Goldsack, K. W. D. Ledingham, P. A. Norreys, M. A. Sinclair, M.-S. Wei, M. Zepf, and K. Krushelnick, *Propagation instabilities of high-intensity laser-produced electron beams*, *Phys. Rev. Lett.* **90** (2003) 175001.
- [256] A. Bret, M.-C. Firpo, and C. Deutsch, *Characterization of the initial filamentation of a relativistic electron beam passing through a plasma*, *Phys. Rev. Lett.* **94** (2005) 115002.
- [257] M. Tabak *et al.*, *Ignition and high gain with ultrapowerful lasers*, *Phys. Plasmas* **1** (1994) 1626.
- [258] R. Kodama *et al.* *Nature* **412** (2001) 798.
- [259] J.-P. Blaizot and E. Iancu, *Nonabelian plane waves in the quark - gluon plasma*, *Phys. Lett.* **B326** (1994) 138–144, [hep-ph/9401323].
- [260] J. B. Kogut and L. Susskind, *Hamiltonian formulation of wilson's lattice gauge theories*, *Phys. Rev.* **D11** (1975) 395.
- [261] K. G. Wilson, *Confinement of quarks*, *Phys. Rev.* **D10** (1974) 2445–2459.
- [262] L. D. Landau and E. M. Lifschitz, *Lehrbuch der Theoretischen Physik, Klassische Feldtheorie*. Harri Deutsch, Thun und Frankfurt am Main, 1997.
- [263] C. Greiner and S. Leupold, *Interpretation and resolution of pinch singularities in non-equilibrium quantum field theory*, *Eur. Phys. J.* **C8** (1999) 517–522, [hep-ph/9804239].

Danksagung

Zuallererst möchte ich mich bei meinen Eltern für Ihre Unterstützung bedanken, die mir das Studium der Physik und die Erstellung dieser Arbeit erst ermöglicht hat.

Mein Dank gilt auch besonders Prof. Dr. Carsten Greiner für die Themenstellung und die Betreuung dieser Arbeit. Mit großem Interesse hat er sie begleitet und ihre Entwicklung verfolgt, mir aber auch in vielen Punkten die nötige Freiheit gelassen.

Ebenso danke ich Dr. Michael Strickland für die tolle Zusammenarbeit, seine Hilfe und Unterstützung bei Problemen, viele erleuchtende Diskussionen und auch für das Korrekturlesen dieser Arbeit.

Ich danke JProf. Dr. Adrian Dumitru für die gute Zusammenarbeit, Hilfsbereitschaft und viele hilfreiche Diskussionen.

Dr. Yasushi Nara danke ich für die Einführung in die numerische Simulation und seine Geduld, mit der er alle meine Fragen beantwortet hat.

Ich danke Dr. Zhe Xu, Oliver Fochler und Dr. Paul Romatschke für viele hilfreiche Diskussionen und Erläuterungen ihrer Arbeit.

Zudem danke ich meinem Zimmerkollegen Oliver Fochler für viele auch über die Physik hinausführende Gespräche, die großartige Arbeitsatmosphäre und eine tolle Zeit an der Uni.

Ich danke Barbara Betz, JProf. Dr. Marcus Bleicher, Andreas Ipp, Mauricio Martinez, Hannah Petersen und Sascha Vogel für einige hilfreiche Diskussionen und/oder Erklärungen.

Auch danke ich Prof. Dr. Horst Stöcker für sein Interesse an meiner Arbeit.

Ich danke Joe Laperal-Gomez, Denise Meixler, Gabriela Meyer, Veronica Palade, Daniela Radulescu und Astrid Steidl für ihre Hilfe in vielen Angelegenheiten.

Alexander Achenbach, Thilo Kalkbrenner und Oliver Fochler danke ich für ihre schnelle Hilfe bei all meinen Computerproblemen.

Ebenso danke ich dem Team des Center for Scientific Computing für die Bereitstellung von enorm viel Rechenleistung und ihre Hilfe im Falle von Problemen.

Ich danke dem Institute for Nuclear Theory and der University of Washington, an dem ein Teil dieser Arbeit entstanden ist, für seine Gastfreundschaft und Unterstützung.

Diese Arbeit wurde von der Deutschen Forschungsgemeinschaft unterstützt (DFG Grant GR 1536/6-1).

Acknowledgments

First I want to thank my parents for their support, which made my studies and this work possible.

I thank my supervisor Prof. Dr. Carsten Greiner for his advise and help, for his continued interest in my work and for giving me a lot of freedom, which is so important in research.

I thank Dr. Michael Strickland for great collaboration, his help and advise, many enlightening discussions and for proof reading this work.

I thank JProf. Dr. Adrian Dumitru for his collaboration, his constant will to help, and for many useful discussions.

I thank Dr. Yasushi Nara for introducing me to the numerical simulation and for his patience in answering all my questions.

I thank Dr. Zhe Xu, Oliver Fochler, and Dr. Paul Romatschke for many helpful discussions and explanations of their work.

In addition I thank my office-mate Oliver Fochler for many additional discussions beyond physics, a fun work environment and a great time at the university.

I thank Barbara Betz, JProf. Dr. Marcus Bleicher, Andreas Ipp, Mauricio Martinez, Hannah Petersen and Sascha Vogel for some helpful discussions and/or explanations.

I also thank Prof. Dr. Horst Stöcker for his interest in my work.

I thank Joe Laperal-Gomez, Denise Meixler, Gabriela Meyer, Veronica Palade, Daniela Radulescu and Astrid Steidl for their help with many issues.

I thank Alexander Achenbach, Thilo Kalkbrenner and Oliver Fochler for their help with all my computer problems.

I also thank the team of the Center for Scientific Computing for providing a huge amount of computer power and their help in case of problems.

I thank the Institute for Nuclear Theory at the University of Washington, where part of this work was done, for its hospitality and support.

This work was supported by the Deutsche Forschungsgemeinschaft (DFG Grant GR 1536/6-1).

Index

- Anisotropy, 31
- Background field gauge, 12
- Bremsstrahlung, 111
- Buneman-Boris-method, 71
- Collisions, 36, 45, 72
 - BGK collision term, 45
 - Boltzmann collision term, 73
 - Effect on instabilities, 52, 89
- Color factor, 116
- Color Glass Condensate, 32, 42
- Compton scattering, 113
- CPIC, 68
- Cross section, 73, 74, 113
- Debye mass, 27, 33
- Dispersion relations, 27, 34, 105
- Elliptic flow, 5
- Equilibration, 5, 36
- Fermionic collective modes, 101
- Filamentation, 37
- Fluctuation dissipation relation, 161
- Gauge fixing, 12, 141
- Generating functional, 13, 14
- Ghost fields, 13
- Gradient expansion, 17, 19
- HL approximation, 119
- HTL approximation, 26, 27
- Induced current, 11, 19, 23, 46, 48
- Instabilities, 35
 - Growth rate of, 35
 - Weibel instability, 35–37, 85, 143
- Isotropic limit, 27, 33, 125
- Isotropization, 5, 38, 41, 91
- Jets, 7, 77, 93
- Kadanoff-Baym equations, 19
- Keldysh formalism, 112
- KMS relation, 122
- Kogut-Susskind Hamiltonian, 63, 149
- Lattice QCD, 3
- Lattice units, 63
- Mandelstam variables, 75, 114
- Matrix element, 113
- Mean field approximation, 16
- Momentum diffusion, 77
- Momentum exchange, 76
- Nyquist analysis, 106, 108
- Particle-In-Cell, 64
- Photon production, 111
 - Hard contribution, 117
 - Production rate, 112
 - Soft contribution, 119
- \hat{q} , 80
- Relative velocity, 74, 157
- Separation scale, 77
- Structure functions, 33
- Tensor decomposition, 33
- Transition probability, 74
- Vlasov equation, 21, 61
 - Gluon Vlasov equation, 21
 - Quark Vlasov equation, 22
- Wong equations, 59

Lebenslauf

Persönliche Daten

Name: Björn Peter Schenke
Geburtsdatum: 13. September 1978
Geburtsort: Iserlohn
Nationalität: Deutsch

Adresse:

Im Holzhain 28
61206 Wöllstadt
Deutschland
E-Mail: schenke@th.physik.uni-frankfurt.de

Ausbildung

- | | |
|--------------|--|
| Juni 1998 | Abitur
Augustinerschule, Friedberg (Hessen), Gymnasium
Abschlussnote: 1,4 |
| Oktober 1999 | Studium an der <i>Justus-Liebig-Universität, Gießen</i>
Vorlesungen bei <ul style="list-style-type: none">• PD Dr. Adam• Prof. Dr. Bartsch• Prof. Dr. Beutelspacher• Prof. Dr. Bolterauer• Prof. Dr. Buhmann• Prof. Dr. Bunde• PD Dr. Dormeyer• Prof. Dr. Grün• Prof. Dr. Kohl• PD Dr. Lani-Wayda• Prof. Dr. Metag• Prof. Dr. Meyer• Prof. Dr. Mosel• Dr. Novotny• PD Dr. Ritman• Prof. Dr. Salzborn• Prof. Dr. Schartner |

- September 2001 Vordiplom in Physik
Abschlussnote: 1,0
- September 2001 Hauptstudium an der *Justus-Liebig-Universität, Gießen*
Vorlesungen bei (siehe oben)
- September 2002 Auslandsaufenthalt an der
University of Washington, Seattle, USA
im Rahmen des ISAP Programms (DAAD) der
Universität Gießen
Vorlesungen bei
- Prof. Dr. Boynton
 - Prof. Dr. Bulgac
 - Prof. Dr. Ellis
 - Prof. Dr. Kaplan
 - Prof. Dr. Nelson
 - Independent Studies bei Prof. Dr. Bardeen
- Juli 2003 Hauptstudium an der
Johann Wolfgang Goethe-Universität, Frankfurt
Vorlesungen bei
- PD Dr. Bratkovskaya
 - JProf. Dr. Dumitru
 - Prof. Dr. Gyulassy
 - Prof. Dr. Kersting
 - Prof. Dr. Mishustin
- November 2004 Diplom in Physik
Abschlussnote: 1,0 - mit Auszeichnung bestanden
Titel der Diplomarbeit:
“Dilepton production from hot hadronic matter in nonequilibrium”
Betreuer: Prof. Dr. C. Greiner
- Dezember 2004 Arbeit an der Doktorarbeit
an der *Johann Wolfgang Goethe-Universität, Frankfurt*
Voraussichtliches Ende: 2008
Betreuer: Prof. Dr. C. Greiner

Berufserfahrung

Ersatzdienst	Juli 1998 bis August 1999 Lebenshilfe, Wetteraukreis - Friedberg Familienentlastender Dienst Betreuung von Menschen mit geistiger Behinderung
Nebentätigkeit	seit September 1993 Ernst Stähler KG Friedberg - Friedberg EDV Betreuung
Semesterjobs	Oktober 2001 bis Juli 2002 <i>Justus-Liebig-Universität, Gießen</i> Betreuung des physikalischen Praktikums für Biologen Oktober 2003 bis Juli 2004 <i>Johann Wolfgang Goethe-Universität, Frankfurt</i> Betreuung der Übungen zur Thermodynamik und Quantenmechanik II
Wissenschaftlicher Mitarbeiter	seit November 2004 <i>Johann Wolfgang Goethe-Universität, Frankfurt</i> Forschung (siehe Publikationen) und Lehre in Übungen zu den Vorlesungen Kosmologie, allgemeine Relativitätstheorie, Mechanik und Vielteilchentheorie, Mitbetreuung von Diplo- manden auf dem Gebiet der Nichtgleichgewichts-Feldtheorie sowie der QCD-Plasma-Simulationen

Fremdsprachen

- Englisch (Verhandlungssicher)
- Französisch (gute Kenntnisse)
- Japanisch (Basis-Kenntnisse)

Liste der Publikationen**Referierte Publikationen**

1. B. Schenke and M. Strickland
“Photon production from an anisotropic quark-gluon plasma,”
Phys. Rev. D **76** (2006) 025023 [arXiv:hep-ph/0611332].

2. B. Schenke and C. Greiner
“Dilepton yields from Brown-Rho scaled vector mesons including memory effects,”
Phys. Rev. Lett. **98** (2007) 022301 [arXiv:hep-ph/0608032].
3. B. Schenke and C. Greiner
“Nonequilibrium dilepton production in dropping mass scenarios,”
Nucl.Phys.A**785** (2007) 170c
4. B. Schenke and M. Strickland
“Fermionic collective modes of an anisotropic quark-gluon plasma,”
Phys. Rev. D **74** (2006) 065004 [arXiv:hep-ph/0606160].
5. B. Schenke and C. Greiner
“Nonequilibrium Description Of Dilepton Production In Heavy Ion Reactions,”
J. Phys. Conf. Ser. **35** (2006) 398
6. B. Schenke, M. Strickland, C. Greiner and M. H. Thoma
“A model of the effect of collisions on QCD plasma instabilities,”
Phys. Rev. D **73** (2006) 125004 [arXiv:hep-ph/0603029].
7. B. Schenke and C. Greiner
“Dilepton production from hot hadronic matter in nonequilibrium,”
Phys. Rev. C **73** (2006) 034909 [arXiv:hep-ph/0509026].
8. B. Schenke and C. Greiner
“Statistical description with anisotropic momentum distributions for hadron production in nucleus nucleus collisions,”
J. Phys. G **30** (2004) 597 [arXiv:nucl-th/0305008].

weitere Publikationen

1. A. Dumitru, Y. Nara, B. Schenke, and M. Strickland
“Jet broadening in unstable non-Abelian plasmas,”
eingereicht bei Phys. Rev. Lett. [arXiv:0710.1223].
2. C. Greiner and B. Schenke
“Dileptons from vector mesons with dropping masses in a nonequilibrium quantum field theoretical framework,”
To appear in the proceedings of 22nd Winter Workshop on Nuclear Dynamics, La Jolla, California, 11-19 Mar 2006
arXiv:hep-ph/0606028.
3. B. Schenke and C. Greiner
“Dilepton production from non-equilibrium hot hadronic matter,”
Appeared in the proceedings of the 43rd International Winter Meeting on Nuclear Physics, Bormio, Italy, 13-20 Mar 2005
arXiv:hep-ph/0504278.

Vorträge

- 03.01.2005
Dilepton production from hot hadronic matter in nonequilibrium
37. RNM Workshop, GSI - Darmstadt, Deutschland
- 08.03.2005
Dilepton production from hot hadronic matter in nonequilibrium
69. Jahrestagung der DPG, Berlin, Deutschland
- 16.03.2005
Dilepton production from hot hadronic matter in nonequilibrium
XLIII International Winter Meeting on Nuclear Physics, Bormio, Italien
- 09.06.2005
Dilepton production from hot hadronic matter in nonequilibrium
Workshop on Electromagnetic probes of hot and dense matter, ECT*, Trento, Italien
- 26.09.2005
Nonequilibrium dilepton production from hot hadronic matter
Seminarvortrag bei der Nuclear Theory Group des
Lawrence Berkeley National Laboratory, Berkeley, USA
- 24.03.2006
Dilepton yield from Brown-Rho scaled vector mesons including memory effects
70. Jahrestagung der DPG, München
- 24.03.2006
The effect of collisions on QCD plasma instabilities
70. Jahrestagung der DPG, München
- 11.05.2006
Nonequilibrium dilepton production in dropping mass scenarios
International Conference on Strong and Electroweak Matter
Brookhaven National Laboratory, Upton, New York, USA
- 26.09.2006
QGP instabilities under the influence of collisions
and
Fermionic collective modes of an anisotropic QGP
INT Workshop on Non-Equilibrium Quark-Gluon Plasma
Institute for Nuclear Theory, University of Washington, Seattle, Washington, USA
- 12.03.2007
Photon production from an anisotropic quark-gluon-plasma
71. Jahrestagung der DPG, Gießen
- 22.06.2007
Quantum transport with memory effects
Workshop on Electromagnetic probes of strongly interacting matter, ECT*, Trento, Italien

- 25.07.2007
CPIC - a cutoff free parton cascade
INT Special Seminar
Institute for Nuclear Theory, University of Washington, Seattle, Washington, USA
- 13.09.2007
Simulations of QGP instabilities in A+A collisions
Eingeladener Vortrag beim Workshop on Heavy Ion Physics Perspectives
Virtual Institute on Strongly Interacting Matter, Bad Liebenzell
- 08.02.2008
QGP collective effects and jet transport
Quark Matter 2008, Jaipur, Indien
- 13.03.2008
Jet propagation and QGP collective phenomena
72. Jahrestagung der DPG, Darmstadt

weitere Workshops und Präsentationen

- IPP Summer University for Plasma Physics
17-21 September 2001
MPI für Plasmaphysik, Garching
- Workshop of the Virtual Institute:
Dense Hadronic Matter & QCD phase transition
2.-4. Juli 2004
Physik-Zentrum Bad Honnef
- Workshop on In-Medium Hadron Physics
11.-13. November 2004
Justus-Liebig-Universität, Gießen
- Präsentation beim Interdisciplinary Workshop on
Progress in Nonequilibrium Green's Functions III
22.-26. August 2005, Universität Kiel
- INT Workshop: From RHIC to LHC: Achievements and Opportunities
25. September - 15. Oktober 2006
Institute for Nuclear Theory, University of Washington, Seattle, Washington, USA
- XXXVIII. Arbeitstreffen Kernphysik Schleching
22. Februar - 1 März 2007
Schleching
- Präsentation beim Workshop ETD-HIC
Early Time Dynamics in Heavy Ion Collisions
16. Juli - 19. Juli 2007
McGill University, Montreal, Kanada